Numerical study of axisymetric-bodies freely falling in Newtonian fluids

Marcin Chrust

UNIVERSITÉ DE STRASBOURG

École Doctorale Mathématiques,
Sciences de l'Information et de l'Ingénieur -
Institut de Mécanique des Fluides et des Solides de Strasbourg

THÈSE présentée par :

Marcin Chrust

sutenue le : 20 septembre 2012

pour obtenir le grade de: **Docteur de l'Université de Strasbourg**

Discipline : Mécanique des Fluides

Etude numérique de la chute libre d'objets axisymétriques dans un fluide newtonien

THÈSE dirigée par :

M. Dušek Jan	Professeur, Université de Strasbourg

RAPPORTEURS :

M. Magnaudet Jacques	DR CNRS, IMFT, Toulouse, France
M. Leweke Thomas	DR CNRS, IRPHE Marseille, France

AUTRES MEMBRES DU JURY :

M. Climent Eric	Professeur, IMFT, Toulouse, France
M. Uhlmann Markus	Professeur, IH KIT, Karlsruhe, Allemagne
M. Brancher Jean-Pierre	Professeur, LEMTA, Nancy, France

Équipe ≪ Instabilité, Turbulence et Diphasique ≫
IMFS - FRE3240 - CNRS/UdS

Marcin CHRUST

Etude numérique de la chute libre d'objets axisymétriques dans un fluide newtonien

Résumé

La mémoire présente une étude numérique des trajectoires non-verticales d'objets en chute ou en ascension libre dans un fluide newtonien initialement au repos. Une méthode numérique originale combinant une discrétisation spatiale spectrale et la décomposition du domaine a été implémentée à cet effet. Le code obtenu a été exploité pour apporter de nouvelles connaissances sur des objets fixes et objets libres. Pour les objet fixes, ellipsoïdes et cylindres, l'étude très complète des divers états de la transition a permis d'établir un lien entre le scénario de transition de la sphère et du disque infiniment mince. La simulation numérique d'objets libres a apporté des résultats très complets sur la chute de disques minces et de cylindres de faible épaisseur. Plusieurs questions soulevées dans les travaux précédents ont trouvés des réponses claires. Une étude paramétrique exhaustive, jamais abordée précédemment, portant sur des ellipsoïdes est décrite dans le dernier chapitre du mémoire.

mots-clés: chutte libre, transition au chaos, instabilité du sillage, régimes transitionnelles, bifurcation

Abstract

The manuscript presents a numerical study of non-vertical trajectories of bodies falling or rising freely in a Newtonian fluid initially at rest. The original numerical method combining a spectral spatial discretization and the decomposition of the domain was implemented. The developed code was used to study fixed and freely moving objects. For the fixed bodies, spheroids and cylinders, a very complete study of various transitional regimes was carried out and established a link between the transition scenario of a sphere and of a disc. The numerical simulation of free bodies brought about the results on path instabilities of discs and cylinders of small thickness. Several questions raised in previous studies were clearly answered. An exhaustive parametric study, that has never been taken up before, of freely moving spheroids is described in the last chapter of the manuscript.

keywords: free fall, transition to chaos, wake instability, transitional regimes, bifurcation

Remerciements

Writing a thesis is a great scientific and personal challenge for the author. Tackling this challenge is far easier with the helping hand and kindness of surrounding people. I would like to express here my sincere gratitude to my colleagues and to my nearest and dearest for their support and sympathy.

First of all, I would like to thank Jan Dušek, the director of my thesis. I had a unique chance to work with an outstanding researcher. This thesis would have never been accomplished without him. I would like to thank him for his valuable remarks, his patience and his great scientific contribution to my work. He would always answer my numerous questions and was always available for me. I would like to thank also sincerely Gilles Bouchet for recruiting me for the PhD position, for his advises and for his continuous support during my stay in Strasbourg.

I would like to thank successive directors of the Institute of Fluid and Solid Mechanics in Strasbourg, Yves Remond and Robert Mose for giving me a warm reception in the Laboratory. I would like to thank also Michael Essa, our IT specialist, for his support and kindness. I thank also Romaric David from the IT direction of the University for helping me solve several problems related to my calculations at the High Performance Computing center.

I would like to thank the whole "ITD" team. In particular, I am in debt to Thibaut Deloze for helping me with patience and sympathy with all the administrative procedures and for his support. I thank Cyril, Daniel, Dhiraj, Hassan, Tanvir, Emilie and Anthony for their company, great sense of humor and interesting discussions. I thank also Yannick Hoarau for his kindness, advice and support. It was a great pleasure to spend these three years with you!

I would like to thank also Sophie Goujon-Durand, Eduardo Wesfreid and Jacek Rokicki - the directors of my internship at PMMH ESPCI. It is thanks to them that my scientific career ever started.

I would like to thank Jacques Magnaudet and Thomas Leweke for their exhaustive reports and precious remarks. I would also thank examiners - Eric Climent and Markus Uhlmann for interesting questions and valuable discussion.

I would like to thank my family. My grandparents, parents and my brother supported me during whole my life and it is thanks to them that I am where I am today. I am also thankful to the family of my fiancée for their support.

Finally, I would like to thank Dominika Klosowska, my fiancée, for her patience, advises, continuous support, kindness and simply for being here with me in Strasbourg during the last three years. Without her I would have never accomplished this thesis.

Contents

Résumé: Etude numérique de la chute libre d'objets axisymétriques dans un fluide newtonien

La compréhension de l'origine et de la nature des trajectoires non-verticales d'objets en chute ou en ascension libre dans un fluide initialement au repos est d'une grande importance dans de nombreux domaines scientifiques et industriels, tels que la météorologie, la sédimentation ou le génie chimique. Ces trajectoires complexes, telles que celle d'un confetti virevoltant dans l'air, ont toujours intrigué la communauté des scientifiques. Les grands noms de la physique s'y sont intéressés, en particulier da Vinci, Newton, Kirchoff, Maxwell et Eiffel. Plus récemment, des expériences (Willmarth *et al.* (1964), Field *et al.* (1997), Fernandes *et al.* (2007)) ont attiré l'attention sur la pertinence de la théorie des instabilités et des systèmes dynamiques non-linéaires pour l'explication de ces comportements complexes. L'approche expérimentale présente néanmoins quelques inconvénients, tels qu'un contrôle difficile des propriétés physiques du système et des conditions aux limites, ainsi qu'une difficulté pour réaliser des mesures réellement non-intrusives. L'approche numérique s'est avérée la mieux adaptée à mener cette étude dans le cas d'un objet sphérique (Ghidersa & Dušek (2000), Jenny *et al.* (2004), Jenny & Dušek (2004), Kotouč (2008)). La présente thèse s'est donnée pour objectifs d'adapter le code spectral (ayant été développé pour l'étude de la chute libre d'objets sphériques Ghidersa & Dušek (2000), Jenny & Dušek (2004)) à la simulation d'objets axisymétriques de forme plus générale et d'étudier le scénario de transition à la turbulence de deux classes d'objets axisymétriques, les cylindres et les ellipsoïdes de révolution.

L'efficacité et la précision du code développé précédemment reposent sur une discrétisation spatiale en modes de Fourier dans la direction azimutale. Dans le cas d'objets en chute (ou ascension) libre, l'utilisation d'un domaine de calcul fixe par rapport à l'objet nécessite de faire subir au domaine les rotations de l'objet. Or, le sillage de l'objet reste essentiellement vertical et, pour les régimes de transition, de forte amplitude très loin en aval de l'objet. Dans le cas d'un objet sphérique, la solution adoptée a consisté à modéliser la rotation de la sphère par une condition de non-glissement à la surface de l'objet. Dans le cas des objets axisymétriques de forme quelconque traités dans la cadre de cette thèse, nous avons opté pour l'utilisation d'un domaine cylindrique pour simuler le sillage et d'un domaine résolvant les détails de l'écoulement proche de l'objet. En conséquence, le domaine cylindrique des précédentes études a été décomposé en deux parties : un sous-domaine sphérique, contenant l'objet et tournant avec ce dernier, complété par un sous-domaine cylindrique vertical (cf. Figure 2.1). Sur chacun des sous-domaines (de géométrie axisymétrique), la discrétisation spatiale initiale a été conservée. La re-connexion a été faite par une approche de type 'décomposition du domaine sans recouvrement' (méthode qui n'avait jusqu'alors jamais été utilisée dans un contexte "spectral"), l'interface sphérique faisant le lien entre les deux sous-domaines. Elle est discrétisée par un développement en fonctions sphériques. Compte tenu de

l'optimalité de la représentation du groupe de rotation par la base des fonctions sphériques, le surcoût de calcul nécessaire pour le raccordement dynamique des sous-domaines est très faible alors que la précision reste pleinement conservée. Pour le couplage des degrés de liberté de l'objet solide avec ceux de l'écoulement, nous avons adapté la méthode pleinement implicite de Jenny & Dušek (2004) assurant une stabilité numérique indépendamment de la masse ajoutée de l'objet, sans surcoût de calcul. La formulation mathématique et la description de la méthodes numérique font l'objet des chapitres 2 et 3 de la thèse.

Le phase d'exploitation du code ainsi modifié comporte deux volets d'étude, l'un portant sur les objets fixes et l'autre sur les objets libres. Le cas des objets axisymétriques fixes est caractérisé par deux paramètres sans dimension, le nombre de Reynolds ($Re = U_\infty d/\nu$, où U_∞ est la vitesse de l'écoulement loin en amont de l'objet, d le diamètre mesuré perpendiculairement à l'axe de l'objet et ν la viscosité cinématique du fluide) et le rapport d'aspect $\chi = d/a$ où a est la longueur de l'axe polaire pour les ellipsoïdes ou la hauteur pour les cylindres. Dans la suite, on appellera 'disque' le cas limite d'un cylindre de hauteur nulle (de rapport d'aspect infini). Au début de la thèse, seuls les cas extrêmes d'une sphère Jenny *et al.* (2004) et d'un disque Fabre *et al.* (2008) avaient été finement explorés. Or, les deux scénarios correspondants s'avèrent être considérablement différents. Dans une étude paramétrique extensive, nous avons ainsi entrepris de couvrir la gamme complète des rapports d'aspect (de l'unité à l'infini) des ellipsoïdes et des cylindres. Nous avons ainsi établi le lien entre les deux cas extrêmes. Alors qu'un des traits remarquables des scénarios relatifs à la sphère, au disque et au cylindre épais est l'absence d'hélicité dans tous les états ordonnés de la transition, nous avons mis en évidence un état à hélicité non-nulle pour des rapports d'aspect intermédiaires (par ex. $1.1 < \chi < 2.3$ pour les ellipsoïdes). La cartographie très complète des divers états de la transition en fonction du nombre de Reynolds et du rapport d'aspect pour des ellipsoïdes et pour des cylindres fait l'objet du chapitre 4 et a été publiée dans l'article Chrust *et al.* (2010).

Un travail expérimental récent Szaltys *et al.* (2011) a constaté l'impossibilité de retrouver le scénario théorique prédit pour un disque (ou un cylindre plat) placé perpendiculairement à l'écoulement. L'hypothèse que cette observation provient de l'impossibilité que l'on a de réaliser une configuration parfaitement axisymétrique a été confirmée en étudiant des disques inclinés par rapport à l'écoulement. Le scénario théorique n'a été retrouvé que pour une inclinaison très faible, de moins de 4 degrés. Au-delà, le plan de symétrie sélectionné par l'inclinaison reste stable. La bifurcation primaire est alors de type Hopf et il est intéressant de constater que son seuil ne varie pas d'une manière monotone avec l'angle d'inclinaison. Les détails de cette étude sont donnés au chapitre 5.

La simulation numérique d'objets libres nécessite la résolution des équations de Navier-Stokes couplées aux équations du mouvement du solide. L'adimensionalisation du problème est basée sur l'échelle de la force résultant de la masse de l'objet et de sa flottabilité $(m-\rho V)g$ (où m est la masse du solide, V son volume et ρ la masse volumique du fluide). En prenant la masse de référence ρd^3, on obtient l'échelle de l'accélération qui définit l'échelle de la vitesse. C'est cette échelle de vitesse qui remplace celle de la vitesse de l'écoulement. Le nombre sans dimension G, exprimant l'inverse de la viscosité adimensionnée et jouant le rôle du nombre de Reynolds, a été appelé (Jenny *et al.*, 2004) nombre de Galilée. Dans leur expression la plus générale, les équations couplées peuvent avoir jusqu'à 5 paramètres indépendants. En se

limitant à des objets homogènes d'une classe donnée (cylindres, ellipsoïdes), on limite ainsi le nombre de paramètres à 3. Nous avons choisi le nombre de Galilée, le rapport d'aspect et la masse adimensionnée $m^* = m/(\rho d^3)$ définissant l'inertie de l'objet d'une manière équivalente au moment d'inertie adimensionné de Willmarth *et al.* (1964) et Field *et al.* (1997).

Nous avons mené une étude paramétrique pour des disques libres ($\chi = \infty$) couvrant la plage de masses adimensionnées m^* variant de zéro à 10. Il y a encore très peu de résultats numériques portant sur ce problème. La thèse d'Auguste (2010) présente les seuils d'apparition du mouvement oscillant périodique, vertical en moyenne (appelé zig-zag) pour 6 valeurs du moment d'inertie adimensionnné. Nous avons retrouvé les mêmes seuils. Nous avons étendu l'étude à l'ensemble du plan des paramètres G, m^* avec $G = \sqrt{m^* g d^3}/\nu$ allant jusqu'à 500. Le scénario de transition dépend fortement de m^* comme le montre la Figure 6.20 du chapitre 6 de la thèse. Nous distinguons les trajectoires suivantes :

1. chute verticale ;
2. état "zig-zag" ;
3. état virevoltant décrit dans la littérature expérimentale comme "tumbling" ;
4. état intermittent (entre un état "zig-zag" et un état "tumbling") ;
5. états chaotiques caractérisés par des trajectoires tri-dimensionnelles peu éloignées de la verticale, trouvés également dans Auguste (2010) pour de très petites inerties et observés aussi expérimentalement Ern *et al.* (2012);
6. états hélicoïdaux.

Le scénario pour le disque infiniment léger ($m^* = 0$) s'est avéré très particulier, car la chute verticale devient instable suite à l'apparition d'oscillations de basse fréquence à un nombre de Galilée légèrement inférieur à 80. Très rapidement, les oscillations deviennent chaotiques (comme décrit au point 5). Un état ordonné "zig-zag" à une fréquence plus élevée n'est retrouvé que pour $G \geq 180$. Cet état co-existe avec l'état chaotique entre $G = 120$ et $G = 180$. L'interaction des deux fréquences pourrait être à l'origine de l'état chaotique presque vertical susceptible d'expliquer une observation expérimentale très tardive des oscillations pour un cylindre plat (Fernandes *et al.*, 2007). On constate, de plus, que la bifurcation donnant naissance à l'état "zig-zag" est sous-critique dans un grand intervalle de valeurs intermédiaires de m^* avec une large plage de coexistence des deux états. En accord avec les observations de Field *et al.* (1997), nous trouvons que l'état virevoltant domine le scénario pour les inerties (m^*) élevées.

Un récent article expérimental (Fernandes *et al.*, 2007) a soulevé la question de l'explication d'une apparition tardive des instabilités observée pour un cylindre plat en ascension libre sous l'effet de la poussée d'Archimède. Contrairement aux attentes intuitives et à l'observation faite dans le cas d'un objet sphérique, la trajectoire du cylindre est restée verticale jusqu'à des nombres de Reynolds auxquels le sillage du même cylindre maintenu fixe présente déjà des instabilités. Le chapitre 7 présente une explication à la lumière des résultats de simulations directes. Le phénomène est dû en partie à un effet stabilisant

des degrés de libertés supplémentaires de l'objet libre. Cet effet surprenant, prédit tout récemment théoriquement par Fabre *et al.* (2012), a été confirmé en mettant en évidence le décalage du seuil de la bifurcation régulière du sillage du cylindre pour des rapports d'aspect proches de 10. A partir de ce rapport d'aspect, le décalage observé est, cependant, beaucoup plus important. Il s'explique par le scénario mis en évidence pour le disque infiniment fin de faible inertie ($m^* \sim 0$) au chapitre 6. Ce sont les états instationnaires de très faible amplitude qui retardent l'apparition des oscillations expérimentalement observables.

Finalement, le chapitre 8 présente le scénario de transition mis en évidence pour des ellipsoides applatis de rapports d'aspect variant de l'infini (disques avec une distribution inhomogène de masse) jusqu'à 1.5 (1 étant le rapport d'aspect d'une sphère parfaite). Le but de l'étude consiste à établir le lien entre les résultats obtenus pour des disques au chapitre 6 et le scénario connu pour les objets sphériques. Il s'agit d'une étude paramétrique comportant trois paramètres: le rapport d'aspect caractérisant la forme, la masse adimensionné m^* ou, d'une manière équivalente, le rapport des masses volumiques du solide et du fluide porteur et le nombre de Galilée. Un grand nombre de simulations est, en conséquence nécessaire, pour fournir une information complète. Les résultats obtenus permettent de conclure que le scénario du disque avec les états caractéristiques 'zig-zag' et 'virevolte' est limité aux ellipsoides plats de rapport d'aspect n'excédant pas 3. Pour les ellipsoïdes de forme proche de celle de la sphère, on retrouve un scénario similaire à celui mis en évidence pour la sphère avec, cependant, des différences dues à la forme asphérique de l'objet qui l'empêche de tourner.

Les tests numériques, l'accord avec les résultats déjà connus, ainsi que la richesse des scénarios mis en évidence justifient l'approche numérique que nous avons adoptée pour cette étude.

Chapter 1

Introduction

1.1 Free motion of solid bodies

The nature and origins of non-straight paths of bodies falling or ascending freely in a fluid have always triggered interest of the scientific community. The origins of the topic date back to the foundations of the modern mechanics and to such honored names as Newton, Maxwell, Kirchoff and others. In his revolutionary publication Newton (1726) proposed for the first time not only the classical laws of motion, the law of universal gravitation and the derivation of Kepler's laws of planetary motion, but also described several experiments devoted to the motion of solids in fluids. In order to measure the resistance of fluids, Newton "procured a square wooden vessel" and "filled it with rain water", "and having provided globes made up of wax, and lead included therein, [...] noted the times of the descents of these globes [...]". He observed that "the globes [...] oscillated about their centers". In another experimentation hog's bladders formed into spherical orbs "were let fall from the lantern on the top of the cupola of the same church [St. Paul's in London] ... But the bladders did not always fall straight down, but sometimes fluttered a little in the air, and waved to and fro as they were descending". Maxwell (1853), in turn, points out that "every one must have noticed that when a slip of paper falls through the air, its motion, although undecided and wavering at first, sometimes becomes regular". It was incomprehensible and inspiring at the same time, that a body of a regular shape, initially at rest, freely falling in air could follow a non-straight path. Another intriguing examples of path instabilities found in daily life are, for instance, those of confetti falling in the air or of a coin dropped in the water.

Understanding the reasons of non-straight paths of objects falling or rising under the effect of gravity, buoyancy and hydrodynamic forces in a fluid is a major issue in many domains of science, as well as in many industrial applications. In meteorology it is, for example, of interest to predict the trajectories of weather balloons, as they are shaped by winds and wake instabilities. A French meteorologist Léon Philippe Teisserenc de Bort was one of the first to use unmanned balloons, which led to the discovery of the stratosphere. Nowadays they are commonly used (routine releases are scheduled in over 800 locations all over the world each day) to provide information on the temperature, winds and pressure for weather forecasting.

Figure 1.1: Launching of a weather balloon. Photo: U.S. Navy.

Another field of applications involve the study of the fall and growth of snowflakes and raindrops in the atmosphere. Especially important is the understanding of the mechanism of the build up of hailstones and the prediction of their trajectories to prevent damage to automobiles, roofs, livestock and crops. Kry & List (1974) found that the growth of spheroidal hailstones is closely related to their angular motion, which they called symmetric gyration, in which symmetrically equivalent points on the surface are equally exposed to the flow.

Sedimentology is a domain of science that involves the study of sediments, which are natural materials, that are created by weathering and erosion. Subsequently, they are transported by fluids: winds in air or currents in water. It is of interest to study the processes that result in their deposition. It is crucial, for instance, to understand the sedimentation of silt in river banks and the transport of pollutants, which threaten the water quality and the wildlife. The study of sedimentation and spread of volcanic ashes containing fragments of pulverized rocks, minerals and volcanic glass (of diameter less than 2mm), created during volcanic eruptions (Walker, 1981) is particularly important for the aeronautical industry. The ashes can seriously affect the air traffic due to several reasons (Cassadevall, 1992). One of them is the reduction of the visibility and of the runway friction coefficients (especially when the ash is wet). But the most serious is the potential damage to the engines due to

increased wear. The ashes can also cause damage to ground vehicles by abrading or scratching the moving surfaces or by clogging the air intake filters. Modeling of the spread and sedimentation of the ash particles is therefore crucial for taking adequate precaution steps.

Figure 1.2: Eruption of a volcano beneath Iceland's Eyjafjallajokull glacier. Photo: Icelandic Coast Guard.

For very small particles, the particle transport problem can be treated in the framework of statistical physics (see e.g. Russel *et al.*, 1992). Random movement of particles suspended in a fluid, called the Brownian motion (Einstein & Fürth, 1956), is a simple continuous-time stochastic process that can be considered as approximation of a random physical process. For larger particles, the hydrodynamic forces must be accounted for.

Studying of the motion of freely falling objects is also central in biological sciences. The spread of seeds from plants, for example, have cardinal effects on the structure of plant populations. Different species have developed various dispersal mechanisms, one of which is wind dispersal: seeds can be lifted by a breeze and transported to distant locations or they can fall directly to the ground following complicated paths. These mechanisms play a major role in migration and mixing of the species and are main factors maintaining the biodiversity (Augspurger, 1996).

In chemistry, the potential applications involve centrifuges and dust collectors, that exploit the sedimentation principle (centripetal acceleration causes denser particles to separate along the radial direction), pneumatic conveyors and chemical reactors including fluidized beds, the design of which relies on the knowledge of the drag coefficient of suspended particles.

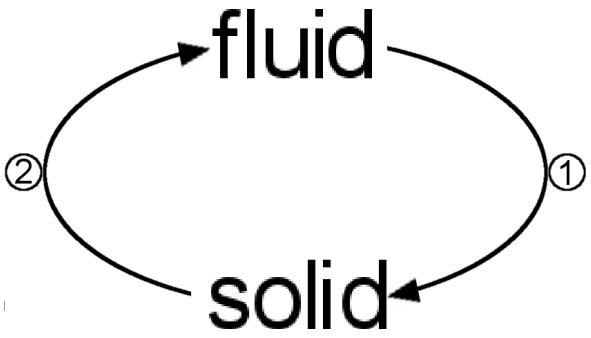

Figure 1.3: Fluid-Solid coupling. (1) fluid exerts a hydrodynamic force on the solid and (2) the solid introduces a disturbance to the fluid.

1.2 Physics of the problem

The motion of a particle immersed in a fluid is governed by mutual interactions of the fluid and solid phases (known in the literature as Fluid-Solid Interactions, FSI). Fluid exerts a hydrodynamic force on a particle. At the same time a particle disturbs the flow (see Figure 1.3). In what follows, the volumetric mass and kinematic viscosity of the continuous phase are considered constant and the fluid is assumed to be incompressible. The flow is then governed by the Navier-Stokes equations:

$$\frac{\partial \mathbf{v}}{\partial t} + (\mathbf{v} \cdot \nabla)\mathbf{v} \; = \; -\nabla p + \frac{1}{Re}\nabla^2 \mathbf{v} \tag{1.1}$$

and

$$\nabla . \mathbf{v} \; = \; 0 \tag{1.2}$$

where $Re = U_\infty d/\nu$ is the Reynolds number representing inverse of the non-dimensionalized kinematic viscosity (ν). These equations have to be completed by the initial and boundary conditions. The domain is considered to be infinite with the fluid being at rest on its limits. In practice the domain is finite. However, its size should be sufficiently large, so that the flow is not altered due to the introduced confinement. The interaction between the solid, which moves with a velocity $\mathbf{u}$ and rotates with the angular velocity $\mathbf{\Omega}$, and the fluid is due to the no-slip boundary condition on its surface S. This boundary condition is expressed by:

$$\mathbf{v}|_S = \mathbf{u} \; + \; \mathbf{\Omega} \times \mathbf{r}|_S \tag{1.3}$$

where $\mathbf{v}|_S$ is a velocity of the fluid, that is in contact with the solid and $\mathbf{r}$ is the position vector of a point on its surface.

The difficulty in solving the coupled solid-fluid problem governed by equations (2.56,2.57) and (1.4), respectively, consists in resolving all the scales present in the problem. Moving particle introduces the energy to the surrounding fluid, that in turn governs the evolution of large scale flow structures. The two-way coupling between a particle and continuous phase is non-trivial and requires careful treatment.

Calculation of forces (1.7, 1.8 and 1.9 defined in section 1.3) acting on the accelerating spherical particle submerged in a fluid is a complicated task (Magnaudet, 1997). It was shown that standard particle models do not predict the trajectories of a spherical particle that moves with a speed corresponding to transitional regimes (Karamanev & Nikolov, 1992). The discrepancy appears to be especially striking for light ascending spheres. Nonetheless, satisfactory results were obtained, when the flow can be considered as uniform on the particle scale. However, as soon as the scale of structures present in the wake is comparable to that of a particle (super-critical regimes in the case of a sphere), the flow can be no longer considered as uniform. The direct resolution of the flow around a particle is then required to account for the strong coupling of the fluid and solid phases.

1.3 Phenomenological models

Modeling of multi-particle suspensions is an even more challenging task since in addition to the present solid-fluid interactions it also involves interactions between particles that can have non-negligible consequences (especially when the concentration is high). The thesis of Caballina (2002) presents an exhaustive overview of the existing approaches adopted to solve this complex two-phase problem. The simplest one consists in considering the fluid and solid phases as an equivalent mono-phase medium, whose volumetric mass is a function of the concentration of the dispersed phase. The flow is then governed by the homogenized Navier-Stokes equations and the interactions between two phases are modeled by introducing a tensor of mixing constraints and the Reynolds tensor associated with the fluctuations of the velocity induced by the presence of the solid phase. Particles are not resolved and are considered to be simply convected by the flow. Models based on this approach are called in the literature Eulerian models. Their validity is limited by the assumption that the scale of particles is negligible in comparison with the scales present in the flow.

Another approach consists in considering both the fluid and solid phases as distinct media. The continuous phase is resolved using Eulerian approach through the solution of the Navier-Stokes equations possibly augmented by a source term modeling the action of the solid phase on the fluid one to account for the two way coupling. The solid phase is resolved using the Lagrangian approach consisting in integration of the equation 1.4. The forces acting on a single particle listed in the equation 1.6 are modeled phenomenologically (see Tanabe & Kaneko, 1994; Mahadevan *et al.*, 1999; Caballina, 2002).

The three translational degrees of freedom of a particle obey the motion equation 1.4:

$$m\frac{d\mathbf{u}}{dt} = (m - m_f)\mathbf{g} + \mathbf{F} \tag{1.4}$$

where m and m_f is a mass of the particle and of a volume of the displaced fluid respectively, $\mathbf{u}$ is the velocity of the center of mass of a particle and $\mathbf{g}$ represents a vector of the gravitational acceleration. In a sub-critical regime, a particle placed in a steady homogeneous flow follows a vertical path. The driving force (resulting from gravity and buoyancy) is counterbalanced by the hydrodynamic drag $\mathbf{F} = \mathbf{F_D}$. The derivative on the left hand side of equation 1.4 is equal to zero in this case. Non-dimensionalization of the drag force yields the drag coefficient:

$$C_D = \frac{F_D}{\frac{1}{2}\rho u^2 S} \tag{1.5}$$

In the sub-critical regime, the problem simplifies then to the modeling of the drag force. For the case of a sphere phenomenological models of C_D (Schiller & Neumann, 1933; Brown & Lawler, 2003) are in a very good agreement with the direct numerical simulations (DNS) as shown by Magnaudet *et al.* (1995).

As soon as the velocity of a particle starts to vary, the acceleration effects appear. Moreover, the shear of the flow must often be accounted for. The instantaneous force acting on a particle contains, along with the drag force $\mathbf{F_D}$ present before, the supplementary terms:

$$\mathbf{F} = \mathbf{F_D} + \mathbf{F_{ma}} + \mathbf{F_h} + \mathbf{F_L}, \tag{1.6}$$

where $\mathbf{F_{ma}}$, $\mathbf{F_h}$ and $\mathbf{F_L}$ are the added mass, history and lift forces respectively. The added mass force accounts for the inertial effects. It is a force exerted by a particle to accelerate the surrounding fluid. It is expressed by:

$$\mathbf{F_m} = C_{ma} m_f (\frac{d\mathbf{v}}{dt} - \frac{d\mathbf{u}}{dt}), \tag{1.7}$$

with C_{ma} being the added mass coefficient equal to $C_{ma} = 1/2$ for a sphere (Magnaudet *et al.*, 1995). The history force, proposed independently by Boussinesq (1985) and Basset (1888), represents an effort necessary for the flow to adapt to the boundary conditions imposed by the motion of a particle. It can be expressed using the integral formulation (see e.g. Magnaudet, 1997):

$$\mathbf{F_h} = \int_0^t K(t-\tau)(\frac{\partial \mathbf{v}}{\partial \tau} - \frac{\partial \mathbf{u}}{\partial \tau})\, d\tau, \tag{1.8}$$

where the kernel $K(t-\tau)$ depends on the process of the diffusion of the vorticity. Calculation of the history force is computationally expensive, however, especially for bubbles, it cannot be neglected when fluctuations of the velocities between phases become important (Rivero *et al.*, 1991). If the vorticity is present in the flow, the lift force must be also considered. It is expressed by:

$$\mathbf{F_L} = -C_L m_f (\mathbf{u} - \mathbf{v}) \times \omega, \tag{1.9}$$

where the vorticity in the absence of the rotation of a particle is given by $\omega = \nabla \times \mathbf{v}$. For an inviscid fluid and a spherical particle $C_L = 0.5$ according to Auton (1983). For moderate Reynolds numbers, C_L is a function of shear present in the flow $A_\omega = d|\omega|/|\mathbf{u} - \mathbf{v}|$ and tends to the asymptotic value as $C_L = 0.5 - 4.0Re^{-1}$ (Komori & Kurose, 1996).

The size of the particle and the boundary layers are, nonetheless, not resolved resulting in similar drawbacks as those of Eulerian models.

Maxey & Riley (1983) propose a model that resolves the size of the particle accounting for the disturbance that it introduces to the flow. However, the boundary layer is not yet resolved. The model applies to small Reynolds numbers at which the scale of the boundary layer thickness and of the particle size are comparable.

The above mentioned techniques, rely strongly on the modeling and do not apply to transitional regimes. Reliable prediction of sedimenting flows can be obtained only if all the involved scales are taken into account, meaning that particles' boundary layers have to be resolved. This can be achieved by direct numerical simulations. However, even today the simulation of multi-particle flows is too expensive computationally and can be carried out only on super-computers (García-Villalba *et al.*, 2012). Hence, before addressing a complicated sedimentation problem, first a single particle problem must solved and understood. Single particle solutions provide also a useful benchmarking.

Unavailability of accurate theoretical models in the transitional regimes explains why the free fall of solids was intensively studied experimentally. The development of sophisticated optical techniques, namely of high-speed imaging, particle image velocimetry (PIV) and of visualization methods and post-processing tools allowed for a precise tracking of all 6 degrees of freedom of the body as well as for the measurement of the velocity field (with the 3d PIV it is now possible to obtain velocity field in a volume). Researchers focused their attention mainly on the prototypical bodies possessing the axis of symmetry, namely on a sphere and on a disc. The advantage of considering these geometries is that their wakes are initially axisymmetric. They are therefore particularly well suited for the stability studies relying on the linearization of the Navier-Stokes equations around an axisymmetric solution. Nonetheless, the experimental approach also presents certain drawbacks for theoretical interpretations. Namely, it is difficult to control precisely physical parameters of the system and the boundary conditions, as well as to access in a non-intrusive manner all the relevant physical quantities. Another issue are the high costs of experimental equipment.

Having in mind that the path of a freely falling solid is a result of interplay of the fluid and solid degrees of freedom (commonly known as fluid-structure interaction), it is primordial to elucidate the transition scenario of their fixed counterparts. Knowledge of the regimes and bifurcation mechanisms provides a clue to the explanation of the behavior of freely moving bodies. First attempts to predict the transition in wakes were made in the framework of the parallel flow theory. The viscous parallel linear analysis of Monkewitz (1988) predicted for the axisymmetric bodies that the mode with azimuthal wave number m=1 (helical mode) becomes the most unstable. However, theoretical considerations based on the parallel flow theory have failed to provide quantitatively reliable predictions for wakes (Dušek *et al.*, 1994). A fully three dimensional linear stability analysis capable of precise predictions of the bifurcation thresholds was first given by Natarajan & Acrivos (1993) for the case of a sphere and a thin disc. They found a regular primary bifurcation threshold and predicted a secondary Hopf bifurcation. Recent development of numerical methods and rapid increase of computational power of computers allowed for a fully free dimensional simulations capable of capturing the breaking of axisymmetry of the wake (Johnson & Patel, 1999; Ghidersa & Dušek, 2000; Tomboulides & Orszag, 2000).

1.4 Loss of axisymmetry in flows

The wake of axisymmetric bodies for sufficiently low Reynolds numbers is steady and axisymmetric. The subsequent transitions that break the spatio-temporal symmetry of the

flow might be to some extent predicted by considering the linear stability analysis of the base flow. A similar situation is to be expected more generally for any axisymmetric flow. In the context of the sphere wake, a theoretical weakly non-linear model focusing on the case of a regular bifurcation was given by Ghidersa & Dušek (2000). The case of a Hopf axisymmetry breaking bifurcation was discussed by Danaila *et al.* (1998). The interplay of both bifurcations is analyzed in a recent paper by Meliga *et al.* (2009). The present section is limited to the analysis of a single bifurcation.

The axisymmetric flow satisfying Navier-Stokes equations written in cylindrical coordinates (z, r, θ), where z is the axial, r radial and θ azimuthal coordinates respectively, is independent of θ. The linear stability of the axisymmetric solution can be studied considering a perturbed flow field $(\mathbf{v}, p)$:

$$\mathbf{v} = \mathbf{V} + \mathbf{v}', \tag{1.10}$$
$$p = P + p', \tag{1.11}$$

where $(\mathbf{V}, P), (\mathbf{V} \equiv (V_z, V_r, V_\theta)^T)$ is the axisymmetric solution. $(\mathbf{v}', p')$ are the infinitesimal perturbations that can be expressed through the complex eigen-functions $\mathbf{\Phi}$ and Π associated with the eigenvalue λ:

$$\mathbf{v}' = \alpha e^{\lambda t}\mathbf{\Phi} + c.c., \tag{1.12}$$
$$p' = \alpha e^{\lambda t}\Pi. + c.c., \tag{1.13}$$

where α is a small, arbitrary, complex constant. $c.c$ stands for complex conjugate. The perturbations will be either amplified or damped, according to the sign of the real part of λ, depending on the solution of the eigenvalue problem:

$$\nabla \cdot \mathbf{\Phi} = 0, \tag{1.14}$$
$$\lambda\mathbf{\Phi} + \mathcal{L}[\mathbf{V}]\mathbf{\Phi} + \nabla\Pi = 0, \tag{1.15}$$

obtained by the linearization of the Navier-Stokes equations around the axisymmetric solution $(\mathbf{V}, P)$. $\mathcal{L}$ is a linear operator that commutes with the rotation operator $\partial/\partial\theta$, since the base flow is independent of θ. Hence, the eigenfunctions of both operators can be expressed in the following form:

$$\mathbf{\Phi}(z, r, \theta) = \sigma(m)\phi_m(z, r)\, e^{-im\theta}, \tag{1.16}$$
$$\Pi(z, r, \theta) = \pi_m(z, r)\, e^{-im\theta} \tag{1.17}$$

where $\sigma(m) = \mathrm{diag}(1, 1, -isgn(m))$ and m is the azimuthal wave number $\phi_m(z, r)$ $\equiv (\phi_{m,z}, \phi_{m,r}, \phi_{m,\theta})^T$ is an array of the azimuthal modes of the axial, radial and azimuthal velocity respectively. The imaginary factor $-isgn(m)$ is related to the complex representation of plane rotations discussed by Jenny & Dušek (2004). With the formulation (1.16),

the eigenvalue problem (1.14) and (1.15) can be decomposed into a sequence of independent eigenvalue problems in azimuthal sub-spaces:

$$\nabla_{|m|} \cdot \phi_m = 0, \tag{1.18}$$
$$\lambda_m \phi_m + \Lambda_m[\mathbf{V}]\phi_m + \nabla_{|m|}\pi_m = 0. \tag{1.19}$$

The eigenvalues λ_m depend on the azimuthal wave number m. If no swirl is present, i.e. if the axisymmetric flow has no azimuthal velocity, the operator Λ_m and thus also the eigenvalues λ_m are independent of the sign of m: $\lambda_m = \lambda_{|m|}$. The bifurcation sets in when the first real part of $\lambda_{|m|}$ becomes positive. Four distinct cases summarized in Table 1.1 can be expected depending on the azimuthal wave number and on the imaginary part of the first eigenvalue to become unstable.

	$m = 0$	$m \neq 0$
$Im(\lambda) = 0$	Steady axisymmetric	Steady non-axisymmetric
$Im(\lambda) \neq 0$	Unsteady axisymmetric	Unsteady non-axisymmetric

Table 1.1: Characteristics of the perturbed flow depending on the azimuthal wavenumber and on the imaginary part of the first eigenvalue to become unstable.

The axisymmetry gets broken if $m > 0$ (negative values are equivalent if no swirl is present). The most unstable eigenvalue is mostly in the $m = 1$ sub-space, however, Kotouč *et al.* (2009*b*) have evidenced regular bifurcations in $m = 2$ and $m = 3$ subspaces in the opposing flow past a heated sphere. The weakly non-linear effects at a regular axisymmetry breaking bifurcation were described to the third order of the instability amplitude A by Ghidersa & Dušek (2000) by a real Landau model:

$$\frac{dA}{dt} = (\lambda - C|A|^2)A, \tag{1.20}$$

where λ is the real positive eigenvalue and C a real constant (as opposed to the Landau model pertaining to the Hopf bifurcation where the constants are complex). The amplitude A is, however, complex. The bifurcation is super-critical if $C > 0$. The growth rate λ of the instability is proportional to the parameter $\varepsilon = (Re - Re_{c,I})/Re_{c,I}$ close to the threshold and the saturation amplitude $|A|$ is proportional to $\sqrt{\varepsilon}$. The third order model makes it clear that the phase of the amplitude is arbitrary. A more detailed analysis shows that a real amplitude A corresponds to a flow having a planar symmetry with respect to the plane defined by the base flow direction and the real axis in a perpendicular plane. The arbitrary phase account for the arbitrary orientation of the symmetry plane.

A weakly non-linear theory of the Hopf bifurcation was presented by Danaila *et al.* (1998). The cited paper suggests a 5-th order model required for explaining the dynamics of a jet. Only a third order model will be discussed here. If the unstable eigenvalue in the problem (1.18,1.19) has a non-zero imaginary part, the instability generates two helical modes of opposite helicity corresponding to the unstable ($\gamma > 0$) complex eigenpair $\gamma \pm i\omega$. The

helical modes are characterized by complex amplitudes A_+ and A_-. Any two-dimensional vectorial quantity in the plane normal to the base flow direction, say yOz plane, (e.g. the lift) is representable as a complex function of time (see Jenny & Dušek, 2004) $u_+ = u_y + iu_z$ expressed as:

$$u_+ \;=\; A_+(t)e^{i\omega t} + A_-(t)e^{-i\omega t}. \tag{1.21}$$

A weekly non-linear third order approximation of the dynamics of the axisymmetry breaking by a Hopf bifurcation yields the following equations for the amplitudes $A_\pm$ (Danaila *et al.*, 1998)

$$\frac{dA_\pm}{dt} \;=\; \left[\gamma - (C|A_\pm|^2 + D|A_\mp|^2)\right] A_\pm. \tag{1.22}$$

where C and D are complex constants, the same in both equations with upper and lower sign to account for the symmetry with respect to the change of the sign of helicity. A simple calculation shows that Eqs. (1.22) have two types of asymptotic solutions:

a) one of $|A_+|$ or $|A_-|$ zero, the other equal to $(\gamma/C_r)^{-1/2}$,

b) both modules equal and $|A_+| = |A_-| = [\gamma/(C_r + D_r)]^{-1/2}$.

(C_r and D_r stand for real parts of C and D. Both C_r and D_r are assumed to be positive.) For $C_r < D_r$ the solution a) is stable and b) is unstable. The converse is true for $D_r < C_r$. The imaginary parts of C and D yield a non-linear shift of angular frequency. As a result, Eq. (1.21) yields asymptotic states:

$$u_{+,\infty} \;=\; \left[|A_{+,\infty}|e^{i(\omega' t - \varphi_+)} + |A_{-,\infty}|e^{-i(\omega' t - \varphi_-)}\right] \tag{1.23}$$

where $\omega' = \omega + \Delta\omega$ is the angular frequency of the limit cycle and $\varphi_\pm$ phase shifts determined by the initial perturbation. The trajectory in the complex plane in the case a) is a circle and in the case b) a straight line the inclination of which is given by the phase shifts, i.e. by initial conditions. Danaila *et al.* (1998) show that higher order non-linear effects may results in states with unequal amplitudes $|A_{+,\infty}| \neq |A_{-,\infty}|$ yielding a flattened ellipse instead of a straight line or a circle. (See Figure 1.4.)

In regimes where the modulus of the amplitude of both helical modes is the same we find a planar symmetry. The net helicity is zero. In the case of wakes of solid bodies, the lift oscillates with a zero mean value in the same way as Figure 1.4b. In contrast, if the amplitudes are not equal, the corresponding states will be called "with non zero helicity".

1.5 Wake of a fixed sphere

Flow around a fixed sphere has received a lot of attention over the past decades. The understanding of its transitions can be considered as a necessary prerequisite for the study of freely moving spheres. At the same time, fixed configuration is much simpler to study owing to the suppression of the body's degrees of freedom. Non-dimensionalization of the

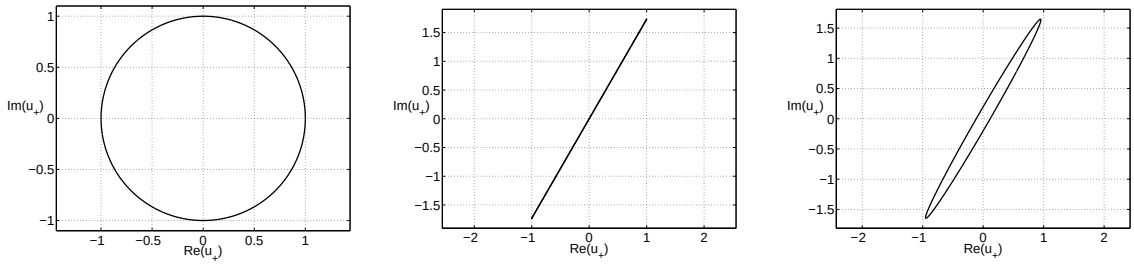

(a) *(b)* *(c)*

Figure 1.4: Paths in the complex plane of the modeled complex velocity of Eq. 1.23 for a) a single non zero amplitude, $A_{-,\infty} = 0$, b) two equal amplitudes $|A_{+,\infty}| = |A_{-,\infty}|$ and c) for $|A_{-,\infty}| = 0.9|A_{+,\infty}|$.

Navier-Stokes equations with the diameter of a sphere and the free stream velocity yields the Reynolds number as a single parameter of the study.

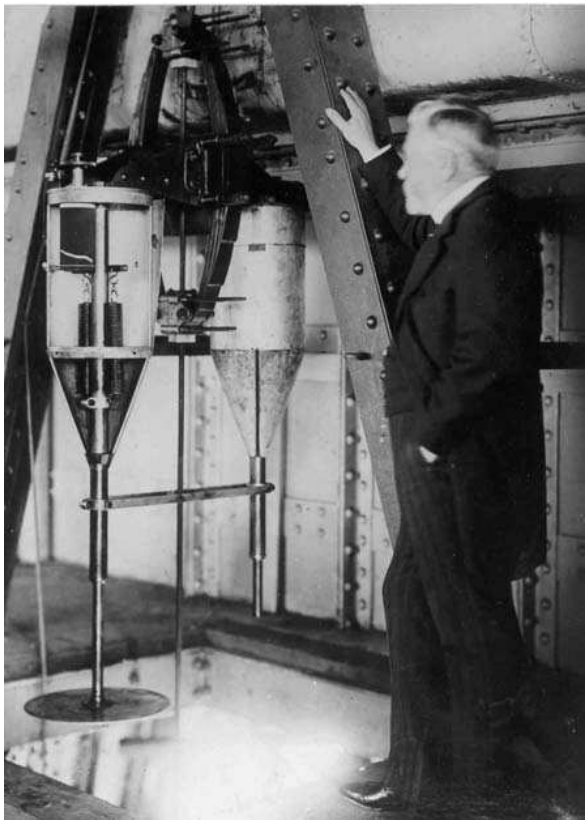

Figure 1.5: G. Eiffel with the drop test machine. Eiffel tower.

In spite of the simple geometry of a sphere, its wake can be fully three-dimensional and can contain complicated vortical structures. It undergoes a series of transitions as the Reynolds number is increased. For very low Reynolds numbers, the flow exhibits perfect upstream-downstream symmetry and separates upon increasing the free stream velocity. The flow maintains axial symmetry and a vortex forms at the rear stagnation point of the sphere (Magarvey & Bishop, 1961*a*). The flow separation is widely accepted to occur at $Re_{sep} = 20$, although different researchers evidence slightly different results: Rimon & Cheng (1969) suggest $Re_{sep} = 10$ while Taneda (1956) experimentally showed it to occur at $Re_{sep} = 24$. Streaklines of flow visualizations show a rectilinear thread downstream the sphere when dye is injected upstream, as a manifestation of axial symmetry.

The primary bifurcation breaks the axial symmetry introducing a steady non axisymmetric wake consisting of a separation bubble followed by two trailing counter-rotating vortices. Axial symmetry is replaced by a planar symmetry. The double-thread flow structure is easily visualized with streaklines in experiments in a water channel using the dye injection on the surface of the sphere as well as evidenced by the PIV measurements. The early experimental results underestimated the threshold of the first bifurcation. Taneda (1956) found it at $Re_I = 130$ and identified the next regime as unsteady. Other studies show that the wake becomes asymmetric, but remains steady (Magarvey & Bishop, 1961*a*; Levi, 1980). Magarvey & Bishop (1961*a*) found the threshold for $Re_I = 210$, however they did not interpret it as a breaking of axisymmetry. The results of Ormières & Provansal (1999) ($180 < Re_I < 200$) and Nakamura (1976) ($Re_I = 190$) were relatively close to the numerical results $Re_I = 210 - 212$ found by Tomboulides *et al.* (1993), Johnson & Patel (1999) and Ghidersa & Dušek (2000). The difference in the first bifurcation threshold between the experimental and numerical results was attributed by Ormières & Provansal (1999) to the sensibility of the primary regular bifurcation to the holding. Careful treatment allowed Gumowski *et al.* (2008) to obtain the primary bifurcation threshold in agreement with the numerical results.

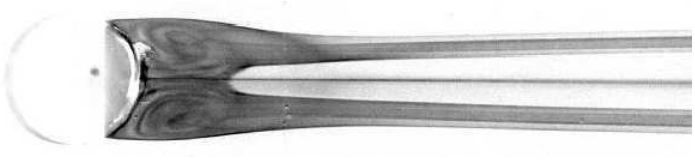

Figure 1.6: Streaklines showing a bifid wake. The plane of symmetry is imposed by the holding; $Re = 250$. Przadka *et al.* (2008).

The linear stability analysis carried out by Natarajan & Acrivos (1993) and later on by Ghidersa & Dušek (2000) confirmed the results of the viscous parallel linear analysis of Monkewitz (1988) showing that the eigenvalue corresponding to the mode with the azimuthal wave number $m = 1$ is the first to become unstable. The unstable eigenvalue was found to be real, i.e. the bifurcation responsible for the first transition is of a regular type.

The secondary, Hopf, bifurcation replaces the steady, planar symmetric flow with unsteady, however still planar symmetric flow. The unsteady state has not only a zero helicity but, moreover, the symmetry plane of both bifurcations is the same. This not necessarily

the case in all configuration, e.g., it does not hold for a thin disc. Streaklines show periodic shedding of connected hairpin vortices. The transition is numerically predicted to occur at Re slightly exceeding 270 ($Re = 270$ Johnson & Patel (1999), $Re = 272.3$ Ghidersa & Dušek (2000)). The onset of unsteadiness is observed as fluctuations (peristaltic instability) of the double thread wake in experiments. Ormières & Provansal (1999) found the threshold at $Re = 273$. Gumowski *et al.* (2008) found, experimentally, that the undulation of the double thread wake starts at the Reynolds number of $Re = 265$. When the Reynolds number is increased, the amplitude of oscillations starts to rise and eventually the vortex shedding with transversal vorticity is added to the flow in the form of hairpins.

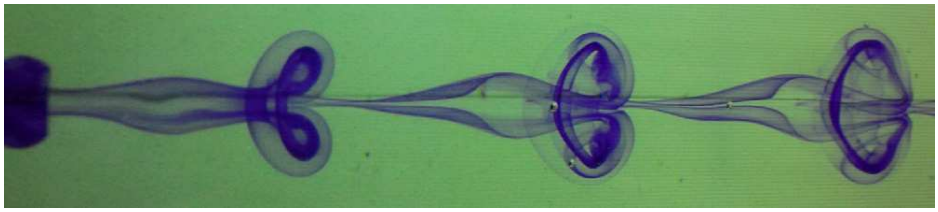

Figure 1.7: Wake behind a sphere in hairpin-shedding regime. Szaltys *et al.* (2011).

The subsequent stages of transitions are less widely known. Bouchet *et al.* (2006) evidenced numerically the appearance of the second frequency equal to about one third of the base frequency at the Reynolds number $Re \approx 325$ leading to a quasi-periodic state. Upon a further increase of the Reynolds number, the flow preserves the planar symmetry but undergoes a sequence of subharmonic bifurcations. Above $Re = 350$, the symmetry plane is lost and vortical structures are shed downstream irregularly in random directions. The chaotic regime was first observed experimentally by Sakamoto & Haniu (1995) for Reynolds numbers exceeding $Re = 420$ and numerically by Mittal (1999) for the Reynolds number between 350 and 375.

1.6 Transition scenarios of fixed discs and cylinders

The wake of a thin disc and that of flat cylindrical bodies has been taken up only in a handful of recent, mostly numerical and theoretical papers. For a cylinder, the aspect ratio is defined as $\chi = d/h$ where d is the cylinder diameter and h the cylinder height. In what follows, a "thin disc" is considered to correspond to an infinite aspect ratio while if the body is cylindrical with non zero height it will be called flat cylinder if $\chi > 1$. It appears that the transition scenario in these wakes differs considerably from that of the fixed sphere wake, furthermore the transition process involves new features that do not exist in the sphere wake. The present literature on the transition from a steady symmetric to a chaotic flow over a thin disc or a flat cylinder reveals seven transition stages.

- *(a):* In all investigated configurations, the thin disc ($\chi = \infty$), considered by Natarajan & Acrivos (1993), Fabre *et al.* (2008) and Meliga *et al.* (2009), and flat cylinders of aspect ratio larger than one, investigated by Fernandes *et al.* (2007) ($\chi = 2$ through

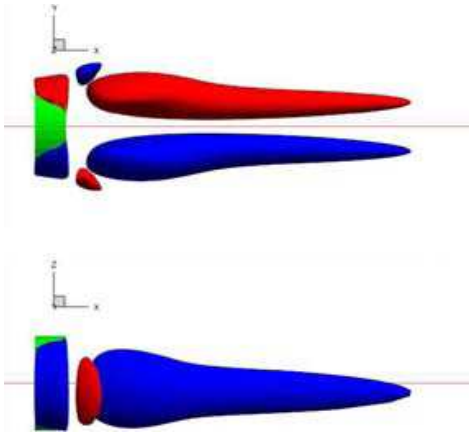

Figure 1.8: Steady non-axisymmetric flow behind a fixed cylinder. Stream-wise iso-vorticity contours. $\chi = 3, Re = 165$. Auguste *et al.* (2010).

10), Shenoy & Kleinstreuer (2008) ($\chi = 10$) and Auguste *et al.* (2010) ($\chi = 3$), the primary bifurcation is regular in the $m = 1$ azimuthal subspace leading to a *steady non-axisymmetric* but planar symmetric state, the symmetry plane of which has an arbitrary orientation selected by initial conditions (see section 1.4). The breaking of axisymmetry yields a steady lift oriented in the symmetry plane. This state is denoted as SS (steady state) in Fabre *et al.* (2008) and Meliga *et al.* (2009) and 'steady asymmetric' in Shenoy & Kleinstreuer (2008). The threshold of the primary bifurcation has been given by Fernandes *et al.* (2007) as a function of χ for cylinders of finite aspect ratio. In the cited bibliography, there is a good consensus as for the critical Reynolds number value of Re_1 for a thin disc. It is found between 115 and 117. The steady asymmetric state is visualized in Figure 1.8.

- *(b):* While the steady non-axisymmetric state is common to all investigated cases, including that of a sphere, the secondary bifurcation, albeit of Hopf type in all cases, has been found to lead to a specific *periodic state without planar symmetry* for a thin disc and a cylinder of aspect ratio $\chi = 10$. This state is characterized by a 'kinking of trailing vortices' past the body (Shenoy & Kleinstreuer, 2008, see) generating an oscillating component of the lift. While the mean lift lies in the symmetry plane selected at the primary bifurcation, the oscillating component is perpendicular. As a consequence, it has been called RSB (reflectional symmetry breaking) by Fabre *et al.* (2008), MM_π (mixed mode with phase π) state by Meliga *et al.* (2009), 'steady 3D periodic with regular rotation of the separation region' by Shenoy & Kleinstreuer (2008) or 'yin-yang' by Auguste *et al.* (2010). For the thin disc the critical Reynolds number Re_2 was found between 121 and 125.6. The reflectional symmetry breaking state is visualized in Figure 1.9.

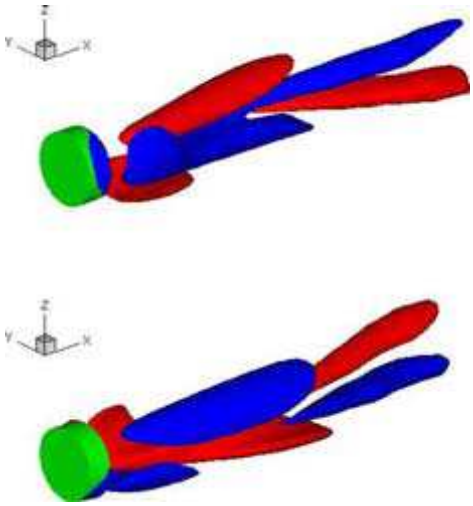

Figure 1.9: Periodic flow without planar symmetry behind a fixed cylinder. Stream-wise iso-vorticity contours. $\chi = 3, Re = 182$. Auguste *et al.* (2010).

- *(c):* Alternatively, for $\chi = 3$, Auguste *et al.* (2010) evidenced a transition to the *periodic state with planar symmetry* as observed many times in the sphere wake (Johnson & Patel, 1999, see e.g.) at the secondary bifurcation. In this state, the lift oscillates in the symmetry plane and keeps a non zero mean value. It has been called RSP state by Fabre *et al.* (2008), MM_0 state by Meliga *et al.* (2009) or 'zig-zig' by Auguste *et al.* (2010). The change of the bifurcated state does not significantly influence the trend of the critical Reynolds number as a function of the aspect ratio. It was fitted to a smooth function by Fernandes *et al.* (2007). The reflectional symmetry preserving state is visualized in Figure 1.10.

- *(d):* State (c) is to be distinguished from the *periodic state with a zero mean lift* although both have a symmetry plane. The mean value of the oscillating lift in the periodic state without planar symmetry *(b)* has been observed to vanish until the planar symmetry is recovered (but with a symmetry plane perpendicular to that chosen at the primary bifurcation). The lift oscillates in this symmetry plane with a zero mean value. This *periodic state with a zero mean lift* has been observed for the thin disc and for the cylinder of aspect ratio $\chi = 10$. It is to be noted that the same state arises in the case when the Hopf bifurcation directly breaks the axisymmetry of the flow, which happens for the opposing flow in the wake of a heated sphere (see Kotouč *et al.*, 2009*a*). In the bibliography concerning discs, this state is called SW (standing wave) mode (Fabre *et al.*, 2008; Meliga *et al.*, 2009) or 'unsteady with plane of symmetry and zero lift force' (Shenoy & Kleinstreuer, 2008). Its threshold has been found at $Re \approx 140$ (Fabre *et al.*, 2008) and 143 (Meliga *et al.*, 2009).The reflectional symmetry preserving state with a zero mean lift is visualized in Figure 1.11.

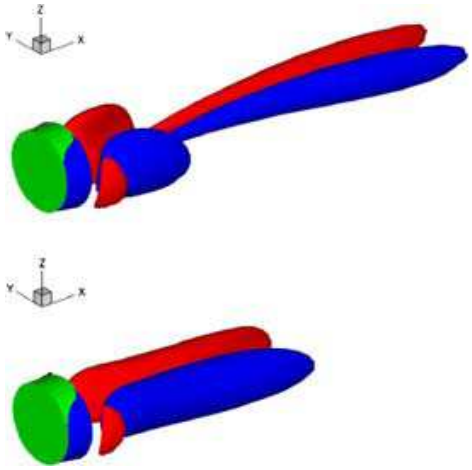

Figure 1.10: Periodic flow with planar symmetry behind a fixed cylinder. Stream-wise iso-vorticity contours. $\chi = 3, Re = 182$. Auguste *et al.* (2010).

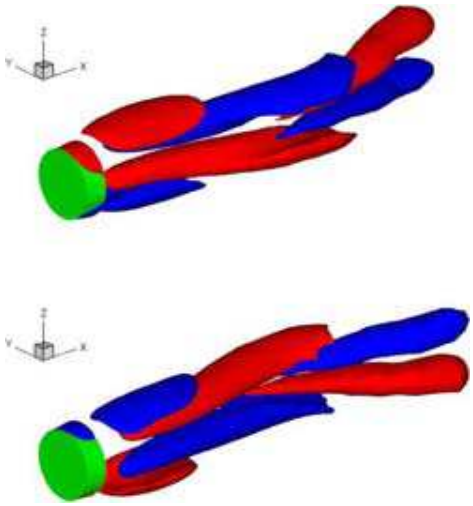

Figure 1.11: Periodic flow with planar symmetry and zero mean lift behind a cylinder. Stream-wise iso-vorticity contours. $\chi = 3, Re = 216$. Auguste *et al.* (2010).

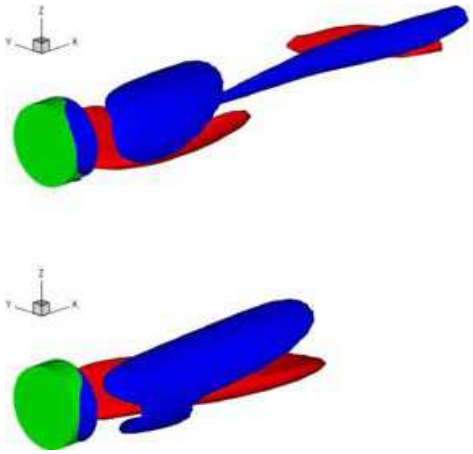

Figure 1.12: State with a non zero helicity. Stream-wise iso-vorticity contours. $\chi = 3, Re = 187$. Auguste *et al.* (2010).

- *(e):* In a single case, that of the cylinder with $\chi = 3$ Auguste *et al.* (2010), reported the existence of a *state with non zero helicity*. The net non zero helicity arises due to unequal amplitudes of spiral modes appearing in the weakly non-linear analysis of Fabre *et al.* (2008) and Meliga *et al.* (2009) (see section 1.4). On the time scale of a vortex shedding period, the helicity yields an elliptic path of the lift. The latter moves periodically in the plane perpendicular to the flow axis so that the lift path can roughly be described as a slowly oscillating or rotating ellipse. Because of the two scales present and of the form of the lift trajectory the state is called 'quasiperiodic pulsating' or 'knit-knot' by Auguste *et al.* (2010). Similar states have also been observed in the opposing flow past a heated sphere by Kotouč *et al.* (2009*a*). The state with a non zero helicity is visualized in Figure 1.12.

- *(f):* The transition to chaos is preceded by a *quasi-periodicity* characterized by the presence of a slower frequency close to 1/3 of the 'leading frequency' of the previous regimes Fabre *et al.* (2008). The same behavior has been observed in the unheated and heated sphere wake (Bouchet *et al.*, 2006; Kotouč *et al.*, 2009*b*). A similar modulation sets in states with non zero net helicity (Kotouč *et al.*, 2009*b*).

- *(g):* The *chaotic states* have no symmetry. The lift coefficient describes a chaotic path in the plane perpendicular to the flow axis.

In spite of a significant progress in the understanding of the transition scenario of flat axisymmetric bodies, especially of a thin disc, the existing bibliography does not provide a more systematic picture taking into account variations of the aspect ratio. For flat cylinders the parametric study of the first two bifurcation thresholds of Fernandes *et al.* (2007) can be improved, extended and refined with account of the progress in identification of more complex regimes. The linear analysis of Natarajan & Acrivos (1993) takes up the thin disc

and a sphere as two extreme cases. The link between them is represented rather by oblate spheroids than by flat cylinders. The former have, however, never been investigated. The wakes of cylinders and those of spheroids can both be characterized by just two parameters allowing a relatively easily feasible two parametric study providing an exhaustive picture of the transition scenario. This missing investigation was undertaken in the framework of this thesis.

1.7 Freely falling axisymmetric bodies in a fluid initially at rest

The development of modern experimental techniques over the recent decades and the emergence of numerical methods shed some light on the nature of complex trajectories of axisymmetric bodies freely falling or rising in a fluid initially at rest. A sphere and flat cylinders received the most attention, as the transitional regimes of their fixed counterparts were extensively studied (see sections 1.5 and 1.6). Other geometries, namely the oblate spheroids, were, according to our knowledge, not studied experimentally because their manufacturing is more delicate and requires more precision.

1.7.1 Freely falling and rising spheres

The transitional regimes of freely falling spheres can be characterized by two non-dimensional parameters. The velocity of the fall or ascension of a sphere is uniform only when the wake is axisymmetric. In the transitional regimes the asymptotic velocity is non-uniform and the Reynolds number based on this velocity can no longer be used. Instead, the effective acceleration (resulting from the buoyancy and the mass of the body) yields a velocity scale $\sqrt{|\rho_s/\rho_f - 1|gd}$, where ρ_s and ρ_f is the density of the solid and fluid respectively, g is the gravitational acceleration and d the diameter of a sphere. This velocity scale replaces the linear velocity of fixed body configurations. The non-dimensionalization of the Navier-Stokes equations then brings about a new non-dimensional parameter named the Galileo number (G):

$$G = \frac{\sqrt{|\rho_s/\rho_f - 1|gd^3}}{\nu}, \tag{1.24}$$

where ν is the kinematic viscosity of the fluid. The Galileo number represents the inverse of the non-dimensionalized kinematic viscosity and plays a role of the Reynolds number in the Navier-Stokes equations. In a sub-critical regime, corresponding to the vertical trajectory, the Galileo and Reynolds numbers are directly related through the expression:

$$C_D(Re) = \frac{4G^2}{3Re^2}, \tag{1.25}$$

where C_D is the drag coefficient. The second non-dimensional parameter required to completely describe the transitional regimes is the solid to fluid density ratio: (ρ_s/ρ_f).

The early stages of the transition of a fixed sphere wake proved to be similar to the regimes found for freely moving spheres. This similarity was implicitly assumed in the

earliest studies. Magarvey & MacLatchy (1965) observed the wake of freely falling spheres. They found that their trajectories deviated from the vertical direction once the wake ceased to be axisymmetric. In the same way as for the fixed case, the first bifurcation is regular and marked by the appearance of a non-zero lift force responsible for an oblique path. Goldburg & Florsheim (1966) found, for $Re = 300$ ($G \approx 220$) and the density ratio ($\rho_s/\rho_f = 1.12$), that the wake oscillates with a base frequency $St \approx 0.07$. Magarvey & Bishop (1961*b*) studied immiscible liquid drops and found the unsteady wake for the Reynolds number $Re = 350$ and density ratios ($1 < \rho_s/\rho_f = 1.6$). They observed that the found characteristic frequency $St = 0.12$ is in good agreement with that obtained for a fixed sphere. This result should be treated, however, with caution as the comparison of the liquid drops with a solid sphere is not straightforward. The inclusions may deform and the non-slip boundary condition on their surface is questionable. Lunde & Perkins (1998) studied experimentally spherical bubbles rising in still tap water for the Reynolds number range from about 700 to 1300. They observed fluttering planar and helicoidal (spiraling) trajectories. More recently, the experiments of Wu & Gharib (2002) demonstrated a relation between the shape and path of small air bubbles rising in clean water. They noticed that bubbles in the diameter range $0.1 - 0.2$ *cm* assume two steady shapes, that of a sphere and of an ellipsoid (depending on the size of the capillary tube from which they were detached). They found that small spherical bubbles rise rectilinearly (the Reynolds number based on their diameter is therefore sub-critical), while the larger ones follow zigzag paths. They observed spiraling paths for ellipsoidal bubbles and remarked that they moved significantly faster then spherical ones of equivalent volume. Wu & Gharib (2002) explain their observation by the presence of impurities at the surface of spherical bubbles. Numerical simulations carried out by Mougin & Magnaudet (2002) for a rigid spheroidal bubble of aspect ratio (defined as the ratio of the large to small diameter) $\chi = 2.5$ found that the initial zigzag path transforms upon the increase of the Galileo number into a spiral confirming the experimental observations of Wu & Gharib (2002).

The knowledge of the transition scenario in the wake of freely falling spheres gained by the first experimental and numerical studies of both rigid spheres and deformable or rigid bubbles was far from being complete until the numerical study (see Jenny *et al.*, 2003, 2004; Jenny & Dušek, 2004) exploring the whole parametric space spanned by the two non-dimensional parameters: the density ratio ($0 < \rho_s/\rho_f < \infty$) and the Galileo number $150 < G < 350$. Their results are summarized in a state diagram reproduced in Figure 1.13.

The exhaustive study of Jenny (2003) motivated a subsequent experimental investigation undertaken by Veldhuis & Biesheuvel (2007), which evidenced the existence of transitional regimes, whose description ('the main features of the motion of the spheres') is in good agreement with numerical results. They remarked, however, the differences in found dominant frequencies in unsteady regimes. For light spheres, the reported frequencies show that the zigzagging regime observed experimentally is rather the rapidly oscillating one found to coexist with chaotic states than the slow zig-zag arising when the amplitude of oblique oscillations makes the trajectory toggle to the opposite side of the vertical. Their visualizations present a bifid wake, characteristic for a steady asymmetric regime of a fixed sphere, in wakes of free spheres contrary to the prediction of Jenny (2003).

The extensive experimental study carried out by Horowitz & Williamson (2010*a*) for

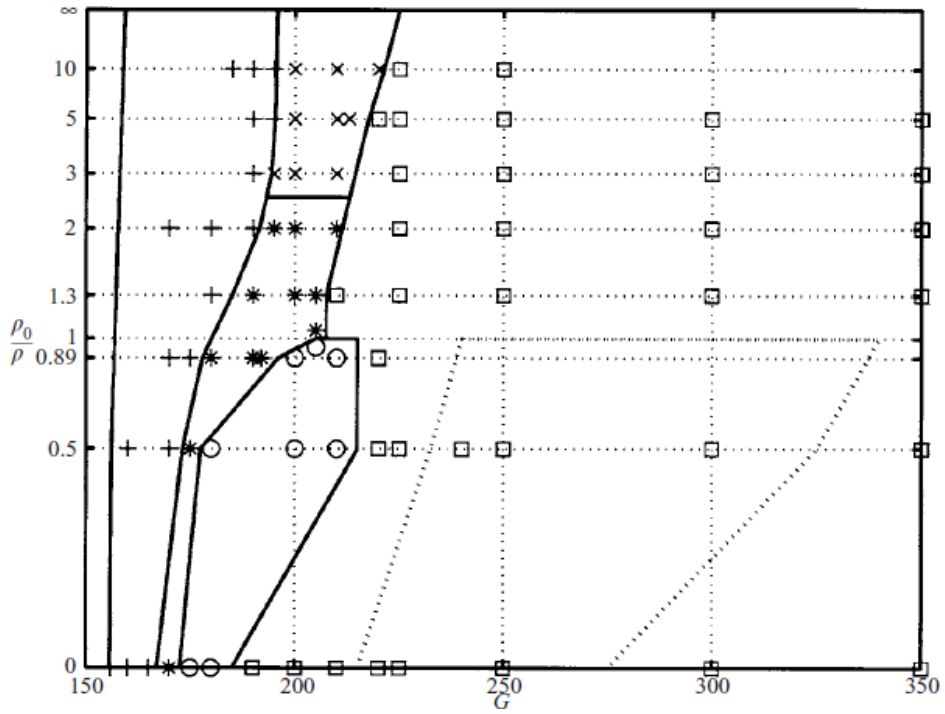

Figure 1.13: Diagram of the asymptotic states of the trajectory of a free sphere. The vertical axis is plotted proportionally to $(\rho_0 - \rho)/(\rho_0 + \rho)$, but is labelled in ρ_0/ρ. To the left of the primary bifurcation (leftmost line) the wake is axisymmetric. The symbols denote the simulations: +, steady and oblique; $*$, oblique and oscillating regime with low frequency ($0.045 <= f <= 0.068$); $\times$, oblique and oscillating regime with high frequency ($f \approx 0.180$); , zigzagging periodic regime ($0.023 <= f <= 0.035$); □, three-dimensional chaotic regime. The domain of coexistence of a chaotic and a periodic state ($f = 0.14$) is approximately delimited by the dotted line. Source: Jenny (2003).

freely falling or ascending spheres aimed at determining the critical density ratio ρ_s/ρ_f^* (which they call critical mass m_{crit}^*) below which a sphere will vibrate (zigzagging periodic regime). They demonstrated that such critical ratios exist and are essentially constant over wide ranges of the Reynolds number:

$$m_{crit}^* \approx 0.4, Re = 260 - 1550, \tag{1.26}$$

$$m_{crit}^* \approx 0.6, Re = 1550 - 15000, \tag{1.27}$$

Above this critical mass m_{crit}^* spheres moved basically rectilinearly: vertically or obliquely. The jump in the critical mass seems reasonable as the dynamics change upon the transition of the flow from laminar to turbulent. They remarked that, in contrast with previous studies, over a wide range of density ratios ($0.4 < m* < 1$) spheres rose without oscillations, which agrees well with predictions of critical mass in vortex induced vibration experiments with

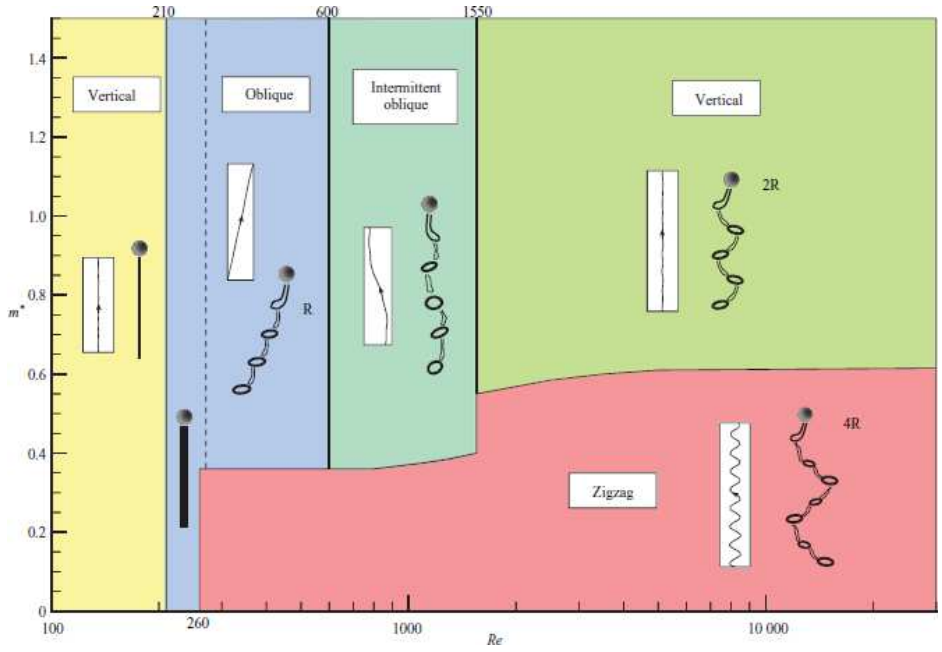

Figure 1.14: Map of regimes of sphere motion and associated wake patterns in the m^*, Re plane. Typical trajectories are shown for each regime. Source: Horowitz & Williamson (2010*a*).

elastically mounted spheres carried out previously by the authors. The summary of the results is presented in a form of a map of regimes of sphere motion reproduced here in Figure 1.14.

Horowitz & Williamson (2010*a*) define several wake modes characterizing the found regimes. They are reproduced in Figure 1.15. They found that the wake in the steady oblique regime $m^* > m^*_{crit}$ and $Re = 270 - 600$ is characterized by the shedding of a single sided chain of vortex rings, which they define as the 'R' mode. For greater Reynolds numbers $Re > 1550$ the shedding mode comprised a double-sided chain of vortex rings, referred to as '2R' mode in Figure 1.15. In between, for Reynolds numbers $600 < Re < 1550$ and the concerned mass ratios m^*, they evidenced intermittent oblique motion with the vortex rings in the body wake being shed with different orientations in an irregular manner. They discovered that the periodic zigzag motion describes a wake composed of four vortex rings formed in each cycle of body motion, which they called '4R' mode.

The slow zigzagging regime evidenced by Jenny *et al.* (2004) has never been observed in the experiments. A possible explanation might be that small imperfections of spheres used in experiments are sufficient to suppress this state. Moreover, numerical simulations tend to predict significant qualitative changes for $m^*_{crit} \approx 1$ instead of 0.4. Elucidation of this disagreement would require a joint experimental and numerical study conducted at the same time.

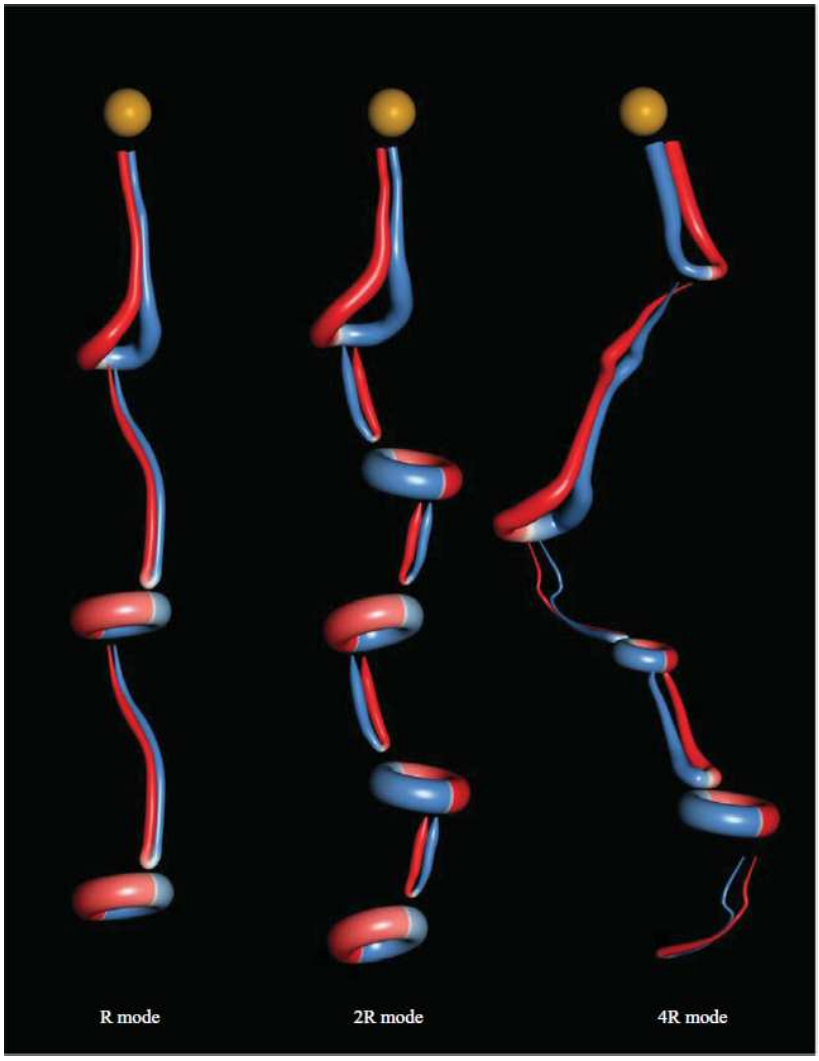

Figure 1.15: The family of periodic wake modes for rising and falling spheres. Source: Horowitz & Williamson (2010*a*).

1.7.2 Freely falling and rising discs and cylinders

Freely falling or rising discs and cylinders constitute another class of axis-symmetric bodies, that have attracted and continue to attract a lot of attention. This is, to a large extent, due to experimental papers, that serve now as a reference in the field. Field *et al.* (1997) in their letter to Nature provided an exhaustive overview (comprising the work of Willmarth *et al.* (1964) and of Stringham *et al.* (1969)) of experimentally evidenced transitional regimes present in the scenario of thin discs. They identified five parameters relevant in the study: the disc diameter d, thickness t and density ρ_s, as well as the fluid density ρ_f and kinematic viscosity ν, which yield three non-dimensional parameters: the dimensionless moment of

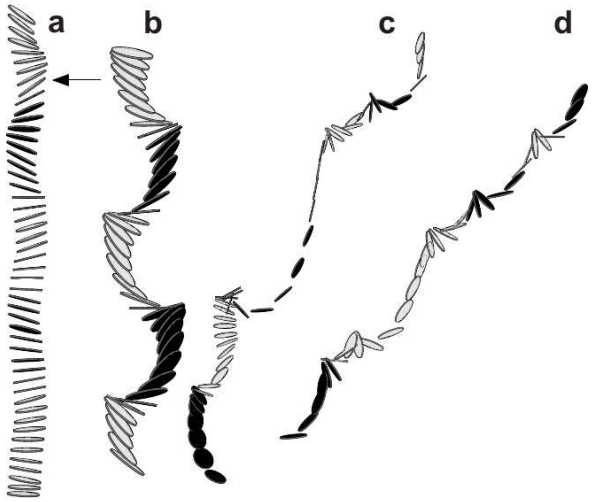

Figure 1.16: Trajectories of falling discs, obtained by imaging from the side using a video camera; (a), Steady-falling regime. The arrow represents an extrema of motion. (b), Periodic-oscillating motion observed and (c). Typically, a disc in this regime will oscillate with larger and larger amplitude until its angle is so high that it actually flips over. It then tumbles several times and then suddenly jumps back to oscillating behavior. (d), Tumbling motion, the disc turns continuously end-over-end while drifting in one direction. Source: Field *et al.* (1997).

inertia $I^* = I_{disc}/\rho_f d^5 = \pi\rho t/64\rho_f d$, the Reynolds number $Re = Ud/\nu$, where U is the mean vertical disc velocity and the aspect ratio d/t. Considered discs were thin and therefore the last parameter was neglected as non-significant. The investigation of the dependence of the disc's dynamics on the two retained dimensionless parameters allowed Field *et al.* (1997) to identify four distinct transitional regimes: 'steady falling', 'periodic oscillating', 'chaotic' and 'tumbling' represented in Figure 1.16.

The obtained results were presented in a form of a state diagram, reproduced in Figure 1.17, as a function of the two non-dimensional parameters (Re, I^*). The domains of existence of distinct regimes were clearly delimited and found to agree with the results obtained previously by Willmarth *et al.* (1964) and Stringham *et al.* (1969). In order to gain the physical insight into dynamics of the disc, Field *et al.* (1997) interpreted observed regimes from the point of view of dynamical systems and showed that the transition from the periodic oscillations to the chaotic regime can be illustrated by one dimensional maps with the angle θ between the disc's normal and the vertical direction as a single parameter. This observation confirms that the whole solid-fluid configuration behaves like a low-dimensional dynamical system. The authors raise also a question whether the evidenced tumbling regime is periodic in nature as they observed that its rotational period vary in time. Therefore, they do not exclude that the tumbling regime is also characterized by chaotic dynamics. They note however, that for high values of I^* (obtained using paper discs in air) the rotational period appeared constant.

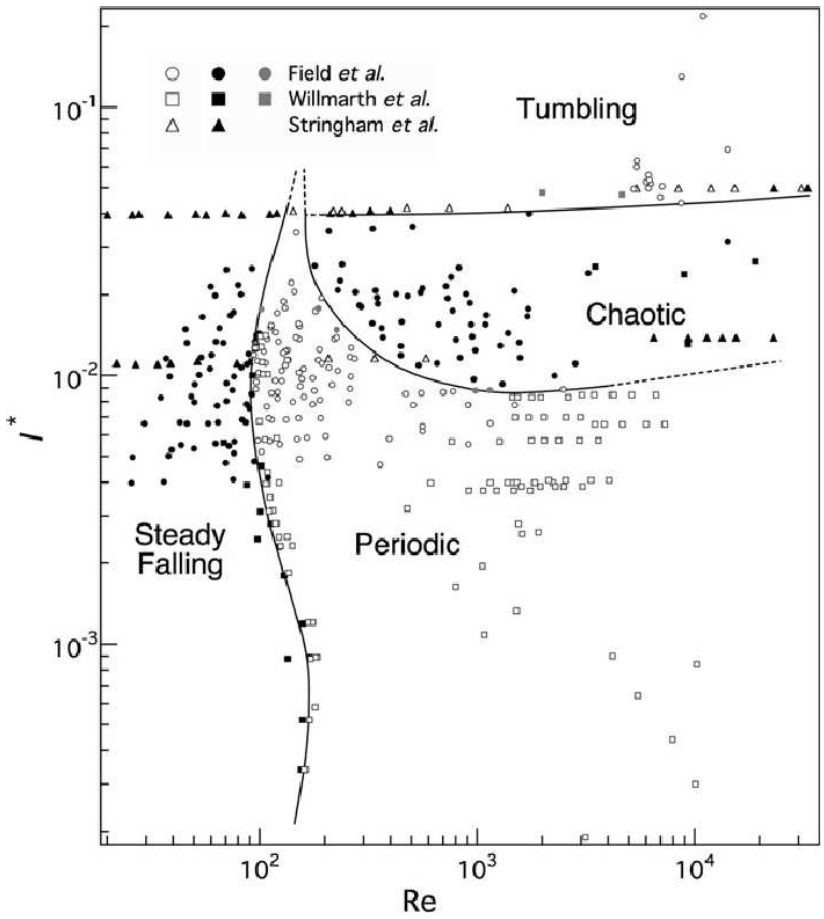

Figure 1.17: Phase diagram showing the dynamical behavior of falling discs as a function of the two parameters I^* (dimensionless moment of inertia) and Re (Reynolds number) obtained from experimental data. Filled symbols represent discs with steady falling or chaotic behavior, and open symbols periodic or tumbling behavior. Grey symbols represent cases judged to lie on the border between two regimes. Source: Field *et al.* (1997).

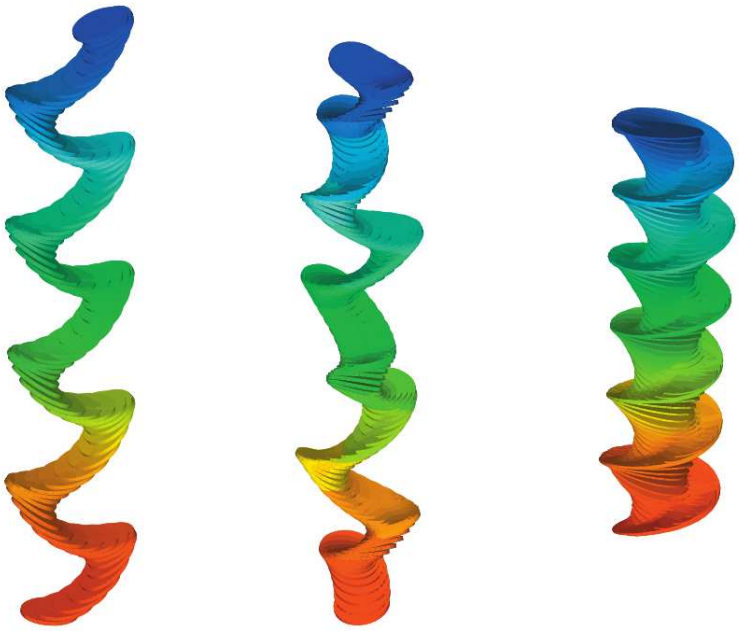

Figure 1.18: Collage of consecutive three-dimensional positions and orientations for falling discs from experiments. Three typical motions are shown, from left to right: planar zigzag ($I^* = 2.95 \times 10^{-3}$, $Re = 1350$, $d = 30mm$),transitional ($I^* = 1.47 \times 10^{-3}$, $Re = 935$, $d = 30mm$), and spiral ($I^* = 2.15 \times 10^{-3}$, $Re = 630$, $d = 28mm$). Source: Zhong *et al.* (2011).

All the trajectories reported by Field *et al.* (1997) were planar. The recent experimental study of Zhong *et al.* (2011) of free thin disc motion revealed the existence of non-planar trajectories. They identified two new types of motion, for discs having small moments of inertia I^*, which they called spiral and transitional states. They observed that the initial planar zigzag motion is destabilized by the growth of the secondary oscillation in the normal direction. The direction of the rotation begins to drift and the disc starts to rotate about its symmetry axis which lead eventually to a spiral motion. The axial rotation, essential for the appearance of the observed non-planar motions, can be triggered more easily for smaller I^* explaining why they were not reported for higher moments of inertia. Figure 1.18 reproduces the new states found by Zhong *et al.* (2011).

Few years ago Fernandes *et al.* (2007) studied experimentally freely rising rigid cylinders in a fluid of the density close to that of the solid body ($\rho_s/\rho_f \approx 1$). They investigated the role of the Reynolds number based on the mean rise velocity u_m in the range $80 \leq Re \leq 330$ on the dynamics of flat cylinders of the aspect ratio in the range $1.5 \leq \chi \leq 20$. They observed that the trajectories of the cylinders are essentially two-dimensional. At the critical Reynolds number Re_{cf1} the steady vertical motion is replaced by the unsteady regime characterized by the periodic oscillations of the body velocity and orientation. The threshold was found to depend on the aspect ratio. Figure 1.19 presents the obtained results. Fernandes *et al.*

(2007) carried out at the same time direct numerical simulations of the flow past fixed cylinders. They determined the threshold of the primary regular bifurcation $Re^*_{cf1}(\chi)$ that breaks the axial symmetry of the wake and the threshold $Re_{cf2}(\chi)$ of the Hopf bifurcation that leads to wake oscillations. The comparison with fixed bodies allowed them to propose an explanation of the effect of the body shape on the dynamics of the wake. They noticed that the appearance of the path instability for thick discs ($\chi < 6$) is triggered by the wake instability observed for fixed bodies with the critical Reynolds number $Re_c(\chi)$ being close to $Re_{cf1}(\chi)$ and with the characteristic frequency close to the one observed for fixed bodies. The threshold for thin cylinders ($\chi > 6$) lies, however, significantly above $Re_{cf1}(\chi)$. The authors suspect that the instability is delayed due to the flow corrections induced by the translation and rotation of freely moving bodies. They remark, however, that in a range $Re_{cf1} < Re < Re_c$ the flow might be already unstable causing only tiny oscillations of the body, that cannot be captured by the experiment. More recently, Ern *et al.* (2012) reported the detection of "tiny, mostly erratic, movements" of thin discs ($\chi \to \infty$) in this range of the Reynolds numbers. These observations agree with the results of direct numerical simulations carried out by Auguste (2010), who reports the existence of small amplitude non-vertical regimes preceding the appearance of large planar oscillations (their thresholds agree well with the results of Fernandes *et al.* (2007)) for discs of the aspect ratio $\chi \geq 10$. For $\chi = 10$, Auguste (2010) found that the primary instability is regular and leads to the steady oblique regime. This result motivated the theoretical study of Fabre *et al.* (2012) devoted to cylinders of various aspect ratios (and a sphere) limited to the case for which the angle of incidence of the disc remains small. Assuming that the first bifurcation is regular (resulting in steady wake), by using a weakly nonlinear expansion of the Navier-Stokes equations, they predicted the existence of the steady oblique regime. Its threshold was found to be independent of the body-to-fluid density ratio.

The aforementioned studies of the path instabilities of freely falling and rising discs revealed very complex and rich dynamics that is far from being fully understood. In particular, exhaustive parametric numerical study is still missing. It will be undertaken in the framework of the present thesis.

1.8 Numerical methods

Accurate and efficient simulations of freely falling or rising discs and, more generally, flat bodies proved to be a real challenge. Nonetheless, numerical simulations have an important advantage over experiments consisting in a precise control of the boundary and initial conditions. They are therefore usually better suited to determine asymptotic states, to evidence bi-stability and to distinguish an inherently chaotic behavior from experimental disturbances (Ern *et al.*, 2012). Auguste (2010) carried out recently fully three-dimensional direct numerical simulations, using finite volume code, of freely falling cylinders. He achieved a good agreement with the experimental results obtained by Fernandes *et al.* (2007). However, for certain parameters of the study (high non-dimensionalized moment of inertia implying long oscillation periods and hence long simulation times) the computing time required exceeded available resources. Indeed, as stated by Ern *et al.* (2012): "DNS requires the development

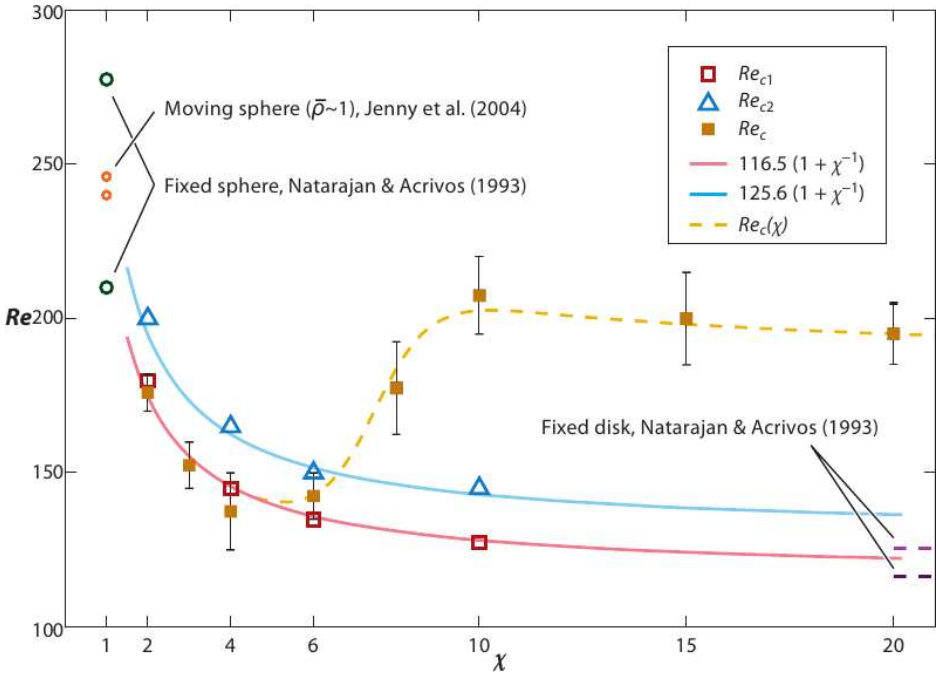

Figure 1.19: Critical Reynolds numbers characterizing the onset of instabilities of short cylinders of aspect ratio χ. Re_{c1} is the steady bifurcation of the flow past the fixed body (DNS), Re_{c2} is the Hopf bifurcation of the flow past the fixed body (DNS), and Re_c is the onset of the path oscillation of the freely rising body (experiments); the dashed line is an empirical fit of $Re_c(\chi)$. Source: Fernandes *et al.* (2007).

of specific algorithms capable of solving properly the coupled body-fluid problem and of dealing with the outflow boundary condition, both with an accuracy compatible with the usual requirements of stability problems". These goals are far from being easy to meet. A high-order method, capable of accurately resolving boundary layers and all scales present in a flow, having minimal numerical dispersion and dissipation, is required. Moreover, the numerical method must be as efficient as possible because the investigation of transitional regimes, responsible for non-straight trajectories, may require simulation of extremely long physical times.

Jenny & Dušek (2004) developed a spectral-spectral element method for the simulation of freely moving spheres. Its efficiency relied on the spatial discretization by spectral elements in the axial-radial plane and Fourier modes in the azimuthal direction. Ghidersa & Dušek (2000) demonstrated that this discretization perfectly mimics the onset of axisymmetry breaking in flows (see section 1.4). Use of a body-fitted mesh, allowing for an accurate resolution of boundary layers, required the whole computational domain to follow the translational movement of the body. The rotational degrees of freedom were modeled by a non-slip boundary condition on the rotating sphere's surface. The used cylindrical domain, reproduced in Figure 1.20, was sufficiently elongated in the vertical direction to capture the wake (it remains essentially vertical in transitional regimes and is still present far downstream of the body). An appropriate outflow condition minimized the influence of the boundary on the simulated physics allowing the wake to leave through the remote cylinder basis without perturbation. The principal innovation presented by Jenny & Dušek (2004) consisted in an implementation of an implicit coupling of the solid body and fluid equations accounting for all solid to fluid density ratios (down to zero) and degrading neither the accuracy of the time discretization nor the efficiency of the algorithm.

The modeling of dynamics of moving bodies requires the resolution of additional, ordinary differential, motion equations coupled with the partial differential equations of the continuous phase (see section 1.2). The simplest approach consists in using explicitly (hence comes the commonly used name 'explicit' coupling) the flow field at the previous time step to evaluate the hydrodynamic force and torque at the current step. This weak coupling is frequently employed for simulation of sedimenting particles (see e.g. Uhlmann, 2008). However, a special care must be taken for light particles as argued, for instance, by Hu *et al.* (2001) and Jenny *et al.* (2004). The explicit method looses its numerical stability as soon as the particle mass becomes comparable to its added mass. I.e., for a solid/fluid density ratio of 0.5 in the case of spheres. For flat objects, like discs, the added mass can very often largely exceed the actual mass even for sedimenting bodies.

Maxey & Patel (2001) proposed a force coupling method as a simple and efficient numerical model for multi-particle flows. Its application is however limited to small slip velocities because it does not resolve the flow details at the particle surface. Recently this method, initially developed for spherical particles, was extended to ellipsoids by Liu *et al.* (2009). It was demonstrated to provide approximate results for the particle motion and the flow field for viscous Stokes flow and small Reynolds numbers in agreement with direct numerical simulations. Most numerical methods developed for the simulation of multi-particle flows account for the fluid-solid interaction implicitly.

The fictitious domain methods comprise Immersed Boundary Methods (IBM) and dis-

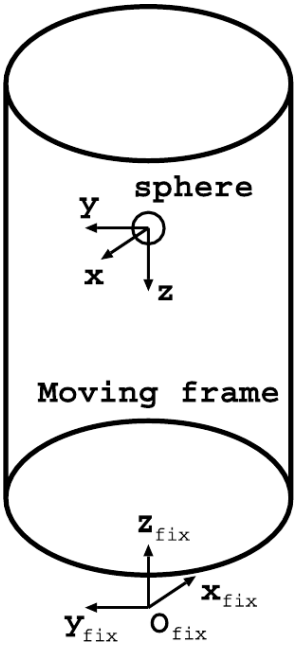

Figure 1.20: Computational domain for the simulation of a freely moving sphere. Source: Jenny & Dušek (2004).

tributed Lagrangian methods (DLM). They can be potentially used for simulation of moving bodies of arbitrary shape. Therefore their possible domain of applications is far more general than a single particle problem. Kim *et al.* (2001) presented an immersed boundary method, based on a finite-volume approach on a staggered grid with a fractional step discretization in time, for the simulation of complex geometries. It consisted in introducing a momentum forcing and mass source/sink on the body surface or inside the body in order to satisfy the non-slip boundary condition on the immersed boundary and the conservation of mass in cells containing it. This was achieved by using a stable second-order interpolation scheme for the evaluation of the momentum forcing on the immersed boundary. Similar approach was proposed by Udaykumar *et al.* (2001), who employed a mixed Eulerian-Lagrangian framework to treat the moving immersed boundary as a sharp interface. In fractional step schemes used in the aforementioned immersed boundary methods, the most time consuming step is the solution of the pressure Poisson equation. Udaykumar *et al.* (2001) remedied this important drawback by using a multigrid method accounting for the presence of the sharp, immersed boundary.

The distributed Lagrangian method (DLM) of Glowinski *et al.* (2001) enforces the velocity field of a solid body by constraints satisfied using forcing terms playing the role of Lagrange multipliers. It is well suited for the simulation of particulate flows accounting for body–body and body–wall collisions (see Figure 1.21). The immersed boundary method of Peskin (2002) uses a mixed Eulerian-Lagrangian approach: fluid degrees of freedom are treated in Eulerian and solid in Lagrangian frame. It was recently applied by Uhlmann

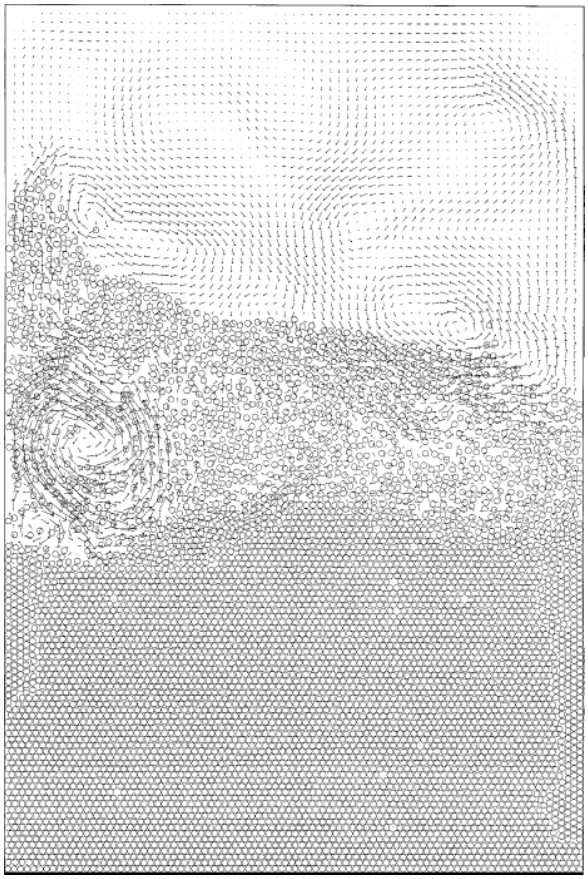

Figure 1.21: Sedimentation of 6400 particles. Source: Glowinski *et al.* (2001).

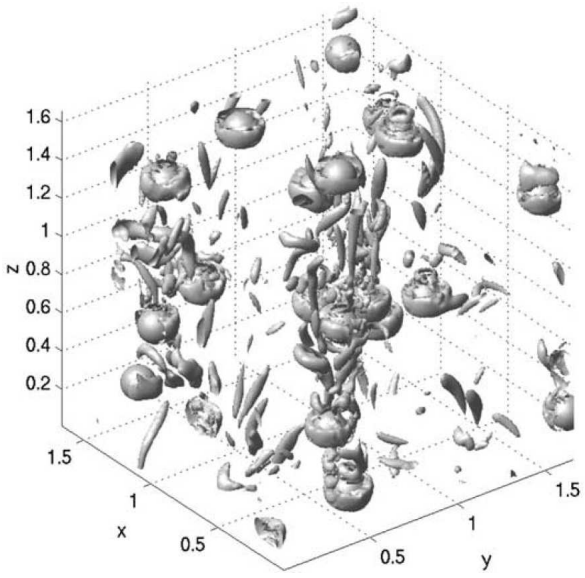

Figure 1.22: Visualization of the instantaneous flow field (iso-surfaces of positive values of the Laplacian of pressure, indicating vortex cores) and particle positions in a multi-particle simulation ($N_p = 1000$). A part of the computational domain is represented. Source: Uhlmann (2005).

(2005) to study the sedimentation of solid spherical particles in a fluid. An improved efficiency was achieved by incorporation of the Peskin's delta function approach directly into the formulation of the fluid-solid interaction force facilitating the transfer between Eulerian and Lagrangian variables and avoiding the restriction on the time step. The marker points are fixed only to the solid body surface and thus do not increase the number of degrees of freedom. This method was successfully employed for the simulation of multi-particle suspensions with the number of particles going up to $N_p = 10^5$ (see Figure 1.22). Höfler *et al.* (1998) developed an approach that enforces the interaction between the solid and the surrounding fluid through a penalty method instead of the multiplier technique.

A finite element technique based on moving unstructured grid has been developed and tested in 2D (see Hu, 1996) and 3D (see Hu *et al.*, 2001) as another alternative for simulation of multi-particle flows. The formulation developed for generalized Galerkin finite elements used a single variational formulation incorporating both the particle and fluid equations of motion. The hydrodynamic forces and moments are not computed explicitly and the motion of solid particle is handled by an arbitrary Lagrangian-Eulerian (ALE) technique. The method involves dynamic adaptive meshing yielding a moving body fitted mesh (see Figure 1.23). This allows the refinement in the boundary layers. However, the re-meshing brings about non-negligible additional costs (a Poisson equation to solve) and numerical difficulties (treatment of geometric singularities). The paper of Hu *et al.* (2001), presenting the ALE method, shows that a weak formulation yields a common matrix formulation involving both solid and fluid degrees of freedom (see the combined fluid-solid formulation of Hu *et al.*, 2001).

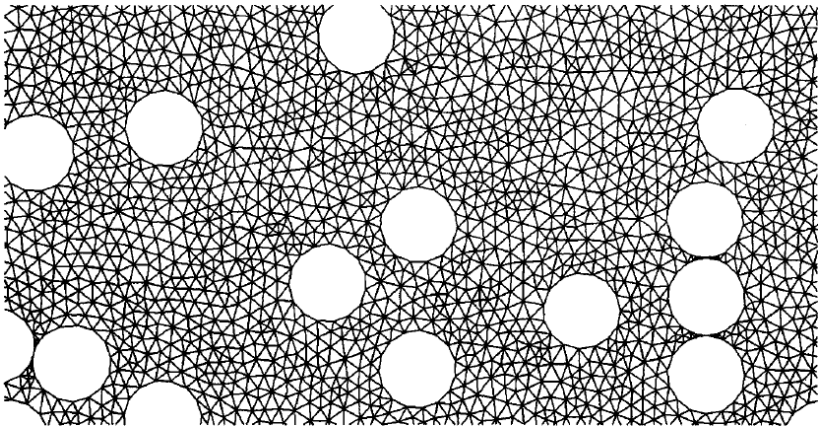

Figure 1.23: Body fitted finite element mesh used for simulation of 100 circular cylinders (zoomed view). Costly remeshing is required. Source: Hu (1996).

The matrix to inverse is, however, no longer symmetric which increases the computing costs. The same weak formulation is also applied in the framework of the DLM method by Glowinski *et al.* (2001) making both the DLM and ALE methods potentially applicable independently of the added mass.

The fully implicit formulation used by Jenny *et al.* (2004) benefits from the geometrical context of a single spherical body and of the Fourier azimuthal decomposition, which make it possible to obtain an almost negligible increase of computing costs without any tradeoff concerning the stability of the algorithm.

Since the added mass represents the main obstacle for the explicit solid-fluid coupling, the Kirchhoff equations have been used to extract the added mass term from the hydrodynamic force. The method was used to simulate the motion of an undeformable bubble by Mougin & Magnaudet (2002). This simple approach performs, however, less satisfactorily because it accounts only for pressure effects on the particle acceleration while, for a non zero time-step viscous effects are also present.

Recently, a series of numerical simulations focused on the settling motion of non-spherical bodies. Pan *et al.* (2005) (see also Pan *et al.*, 2002) presented numerical simulations, using Lagrangian multiplier based fictitious domain method, of fluid-ellipsoid interactions for an ellipsoid moving in a narrow channel, as well as of the interactions between a pair of ellipsoids. They observed, as could have been expected, that a settling ellipsoid moves to the center of a channel and continues to move with its broad side perpendicular to the main stream direction. A pair of ellipsoids settle side-by-side interacting with each other periodically. Fonseca & Herrmann (2005), using a constrained-force technique, studied the settling motion of one falling oblate ellipsoid. However, the attempt to reproduce the transitional regimes observed by Field *et al.* (1997) did not yield convincing results. In particular they could not find the tumbling regime. The lack of accuracy and the computing costs are still an obstacle for applying these codes to transitional regimes. A relatively efficient treatment of a moving geometry applied to the investigation of the path transition of a freely falling sphere based

on an implementation of the chimera method was recently described by Deloze *et al.* (2010). The method is not limited to spherical objects but the fully three-dimensional finite volume formulation, required by the presence of solid walls, is much heavier and less accurate than the spectral approach applicable to an unconfined object. In such a case, a moving mesh is not an absolute necessity.

Shenoy & Kleinstreuer (2010) studied, using a commercial finite-volume based code, freely falling cylinders of aspect ratios $\chi = 2$ and 4 in a zig-zagging regime. Their entire spherical domain turned with the solid body and was truncated at a relatively short distance of 20 diameters from the body. As they set the Dirichlet boundary conditions on the outer domain surface, the wake was not allowed to leave undisturbed. To see this, it is sufficient to realize that, at the threshold of the transition in the wake of a sphere (at the Reynolds number of 212), the velocity deficit is still about 20% at this distance. At the same time, most of the mesh points were useless because the body perturbs the flow only in a small fraction of the domain volume.

Bönisch *et al.* (2005) noted that, if the hydrodynamic force is the main needed result, a relatively small computational domain may be sufficient provided an outflow condition respecting the structure of the remote wake is used. It is well known, that the velocity deficit of the self-similar wake is proportional to the drag. The computation of the drag can thus be coupled with the outflow boundary condition to obtain an iterative procedure yielding the drag on a relatively small computational domain. The procedure was improved to account for non-symmetric flows to a second order of the asymptotic development by Bönisch *et al.* (2008) and, though developed for steady flows, it was applied to the simulation of the periodically oscillating and tumbling two-dimensional plate (Bönisch & Heuveline, 2007). The reliability of the method was, however, not demonstrated for unsteady flows at high Reynolds numbers in 3D. Also, very often, information on the wake structure is sought along with the movement of the body. In this case the simulation of the remote wake remains necessary.

In this thesis, a generalization of the approach developed by Jenny & Dušek (2004), which proved to be both reliable and efficient for simulation of transitional regimes of a spherical body (Jenny *et al.*, 2004), to the case of axisymmetric bodies of a more general shape (discs, cylinders and oblate spheroids) will be presented. This approach is well suited for several reasons: I.) physics of the problem require a rather long cylindrical domain to capture the wake of the body; II.) the Fourier azimuthal decomposition appears to best express the physics of the transition, which explains its rapid convergence. III.) body-fitted mesh enables considerable local refinement in boundary layers. To accommodate the movement of the non-spherical body with respect to the vertical cylindrical domain (the rotation of a non-spherical body modifies the domain symmetry), a new approach based on the decomposition of the computational domain will be proposed.

1.9 Objectives of this thesis

The purpose of the present thesis can be summarized as follows:

- Development of a reliable, efficient spectral–spectral element code for the simulation of fixed and freely falling/ascending axisymmetric bodies in a Newtonian fluid,

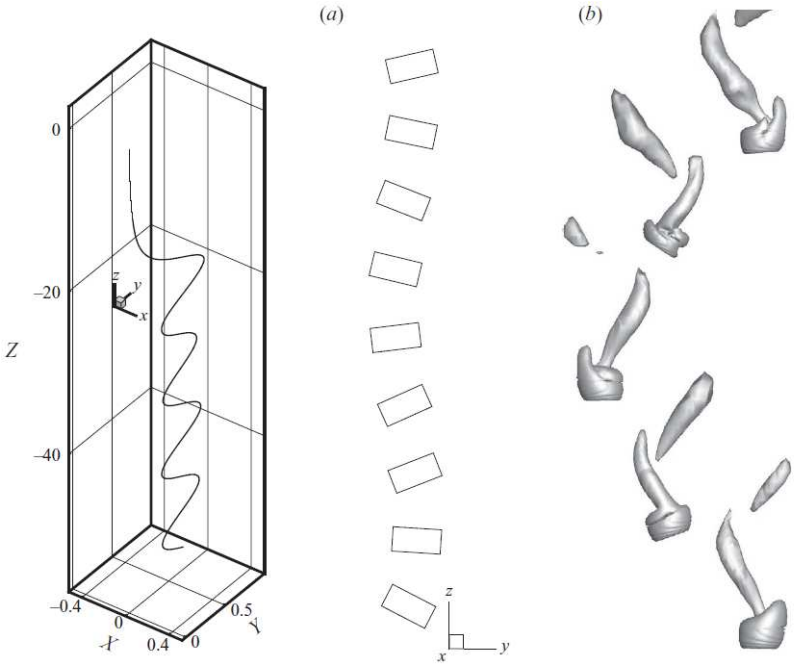

Figure 1.24: Trajectory of a freely falling disc of $\chi = 2$ at $Re = 240$: (a) three-dimensional trajectory of the disc; (b) motion of the disc in its oscillation plane; (c) vortex structures behind the disc visualized using the λ_2-criterion for single period of oscillation. Source: Shenoy & Kleinstreuer (2010).

- Establishment of a link between the transition scenario of a fixed sphere and of a disc by carrying a parametric study covering the whole range of aspect ratios $1 < \chi < \infty$ and Reynolds numbers $100 < Re < 400$,
- Study of the transitional regimes present in the scenario of freely falling discs, cylinders and oblate spheroids.

Chapter 2

Mathematical formulation

2.1 Fixed cylinders and oblate spheroids placed perpendicularly to a uniform flow

We consider fixed rigid cylinders and oblate spheroids, characterized by the aspect ratio defined for cylinders in section 1.6 and given by $\chi = d/a$ for oblate spheroids (where d is the transverse diameter and a the length of the streamwise axis of the spheroid), placed in a uniform unconfined flow. The flow of an incompressible fluid past fixed bodies is governed by the Navier-Stokes equations:

$$\nabla \cdot \mathbf{v} = 0, \tag{2.1}$$

$$\frac{\partial \mathbf{v}}{\partial t} + (\mathbf{v} \cdot \nabla)\mathbf{v} = -\frac{1}{\rho}\nabla p + \nu \nabla^2 \mathbf{v}. \tag{2.2}$$

The dynamic pressure field is denoted p, ρ is the density and ν is the kinematic viscosity of the fluid. The operator ∇ is defined in the Cartesian coordinates (x, y, z) by $\nabla = [\frac{\partial .}{\partial x}, \frac{\partial .}{\partial y}, \frac{\partial .}{\partial z}]$.

The Navier-Stokes equations can be non-dimensionalized using the free-stream velocity v_∞ as a reference velocity, d the diameter of cylinders or spheroids as a reference length, ρv_∞^2 as a reference pressure and d/v_∞ as a reference time. Then their non-dimensional form writes (the * symbol used conventionally to denote non-dimensionalized quantities is omitted here):

$$\nabla \cdot \mathbf{v} = 0, \tag{2.3}$$

$$\frac{\partial \mathbf{v}}{\partial t} + (\mathbf{v} \cdot \nabla)\mathbf{v} = -\nabla p + \frac{1}{Re}\nabla^2 \mathbf{v}, \tag{2.4}$$

where Re is the Reynolds number:

$$Re = \frac{v_\infty d}{\nu}. \tag{2.5}$$

The flow past fixed cylinders and spheroids is governed by only two dimensionless parameters – the Reynolds number and the aspect ratio.

2.2 Cylinders and oblate spheroids freely ascending or falling in a fluid initially at rest

A solid body immersed in a fluid is buoyed up by the Archimedes force equal to the weight of the fluid it displaces. It is also subjected to the hydrodynamic forces exerted by the surrounding fluid. The incompressible flow around the body is governed by the Navier-Stokes equations. They will be solved in the cylindrical computational domain represented in Figure 2.1. The cylinder axis is vertical. The center of the body is placed at the cylinder axis at a distance L_u from the upstream cylinder basis and L_d from the outflow basis. The radius of the cylindrical domain is denoted R_c. The domain is decomposed into a spherical sub-domain with center O and radius R_s ($d/2 < R_s < R_c$) rotating with the body and the remaining volume of the cylinder. The velocity field $\mathbf{v}$ is measured with respect to a fixed frame $(O_{fix}, x_{fix}, y_{fix}, z_{fix})$ with the z_{fix} axis oriented opposite to the vector of the effective gravitational and buoyant acceleration

$$\mathbf{g}_{eff} = \left(\frac{\rho_s}{\rho} - 1\right)\mathbf{g}, \tag{2.6}$$

i.e. upward for sedimenting and downward for ascending bodies. In Eq. (2.6), ρ_s stands for the average solid density, ρ for the fluid density and $\mathbf{g}$ is the vector of gravitational acceleration. The frame (O, x_c, y_c, z_c) of the cylindrical domain is translated with the body velocity $\mathbf{u}$ keeping the axes parallel to the fixed frame, while the axes of the frame (O, x_s, y_s, z_s) of the spherical sub-domain share partially the body rotation. Due to the axisymmetry of the body, it is not necessary to transmit the rotation with respect to its symmetry axis to the local frame. As a consequence, the x_s and y_s projections of the angular velocity vector $\boldsymbol{\omega}$ of the spherical sub-domain will be equal to the corresponding components of the angular velocity $\boldsymbol{\Omega}$ of the body while the z_s projection will be kept zero. The body is thus allowed to rotate about its axis with a non-zero angular velocity $\boldsymbol{\Omega} - \boldsymbol{\omega}$ with respect to the spherical sub-domain. The incompressible Navier-Stokes equations, written for a velocity field defined with respect to a fixed frame and projected onto a moving frame, take the following form:

$$\nabla.\mathbf{v} = 0, \tag{2.7}$$

$$\frac{\partial \mathbf{v}}{\partial t} + [(\mathbf{v} - \mathbf{u} - \omega \times \mathbf{r}) \cdot \nabla]\mathbf{v} + \omega \times \mathbf{v} = -\frac{1}{\rho}\nabla p + \nu \nabla^2 \mathbf{v}, \tag{2.8}$$

where p denotes the pressure field, ρ the density of the fluid and ν represents its kinematic viscosity. The domain decomposition reduces the mesh deformation to the relative rotation of the spherical sub-domain. At the same time, the outer sub-domain has a fixed vertical orientation, which will simplify the treatment of the boundary conditions and facilitate the physical interpretation of the results.

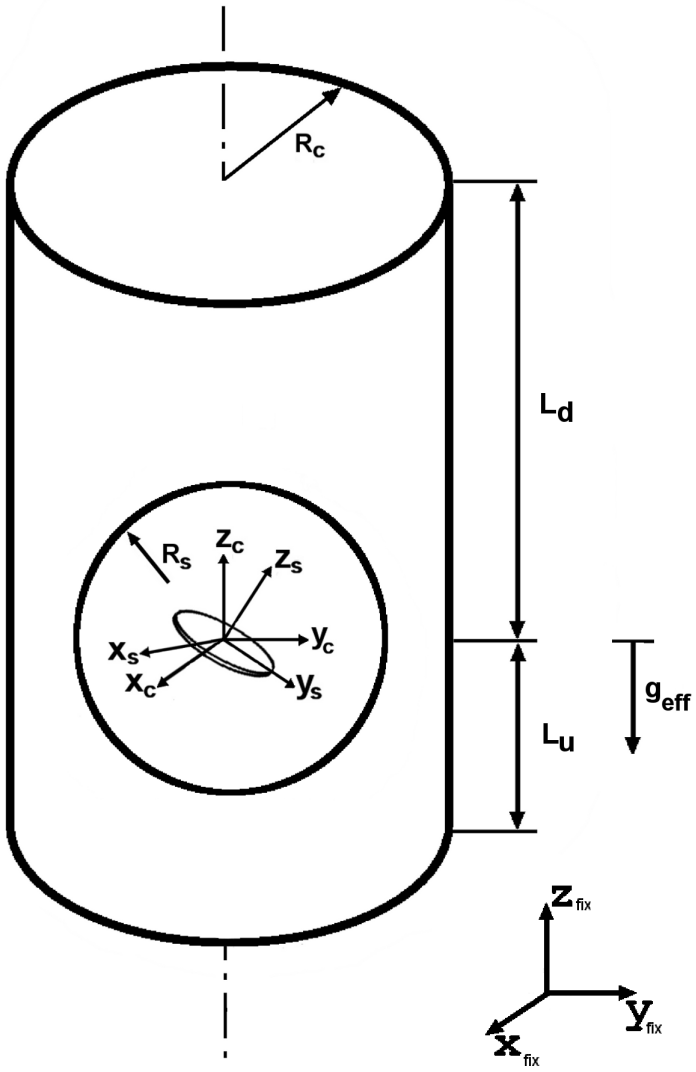

Figure 2.1: Geometry of the problem.

The solid body degrees of freedom are governed by the Newton equations of motion. Written for a velocity field defined with respect to a fixed frame and projected onto a moving frame, they assume the following form:

$$m\left(\frac{d\mathbf{u}}{dt}+\boldsymbol{\omega}\times\mathbf{u}\right) = \mathbf{F}_{fl}(\mathbf{v},p)+(m-\rho V)\mathbf{g} \tag{2.9}$$

$$\mathbf{I}\frac{d\boldsymbol{\Omega}}{dt}+\boldsymbol{\omega}\times(\mathbf{I}\boldsymbol{\Omega}) = \mathbf{M}_{fl} \tag{2.10}$$

where m is the mass of the body and $\mathbf{I}$ is the diagonal tensor of moment of inertia. $\mathbf{F}_{fl}$ and $\mathbf{M}_{fl}$ are the hydrodynamic force and torque exerted by the fluid, respectively. They depend on the flow field and thus couple the solid body equations (2.9) and (2.10) with the equations governing the continuous phase (2.7) and (2.8). They are obtained by integrating the pressure and shear stress at the body surface:

$$\mathbf{F}_{fl} = \int_S \mathbf{f}\, dS, \tag{2.11}$$

$$\mathbf{M}_{fl} = \int_S \mathbf{r}_S \times \mathbf{f}\, dS, \tag{2.12}$$

$$f_i = 2\mu S_{i,j} n_j - p\, n_i, \tag{2.13}$$

$$S_{i,j} = \left(\frac{\partial v_i}{\partial x_j} + \frac{\partial v_j}{\partial x_i} \right), \tag{2.14}$$

where $\mathbf{r}_S$ is the position vector of a point on the body surface S, $\mathbf{n}$ is a vector normal to the body surface, $\mathbf{f}$ is the stress force per unit surface given by equation (2.13). Eq. (2.10) must be solved in the system of principal axes of inertia (to get a constant moment of inertia), i.e. in the rotating system:

$$I^{(j)} \frac{d\Omega_j}{dt} + e_{j,k,\ell} \omega_k I^{(\ell)} \Omega_\ell = M_{fl_j} \tag{2.15}$$

where $e_{j,k,\ell}$ is the Levi-Civita symbol, Ω_j are the components of the angular velocity of the rotation of the body, M_{fl_j} are components of the hydrodynamic torque in the frame of principal axes and $I^{(j)}$ are the principal moments of inertia. For axisymmetric bodies we have $I^{(1)} = I^{(2)} \equiv I$ and $I^{(3)} = \alpha I$ where $\alpha \neq 1$. E.g., for the disc we have $I^1 = I^2 = md^2/16$ and $I^3 = md^2/8$, i.e. $I = md^2/16$ and $\alpha = 2$. Again, the axisymmetry with respect to the 3-axis makes it possible to follow only the rotation with respect to the first two axes by the reference frame of the spherical sub-domain:

$$\omega_j = \Omega_j; \quad j = 1, 2, \tag{2.16}$$

$$\omega_3 = 0. \tag{2.17}$$

Written in more detail for an axisymmetric body, Eq. (2.15) becomes

$$I \frac{d\Omega_1}{dt} + \alpha I \Omega_2 \Omega_3 = M_{fl_1} \tag{2.18}$$

$$I \frac{d\Omega_2}{dt} - \alpha I \Omega_1 \Omega_3 = M_{fl_2} \tag{2.19}$$

$$\alpha I \frac{d\Omega_3}{dt} = M_{fl_3}. \tag{2.20}$$

Introducing complex $U(1)$-coordinates, $\Omega_+ = \Omega_x + i\Omega_y$ and $M_{fl_+} = M_{fl_x} + iM_{fl_y}$, we replace Eqs. (2.18) and (2.19) by

$$I\frac{d\Omega_+}{dt} - i\alpha I\Omega_+\Omega_3 = M_{fl_+}. \tag{2.21}$$

The problem of a body moving freely under the effect of gravity, buoyancy and hydrodynamic forces in a fluid is thus governed by the set of equations (2.7–2.14). It remains to cast these equation in a dimensionless form. The Reynolds number, characterizing the flow past fixed bodies defined in section 2.1, is not a suitable parameter as the terminal velocity of the body is not know a priori. For the case of a freely moving sphere, Jenny & Dušek (2004) defined the acceleration scale by the effective gravity g_{eff} (2.6). This acceleration scale defines the reference velocity and time scales:

$$U_{ref} = \sqrt{\left|\frac{\rho_s}{\rho} - 1\right| gd}, \tag{2.22}$$

$$\tau = \sqrt{\frac{d}{|\rho_s/\rho - 1|\, g}}. \tag{2.23}$$

The reference velocity scale U_{ref} replaces the velocity scale based on the free-stream velocity of the flow. The non-dimensionalization of the Navier-Stokes equations with respect to these reference scales yields only one dimensionless parameter, the Galileo number, that plays the role of the Reynolds number and expresses the inverse of non-dimensionalized kinematic viscosity:

$$G_{sphere} = \tilde{G} = \frac{\sqrt{|\rho_s/\rho - 1|\, \mathbf{g}d^3}}{\nu}. \tag{2.24}$$

For the moment, we consider the non-dimensionalization of solid body equations separately for infinitely thin homogeneous discs and bodies of finite volumes (homogeneous cylinders and oblate spheroids).

a) Disc

For an infinitely thin disc the buoyancy tends to zero. The hydrodynamic force appears in units $\rho g d^3$ and the mass in units ρd^3. I.e.

$$\mathbf{F}^*_{fl} = \frac{\mathbf{F}_{fl}}{\rho g d^3}, \tag{2.25}$$

$$\mathbf{M}^*_{fl} = \frac{\mathbf{M}_{fl}}{\rho g d^4}, \tag{2.26}$$

$$m^* = \frac{m}{\rho d^3}, \tag{2.27}$$

$$I^* = \frac{I}{\rho d^5}. \tag{2.28}$$

The non-dimensionalization of the moment of inertia is in agreement with that of Field *et al.* (1997). Instead of taking I^* as a free parameter we chose rather m^*. We have then:

$$I^* = m^*/16. \tag{2.29}$$

The non-dimensionalized movement equations become for a disc:

$$\begin{aligned} \frac{d\mathbf{u}}{dt} + \omega \times \mathbf{u} &= \frac{1}{m^*}\mathbf{F}_{fl}(\mathbf{v}, p) + \mathbf{k}_{fix} && (2.30)\\ \frac{d\Omega_3}{dt} &= \frac{8}{m^*}M_{fl_z} && (2.31)\\ \frac{d\Omega_+}{dt} - 2iI\Omega_+\Omega_3 &= \frac{16}{m^*}M_{fl_+} && (2.32) \end{aligned}$$

b) Bodies with non-zero volume

For bodies of non-zero volume V the non-dimensionalization with respect to the scales (2.22) and (2.23) yields:

$$\begin{aligned} \frac{\rho_s}{\rho}\left(\frac{d\mathbf{u}}{dt} + \omega \times \mathbf{u}\right) &= \frac{1}{V^*}\mathbf{F}_{fl}(\mathbf{v}, p) + \mathbf{k}_{fix} && (2.33)\\ \frac{\rho_s}{\rho}\frac{d\Omega_3}{dt} &= \frac{1}{\alpha J^*}M_{fl_z} && (2.34)\\ \frac{\rho_s}{\rho}\left(\frac{d\Omega_+}{dt} - i\alpha\Omega_+\Omega_3\right) &= \frac{1}{J^*}M_{fl_+} && (2.35) \end{aligned}$$

where $V^* = V/d^3$ and $J^* = I/(\rho_s d^5)$. Eqs. (2.30 - 2.32) can be considered as a special case of Eqs. (2.33 - 2.35) for $\rho_s/\rho = 1, \alpha = 2$ and $I^* = m^*/16$ with m^* as free parameter. However, the limit of the infinite density ratio ρ_s/ρ is not obvious. For specific classes of geometry V^*, J^* and α can be expressed in terms of the aspect ratio:

- oblate spheroids of aspect ratio χ: $(a = d/2, c = d/(2\chi))$:

$$\begin{aligned} V^* &= \frac{\pi}{6\chi} && (2.36)\\ J^* &= V^*\left(\frac{1}{\chi^2} + 1\right)/20 = \frac{\pi}{\chi}\left(\frac{1}{\chi^2} + 1\right)/120 && (2.37) \end{aligned}$$

$$\alpha = \frac{2}{\left(1 + \frac{1}{\chi^2}\right)} \tag{2.38}$$

- cylinders of aspect ratio $\chi = d/h$:

$$V^* = \frac{\pi}{4\chi} \tag{2.39}$$

$$J^* = V^*\left(\frac{1}{4}+\frac{1}{3\chi^2}\right)/4 = \frac{\pi}{16\chi}\left(\frac{1}{4}+\frac{1}{3\chi^2}\right) = \frac{V^*}{16}\left(1+\frac{4}{3\chi^2}\right) \tag{2.40}$$

$$\alpha = \frac{2}{1+\frac{4}{3\chi^2}} \tag{2.41}$$

The two non-dimensionalizations based on the acceleration scale given by the effective gravity g_{eff}, introduced in points **a)** and **b)** have the following disadvantage. The asymptotic terminal velocity strongly depends on non-dimensionalized mass. Indeed, consider the drag coefficient C_D of a disc known to be close to one at sufficiently high Reynolds numbers. Then the vertical component of the force $\mathbf{F}_{fl}$ equals:

$$F_{fl,z} = C_D\frac{\pi}{8}\rho d^2 U_\infty^2 \tag{2.42}$$

where U_∞ is assumed to be (at least approximately) a constant terminal velocity. The non-dimensionalized version of Eq. (2.42) writes for both ways of non-dimensionalization:

$$F_{fl,z} = C_D\frac{\pi}{8}U_\infty^2 \tag{2.43}$$

Eqs. (2.30) or (2.33) yield the terminal velocity:

$$U_\infty^{disc} = \sqrt{\frac{8m^*}{\pi C_D}}; \quad U_\infty^{body} = \sqrt{\frac{8V^*}{\pi C_D}} \tag{2.44}$$

The factor $\sqrt{8/\pi}$ is equal about 1.6, but the non-dimensionalized mass and volume m^* and V^* can be very small both for light discs and flat bodies with large aspect ratio. It is clear that a better non-dimensionalization consists in including the non-dimensionalized mass in the velocity and acceleration scales. The non-dimensionalized velocity is thus defined as:

$$\mathbf{v}^*_{disc} = \frac{\mathbf{v}}{\sqrt{m^* g d}} \tag{2.45}$$

for an infinitely thin disc and

$$\mathbf{v}^*_{body} = \frac{\mathbf{v}}{\sqrt{V^* g_{eff} d}} \tag{2.46}$$

with g_{eff} defined in Eq. (2.6) for bodies of non-zero volume. With this non-dimensionalization the Galileo number becomes:

$$G_{disc} = \frac{\left(m^* g d^3\right)^{\frac{1}{2}}}{\nu}; \quad G_{body} = \frac{\left(V^* g_{eff} d^3\right)^{\frac{1}{2}}}{\nu} \tag{2.47}$$

This keeps the flow equations (2.56,2.57) formally unchanged but yields movement equations for a body of non-zero volume:

$$V^* \frac{\rho_s}{\rho} \left(\frac{d\mathbf{u}}{dt} + \omega \times \mathbf{u} \right) = \mathbf{F}_{fl}(\mathbf{v}, p) + \mathbf{k}_{fix} \tag{2.48}$$

$$\alpha J^* \frac{\rho_s}{\rho} \frac{d\Omega_3}{dt} = M_{fl_z} \tag{2.49}$$

$$J^* \frac{\rho_s}{\rho} \left(\frac{d\Omega_+}{dt} - i\alpha\Omega_+\Omega_3 \right) = M_{fl_+} \tag{2.50}$$

The limit of the thin disc is obtained by letting $\rho_s/\rho \times V^*$ tend to a finite limit m^*. I.e., by introducing m^* and $I^* = \rho_s/\rho J^*$ both for thin discs and bodies of non-zero volume we obtain a common system of movement equations for both cases.

$$m^* \left(\frac{d\mathbf{u}}{dt} + \omega \times \mathbf{u} \right) = \mathbf{F}_{fl}(\mathbf{v}, p) + \mathbf{k}_{fix} \tag{2.51}$$

$$\alpha I^* \frac{d\Omega_3}{dt} = M_{fl_z} \tag{2.52}$$

$$I^* \left(\frac{d\Omega_+}{dt} - i\alpha\Omega_+\Omega_3 \right) = M_{fl_+} \tag{2.53}$$

To sum up, the non-dimensionalization based on the acceleration scale defined by the effective gravity g_{eff} used in Jenny & Dušek (2004) is no longer convenient as it does not account for infinitely thin bodies. To accommodate bodies of arbitrary form, including infinitely thin discs and spheroids having, nominally, a zero volume, we base the non-dimensionalization on the scale of the force resulting from the weight and buoyancy $(m - \rho V)\mathbf{g}$, where m is the mass and V the volume of the body. Taking a reference mass equal to ρd^3 (i.e. non-dimensionalizing w.r.t. the fluid density and the body diameter) we thus get an acceleration scale $|m - \rho V|g/(\rho d^3)$ yielding a velocity scale:

$$U_{ref} = \sqrt{|m^* - V^*|gd}, \tag{2.54}$$

where m^* and V^* stand for the non-dimensionalized mass and volume of the body:

$$m^* = \frac{m}{\rho d^3}, \quad V^* = \frac{V}{d^3}. \tag{2.55}$$

The non-dimensionalization using the velocity scale (2.54) and the diameter d yields the incompressible Navier-Stokes equations, written for a velocity field defined with respect to a fixed frame and projected onto a frame translating and rotating with the body, in the following form:

$$\frac{\partial \mathbf{v}}{\partial t} + [(\mathbf{v} - \mathbf{u} - \boldsymbol{\omega} \times \mathbf{r}) \cdot \nabla]\mathbf{v} + \boldsymbol{\omega} \times \mathbf{v} = -\nabla p + \frac{1}{G}\nabla^2 \mathbf{v} \tag{2.56}$$

and

$$\nabla . \mathbf{v} = 0 \tag{2.57}$$

where $\mathbf{u}$ is the translation velocity and $\boldsymbol{\omega}$ the angular velocity of the moving frame. The Galileo number G appearing in Eq. (2.56) is given by

$$G = \frac{\sqrt{|m^* - V^*|gd^3}}{\nu}. \tag{2.58}$$

This definition of the Galileo number applies both for homogeneous and inhomogeneous bodies and is valid in the limit of zero volume (for infinitely thin discs). For the case of a sphere, it differs by a factor $\sqrt{\pi/6} \approx 0.724$ from $\tilde{G}$ of Jenny & Dušek (2004).

Boundary conditions on the body surface S account for the translation and rotation with respect to the fixed frame:

$$\mathbf{v}|_S = \mathbf{u} + \omega \times \mathbf{r}|_S \tag{2.59}$$

where $\mathbf{r}$ is the position vector of a point of the surface.

The full system of Navier-Stokes equations (2.56) and (2.57) and of motion equations (2.51) through (2.53) depends, in general, on non-dimensional parameters G, m^*, V^*, I^*, α and on the shape of the body, often parametrized by the aspect ratio χ. For homogeneous bodies of well defined shape, the number of parameters reduces to three (G, m^*, χ), e.g. for homogeneous spheroids and cylinders, or to two (G, m^*) for infinitely thin homogeneous discs.

Chapter 3

Numerical method

The content of this chapter was submitted to the Journal of Computational Physics.

3.1 Principles of the spectral–spectral element method

The numerical method used as the basis for the present development was described by Ghidersa & Dušek (2000) and Jenny & Dušek (2004). The spatial discretization takes advantage of the axisymmetry of the computational domain for expanding the variables into a rapidly converging azimuthal Fourier series. The so obtained azimuthal Fourier modes are functions of only the radial distance r and of the axial projection z. They obey a set of two-dimensional equations coupled via the advective terms. The discretization in the radial–axial plane (r, z) uses the spectral element decomposition (Patera, 1984). The time discretization is chosen in view of solving high Reynolds number flows. In this case the adopted time splitting approach, used already by Patera (1984), is both accurate and efficient. The non-linear terms are treated explicitly (in our case we use the third order Adams-Bashforth method), which un-couples linear two-dimensional Stokes-like problems in individual azimuthal subspaces numbered by the azimuthal wavenumber m. The latter are solved by splitting the pressure – velocity coupling into a Poisson pressure equation and a Helmholtz equation for the velocity. In the literature (e.g. Karniadakis *et al.* (1991)), the splitting is considered before the discretization. Kotouč *et al.* (2008) have noted that, if the whole augmented matrix of the Stokes-like problem is created, the matrix obtained by multiplying the discretized divergence by the discretized gradient is not exactly the same as that of the diffusion operator. The so obtained improvement of accuracy was combined with a considerable reduction of computational costs achieved by replacing the iterative (conjugate gradient) pressure solver by a direct method.

To facilitate the presentation of the next sub-sections, let us mention the principle of the spectral element decomposition representing, on its own, an example of a domain decomposition without overlapping. The spectral elements are discretized by Gauss-Lobatto-Legendre collocation points (see Karniadakis *et al.* (1991)). The values at the collocation points are stored separately for each spectral element. This brings about a redundant storage because the points at element interfaces physically coincide. E.g., a scalar variable discretized on a

2D mesh composed of K spectral elements with $N \times N$ collocation points is stored as an array of $K \times N^2$ components while only $n < K\,N^2$ variables are independent. Be U the stored array and V the reduced array of independent variables, the mapping

$$U \;=\; \mathbf{E}V \tag{3.1}$$

is given by copying the same value to all physically superimposed points. ($\mathbf{E}$ is a real matrix composed of zeros and ones.) The number of times the points are superimposed is called their multiplicity. An elliptic operator $\mathcal{A}$ is first discretized without taking account of the reconnection of the spectral elements, i.e. considering the components of array U as independent. This results in a discretization matrix $\mathbf{A}$ approximating the functional used in the variational formulation of the solved problem

$$\mathcal{A}\,u \;=\; f; \quad \text{on}\,\mathcal{D}, \tag{3.2}$$

$\mathcal{D}$ being the computational domain, in the following way:

$$\mathcal{J}(u) \;=\; \frac{1}{2}\int_{\mathcal{D}} (\overline{u}\,\mathcal{A}u \;-\; \overline{u}f)\,d\mathcal{D} \;\approx\; \frac{1}{2}U^{\dagger}\,\mathbf{A}\,U \;-\; U^{\dagger}\,\mathbf{M}\,F, \tag{3.3}$$

where $\mathbf{M}$ is a diagonal 'mass matrix' accounting for the integration weights and F is the array of values of the right hand side function f at the collocation points. We use a complex notation in view of the application to complex Fourier azimuthal modes. To arrive at the discretized equations, a gradient with respect to independent variables of the approximated functional is taken, i.e. U is replaced by (3.1). This results in the matrix equation:

$$\mathbf{E}^{\dagger}\mathbf{A}\mathbf{E}\,V \;=\; \mathbf{E}^{\dagger}\mathbf{M}\,F. \tag{3.4}$$

Since, actually, V is not the stored array, Eq. (3.4) must be expanded onto the redundant representation U:

$$\mathbf{E}\mathbf{E}^{\dagger}\mathbf{A}\,U \;=\; \mathbf{E}\mathbf{E}^{\dagger}\mathbf{M}\,F. \tag{3.5}$$

The operation $\mathbf{E}\mathbf{E}^{\dagger}$ amounts to summing the values at the physically identical points and distributing the result to the stored cells. It is commonly called "direct stiffness sum" (Patera, 1984; Baker, 1983). When used in the conjugate gradient iteration, the matrix operation on the LHS of Eq. (3.5) needs to be completed by an approximation of the L^2 norm of the residual and by a preconditioner. The residual, e.g., at the beginning of the iteration procedure, the RHS of Eq. (3.5), cannot be directly used to express the approximated L^2 norm $F^{\dagger}\,\mathbf{M}\,F$ because we do not dispose of the 'raw' values of F (before the application of the direct stiffness sum). Let $\boldsymbol{\mu}$ be the diagonal matrix with inverse multiplicities at the diagonal. Then

$$\mathbf{E}^{\dagger}\boldsymbol{\mu}\mathbf{E} \;=\; \mathbf{1}, \tag{3.6}$$

where $\mathbf{1}$ is the identity matrix. Moreover, for all 'physical' $U = \mathbf{E}V$, we have

$$\mathbf{E}\mathbf{E}^{\dagger}\mathbf{M}U \;=\; \tilde{\mathbf{M}}U. \tag{3.7}$$

where $\tilde{\mathbf{M}}$ is the diagonal matrix obtained by applying the direct stiffness sum to the diagonal of the mass matrix $\mathbf{M}$. It can thus be seen that, if we denote $Y = \mathbf{E}\mathbf{E}^{\dagger}\mathbf{M}F$,

$$\int_{\mathcal{D}} \overline{f} f \, d\mathcal{D} \approx F^{\dagger} \mathbf{M} F = Y^{\dagger} \boldsymbol{\mu} \tilde{\mathbf{M}}^{-1} Y. \tag{3.8}$$

The preconditioner uses the diagonal $\mathbf{D}$ of the 'raw' matrix $\mathbf{A}$. If $\mathbf{A}$ is replaced by $\mathbf{D}$ on the LHS of Eq. (3.5) the same direct stiffness operation as in Eq. (3.7) results. The preconditioner $\mathbf{P}$ is thus obtained as the diagonal matrix obtained by the inverse of the result of the direct stiffness sum applied to the 'raw' diagonal of $\mathbf{A}$:

$$\mathbf{P} = \tilde{\mathbf{D}}^{-1} \tag{3.9}$$

$\tilde{\mathbf{D}}$ being defined by Eq. (3.7) with $\mathbf{M}$ replaced by $\mathbf{D}$.

3.2 Domain decomposition

The simulation of an arbitrary movement of a disc (or a non-spherical body in general) requires the splitting up of the computational domain into a cylindrical part with a vertical axis and a spherical part the axis of which coincides with that of the disc. The translation of the disc center will be accounted for by translating the whole composite domain with respect to a fixed frame. The velocity field will be expressed with respect to this frame in the way described in Jenny & Dušek (2004). Because the falling body is no longer spherical, the local mesh representing a spherical sub-domain enclosing the disc must rotate with respect to the cylindrical part. The mapping at this gliding boundary thus involves a rotation of a spherical surface.

3.2.1 Rotations

A general rotation is described by Euler angles. It is obtained in three stages (see Figure 3.1). Let X, Y, Z be the reference Cartesian coordinate system and be Z' the polar axis of the new one. An arbitrarily oriented unit vector is defined by a polar angle Ψ and an azimuthal angle Θ as follows:

$$\mathbf{u}_{Z'}|_{X,Y,Z} = \begin{pmatrix} \sin(\Psi)\cos(\Theta) \\ \sin(\Psi)\sin(\Theta) \\ \cos(\Theta) \end{pmatrix}. \tag{3.10}$$

The respective equatorial planes XOY and $X'OY'$ (O is the sphere center) are represented by black and blue dashed lines in Figure 3.1. Be OX' the half-line at their intersection. To identify the X-axis with OX' it is sufficient to perform a rotation $\mathcal{R}^{(3)}(\alpha)$ by an angle α with respect to the Z-axis where $\alpha = \Theta - \pi/2$ is the angle between OX and OX'. Next, a rotation $\mathcal{R}^{(1)}(-\Psi)$ by the angle $-\Psi$ brings OZ to the required direction defined by $\mathbf{u}_{Z'}$. In general, the new coordinate system may have equatorial axes $X", Y"$ (represented in Figure 3.2) rotated arbitrarily in the new equatorial plane by an angle β. The last rotation is about

the Z' axis i.e. $\mathbf{R}^{(3)}(\beta)$. It makes it possible to orient the new axes so that the unit vector of the original polar axis is represented in the new frame by coordinates:

$$\mathbf{u}_Z|_{X",Y",Z'} = \begin{pmatrix} -\sin(\Psi)\,\cos(\Phi) \\ -\sin(\Psi)\,\sin(\Phi) \\ \cos(\Psi) \end{pmatrix}. \tag{3.11}$$

This means (see Figure 3.2) that the frame (O,X',Y') is to be rotated by the angle $\beta = (\pi/2 - \Phi)$. In this way we obtain an identity if $\Psi \to 0$ and $\Phi = \Theta$. The opposite sign in Eq. (3.11) can be understood for very small Ψ, for which the planes XOY and $X"OY"$ almost coincide. The projection of the vector $\overrightarrow{ZZ'}$ must be opposite to that of the vector $\overrightarrow{Z'Z}$.

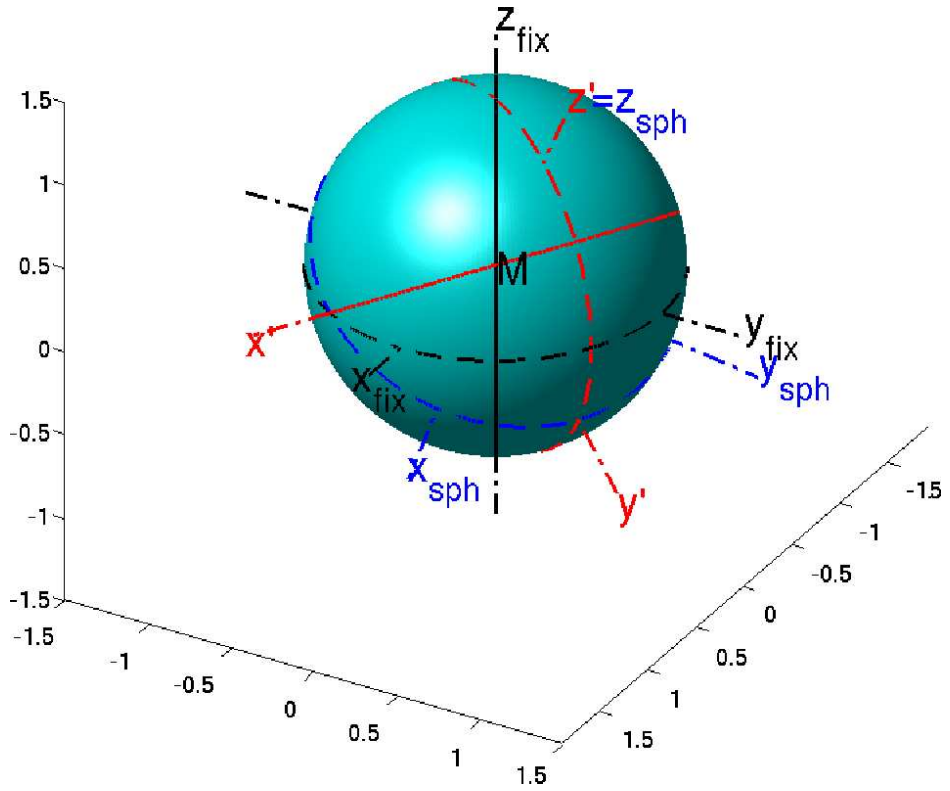

Figure 3.1: Arbitrary rotation of a system of axes. $Z = Z_{fix}$, $Z' = Z_{sph}$: old and new polar axes. Black and blue dashed lines: old and new equators. X_{fix}, Y_{fix} - old, X_{sph} and Y_{sph} - new axes. Black full line: meridian circle for an arbitrary point M. Red dashed and full lines: equator and meridian circle of M for polar axis X'.

The elementary rotations $\mathcal{R}^{(1)}$ and $\mathcal{R}^{(3)}$ (the indices correspond to the numbering of axes in the order X, Y, Z) are described by matrices of 'passive' rotations:

$$\mathbf{R}^{(1)}(\varphi) = \begin{bmatrix} 1 & 0 & 0 \\ 0 & \cos\varphi & \sin\varphi \\ 0 & -\sin\varphi & \cos\varphi \end{bmatrix}, \quad \mathbf{R}^{(3)}(\varphi) = \begin{bmatrix} \cos\varphi & \sin\varphi & 0 \\ -\sin\varphi & \cos\varphi & 0 \\ 0 & 0 & 1 \end{bmatrix}. \tag{3.12}$$

The interpretation of the matrix representation is the following. Be $\{\mathbf{i}_k\}_{k=1}^n$ and $\{\mathbf{j}_k\}_{k=1}^n$ two bases of an n-dimensional linear space. The transformation matrix $\mathbf{V} = \{V_{k,\ell}\}_{k,\ell=1}^n$ is defined as: $\mathbf{j}_k = \sum_\ell V_{\ell,k}\mathbf{i}_\ell$. As a result, if the coordinates of a vector $\mathbf{x}$ are $\mathbf{x} = \sum_\ell x_\ell \mathbf{i}_\ell = \sum_k x'_k \mathbf{j}_k$ then $x_\ell = V_{\ell,k}x'_k$. This means that, if the transformation $\mathcal{V}$ described by the matrix $\mathbf{V}$ is composed with a second one $\mathcal{W}$ given by matrix $\mathbf{W}$: $\mathbf{k}_m = \sum_k W_{k,m}\mathbf{j}_k$, the resulting composed transformation $\mathcal{W} \circ \mathcal{V}$ is defined by the matrix product in the inverse order $\mathbf{VW}$. If the transformation of coordinates is considered $\mathbf{x}' = \mathbf{V}^{-1}\mathbf{x}$, a direct composition results ($\mathbf{x}' = \mathbf{V}^{-1}\mathbf{x}$, $\mathbf{x}'' = \mathbf{V}^{-1}\mathbf{x}' \Rightarrow \mathbf{x}'' = \mathbf{W}^{-1}\mathbf{V}^{-1}\mathbf{x}$). The "passive" rotation matrix describes the transformation of coordinates induced by the rotation of the system of axes by the angle φ. It corresponds thus to $\mathbf{V}^{-1}$. As the inverse is just the transpose for orthogonal matrices, the matrices (3.12) are the transpose of "active" rotation matrices corresponding to $\mathbf{V}$.

As the result:

$$\begin{pmatrix} X \\ Y \\ Z \end{pmatrix} = [\mathbf{R}^{(\ell)}]^T \begin{pmatrix} X' \\ Y' \\ Z' \end{pmatrix} \quad and \quad \begin{pmatrix} X' \\ Y' \\ Z' \end{pmatrix} = \mathbf{R}^{(\ell)} \begin{pmatrix} X \\ Y \\ Z \end{pmatrix} \tag{3.13}$$

In view of the above remark, the full rotation matrix $R(\beta, \Psi, \Phi)$ mapping $0XYZ$ onto $OX"Y"Z'$ is then given by the product:

$$\mathbf{R}(\Theta, \Psi, \Phi) = \mathbf{R}^{(3)}(\pi/2 - \Phi)\, \mathbf{R}^{(1)}(-\Psi)\, \mathbf{R}^{(3)}(\Theta - \pi/2). \tag{3.14}$$

The triple matrix product can be evaluated to yield explicitly:

$$\mathbf{R}^{(3)}(\pi/2 - \Phi)\mathbf{R}^{(1)}(-\Psi) = \begin{bmatrix} \sin\Phi & \cos\Phi\cos\Psi & -\cos\Phi\sin\Psi \\ -\cos\Phi & \sin\Phi\cos\Psi & -\sin\Phi\sin\Psi \\ 0 & \sin\Psi & \cos\Psi \end{bmatrix}, \tag{3.15}$$

$$\mathbf{R}^{(3)}(\pi/2 - \Phi)\mathbf{R}^{(1)}(-\Psi)\mathbf{R}^{(3)}(\Theta - \pi/2) =$$

$$\begin{bmatrix} \sin\Theta\sin\Phi + \cos\Theta\cos\Phi\cos\Psi & -\cos\Theta\sin(\Phi) + \sin\Theta\cos\Phi\cos\Psi & -\cos\Phi\sin\Psi \\ -\sin\Theta\cos\Phi + \cos\Theta\sin\Phi\cos\Psi & \cos\Theta\cos(\Phi) + \sin\Theta\sin\Phi\cos\Psi & -\sin\Phi\sin\Psi \\ \cos\Theta\sin\Psi & \sin\Theta\sin\Psi & \cos\Psi \end{bmatrix} \tag{3.16}$$

The unit vector (3.10) has the coordinates $(0, 0, 1)^T$ in the new coordinate system. The backward transformation to the old coordinate system yields,

$$[\mathbf{R}(\Theta, \Psi, \Phi)]^T \begin{pmatrix} 0 \\ 0 \\ 1 \end{pmatrix} = \begin{pmatrix} \sin(\Psi)\cos(\Theta) \\ \sin(\Psi)\sin(\Theta) \\ \cos(\Psi) \end{pmatrix}. \tag{3.17}$$

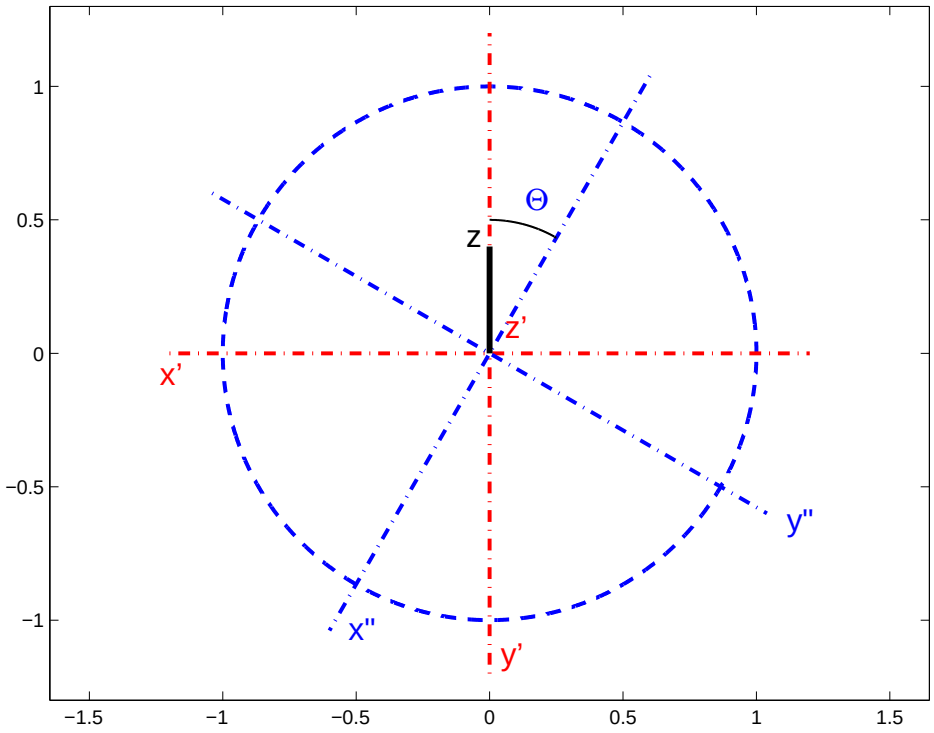

Figure 3.2: Choice of axes in the plane normal to OZ'- axis.

i.e. the vector (3.10), while the forward transformation of the unit vector of the old Z–axis yields

$$\mathbf{R}(\Theta,\Psi,\Phi)\begin{pmatrix}0\\0\\1\end{pmatrix}=\begin{pmatrix}-\sin(\Psi)\,\cos(\Phi)\\-\sin(\Psi)\,\sin(\Phi)\\\cos(\Psi)\end{pmatrix}. \tag{3.18}$$

which is in agreement with Eq. (3.11). The columns of matrix $\mathbf{R}^T$ are coordinates of unit vectors of the new (rotating) frame in the old (fixed) one and, conversely, the columns of $\mathbf{R}$ are coordinates of unit vectors of the old frame in the new one.

As explained in Jenny & Dušek (2004), if the spherical sub-domain is attached to the freely moving and rotating disc, the movement equations provide, at each times step, an angular velocity $\mathbf{\Omega}$ yielding a rotation velocity $\mathbf{\Omega}\times\mathbf{x}$ at each position $\mathbf{x}$ at the sphere surface. The components of the $\mathbf{\Omega}$ vector can be given either in the fixed frame $0XYZ$ or in the moving frame. The change of the position of a given fixed point $(X',Y',Z')^T$ at the sphere surface due to the sphere rotation is thus $d\mathbf{x}=\mathbf{\Omega}\times\mathbf{x}\,dt$. In particular, the unit vectors of the axes of the rotating frame obey the equations

$$\frac{d\mathbf{n}_k|_{X,Y,Z}}{dt}=\mathbf{\Omega}\times\mathbf{n}_k|_{X,Y,Z},\quad k=1,2,3. \tag{3.19}$$

This equation holds in the fixed frame. Conversely, the unit vectors of the fixed frame move

in the opposite direction with respect to the rotating frame. Their derivatives are given in the rotating frame by:

$$\frac{d\mathbf{n}'_k|_{X',Y',Z'}}{dt} = -\mathbf{\Omega} \times \mathbf{n}'_k|_{X',Y',Z'}, \quad k = 1, 2, 3 \tag{3.20}$$

where $\mathbf{n}_k, k = 1 \dots 3$ are columns of $\mathbf{R}^T$. The determination of the Euler angles results from the following three steps:

1. Update the rotation matrix by solving Eq. (3.19) or Eq. (3.20),
2. Orthonormalize the columns (by the Gramm-Schmidt orthonormalization) to enforce orthogonality of the matrix,
3. Compute the angles from the last line and last column of matrix $\mathbf{R}$ expressed in Eq. (3.16).

Since the solid body is assumed to be axisymmetric, the rotation with respect to the OZ' axis will not be transmitted to the rotating frame. As a result $\Omega'_3 = 0$.

3.2.2 Mapping of a scalar quantity on the sphere surface

A scalar quantity f will be expanded in two different Fourier series with azimuthal angles θ and θ' defined with respect to the Z axis of the old frame and Z' axis of the new frame, respectively. Be (X, Y, Z) and (X', Y', Z') the coordinates of a point $\mathbf{x}$, $\|\mathbf{x}\| = R$ on a spherical surface of radius R in the reference and local frames. Then:

$$f(R\sin\varphi\cos\theta, R\sin\varphi\sin\theta, R\cos\varphi) = f(R\sin\varphi'\cos\theta', R\sin\varphi'\sin\theta', R\cos\varphi') \tag{3.21}$$

where φ and φ' stand for the respective polar angles. The (truncated) complex azimuthal expansions implemented in the code (Jenny & Dušek, 2004) write:

$$\begin{aligned} f(R\sin\varphi\cos\theta, R\sin\varphi\sin\theta, R\cos\varphi) &= \sum_{m=-M}^{M} c_m(R\sin\varphi, R\cos\varphi)\, e^{-im\theta} \\ f(R\sin\varphi'\cos\theta', R\sin\varphi'\sin\theta', R\cos\varphi') &= \sum_{m=-M'}^{M'} c'_m(R\sin\varphi', R\cos\varphi')\, e^{-im\theta'} \end{aligned} \tag{3.22}$$

where $c_m(r, z)$ and $c'_m(r', z')$ are the Fourier modes computed in each frame. The truncation is, so far, supposed to be different (M and M') in each frame. The purpose of next subsections is to establish a transformation relation between both sets of Fourier coefficients.

3.2.3 Rotations $\mathbf{R}^{(3)}(\pi/2 - \Phi)$ and $\mathbf{R}^{(3)}(\Theta - \pi/2)$

A rotation $\mathbf{R}^{(3)}(\alpha)$ is accounted for trivially. Be $\hat{f}(\hat{X}, \hat{Y}, Z)$ the function transformed by a rotation by angle α around the $Z - axis$:

$$\hat{f}(R\sin\varphi\cos\hat{\theta}, R\sin\varphi\sin\hat{\theta}, R\cos\varphi) \;=\; \sum_m \hat{c}_m(R\sin\varphi, R\cos\varphi)\, e^{-im\hat{\theta}}. \tag{3.23}$$

The rotation of the frame by an angle α around the $Z - axis$ amounts to seeking the same value of the function

$$f(R\sin\varphi\cos\theta, R\sin\varphi\sin\theta, R\cos\varphi) \;=\; \sum_m c_m(R\sin\varphi, R\cos\varphi)\, e^{-im\theta}. \tag{3.24}$$

at $\hat{\theta} = \theta - \alpha$. Replacing $\theta = \hat{\theta} + \alpha$ in expansion (3.24) and comparing to (3.23), we obtain:

$$\hat{c}_m \;=\; e^{-im\alpha}\, c_m. \tag{3.25}$$

Specifically for $\alpha = \pi/2 - \Phi$ and $\alpha = \Theta - \pi/2$, we obtain $\hat{c}_m = e^{im(\Phi - \pi/2)}\, c_m$ and $\hat{c}_m = e^{-im(\Theta - \pi/2)}\, c_m$, respectively. The principal task consists thus in representing the rotation $\mathbf{R}^{(1)}(\Psi)$.

3.2.4 Rotation $\mathbf{R}^{(1)}(-\Psi)$

In contrast to the previous subsection, this rotation is not with respect to the third axis, that of the azimuthal expansion. We must thus proceed in three stages:

1. map the expansion with respect to the Z-axis to that with respect to the X-axis,
2. rotate by angle $-\Psi$ (multiplication by $e^{im\Psi}$ - see the previous subsection),
3. map back to an expansion with respect to the $Z' - axis$.

The second stage being trivial and the third one being the inverse of the first one, we shall focus on the change of polar axes. Theoretical considerations show that the optimal representation of the rotation group is obtained by an expansion into spherical harmonic functions (Hecht, 2000). Therefore, in order to obtain an optimal efficiency of expansion on a spherical surface, we shall use spherical harmonic functions as an expansion basis. Be φ the polar angle and θ the azimuthal angle. The spherical harmonic functions are defined as (Hecht, 2000):

$$Y_{\ell,m}(\varphi,\theta) \;=\; \sqrt{\frac{(2\ell+1)}{4\pi}\frac{(\ell-m)!}{(\ell+m)!}}\, P_\ell^m(\cos\varphi)\, e^{-im\theta}; \quad m \geq 0, \tag{3.26}$$

$$Y_{\ell,-m}(\varphi,\theta) \;=\; (-1)^m\, \overline{Y_{\ell,m}(\varphi,\theta)}; \quad m < 0 \tag{3.27}$$

where P_ℓ^m are the associated Legendre functions defined in the same way as in the Matlab documentation. (We take the complex conjugates in comparison with the bibliography.) The spherical functions are normalized on the unit sphere surface:

$$\int_0^{\pi}\int_{-\pi}^{\pi} \overline{Y_{\ell',m'}(\varphi,\theta)}\, Y_{\ell,m}(\varphi,\theta)\, \sin\varphi\, d\varphi d\theta \;=\; \delta_{\ell,\ell'}\delta_{m,m'}. \tag{3.28}$$

Assume a function to be expanded in a series of spherical harmonic functions defined by the polar axes OZ (Eq. 3.29) and OX (Eq. 3.30).

$$f(\varphi,\theta) \;=\; \sum_{\ell=0}^{\infty}\sum_{m=-\ell}^{\ell} a_{\ell,m}\, Y_{\ell,m}(\varphi,\theta), \tag{3.29}$$

$$f(\varphi',\theta') \;=\; \sum_{\ell=0}^{\infty}\sum_{m=-\ell}^{\ell} a'_{\ell,m}\, Y_{\ell,m}(\varphi',\theta'). \tag{3.30}$$

For a real function $f(\varphi,\theta)$, the following symmetry condition holds (due to Eq. 3.27):

$$a_{\ell,m} \;=\; (-1)^m\, \overline{a_{\ell,-m}}. \tag{3.31}$$

We seek the transformation yielding the expansion in a series of spherical functions with polar axis OX given the expansion with polar axis OZ. The new Z'-axis is brought to coincide with the X-axis by a $\pi/2$ rotation about the Y-axis. We obtain the following transformation of the unit position vector $\overrightarrow{OM}$ (Note that OX' becomes opposite to OZ.):

$$\overrightarrow{OM} \;=\; \begin{pmatrix} \sin(\varphi)\,\cos(\theta) \\ \sin(\varphi)\,\sin(\theta) \\ \cos(\varphi) \end{pmatrix} \;=\; \begin{pmatrix} \cos(\varphi') \\ \sin(\varphi')\,\sin(\theta') \\ -\sin(\varphi')\,\cos(\theta') \end{pmatrix}. \tag{3.32}$$

This defines the following transformation:

$$\cos(\varphi) \;=\; -\sin(\varphi')\cos(\theta'), \tag{3.33}$$

$$\theta \;=\; \arg(\cos(\varphi') + i\sin(\varphi')\sin(\theta')). \tag{3.34}$$

Projection of the expansion (3.29) onto the basis of spherical functions with polar axis OX yields:

$$a'_{\ell',m'} \;=\; \sum_{\ell=0}^{\infty}\sum_{m=-\ell}^{\ell} d_{\ell',m';\ell,m}\, a_{\ell,m} \tag{3.35}$$

where

$$\begin{aligned} d_{\ell',m';\ell,m} \;&=\; \int_0^{\pi}\int_{-\pi}^{\pi} \overline{Y_{\ell',m'}(\varphi,\theta)} \\ &\quad Y_{\ell,m}\left[\operatorname{acos}(-\sin(\varphi)\cos(\theta)), \arg(\cos(\varphi) + i\sin(\varphi)\sin(\theta))\right] \sin\varphi\, d\varphi d\theta \\ &=\; \int_{-1}^{1}\int_{-\pi}^{\pi} \overline{\tilde{Y}_{\ell',m'}(z,\theta)} \\ &\quad \tilde{Y}_{\ell,m}\left[-\sqrt{1-z^2}\cos(\theta), \arg(z + i\sqrt{1-z^2}\sin(\theta))\right] dz d\theta \end{aligned} \tag{3.36}$$

where $\tilde{Y}$ stands for a spherical function expressed as a function of $cos(\varphi)$. The matrix $\mathbf{d}$ is actually a rotation matrix in the angular momentum representation. As such it can be calculated algebraically. (Eq. 3.36 is not suitable for practical calculation, but served as an alternative expression for debugging.) It is blockwise diagonal

$$d_{\ell',m';\ell,m} \;=\; d^{(\ell)}_{m',m}(\pi/2)\,\delta_{\ell,\ell'}, \tag{3.37}$$

where (Hecht, 2000)

$$d^{(\ell)}_{m',m}(-\pi/2) \;=\; \left[\frac{(\ell-m)!(\ell-m')!}{(\ell+m)!(\ell+m')!}\right]^{1/2} \sum_{n=max(0,m'-m)}^{\ell-m} (-1)^{n+m-m'} \times \frac{(\ell+m+n)!}{(\ell-m-n)!(m+n-m')!n!}\left(\frac{1}{2}\right)^{m+n} \tag{3.38}$$

and $d^{(\ell)}_{m',m}(\pi/2) \;=\; d^{(\ell)}_{m,m'}(-\pi/2)$. The transformation matrix $\mathbf{d}$ is a representation of a rotation identifying the Z-axis with the X-axis. It is thus unitary. Moreover, the matrix elements (3.38) happen to be real

$$\mathbf{d}^T\mathbf{d} = \mathbf{1} \tag{3.39}$$

where $\mathbf{d}^T$ stands for the transpose and $\mathbf{1}$ is the identity matrix. I.e. the inverse transformation of (3.35) is simply defined by the transposed matrix.

The sought rotation $\mathbf{R}^{(1)}(-\Psi)$ is thus obtained in the following way:

1. Switch from the polar axis OZ to OX using Eqs. (3.30) and (3.35).

2. Rotate by angle $-\Psi$ around OX. (see Eq. 3.25)

$$a''_{\ell',m'} \;=\; e^{im'\Psi}a'_{\ell',m'} \tag{3.40}$$

3. Switch back to polar axis OZ using the inverse transformation (3.35).

Formally stated in any l-subspace

$$\mathbf{R}^{(1)}_{(\ell)}(-\Psi) \;=\; \mathbf{d}^{(\ell)}\mathbf{R}^{(3)}_{\ell}(-\Psi)\left(\mathbf{d}^{(\ell)}\right)^{\dagger}, \tag{3.41}$$

where

$$\mathbf{R}^{(3)}_{\ell}(\alpha) = diag(e^{-im'\alpha})_{m=-\ell,\ldots\ell}. \tag{3.42}$$

is the diagonal matrix representing the rotation with respect to the $Z-axis$ in the ℓ subspace (subspace spanned by spherical functions $\{Y_{\ell,m}\}^{\ell}_{m=-\ell}$).

3.3 Complete rotation matrix

The complete rotation matrix $\mathbf{R}(\Phi,\Psi)$ is thus also a direct sum of matrices in ℓ-subspaces having the form:

$$\mathbf{R}(\Phi,\Psi,\Theta)_\ell \;=\; \mathbf{R}^{(3)}_\ell(\pi/2-\Phi)\,\mathbf{d}^{(\ell)}\mathbf{R}^{(3)}_\ell(-\Psi)\left(\mathbf{d}^{(\ell)}\right)^\dagger\,\mathbf{R}^{(3)}_\ell(\Theta-\pi/2). \tag{3.43}$$

It is composed of three trivial diagonal operations and a twofold multiplication by a matrix independent of rotation angles.

3.4 Transformation from the spectral – spectral-element discretization to the expansion into spherical functions

The azimuthal Fourier coefficients on the right hand sides of Eqs. (3.22) are originally discretized in cylindrical coordinates along the $\theta = 0$ meridian. At an arbitrary latitude $\varphi = acos(z)$ their values are given by the Lagrange interpolation between the collocation points situated at the corresponding spectral element face. Assume that φ lies on the k-th element 'face' of the 'object' defining the sphere surface. (The element 'faces' – sides in $2D$ – are listed in two 'objects' specifying the interface in the data file .rea.) Then

$$c_m(R\sin\varphi, R\cos\varphi) \;=\; \sum_{j=1}^{n} h_j^{(k)}(\varphi)c_m(R\sin\varphi_j^{(k)}, R\cos\varphi_j^{(k)}) \;\equiv\; \sum_{j=1}^{n} h_j^{(k)}(\varphi)c_{m;j}^{(k)} \tag{3.44}$$

where $\varphi_j^{(k)}$ stand for collocation points and $h_j^{(k)}$ for Lagrange interpolants ($h_j(\varphi_i) = \delta_{j,i}$). The expanded function will be considered real, thus the knowledge of components associated to positive index $m \geq 0$ is sufficient for their characterization. The azimuthal part of the expansion into spherical functions is already provided by the Fourier azimuthal expansion of the spectral – spectral element discretization. It remains to project onto the normalized associated Legendre functions. The expansion into associated Legendre functions writes:

$$c_m(R\sin\varphi, R\cos\varphi) \;=\; \sum_{\ell=m}^{\ell_{max}} a_{\ell,m}\,\hat{P}_\ell^m(\varphi). \tag{3.45}$$

where $\hat{P}_\ell^m$ are the normalized associated Legendre functions $\hat{P}_\ell^m(\varphi) = Y_{\ell,m}(\varphi,\theta=0)$ satisfying the orthogonality condition

$$\int_0^\pi \hat{P}_\ell^m(\varphi)\,\hat{P}_{\ell'}^m(\varphi)\,\sin\varphi\,d\varphi = \frac{1}{2\pi}\delta_{\ell,\ell'} \tag{3.46}$$

The coefficients $a_{\ell,m}$ are obtained as

$$a_{\ell,m} \;=\; 2\pi\int_0^\pi \hat{P}_\ell^m(\varphi)\,c_m(R\sin\varphi, R\cos\varphi)\,\sin\varphi\,d\varphi. \tag{3.47}$$

The Gaussian integration using the collocation points

$$\varphi_j^{(k)} = \frac{\varphi_1^{(k)} + \varphi_n^{(k)}}{2} + \frac{\varphi_n^{(k)} - \varphi_1^{(k)}}{2}\xi_j \quad \xi_j \in [-1, 1] \tag{3.48}$$

on the interface approximates this relation by the sum

$$a_{\ell,m} = \sum_{k,j} 2\pi\, w_j^{(k)} T_{\ell;k,j}^{(m)}\, c_{m;j}^{(k)}; \quad \ell \geq m \tag{3.49}$$

where k sums over the faces at the interface and j over the internal collocation points, and

$$T_{\ell;k,j}^{(m)} = \hat{P}_\ell^m(\varphi_j^{(k)}). \tag{3.50}$$

The integration weights $w_j^{(k)}$ in Eq. (3.49) are given by the Gauss-Lobatto-Legendre integration except in the first and last element along the meridian, which lie at the domain axis and in which the collocation points are those of a Gauss-Lobatto-Jacobi quadrature accounting for the factor r in the expansion for volume elements in cylindrical coordinates. The weight function $\sin\varphi$ is included in the integration weights in all elements. The values at element interfaces are equal: $c_{m;n}^{(k)} = c_{m;1}^{(k+1)}$ (in the local numbering on the interface). The inverse transformation from the spherical function expansion back to collocation points is given by (3.45).

$$c_{m;j}^{(k)} = \sum_{\ell=m}^{\ell_{max}} \hat{P}_\ell^m(\varphi_j^{(k)})\, a_{\ell,m}. \tag{3.51}$$

The transformation relations (3.49), (3.50) and (3.51) can be written in matrix form as:

$$a = 2\pi \mathbf{T}^T\, \mathbf{W} c, \tag{3.52}$$

$$c = \mathbf{T}\, a, \tag{3.53}$$

where

$$c = \{c_m\}_{m=0}^M \tag{3.54}$$

$$\mathbf{T} = \oplus_{m=0}^M \mathbf{T}_m; \quad \mathbf{T}_m = \{\hat{P}_\ell^m(\varphi_i)\}_{i,\ell} \tag{3.55}$$

$$\mathbf{W} = \oplus_{m=0}^M \mathbf{W}_m; \quad \mathbf{W}_m = \{w_i \delta_{i,j}\}_{i,j} \tag{3.56}$$

(In Eqs. (3.55) and (3.56) a global numbering along the meridian of the sphere $\{i\} = \{k, j\}$ has been introduced.) From equations (3.52) and (3.53), we get

$$\mathbf{T}^T \mathbf{W} \mathbf{T} = \frac{1}{2\pi}\mathbf{1}. \tag{3.57}$$

Note that the direct sums (3.55) and (3.56) sum over azimuthal m–subspaces, whereas the rotation matrix is a direct sum of ℓ–subspaces

$$\mathbf{R} = \oplus_{\ell=0}^{\ell_{max}} \mathbf{R}_\ell. \tag{3.58}$$

3.4.1 Test of the rotation of a scalar quantity on a spherical surface

In order to validate the transformation from the spectral-spectral element discretization to the expansion into spherical functions and the rotation of a scalar function on the spherical surface, the following test was carried out. The axial component of the velocity field of the steady asymmetric flow past a fixed disc was interpolated on the spherical surface and rotated by an angle ψ with respect to the x-axis. The results of the test are summarized in the Table (3.1). The rotated azimuthal expansion is truncated at ℓ_{max} to avoid loss of information.

The results show that the error decreases with increasing ℓ_{max} and that for $\ell_{max} = 20$ about 1% of accuracy is ensured for all rotation angles.

l_{max}/ψ	$\pi/18$	$\pi/9$	$\pi/6$	$\pi/3$	$\pi/2$
12	0.0159	0.0168	0.0179	0.0299	0.0342
16	0.0076	0.0076	0.0081	0.0127	0.0580
20	0.0064	0.0058	0.0060	0.0056	0.0140

Table 3.1: The maximum error defined as $max|f'(\varphi',\theta') - f(\varphi,\theta)|$, where $f'(\varphi',\theta') = \sum_m c'_m(\varphi')e^{-im\theta'}$ and $f(\varphi,\theta) = \sum_m c_m(\varphi)e^{-im\theta}$. The number of azimuthal modes of c_m is equal to ℓ_{max}. Radius of the sphere: $R = d$.

The rotation of the u-component of the velocity field with respect to x-axis by an angle $\psi = -\pi/4$ is illustrated in Figure 3.3.

3.5 Mapping of a vector field on the sphere surface

Along with a scalar quantity, it will be necessary to map a vector field on the spherical surface. A vector field $\mathbf{v}$ is represented in cylindrical coordinates as:

$$\mathbf{v} = v_z\mathbf{k}_3 + v_r\mathbf{u}_r + v_\theta\mathbf{u}_\theta \tag{3.59}$$

where, in Cartesian coordinates with the OZ axis identical with the z-axis of cylindrical coordinates,

$$\mathbf{k}_3 = \begin{pmatrix} 0 \\ 0 \\ 1 \end{pmatrix}, \quad \mathbf{u}_r = \begin{pmatrix} \cos\theta \\ \sin\theta \\ 0 \end{pmatrix}, \quad \mathbf{u}_\theta = \begin{pmatrix} -\sin\theta \\ \cos\theta \\ 0 \end{pmatrix}. \tag{3.60}$$

The Cartesian vector coordinates are closely related to spherical harmonics. If we denote the coordinates of the unit vector (3.32) x, y and z, respectively, and if we introduce $x_\pm = x \pm iy$, it is easily seen that (see Eqs. (3.26) and (3.27))

$$Y_{1,-1} = \sqrt{\frac{3}{8\pi}}x_+; \quad Y_{1,0} = \sqrt{\frac{3}{4\pi}}z; \quad Y_{1,1} = -\sqrt{\frac{3}{8\pi}}x_-. \tag{3.61}$$

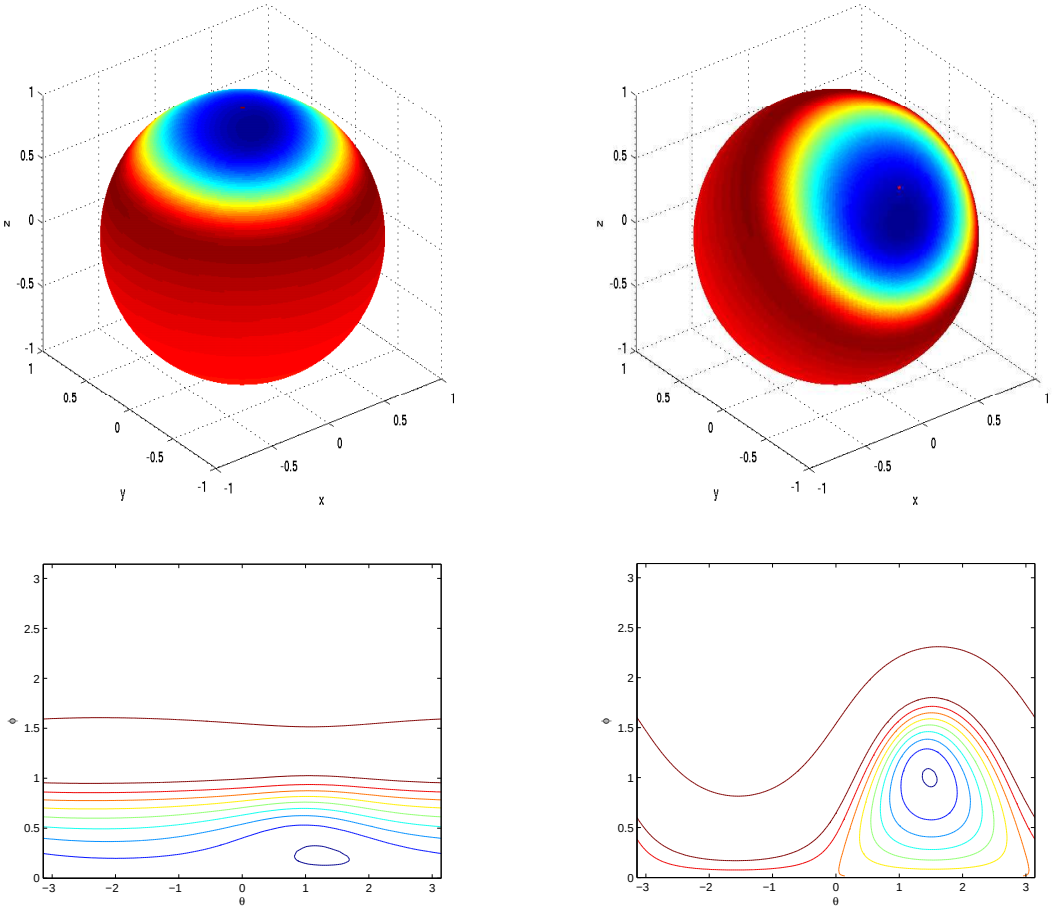

(a), u-component of the velocity field interpolated on a sphere of radius 1

(b), u-component of the velocity field after the rotation with respect to x-axis by $\psi = -\pi/4$

Figure 3.3: Rotation of the u-component of the velocity field with respect to x-axis by an angle $-\psi$

Be $\tilde{v}_\pm = v_r \pm iv_\theta$ the cylindrical $U(1)$ coordinates. The Cartesian $U(1)$ coordinates corresponding to v_z, $\tilde{v}_\pm$ (see Jenny & Dušek, 2004) are v_z, $\tilde{v}_\pm e^{\pm i\theta}$. To obtain quantities transforming like $Y_{1,\mu}$, it is thus more convenient to define the normalized Cartesian coordinates $\hat{v}_\mu$:

$$\hat{v}_{\pm 1} = \mp \frac{1}{\sqrt{2}} \tilde{v}_\mp e^{\mp i\theta}; \quad \hat{v}_0 = v_z \tag{3.62}$$

transforming like $Y_{1,\mu}$. To see how $Y_{1,\mu}$ exactly transform, knowing the transformation of $a_{1,\mu}$, let us write:

$$\sum_{\mu=-1}^{1} a_{1,\mu}\, Y_{1,\mu} \;=\; \sum_{\mu=-1}^{1} a'_{1,\mu}\, Y'_{1,\mu} \;=\; \sum_{\mu=-1}^{1}\sum_{\nu=-1}^{1} r^{(1)}_{\mu,\nu}\, a_{1,\nu}\, Y'_{1,\mu} \tag{3.63}$$

where $r^{(1)}_{\mu,\nu}$ is the representation of the rotation group in the $\ell = 1$ subspace. It is immediately seen that

$$Y_{1,\nu} \;=\; \sum_{\mu=-1}^{1} r^{(1)}_{\mu,\nu} Y'_{1,\mu} \quad \Leftrightarrow \quad Y'_{1,\mu} \;=\; \sum_{\nu=-1}^{1} \overline{r^{(1)}_{\mu,\nu}} Y_{1,\nu}, \tag{3.64}$$

i.e. the transformation is given by the inverse of the transposed matrix which is the complex conjugate one. As the result, we have

$$\hat{v}'_{\mu'} = \sum_{\mu\in\{-1,0,1\}} \overline{r^{(1)}_{\mu',\mu}}\hat{v}_{\mu} \;=\; \sum_{\mu\in\{-1,0,1\}} \hat{v}_{\mu}\,(r^{(1)})^{\dagger}_{\mu,\mu'} \tag{3.65}$$

i.e. the transformation can also be regarded as the multiplication by the transpose of the inverse (Hermitian conjugate) matrix.

The azimuthal decomposition of the cylindrical components of the vector field is defined as:

$$v_z \;=\; \sum_{m=-\infty}^{\infty} c_{z,m}(z,r)e^{-im\theta}, \tag{3.66}$$

$$\tilde{v}_{\pm} \;=\; \sum_{m=-\infty}^{\infty} c_{\pm,m}(z,r)e^{-im\theta}, \tag{3.67}$$

where the coefficients with negative indices in expansion (3.66) and the whole component v_- are redundant but needed for complex matrix operations. The coefficients $c_{z,m}, c_{\pm,m}(z,r)$ are those implemented in the code. Introducing the expansion (3.67) we have

$$\begin{aligned}\hat{v}_{\pm 1} \;&\equiv\; \sum_{m=-\infty}^{\infty} \hat{c}_{\pm,m}(z,r)e^{-im\theta} \;=\; \mp\frac{1}{\sqrt{2}}\sum_{m=-\infty}^{\infty} c_{\mp,m}(z,r)e^{-i(m\pm 1)\theta} \\ &=\; \mp\frac{1}{\sqrt{2}}\sum_{m=-\infty}^{\infty} c_{\mp,m\mp 1}(z,r)e^{-im\theta}.\end{aligned} \tag{3.68}$$

This yields the relation:

$$\hat{c}_{\pm,m}(z,r) \;=\; \mp\frac{1}{\sqrt{2}} c_{\mp,m\mp 1}(z,r). \tag{3.69}$$

The array of coefficients $c_{\pm,m}(z,r)$ is truncated so that $0 \le m \le M$. This defines the coefficients $\hat{c}_{-,m}(z,r)$ for $-1 \le m \le M-1$ and $\hat{c}_{+,m}(z,r)$ for $1 \le m \le M+1$. In order not to loose information it is necessary to take the maximal ℓ at least equal to $M+1$ and not M as it would be the case if only scalar functions were expanded. (The idea to accommodate $c_{-,M}(z,r)$ by considering that the expansion is cyclic with $2M+1$ points around the axis: $c_{-,M}(z,r) = c_{-,-M-1}(z,r)$, i.e. $\hat{c}_{+,M+1}(z,r) = -\hat{c}_{-,M}(z,r)$ appeared to

be misleading because it placed an item belonging to the $M+1$-th space to the $M-th$ subspace.) Expanding further $\hat{c}_{\pm,m}(z,r)$ in the basis of associated Legendre functions:

$$\hat{c}_{\pm,m}(R\cos\varphi, R\cos\varphi) \;=\; \sum_{\ell\geq|m|} \hat{P}_\ell^m(\cos\varphi)\,\hat{a}_{\ell,m}^{(\pm1)} \tag{3.70}$$

we get

$$\tilde{v}_\mp e^{\mp i\theta} \;=\; \pm\sqrt{2}\sum_\ell \sum_{m=-\ell}^{\infty} \hat{a}_{\ell,m}^{(\pm1)} Y_{\ell,m}(\varphi,\theta) \tag{3.71}$$

As for the component v_z, the standard scalar expansion

$$c_{z,m}(R\cos\varphi, R\cos\varphi) \;=\; \sum_{\ell\geq|m|} \hat{P}_\ell^m(\cos\varphi) a_{\ell,m}^{(z)} \tag{3.72}$$

$$v_z \;=\; \sum_\ell \sum_{m=-\ell}^{\infty} a_{\ell,m}^{(z)}\, Y_{\ell,m}(\varphi,\theta) \tag{3.73}$$

can be used. This yields the coefficients $\hat{a}_{\ell,m}^{(0)} = a_{\ell,m}^{(z)}$. The new expansion coefficients represent a tensorial product of $\ell=1$ and ℓ representations. They transform following the formula (see Eq. 3.64):

$$\hat{a'}_{\ell,m'}^{(\mu')} = \sum_{\mu=-1}^{1} \sum_{m=-\ell}^{\ell} \overline{r^{(1)}}_{\mu',\mu} r_{m',m}^{(\ell)} \hat{a}_{\ell,m}^{(\mu)} \tag{3.74}$$

where $r_{m',m}^{(\ell)}$ stands for the rotation matrix elements in the ℓ-subspace.

The resulting algorithm thus uses the same rotation matrices as those obtained in Sec. 3.2.4. If the vectorial expansion $\hat{a}_{\ell,m}^{(\mu)}$ is stored in three columns corresponding to $\mu=-1,0,1$ the operation in Eq. (3.74) assumes the matrix form:

$$\hat{\mathbf{a}'}^{(\ell)} \;=\; \mathbf{r}^{(\ell)}\,\mathbf{a}^{(\ell)}\,(\mathbf{r}^{(1)})^\dagger. \tag{3.75}$$

3.6 Principle of the domain decomposition

To allow for the rotation of the spherical sub-domain, both sub-domains will be un-coupled on the surface of the sphere $|\mathbf{r}| = R_s$. The same spectral – spectral-element discretization as in Jenny & Dušek (2004) can be applied separately to each of the sub-domains. The discretization of the radial-axial plane of both sub-domains can be generated by a single spectral-element mesh such as that represented in Figure 4.1 for an infinitely thin disc. The half circle generating a spherical interface by rotation about the domain axis is represented by a thick line. For reasons discussed below, the half-circle is assumed to separate two circular layers of spectral elements of constant thickness. The meshing need not be conformal across the interface but, for testing, it is useful to have a mesh applicable to a non-decomposed domain. In what follows, the decomposition of the domain $\mathcal{D}$ will write:

$$\mathcal{D} = \mathcal{D}_1 \bigcup \mathcal{D}_2; \quad \mathcal{D}_1^{(0)} \bigcap \mathcal{D}_2^{(0)} = \emptyset \tag{3.76}$$

where $\mathcal{D}_1$ will denote the spherical sub-domain and $\mathcal{D}_2$ the remaining cylindrical one. $\mathcal{D}_1$ and $\mathcal{D}_2$ are considered as closed sets. The common spherical interface $\mathcal{D}_1 \bigcap \mathcal{D}_2$ will be denoted I. ($\mathcal{D}_j^{(0)}, j = 1, 2$ denote the interior of the sets.)

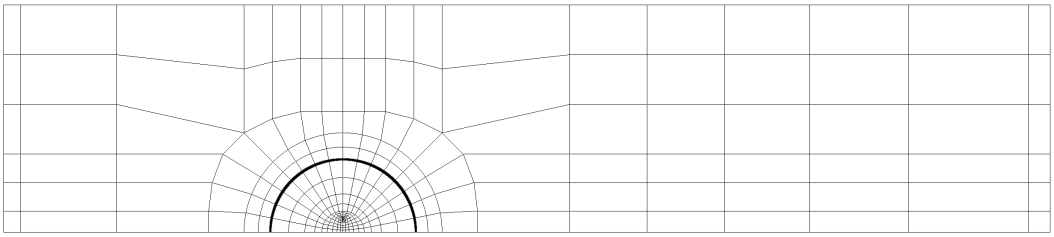

Figure 3.4: The spectral element decomposition of the radial-axial plane. The represented mesh contains 277 elements. It was used for an infinitely thin disc. The thick line shows the position of the spherical interface. In this example, the interface radius is $2.6d$. Upstream, downstream extensions and the radius of the cylindrical domain are equal to $L_u = 12d$, $L_d = 25d$, $R_c = 8d$, respectively.

The de-coupling of the sub-domains is obtained by removing all the collocation points lying on the half circle, which determines the interface. The discretization of the interface by the expansion into spherical harmonics will allow us to re-connect the two sub-domains dynamically. Be $u(\varphi, \theta)$ a scalar function defined on a sphere parametrized by the polar angle φ and the azimuthal angle θ. The spherical function expansion is defined as

$$u(\varphi, \theta) = \sum_{\ell=0}^{\infty} \sum_{m=-\ell}^{\ell} a_{\ell,m} Y_{\ell,m}(\varphi, \theta), \tag{3.77}$$

where $Y_{\ell,m}$ are the spherical functions specified in section 3.2.4. The coefficients of the expansion, truncated at some ℓ_{max}, will be considered to form an array denoted a. The problem

$$\mathcal{A}u = f; \quad \text{on } \mathcal{D}_1 \bigcup \mathcal{D}_2 \tag{3.78}$$

with a Dirichlet boundary condition on a part $\partial\mathcal{D}_D$ of its external boundary

$$u|_{\partial\mathcal{D}_{2,D}} = 0 \tag{3.79}$$

and a Neumann condition on the rest of this boundary

$$\left.\frac{\partial u}{\partial \mathbf{n}}\right|_{\partial(\mathcal{D}_2 - \mathcal{D}_{2,D})} = 0 \tag{3.80}$$

is equivalent to the variational problem defined by the functional

$$\mathcal{J}(u) = \frac{1}{2}\int_{\mathcal{D}_1\cup\mathcal{D}_2} \overline{u}\,\mathcal{A}u\,d\mathcal{D} - \int_{\mathcal{D}_1\cup\mathcal{D}_2} \overline{u}f\,d\mathcal{D}. \tag{3.81}$$

The domain decomposition splits the integrals into two terms

$$\begin{aligned}
\mathcal{J}(u) &= \mathcal{J}_1(u) + \mathcal{J}_2(u), && (3.82)\\
\mathcal{J}_1(u) &= \frac{1}{2}\int_{\mathcal{D}_1} \overline{u}\,\mathcal{A}u\,d\mathcal{D}_1 - \int_{\mathcal{D}_1} \overline{u}f\,d\mathcal{D}_1, && (3.83)\\
\mathcal{J}_2(u) &= \frac{1}{2}\int_{\mathcal{D}_2} \overline{u}\,\mathcal{A}u\,d\mathcal{D}_2 - \int_{\mathcal{D}_2} \overline{u}f\,d\mathcal{D}_2. && (3.84)
\end{aligned}$$

The sub-domains cannot be reconnected by a Neumann condition

$$\begin{aligned}
\left.\frac{\partial u}{\partial n}\right|_{I\cap\mathcal{D}_1} &= \lambda && (3.85)\\
\left.\frac{\partial u}{\partial n}\right|_{I\cap\mathcal{D}_2} &= -\lambda && (3.86)
\end{aligned}$$

because the part of the problem arising on $\mathcal{D}_1$ would have only a Neumann boundary condition and would thus not have a unique solution. For this reason, the reconnection of the sub-domains will be defined by a Dirichlet boundary condition. To allow for the rotation of the sub-domain $\mathcal{D}_1$ inside $\mathcal{D}_2$, we shall require:

$$a_2 = \mathbf{R}a_1 \tag{3.87}$$

where $\mathbf{R}$ is the rotation matrix at the interface (3.58), expressed in the representation of the spherical functions a, mapping the interior $\mathcal{D}_1\cap I$ onto the exterior sub-domain $\mathcal{D}_2\cap I$ and a_k, $k = 1, 2$ are the arrays of coefficients of spherical function expansion obtained by restricting the discretized solution U_k onto the interface and by expanding it using the transformation $\mathbf{T}$ defined by Eqs. (3.49), (3.50) and (3.55,3.56):

$$U_1|_I = \mathbf{T}_1 a_1; \quad U_2|_I = \mathbf{T}_2 a_2. \tag{3.88}$$

Due to the continuity condition at the interface expressed by Eq. (3.87) we can denote $a_1 \equiv a$ and $a_2 = \mathbf{R}a$. As the result, the spectral element representation at the interface is given by

$$U_1|_I = \mathbf{T}_1 a; \quad U_2|_I = \mathbf{T}_2\mathbf{R}a. \tag{3.89}$$

(In Eq. (3.89) $\mathbf{T}_k$ stand for the transformation matrix (3.55)). The discretized counterpart of the functional (3.82) – (3.84) is given by the function

$$J(U_1, U_2) = \frac{1}{2}\left(U_1^\dagger \mathbf{A}_1 U_1 + U_2^\dagger \mathbf{A}_2 U_2\right) - \left(U_1^\dagger \mathbf{M}_1 F_1 + U_2^\dagger \mathbf{M}_2 F_2\right). \tag{3.90}$$

where $\mathbf{A}_1, \mathbf{A}_2$ are matrices discretizing the operator $\mathcal{A}$ on each sub-domain (in the spectral element discretization), $\mathbf{M}_1, \mathbf{M}_2$ are the corresponding mass matrices and U_k, F_k $k = 1, 2$ are

the discretized solutions and right hand sides. On the outer Dirichlet boundary, the values of the solution are imposed and are thus not considered as part of the solution array U_2. Assuming a zero Dirichlet boundary condition, these values do not appear in the discretized formulation, otherwise they contribute to the RHS term. At the interface, Eqs. (3.89) represent Dirichlet boundary conditions for the partial problems in the sub-domains. Such a problem has a unique solution even on $\mathcal{D}_1$. Since the values $U_1|_I$ and $U_2|_I$ are given via the coefficients a of the spherical function expansion they are no longer parts of the sought solution. The latter is now composed of $\hat{U}_1, \hat{U}_2$, values in $\mathcal{D}_1^{(0)}$ and $\mathcal{D}_2^{(0)}$, respectively and of the array a. Separating the values at the interface from those inside the sub-domains ($U_k^T = (\hat{U}_k^T, U_k|_I^T)$ we can rewrite the discretized functional (3.90) by inserting

$$U_1 = \begin{pmatrix} \hat{U}_1 \\ \mathbf{T}_1 a \end{pmatrix}, \quad U_2 = \begin{pmatrix} \hat{U}_2 \\ \mathbf{T}_2 \mathbf{R} a \end{pmatrix} \tag{3.91}$$

for U_1 and U_2. The resulting functional depends on $\hat{U}_1, \hat{U}_2$ and a:

$$\begin{aligned} J(\hat{U}_1, \hat{U}_2, a) &= \frac{1}{2}\Big(\hat{U}_1^\dagger \hat{\mathbf{A}}_1 \hat{U}_1 + 2\hat{U}_1^\dagger \mathbf{A}_{1,I}\mathbf{T}_1 a + a^\dagger \mathbf{T}_1^T \mathbf{A}_{1,II}\mathbf{T}_1 a \\ &+ \hat{U}_2^\dagger \hat{\mathbf{A}}_2 \hat{U}_2 + 2\hat{U}_2^\dagger \mathbf{A}_{2,I}\mathbf{T}_2\mathbf{R} a + a^T \mathbf{R}^\dagger \mathbf{T}_2^T \mathbf{A}_{2,II}\mathbf{T}_2\mathbf{R} a\Big) \\ &- \Big(\hat{U}_1^T \hat{\mathbf{M}}_1 F_1 + \hat{U}_2^T \hat{\mathbf{M}}_2 F_2 + a^T(\mathbf{T}_1^T \mathbf{M}_{1,I} F_1 + \mathbf{R}^\dagger \mathbf{T}_2^T \mathbf{M}_{2,I} F_2)\Big). \end{aligned} \tag{3.92}$$

In Eq. (3.92) the matrices $\mathbf{A}_1$ and $\mathbf{A}_2$ were decomposed in the following way:

$$\begin{aligned} \mathbf{A}_1 = \begin{bmatrix} \hat{\mathbf{A}}_1 & \mathbf{A}_{1,I} \\ \mathbf{A}_{1,I}^T & \mathbf{A}_{1,II} \end{bmatrix}, \qquad \mathbf{A}_2 = \begin{bmatrix} \hat{\mathbf{A}}_2 & \mathbf{A}_{2,I} \\ \mathbf{A}_{2,I}^T & \mathbf{A}_{2,II} \end{bmatrix} \\ \mathbf{M}_1 = \begin{bmatrix} \hat{\mathbf{M}}_1 \\ \mathbf{M}_{1,I} \end{bmatrix}, \qquad \mathbf{M}_2 = \begin{bmatrix} \hat{\mathbf{M}}_2 \\ \mathbf{M}_{2,I} \end{bmatrix}. \end{aligned} \tag{3.93}$$

$\hat{\mathbf{A}}_1$ stands for the restriction to $\mathcal{D}_1^{(0)}$, $\mathbf{A}_{1,I}$ for the mapping from the interface to $\mathcal{D}_1^{(0)}$ and $\mathbf{A}_{1,II}$ is the restriction to the interface. The same holds for $\mathbf{A}_2$. The sought equations result as gradients with respect to $\hat{U}_1, \hat{U}_2$ and a:

$$\hat{\mathbf{A}}_1 \hat{U}_1 + \mathbf{A}_{1,I}\mathbf{T}_1 a = \hat{\mathbf{M}}_1 F_1 \tag{3.94}$$

$$\hat{\mathbf{A}}_2 \hat{U}_2 + \mathbf{A}_{2,I}\mathbf{T}_2\mathbf{R} a = \hat{\mathbf{M}}_2 F_2 \tag{3.95}$$

$$\begin{aligned} \mathbf{T}_1^T \mathbf{A}_{1,I}^T \hat{U}_1 + \mathbf{R}^\dagger \mathbf{T}_2^T \mathbf{A}_{2,I}^T \hat{U}_2 &+ \Big(\mathbf{T}_1^T \mathbf{A}_{1,II}\mathbf{T}_1 + \mathbf{R}^\dagger \mathbf{T}_2^T \mathbf{A}_{2,II}\mathbf{T}_2\mathbf{R}\Big) a \\ &= \mathbf{T}_1^T \mathbf{M}_{1,I} F_1 + \mathbf{R}^\dagger \mathbf{T}_2^T \mathbf{M}_{2,I} F_2. \end{aligned} \tag{3.96}$$

We disregarded so far the reconnection at spectral element interfaces discussed in section 3.1. In the same way as at the spherical interface, there is a redundancy in storing values at

all collocation points. As a matter of fact, in each sub-domain, only an array of independent values V_k, $k = 1, 2$ is relevant. This array is at the basis of the direct solver already implemented. Let us note $\mathbf{E}_k$ the extension to the representation at collocation points consisting in mapping the same independent variable to all physically identical collocation points:

$$\hat{U}_k = \mathbf{E}_k V_k \tag{3.97}$$

Denote V the whole array of independent variables:

$$V = \begin{pmatrix} V_1 \\ V_2 \\ a \end{pmatrix}. \tag{3.98}$$

Eqs. (3.94 - 3.96) become

$$\begin{aligned}
\mathbf{E}_1^T \hat{\mathbf{A}}_1 \mathbf{E}_1 V_1 + \mathbf{E}_1^T \mathbf{A}_{1,I} \mathbf{T}_1 a &= \mathbf{E}_1^T \hat{\mathbf{M}}_1 F_1 && (3.99)\\
\mathbf{E}_2^T \hat{\mathbf{A}}_2 \mathbf{E}_2 V_2 + \mathbf{E}_2^T \mathbf{A}_{2,I} \mathbf{T}_2 \mathbf{R} a &= \mathbf{E}_2^T \hat{\mathbf{M}}_2 F_2 && (3.100)\\
\mathbf{T}_1^T \mathbf{A}_{1,I}^T \mathbf{E}_1 V_1 + \mathbf{R}^\dagger \mathbf{T}_2^T \mathbf{A}_{2,I}^T \mathbf{E}_2 V_2 &+ \left(\mathbf{T}_1^T \mathbf{A}_{1,II} \mathbf{T}_1 + \mathbf{R}^\dagger \mathbf{T}_2^T \mathbf{A}_{2,II} \mathbf{T}_2 \mathbf{R} \right) a \\
&= \mathbf{T}_1^T \mathbf{M}_{1,I} F_1 + \mathbf{R}^\dagger \mathbf{T}_2^T \mathbf{M}_{2,I} F_2. && (3.101)
\end{aligned}$$

The formalism generalizes directly to the vector case. In this case, the arrays V_1, V_2 stand for the values of the whole vector field and a for the vectorial spherical function expansion coefficients detailed in Sec. 3.5

3.7 Conjugate gradient solver

An iterative solver of Krylov type, like that of the conjugate gradients, requires only to define the operation by the discretized operator $\mathcal{A}$. The latter is obtained by Eqs. (3.99, 3.100) and (3.101) by taking either of Eqs. (3.99, 3.100) at a point inside the sub-domains and the equation (3.101) at a point at the interface. At the interface, Eq. (3.101) represents a generalized direct stiffness sum involving the transposed matrices of spherical function expansions and the rotation at the interface.

The formulation (3.99, 3.100) and (3.101) requires a special storage of the coefficients a along with each field. However, these coefficients are used to compute two sets of values at the collocation points at the interface, which carry the same information. The complete fields in each sub-domain are the result of the following matrix operation:

$$U = \mathbf{B}V \quad \Leftrightarrow \begin{pmatrix} \hat{U}_1 \\ \mathbf{T}_1 a \\ \hat{U}_2 \\ \mathbf{T}_2\mathbf{R}a \end{pmatrix} = \begin{bmatrix} \mathbf{1} & \mathbf{0} & \mathbf{0} \\ \mathbf{0} & \mathbf{0} & \mathbf{T}_1 \\ \mathbf{0} & \mathbf{1} & \mathbf{0} \\ \mathbf{0} & \mathbf{0} & \mathbf{T}_2\mathbf{R} \end{bmatrix} \begin{pmatrix} \hat{U}_1 \\ \hat{U}_2 \\ a \end{pmatrix}$$
$$= \begin{bmatrix} \mathbf{E}_1 & \mathbf{0} & \mathbf{0} \\ \mathbf{0} & \mathbf{0} & \mathbf{T}_1 \\ \mathbf{0} & \mathbf{E}_2 & \mathbf{0} \\ \mathbf{0} & \mathbf{0} & \mathbf{T}_2\mathbf{R} \end{bmatrix} \begin{pmatrix} V_1 \\ V_2 \\ a \end{pmatrix} \tag{3.102}$$

Eqs. (3.99, 3.100) and (3.101) are then equivalent to

$$\mathbf{B}^\dagger \mathbf{A}\mathbf{B}\, V = \mathbf{B}^\dagger \mathbf{M} F \tag{3.103}$$

where

$$\mathbf{A} = \mathbf{A}_1 \oplus \mathbf{A}_2 \quad \mathbf{M} = \mathbf{M}_1 \oplus \mathbf{M}_2 \tag{3.104}$$

and

$$\mathbf{B} = \begin{bmatrix} \mathbf{E}_1 & \mathbf{0} & \mathbf{0} \\ \mathbf{0} & \mathbf{0} & \mathbf{T}_1 \\ \mathbf{0} & \mathbf{E}_2 & \mathbf{0} \\ \mathbf{0} & \mathbf{0} & \mathbf{T}_2\mathbf{R} \end{bmatrix} \tag{3.105}$$

If the storage of values a is to be avoided we can store the arrays of the form U as is also the case in the collocation point representation of the original version. Eq. (3.103) then becomes:

$$\mathbf{B}\mathbf{B}^\dagger \mathbf{A} U = \mathbf{B}\mathbf{B}^\dagger \mathbf{M} F \tag{3.106}$$

$\mathbf{B}\mathbf{B}^\dagger$ playing the role of the original direct stiffness sum.

$$\mathbf{B}\mathbf{B}^\dagger = \begin{bmatrix} \mathbf{E}_1\mathbf{E}_1^T & \mathbf{0} & \mathbf{0} & \mathbf{0} \\ \mathbf{0} & \mathbf{T}_1\mathbf{T}_1^\dagger & \mathbf{0} & \mathbf{T}_1\mathbf{R}^\dagger\mathbf{T}_2^\dagger \\ \mathbf{0} & \mathbf{0} & \mathbf{E}_2\mathbf{E}_2^T & \mathbf{0} \\ \mathbf{0} & \mathbf{T}_2\mathbf{R}\mathbf{T}_1^\dagger & \mathbf{0} & \mathbf{T}_2\mathbf{T}_2^\dagger \end{bmatrix}. \tag{3.107}$$

The modified direct stiffness sum consists in applying the original direct stiffness sum inside the sub-domains and in replacing the non-connected values $U_{1,I}$ and $U_{2,I}$ at the interface by $(\mathbf{T}_1\mathbf{T}_1^\dagger U_{1,I} + \mathbf{T}_1\mathbf{R}^\dagger\mathbf{T}_2^\dagger U_{2,I})$ and $(\mathbf{T}_2\mathbf{R}\mathbf{T}_1^\dagger U_{1,I} + \mathbf{T}_2\mathbf{T}_2^\dagger U_{2,I})$. For a non-trivial rotation $\mathbf{R}$ this operation couples the azimuthal modes. As the result, the conjugate gradient algorithm must be applied to the whole arrays including all azimuthal modes. This contrasts with the previous version of the code, where each mode was treated separately. The rotation is applied at each iteration.

We have seen that the conjugate gradient algorithm requires the computation of the L^2-norm of a residual multiplied by a mass matrix and regularized by the direct stiffness sum. The expression (3.8) relied on Eq. (3.6). In order to obtain a similar expression for

the decomposed domain, we must reconsider the computation of the L^2-norm. Eq. (3.8) becomes simply

$$\mathbf{B}^\dagger \boldsymbol{\mu} \mathbf{B} \,=\, \mathbf{1} \tag{3.108}$$

provided the matrix $\boldsymbol{\mu}$ is modified in the following way:

$$\boldsymbol{\mu} \,=\, \mathrm{diag}(\mu_1, \pi\mathbf{W}_1, \mu_2, \pi\mathbf{W}_2), \tag{3.109}$$

where 'diag' stands for a diagonal matrix. It is composed of the values of the inversed multiplicities in the interior of the sub-domains and of the quadrature weights of the numerical integration multiplied by π at the interface. To get Eq. (3.108) we use (see Eq.(3.57))

$$\mathbf{T}_k^T \mathbf{W}_k \mathbf{T}_k = \frac{1}{2\pi}. \tag{3.110}$$

3.7.1 L^2 norm

Let us express the L^2 norm

$$\int_{\mathcal{D}} \overline{u} u \, d\mathcal{D}. \tag{3.111}$$

needed for the implementation of the conjugate gradient method. Taking account of Eqs. (3.91) and (3.97), we have the discrete approximation (see also Eq. (3.92))

$$\begin{aligned} \int_{\mathcal{D}} \overline{u} u \, d\mathcal{D} \;\; &= \;\; U_1^\dagger \mathbf{M}_1 U_1 \,+\, U_2^\dagger \mathbf{M}_2 U_2 \,= \\ V_1^\dagger \mathbf{E}_1^T \hat{\mathbf{M}}_1 \mathbf{E} V_1 \,+\, V_2^\dagger \mathbf{E}_2^T \hat{\mathbf{M}}_2 \mathbf{E} V_2 \;\; &+ \;\; a^\dagger \mathbf{T}_1^T \mathbf{M}_{1,I} \mathbf{T}_1 a \,+\, a^\dagger \mathbf{R}^\dagger \mathbf{T}_2^T \mathbf{M}_{2,I} \mathbf{T}_2 \mathbf{R} a. \end{aligned} \tag{3.112}$$

For a concentric layer of elements on both sides of the interface, the mass matrix at the interface $\mathbf{M}_{1,I}$, $\mathbf{M}_{2,I}$ is proportional to the surface weight matrix $\mathbf{W}$ (Eq. (3.56)). As a result, due to the orthogonality relation (3.46), both matrix products $\mathbf{T}_1^T \mathbf{M}_{1,I} \mathbf{T}_1$ and $\mathbf{T}_2^T \mathbf{M}_{2,I} \mathbf{T}_2$ are proportional to the identity matrix. Denote:

$$\mathbf{T}_1^T \mathbf{M}_{1,I} \mathbf{T}_1 \,=\, k_1 \mathbf{1}, \quad \mathbf{T}_2^T \mathbf{M}_{2,I} \mathbf{T}_2 \,=\, k_2 \mathbf{1}. \tag{3.113}$$

Since also $\mathbf{R}^\dagger \mathbf{R} = \mathbf{1}$, we have $\mathbf{R}^\dagger \mathbf{T}_2^T \mathbf{M}_{2,I} \mathbf{T}_2 \mathbf{R} = k_2 \mathbf{1}$. Taking $a_{\ell,m} = 0$ except for $a_{0,0} = 1$, we get

$$k_j = \frac{Tr(\mathbf{M}_{j,I})}{4\pi}, \quad j = 1, 2. \tag{3.114}$$

As the result:

$$\int_{\Omega} \overline{u} u \, d\Omega = \hat{U}_1^\dagger \hat{\mathbf{M}}_1 \hat{U}_1 \,+\, \hat{U}_2^\dagger \hat{\mathbf{M}}_2 \hat{U}_2 \,+\, (k_1 + k_2) a^\dagger a. \tag{3.115}$$

The RHS of Eq. (3.106) results from an application of the generalized direct stiffness sum. The question is how to calculate its L^2 norm. To see this, let us replace F by the array U of Eq. (3.105):

$$\begin{aligned}\mathbf{B}^\dagger\mathbf{M}U &= \begin{pmatrix} \mathbf{E}_1^T\hat{\mathbf{M}}_1\mathbf{E}_1V_1 \\ \mathbf{E}_2^T\hat{\mathbf{M}}_2\mathbf{E}_2V_2 \\ \left(\mathbf{T}_1^T\mathbf{M}_{1,I}\mathbf{T}_1 + \mathbf{R}^\dagger\mathbf{T}_2^T\mathbf{M}_{2,I}\mathbf{T}_2\mathbf{R}\right)a \end{pmatrix} \\ &= \begin{bmatrix} \mathbf{E}_1^T\hat{\mathbf{M}}_1\mathbf{E}_1 & \mathbf{0} & \mathbf{0} \\ \mathbf{0} & \mathbf{E}_2^T\hat{\mathbf{M}}_2\mathbf{E}_2 & \mathbf{0} \\ \mathbf{0} & \mathbf{0} & (k_1+k_2)\mathbf{1} \end{bmatrix} V \end{aligned} \tag{3.116}$$

where the matrix in Eq. (3.116) is diagonal. Denote $m = (m_1^T, m_2^T, (k_1+k_2)1_I)^T$, where $m_k = diag(\mathbf{E}_k^T\hat{\mathbf{M}}_k\mathbf{E}_k)$, $k = 1, 2$ and 1_I is an array of ones of length equal to the number of coefficients of the expansion at the interface. The array $\tilde{m}$ is its counterpart distributed to collocation points:

$$\tilde{m} = \begin{pmatrix} \mathbf{E}_1 m_1 \\ (k_1+k_2)1_{I,1} \\ \mathbf{E}_2 m_2 \\ (k_1+k_2)1_{I,2} \end{pmatrix}. \tag{3.117}$$

It arises by applying the direct stiffness sum to the array of the (diagonal) elements of the mass matrix inside the sub-domains. Its elements at the interface are replaced by the constant value (k_1+k_2). Denote, further, the diagonal matrix $\tilde{\mathbf{M}} = diag(\tilde{m})$. We have:

$$\mathbf{B}\mathbf{B}^\dagger\mathbf{M}U = \begin{pmatrix} \mathbf{E}_1\mathbf{E}_1^T\hat{\mathbf{M}}_1\mathbf{E}_1V_1 \\ (k_1+k_2)\mathbf{T}_1a \\ \mathbf{E}_2\mathbf{E}_2^T\hat{\mathbf{M}}_2\mathbf{E}_2V_2 \\ (k_1+k_2)\mathbf{T}_2\mathbf{R}a \end{pmatrix} = \tilde{\mathbf{M}}U \tag{3.118}$$

As a consequence if we denote $Y = \mathbf{B}\mathbf{B}^\dagger\mathbf{M}U$ we get

$$\begin{aligned} Y^\dagger\mu\tilde{\mathbf{M}}^{-1}Y &= U^\dagger\mathbf{M}\mathbf{B}\mathbf{B}^\dagger\mu\tilde{\mathbf{M}}^{-1}\mathbf{B}\mathbf{B}^\dagger\mathbf{M}U = \\ U^\dagger\mathbf{M}\mathbf{B}\mathbf{B}^\dagger\mu\mathbf{B}V &= U^\dagger\mathbf{M}\mathbf{B}V = U^\dagger\mathbf{M}U. \end{aligned} \tag{3.119}$$

3.7.2 Preconditioner

The default preconditioner is the inverse of the diagonal of the inverted matrix $\mathbf{A}$. In the space of independent unknown variables, the form of the preconditioner derives from Eqs. (3.94, 3.95, 3.96) if $\mathbf{A}_1, \mathbf{A}_2$ of Eq. (3.93) are replaced by

$$\mathbf{D}_1 = \begin{bmatrix} \hat{\mathbf{D}}_1 & \mathbf{0} \\ \mathbf{0} & \mathbf{D}_{1,I} \end{bmatrix}, \quad \mathbf{D}_2 = \begin{bmatrix} \hat{\mathbf{D}}_2 & \mathbf{0} \\ \mathbf{0} & \mathbf{D}_{2,I} \end{bmatrix} \tag{3.120}$$

where $\hat{\mathbf{D}}_1, \mathbf{D}_{1,I}, \hat{\mathbf{D}}_2, \mathbf{D}_{2,I}$ are diagonal blocs. In the representation (3.98):

$$\mathbf{D}V \;=\; \begin{pmatrix} \hat{\mathbf{D}}_1\hat{U}_1 \\ \hat{\mathbf{D}}_2\hat{U}_2 \\ \left(\mathbf{T}_1^T\mathbf{D}_{1,I}\mathbf{T}_1 + \mathbf{R}^\dagger\mathbf{T}_2^T\mathbf{D}_{2,I}\mathbf{T}_2\mathbf{R}\right) a \end{pmatrix} \tag{3.121}$$

The matrix $\mathbf{T}_1^T\mathbf{D}_{1,I}\mathbf{T}_1+\mathbf{R}^\dagger\mathbf{T}_2^T\mathbf{D}_{2,I}\mathbf{T}_2\mathbf{R}$ is close to diagonal with constant diagonal elements similarly as the matrices (3.113). The matrices $\mathbf{T}_1^T\mathbf{D}_{1,I}\mathbf{T}_1$ and $\mathbf{T}_2^T\mathbf{D}_{2,I}\mathbf{T}_2$ appear to be almost a multiple of a unit matrix, like the matrices (3.113):

$$\mathbf{T}_1^T\mathbf{D}_{1,I}\mathbf{T}_1 \approx d_1\mathbf{1}; \quad \mathbf{T}_2^T\mathbf{D}_{2,I}\mathbf{T}_2 \approx d_2\mathbf{1} \tag{3.122}$$

where d_1 and d_2 are the averages of the diagonal values. The approximations (3.122) are accurate only with about 10^{-3} accuracy. Nevertheless, we can use the diagonal preconditioner

$$\mathbf{P}V \;=\; \begin{pmatrix} \hat{\mathbf{D}}_1^{-1}\hat{U}_1 \\ \hat{\mathbf{D}}_2^{-1}\hat{U}_2 \\ \frac{1}{d_1+d_2}a \end{pmatrix} \tag{3.123}$$

This tradeoff presents no problem for a preconditioner, whose role is to accelerate the convergence. We arrive, again, at a diagonal matrix the inversion of which is trivial.

3.7.3 Preconditioned conjugate gradient algorithm

The preconditioned conjugate gradient algorithm for the solution of the problem $\mathbf{B}\mathbf{B}^\dagger\mathbf{A}x = \mathbf{B}\mathbf{B}^\dagger\mathbf{M}f$ can be summed up in following steps:

- initial condition: $x = x_0$ (usually $x_0 = 0$),
- $r = \mathbf{B}\mathbf{B}^\dagger\mathbf{M}f - \mathbf{B}\mathbf{B}^\dagger\mathbf{A}x_0$,
- $n = r^\dagger\mu\tilde{\mathbf{M}}^{-1}r$,
- $x = x_0$,
- $p' = \mathcal{P}r$,
- $p = p'$
- $\rho = (r^\dagger p')$
- $i = 0$

  repeat
- $i = i + 1$

  if $i > 1$
- $w = \mu\tilde{\mathbf{M}}^{-1}r$,
- $p' = \mathcal{P}r$,

- $\rho' = \rho$,
- $\rho = (r^\dagger p')$,
- $n = r^\dagger w$,
- $\beta = \rho/\rho'$,
- if $n < \epsilon$ then $i = i - 1$, exit loop,
- $p = \beta p + p'$, *endif*
- $w = \mathbf{B}\mathbf{B}^\dagger \mathbf{A} p$
- $\alpha = \rho/(p^\dagger w)$
- $u = u + \alpha p$
- $r = r - \alpha w$

  end repeat

3.7.4 Case of the vector field

The formalism of the section 3.6 generalizes to a vector field by replacing the scalar arrays U_j, $j = 1, 2$, by vector arrays U_j^z, U_j^-, U_j^+, which implies the description of values inside the subdomains by arrays V_j^z, V_j^-, V_j^+ and those at the interface by spherical expansion coefficients $\hat{a}_{\ell,m}^{(\mu)}$ specified in Sec. 3.2.4. The variational formulation is based on the expression of the scalar product $\int_\Omega \mathbf{v} \cdot \mathbf{w} d\Omega$:

$$\int_{\mathcal{D}} \mathbf{v} \cdot \mathbf{w} d\mathcal{D} \;=\; \int_{\mathcal{D}} \left[v_z w_z \;+\; \frac{1}{2}(\overline{v_+} w_+ + \overline{v_-} w_-.) \right] d\mathcal{D} \tag{3.124}$$

The two terms inside the parentheses on the RHS of Eq. (3.124) are actually identical and each of them represents the transverse norm whence comes the factor 1/2. The same structure of expressions appears when the azimuthal expansion with coefficients $c_{\pm,m}$ is introduced:

$$\int_{\mathcal{D}} \mathbf{v} \cdot \mathbf{w} d\mathcal{D} \;=\; \sum_{m=-\infty}^{\infty} \int_{\mathcal{D}} \left[\overline{c_{z,m}} c'_{z,m} + \frac{1}{2}(\overline{c_{+,m}} c'_{+,m} + \overline{c_{-,m}} c'_{-.m}) \right] .d\mathcal{D} \tag{3.125}$$

The prime stands for the coefficients of the vector field $\mathbf{w}$. Note, however, that the factor 1/2 disappears when the modes $\hat{c}$ (Eq. (3.69)) are introduced:

$$\int_{\mathcal{D}} \mathbf{v}\mathbf{w} d\mathcal{D} \;=\; \sum_{m=-\infty}^{\infty} \int_{\mathcal{D}} \left[\overline{c_{z,m}} c'_{z,m} + (\overline{\hat{c}_{+,m}} \hat{c}'_{+,m} + \overline{\hat{c}_{-,m}} \hat{c}'_{-.m}) \right] .d\mathcal{D} \tag{3.126}$$

As a result, we recover standard Euclidean scalar products and the same expansion relations (3.70) as for the scalar case. This makes the generalization of operations at the interface straightforward.

The iterative solver being applied to the vector field, the essential items of the algorithm are the inverse multiplicity matrix μ (Eq. 3.109) and the regularized mass matrix $\tilde{\mathbf{M}}$ (see Eqs. 3.117, 3.118). In view of what has been said, these matrices are applied identically to each of the vectorial components of $\hat{c}$. Since the transformation to $c_{\pm,m}$ is given by a global constant factor $(\pm\sqrt{2})$ the same matrices apply to original azimuthal components. In the implemented algorithm we work with original $c_{\pm,m}$ modes. To account for the factor 2 defining the correct scalar product (3.125), the vectorial matrix μ_{vect} will be defined by taking the direct sum of matrices

$$\mu_{vect} \;=\; \mu \oplus \frac{1}{2}\mu \oplus \frac{1}{2}\mu. \tag{3.127}$$

3.8 Direct solver

The pre-existing direct pressure solver was based on the LDL decomposition of the pressure matrix. The decomposition was done once for all at the beginning of the computation. This strategy holds only for a fixed geometry. A moving mesh implies a continuously evolving pressure matrix. If the version using the multiplication of the discretized divergence times the discretized gradient is used, the motion of the geometry affects the pressure matrix inside the two sub-domains. This would require a new complete decomposition at each time step. For this reason, we go back to the standard approach using the discretized Laplace–Poisson operator. The small loss of accuracy is compensated by a sufficiently refined mesh. In this formulation, if the interface collocation points are masked, the spectral element decomposition in the interior of the sub-domains is insensitive to the motion at the interface. Assuming the real symmetric "raw" matrices (acting separately inside each spectral element) in the sub-domains $j = 1, 2$ to be decomposed as:

$$\mathbf{A}_j = \begin{bmatrix} \hat{\mathbf{A}}_j & \mathbf{A}_{j,I} \\ \mathbf{A}_{j,I}^T & \mathbf{A}_{j,II} \end{bmatrix}, \tag{3.128}$$

where $\hat{\mathbf{A}}_j$ is a restriction to the interior of the sub-domain, $\mathbf{A}_{j,I}$ represents the coupling of the interior with the interface and $\mathbf{A}_{j,II}$ is the restriction to the interface, we can rewrite the matrix $\mathbf{B}^\dagger\mathbf{A}\mathbf{B}$ on the LHS of Eq. (3.103) in the following way:

$$\mathbf{B}^\dagger\mathbf{A}\mathbf{B} \;=\; \begin{bmatrix} \hat{\mathbf{A}} & \mathbf{G} \\ \mathbf{G}^\dagger & \mathbf{A}_{II} \end{bmatrix}, \tag{3.129}$$

where $\hat{\mathbf{A}}$ is the restriction to the interior of the sub-domains

$$\hat{\mathbf{A}} = \begin{bmatrix} \hat{\mathbf{A}}_1 & 0 \\ 0 & \hat{\mathbf{A}}_2 \end{bmatrix}, \tag{3.130}$$

and

$$\mathbf{G} \;=\; \begin{bmatrix} \mathbf{A}_{1,I}\mathbf{T}_1 \\ \mathbf{A}_{2,I}\mathbf{T}_2\mathbf{R} \end{bmatrix}, \tag{3.131}$$

and

$$\mathbf{A}_{II} = \mathbf{T}_1^T \mathbf{A}_{1,II} \mathbf{T}_1 + \mathbf{R}^\dagger \mathbf{T}_2^T \mathbf{A}_{2,II} \mathbf{T}_2 \mathbf{R}. \tag{3.132}$$

We decompose also the right hand side of Eq. (3.103) as $(\hat{F}, F_I)^T$, where:

$$F = \begin{pmatrix} \hat{\mathbf{M}}_1 F_1 \\ \hat{\mathbf{M}}_2 F_2 \end{pmatrix} \tag{3.133}$$

$$F_I = \mathbf{T}_1^T \mathbf{M}_{1,I} F_1 + \mathbf{R}^\dagger \mathbf{T}_2^T \mathbf{M}_{2,I} F_2 \tag{3.134}$$

$$\tag{3.135}$$

The problem (3.103) writes then as

$$\hat{\mathbf{A}} \hat{U} + \mathbf{G} a = F \tag{3.136}$$

$$\mathbf{G}^\dagger \hat{U} + \mathbf{A}_{II} a = F_I \tag{3.137}$$

where $\hat{\mathbf{U}}$ is the array of values at the collocation points in the interior of sub-domains and a is the array of spherical function expansion coefficients. The latter is the solution of:

$$(\mathbf{G}^\dagger \hat{\mathbf{A}}^{-1} \mathbf{G} - \mathbf{A}_{II}) a = \mathbf{G}^\dagger \hat{\mathbf{A}}^{-1} F - F_I. \tag{3.138}$$

The size of the problem (3.138) is relatively small because it is given by the number of coefficients of the spherical function expansion. After a has been computed, $\hat{U}$ results from Eq. (3.136), which can be solved by the pre-existing direct pressure solver.

3.9 Implementation of the direct solver

The aim of the implementation is to restrict the number of inversions of the large matrices $\hat{\mathbf{A}}_1, \hat{\mathbf{A}}_2$. The way how to do becomes obvious if the matrix $\mathbf{G}^\dagger \mathbf{A}^{-1} \mathbf{G}$ is written in more detail:

$$\mathbf{G}^\dagger \hat{\mathbf{A}}^{-1} \mathbf{G} = \mathbf{T}_1^T \mathbf{A}_{1,I}^T \hat{\mathbf{A}}_1^{-1} \mathbf{A}_{1,I} \mathbf{T}_1 + \mathbf{R}^\dagger \mathbf{T}_2^T \mathbf{A}_{2,I}^T \hat{\mathbf{A}}_2^{-1} \mathbf{A}_{2,I} \mathbf{T}_2 \mathbf{R} \tag{3.139}$$

The matrices $\mathcal{P}_k = \mathbf{T}_k^T \mathbf{A}_{k,I}^T \mathbf{A}_k^{-1} \mathbf{A}_{k,I} \mathbf{T}_k$, $k = 1, 2$ can be computed simultaneously by solving the equation

$$\hat{\mathbf{A}} p_{\ell,m} = f_{\ell,m}. \tag{3.140}$$

where $f_{\ell,m} = [\mathbf{A}_{1,I}\{\hat{P}_\ell^m(\varphi_j^{(k)})\}|_{I,1}, \mathbf{A}_{2,I}\{\hat{P}_\ell^m(\varphi_j^{(k)})\}|_{I,2}]$ result from the action of the matrix $\mathbf{A}$ on the Legendre functions expressed at the collocation points at both sides of the interface. These arrays can be computed once for all at the beginning of the computation. The matrix $\mathbf{A}_{II}$ (Eq. (3.132)) depends also only on Legendre functions $\hat{P}_\ell^m$ at the interface. The matrix on the LHS of Eq. (3.137) thus writes:

$$\mathbf{D} = (\mathbf{G}^\dagger \hat{\mathbf{A}}^{-1} \mathbf{G} - \mathbf{A}_{II}) = \mathbf{C}_1 + \mathbf{R}^\dagger \mathbf{C}_2 \mathbf{R} \tag{3.141}$$

where

$$\mathbf{C}_k \;=\; \mathbf{T}_k^T \mathbf{A}_{k,I}^T \hat{\mathbf{A}}_k^{-1} \mathbf{A}_{k,I} \mathbf{T}_k \;-\; \mathbf{T}_k^T \mathbf{A}_{k,II} \mathbf{T}_k; \quad k = 1, 2 \tag{3.142}$$

are independent of the rotations $\mathbf{R}$. It is to be noted that the matrices $\mathbf{C}_k$ are diagonal in m. I.e.

$$C^{(k)}_{\ell,m;\ell',m'} = C^{(k,m)}_{\ell,\ell'} \delta_{m,m'}. \tag{3.143}$$

As explained, the matrices $\mathbf{C}_k$ can be generated once for all without updating at each time step. This computation follows the algorithm:

Proceed within an m-loop, $k = 1, 2$:

1. Map the columns of matrices $\mathbf{T}_k$ to an array of initially empty pressure fields and apply the pressure operator $(\mathbf{A}_k \mathbf{T}_k)$.
2. Extract values at interface $(\mathbf{A}_{k,II} \mathbf{T}_k)$ and mask them in the remaining array $(\mathbf{A}_{k,I} \mathbf{T}_k)$.
3. Apply the direct pressure solver inside the sub-domains to $\mathbf{A}_{k,I} \mathbf{T}_k$ (results in $\hat{\mathbf{A}}_k^{-1} \mathbf{A}_{k,I} \mathbf{T}_k$).
4. Multiply the result by the transposed of the (previously saved) matrices $\mathbf{A}_{k,I} \mathbf{T}_k$ (results in $\mathbf{T}_k^T \mathbf{A}_{k,I}^T \hat{\mathbf{A}}_k^{-1} \mathbf{A}_{k,I} \mathbf{T}_k$).
5. Multiply $\mathbf{A}_{k,II} \mathbf{T}_k$ by the transposed of $\mathbf{T}_k$ (results in $\mathbf{T}_k^T \mathbf{A}_{k,II} \mathbf{T}_k$) and subtract from the matrices obtained at the previous step (results in $\mathbf{C}_k$).
6. $C^{(k,m)}_{\ell,\ell'}$ are $(\ell_{max} - m + 1) \times (\ell_{max} - m + 1)$ matrices. Store them within a single column array of size

$$\sum_m (\ell_{max} - m + 1) \times (\ell_{max} - m + 1) = (\ell_{max} + 1)(\ell_{max} + 2)(2\ell_{max} + 3)/6.$$

The rotation matrix elements $R^{(\ell)}_{m,m'}$ are stored in blocks of the size $(2\ell + 1) \times (2\ell + 1)$ arranged column-wise for $\ell = 0 \ldots \ell_{max}$. The total size of the array is also $(\ell_{max} + 1)(2\ell_{max} + 1)(2\ell_{max} + 3)/3$.

The resulting matrix on interface 2 is to be rotated to interface 1 to form the term $\mathbf{D} = \mathbf{R}^\dagger \mathcal{P}_2 \mathbf{R}$. (The negative indices $m < 0$ have to be considered in the rotation matrix in spite of their redundancy.) The rotation writes as follows:

$$a_{\ell,m} \;=\; \sum_{m'=-\ell}^{\ell} R^{(\ell)}_{m,m'}(-\Phi, -\Psi, -\Theta) \sum_{\ell' \geq |m'|} \mathcal{P}^{(2,|m'|)}_{\ell,\ell'} \sum_{m''=-\ell'}^{\ell'} R^{(\ell')}_{m',m''}(\Phi, \Psi, \Theta)\, a'_{\ell',m''} \tag{3.144}$$

This corresponds to a matrix multiplication: $a_{\ell,m} = \sum_{\ell',|m'|\leq\ell'} D^{(2)}_{\ell,m;\ell',m'}\, a'_{\ell',m'}$ where the matrix elements $D^{(2)}_{\ell,m;\ell',m'}$ are given by:

$$D^{(2)}_{\ell,m;\ell',m'} \;=\; \sum_{|m''|\leq \min(\ell,\ell')} \overline{R^{(\ell)}_{m'',m}(\Phi, \Psi, \Theta)} \mathcal{P}^{(2,|m''|)}_{\ell,\ell'} R^{(\ell')}_{m'',m'}(\Phi, \Psi, \Theta). \tag{3.145}$$

The matrix (3.139) is obviously Hermitian. The term corresponding to the inside of the interface (inside the spherical sub-domain) is singular because it corresponds to solving for the pressure inside a domain with Dirichlet velocity boundary conditions. The cylindrical sub-domain outside the interface has, however, a Neumann velocity condition at the outflow where the pressure is defined, itself, by a Dirichlet condition $p = 0$. As a result, the term denoted (2) outside the interface is non-singular and ensures thus that the whole matrix can be inverted. The later can be inverted directly or by conjugate gradients. The direct inversion becomes quickly too costly, even for matrices 256×256 corresponding to the truncation at $\ell_{max} = 15$. In contrast, the conjugate gradient method converges very rapidly with the preconditioner given by the diagonal of the matrix.

Further savings of CPU time were obtained by reformulating the problem in terms of real and imaginary parts of coefficients $a_{\ell,m}$. This removes the redundancies of the complex formulation and yields a real matrix to be inverted.

3.10 Time integration of solid body equations

3.10.1 Update of solid body velocities

We try to adapt as closely as possible the algorithm of strong coupling presented in Jenny & Dušek (2004). Its formulation is fully implicit. I.e., when solving at the step $(n+1)$ Eqs. (2.33 - 2.35) the flow field used to compute the force and torque is assumed to be taken at the same step:

$$m^* \left(\frac{\mathbf{u}^{(n+1)} - \mathbf{u}^{(n)}}{\Delta t} + \omega^{(n+1)} \times \mathbf{u}^{(n+1)} \right) = \mathbf{F}_{fl}(\mathbf{v}^{(n+1)}, p^{(n+1)}) + \mathbf{k}_{fix} \quad (3.146)$$

$$I^* \alpha \frac{\Omega_3^{(n+1)} - \Omega_3^{(n)}}{\Delta t} = M_{fl_z}(\mathbf{v}^{(n+1)}, p^{(n+1)}) \quad (3.147)$$

$$I^* \left(\frac{\Omega_+^{(n+1)} - \Omega_+^{(n)}}{\Delta t} - i\alpha \Omega_+^{(n+1)} \Omega_3^{(n+1)} \right) = M_{fl_+}(\mathbf{v}^{(n+1)}, p^{(n+1)}) \quad (3.148)$$

The solution is possible due to the linearity of the dependence of the flow field and of the hydrodynamic forces on the boundary conditions. The latter (Eq. (2.59)) depend linearly on the velocities. As explained in Jenny & Dušek (2004) it is sufficient to compute the residual of Eqs. (2.33 - 2.35) for an intermediate flow field $\mathbf{v}_0^{(n+1)}, p_0^{(n+1)}$ obtained with boundary conditions corresponding to $\mathbf{u}^{(n)}$ and $\mathbf{\Omega}^{(n)}$ at the previous time step:

$$\mathbf{R} = \begin{pmatrix} \mathbf{F}_{fl}(\mathbf{v}_0^{(n+1)}, p_0^{(n+1)}) + \mathbf{k}_{fix} \\ M_{fl_z}(\mathbf{v}_0^{(n+1)}, p_0^{(n+1)}) \\ M_{fl_+}(\mathbf{v}_0^{(n+1)}, p_0^{(n+1)}) \end{pmatrix}. \quad (3.149)$$

The update $\mathbf{X} = (\Delta\mathbf{u}, \Delta\mathbf{\Omega})^T$ results as the solution of a set of 6 equations obtained from Eqs. (3.146 - 3.148) by replacing the updates of forces $\mathbf{F}_{fl}(\mathbf{v}^{(n+1)} - \mathbf{v}_0^{(n+1)}, p^{(n+1)} - p_0^{(n+1)})$ and torques $\mathbf{M}_{fl}(\mathbf{v}^{(n+1)} - \mathbf{v}_0^{(n+1)}, p^{(n+1)} - p_0^{(n+1)})$ by the matrix operation:

$$\left(\begin{array}{c} \mathbf{F}_{fl}(\mathbf{v}^{(n+1)} - \mathbf{v}_0^{(n+1)}, p^{(n+1)} - p_0^{(n+1)}) \\ \mathbf{M}_{fl}(\mathbf{v}^{(n+1)} - \mathbf{v}_0^{(n+1)}, p^{(n+1)} - p_0^{(n+1)}) \end{array} \right) = \mathbf{AX} \tag{3.150}$$

the 6 by 6 matrix $\mathbf{A}$ being obtained by solving the Stokes-like problem of the implicit part of the algorithm with boundary conditions on the body corresponding to unit velocities and angular velocities in the direction of principal axes and by computing the corresponding force and torque. In what follows, we call $\mathbf{A}$ the force matrix. For a fixed mesh, this procedure is to be done just once unless the time step changes. In the present case, it might seem that it has to be repeated at each time step because of the continuous rotation of the spherical sub-domain. It is, however, not necessary to use an exact matrix. Indeed, for sufficiently large density ratio ρ_s/ρ a weak coupling is satisfactory. The weak coupling consists in a fully explicit formulation with $\mathbf{v}^{(n+1)}, p^{(n+1)}$ replaced by $\mathbf{v}_0^{(n+1)}, p_0^{(n+1)}$. This amounts to taking $\mathbf{A} = 0$. The role of the implicit formulation is mainly to account for the acceleration of the fluid due to pressure (added mass) and due to viscosity (effect proportional to the time step).

For the purpose of convergence a sufficient approximation is satisfactory. Following possibilities were tested:

1. The matrix can be created solely on the spherical sub-domain with a zero Dirichlet boundary condition at the interface.

2. The matrix can be computed separately on the large cylindrical domain better representing an unconfined situation, but not accounting for the body rotation

3. Due to the axisymmetry of the computational domain all cases of rotation are covered if the body is rotated continuously by 90 degrees around the axis perpendicular to the axis of the cylindrical domain. If the variation of the obtained matrix elements is not very significant, it may be sufficient to cover the interval of angles $\psi \in [0, \pi/2]$ by a small number of points and to generate the matrix by interpolation for any angle ψ .

As shown in the following section, it is sufficient to compute the matrix for a spherical domain with the polar axis aligned with that of the cylindrical sub-domain because the rotation of the spherical domain has a negligible influence on the results. Moreover, the matrix is practically (almost up to machine precision) diagonal which facilitates its inversion. For simplicity of implementation the alternative 3 with angle $\Psi = 0$ was retained

The $U(1)$ coordinates, the diagonality of the matrix $\mathbf{A}$ and its isotropy in the plane normal to the symmetry axis ($A_{1,1} = A_{2,2}$ and $A_{4,4} = A_{5,5}$) make it possible to avoid matrix inversion in the equations for angular velocity. Indeed, solve, firstly, Eq. (3.147) becoming

$$I^* \alpha \frac{\Delta\Omega_3}{\Delta t} - A_{6,6}\Delta\Omega_3 = M_{fl_z}(\mathbf{v}_0^{(n+1)}, p_0^{(n+1)}) \tag{3.151}$$

and yielding the update $\Omega_3^{(n+1)} = \Omega_3^{(n)} + \Delta\Omega_3$. Secondly, solve Eq. (3.148), i.e.:

$$I^* \left(\frac{\Delta\Omega_+}{\Delta t} - i\alpha\Delta\Omega_+\Omega_3^{(n+1)} \right) - A_{4,4}\Delta\Omega_+ = M_{fl_+}(\mathbf{v}_0^{(n+1)}, p_0^{(n+1)}) + i\alpha\Omega_+^{(n)}\Omega_3^{(n+1)}. \tag{3.152}$$

providing the update $\Omega_+^{(n+1)} = \Omega_+^{(n)} + \Delta\Omega_+$.

The translation velocity equations do not uncouple. An exact solution of Eq. (3.146) is obtained by solving 3 coupled equations:

$$\left(\frac{m^*}{\Delta t} + m^*\mathbf{G} - \mathbf{A}_u\right)\Delta\mathbf{u} \;=\; \mathbf{F}_{fl}(\mathbf{v}_0^{(n+1)}, p_0^{(n+1)}) + \mathbf{k}_{fix} - m^*\omega^{(n+1)} \times \mathbf{u}^{(n)} \tag{3.153}$$

where $\mathbf{A}_u = \mathrm{diag}(A_{1,1}, A_{2,2}, A_{3,3})$ and

$$\mathbf{G} = \begin{bmatrix} 0 & 0 & \Omega_2^{(n+1)} \\ 0 & 0 & -\Omega_1^{(n+1)} \\ -\Omega_2^{(n+1)} & \Omega_1^{(n+1)} & 0 \end{bmatrix}. \tag{3.154}$$

An approximate solution is obtained by treating the u_+ equation

$$m^*\left(\frac{\Delta u_+}{\Delta t} \;-\; i\Omega_+^{(n+1)}\Delta u_z\right) \;-\; A_{1,1}\Delta u_+ \;=\; F_{fl,+}(\mathbf{v}_0^{(n+1)}, p_0^{(n+1)}) + \mathbf{k}_{fix,+} + im^*\Omega_+^{(n+1)}u_+^{(n)} \tag{3.155}$$

explicitly, i.e. by setting $\Delta u_z = 0$ in this equation. The so obtained update $u_+^{(n+1)} = u_+^{(n)} + \Delta u_+$ can be used in equation

$$m^*\frac{\Delta u_z}{\Delta t} \;-\; A_{3,3}\Delta u_z \;=\; F_{fl,z}(\mathbf{v}_0^{(n+1)}, p_0^{(n+1)}) + \mathbf{k}_{fix,z} - m^*\left(\omega^{(n+1)} \times \tilde{\mathbf{u}}^{(n+1)}\right)_z \tag{3.156}$$

where $\tilde{\mathbf{u}}^{(n+1)} = (u_1^{(n+1)}, u_2^{(n+1)}, 0)^T$.

Alternatively, Eq. (3.146) can be solved explicitly by replacing the new velocity $\mathbf{u}^{(n+1)}$ by the old one $\mathbf{u}^{(n)}$ in the term $\omega^{(n+1)} \times \mathbf{u}^{(n+1)}$. This amounts to leaving out the matrix $m^*\mathbf{G}$ on the LHS of Eq. (3.153) and reducing the inversion to a diagonal matrix. All three possibilities were tested and were found to yield indistinguishable results. The simplest, third, alternative was retained.

3.10.2 Results of tests of the computation of the force matrix

The tests of generation of the matrix $\mathbf{A}$ brought the following conclusions for the disc at $G = 100$, $\Delta t = 0.001$ and the radius of the spherical domain equal to one. The results are presented for $\Delta t\mathbf{A}$ because its leading terms (due to pressure effects) are independent of Δt and correspond to added mass coefficients. The element $\Delta t A_{1,1}$ is very close to the added mass of the disc.

1. The matrix is very close to diagonal. The largest non-diagonal element is equal to 1.2 $\times$ 10^{-11} (the largest diagonal element being 0.33).

2. The variation of the matrix due to the rotation of the spherical sub-domain is negligible. The relative variation of its diagonal elements for rotation of the spherical sub-domain

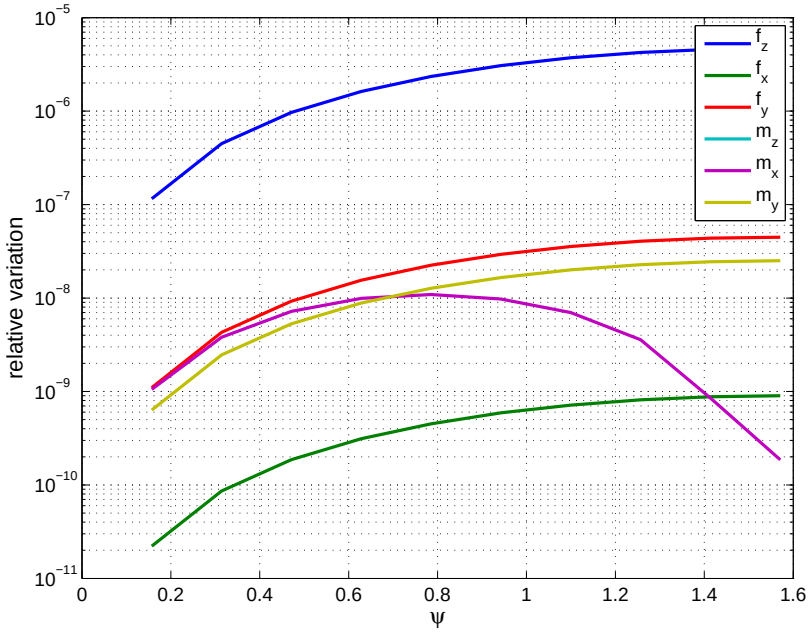

Figure 3.5: Relative variation of diagonal elements of the added mass matrix. The legend indicates the component (f_x, f_y, f_z - force, m_x, m_y, m_z - torque).

about the $x-$axis by angles ψ in the interval $[0, \pi/2]$ is represented in Figure 3.5 for the truncation of the azimuthal and spherical harmonic expansion at the mode 4. The largest relative variation, that of the matrix element $A_{1,1}$ relative to the $z-$component of the force induced by a unit variation of velocity in the $z-$direction, does not exceed 0.5×10^{-5}. This can be explained by a confinement of the acceleration and pressure field essentially inside the spherical domain. This limits the effect of rotation with respect to the cylindrical domain.

3. The length of the spherical harmonic expansion has also a limited effect. Again, this is a consequence of the confinement of the acceleration flow field. Indeed, even if the sub-domains are not rotated with respect of one to the other, the connection at the interface might bring errors if the expansion is truncated at a too low number ℓ. If the flow field does not reach significantly beyond the interface, the expansion has practically no effect. This is actually the case as can be seen if the matrix obtained with the highest mode of expansion $\ell_{max} = 7$ is compared to that obtained for just $\ell_{max} = 1$, the smallest value necessary to capture the hydrodynamic force and torque. The largest relative error is obtained for the $A_{5,5}$ and $A_{6,6}$ elements: 0.28%. For $A_{1,1}$ it is 0.06%.

   This would allow us to re-use the algorithm developed for the sphere where the added mass matrix was computed with the azimuthal expansion truncated to $m \leq 1$. The saving in computing time is, however, negligible in view of the rareness of time step

i	shear and, pressure	pure added mass
1	0.3313	0.3293*
2	0.0034	0
3	0.0034	0
4	0.00049	0
5	0.0111	0.0109
6	0.0111	0.0109

Table 3.2: Diagonal elements of the force matrix $\Delta t A_{i,i}$, $i = 1 \dots 6$ at $G = 100$ and for $\Delta t = 0.001$ ($i = 1, 2, 3$ correspond to added masses and $i = 4, 5, 6$ to 'added moments of inertia'). Middle column values accounting for shear, right column pure pressure effects. *The theoretical value of the added mass of a disc in an infinite domain is 1/3 - see Sherwood & Stone (1997).

updates in an established simulation.

4. The effect of shear is not negligible. In Table 3.2 we present the diagonal elements of the matrix $\Delta t \mathbf{A}$ compared to those of the pure added mass matrix (accounting only for pressure effects).

5. The acceleration field and the associated pressure is represented in Figs. 3.6, 3.7. It is clearly seen that the perturbation hardly extends more than one disc diameter.

The tests show that it is sufficient to compute the matrix of forces $\mathbf{A}$ without accounting for the actual rotation of the sub-domain and, to simplify its inversion, it can be considered as practically diagonal. In real computation these approximations result in negligible degradation of the residual of the movement equations (3.146, 3.147, 3.148) from the machine precision to about 10^{-10}.

3.11 Rotation of the spherical sub-domain and computation of the final velocity and pressure fields

Assuming the moving object to be non-spherical we face the problem of following its movement by the spherical sub-domain. The arbitrary orientation of the spherical sub-domain with respect to the cylindrical one has been described in the static case by the expansion into spherical harmonics. In the case of a freely moving body the issue consists in advancing the sub-domain rotation without deteriorating the accuracy of the solution of the movement equations (3.146, 3.147, 3.148). At the end of a time step, we require that Eqs. (3.146, 3.147, 3.148) be satisfied in the updated frame. As a result, the rotation of the frame of the spherical sub-domain must be carried out before solving the movement equations. The algorithm of the time step runs thus as follows:

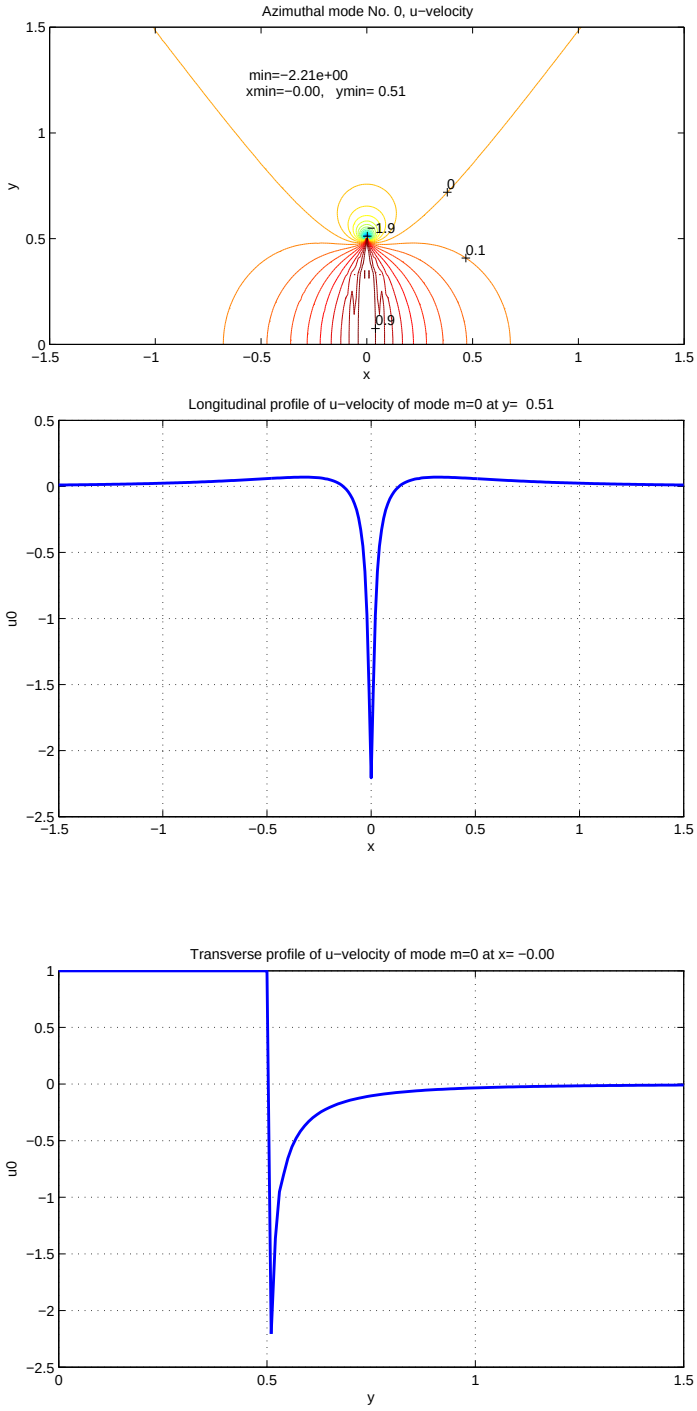

Figure 3.6: The acceleration field generated by a unit acceleration of the disc in the right direction. Upper figure: iso-lines, lower figures: streamwise and transverse profiles.

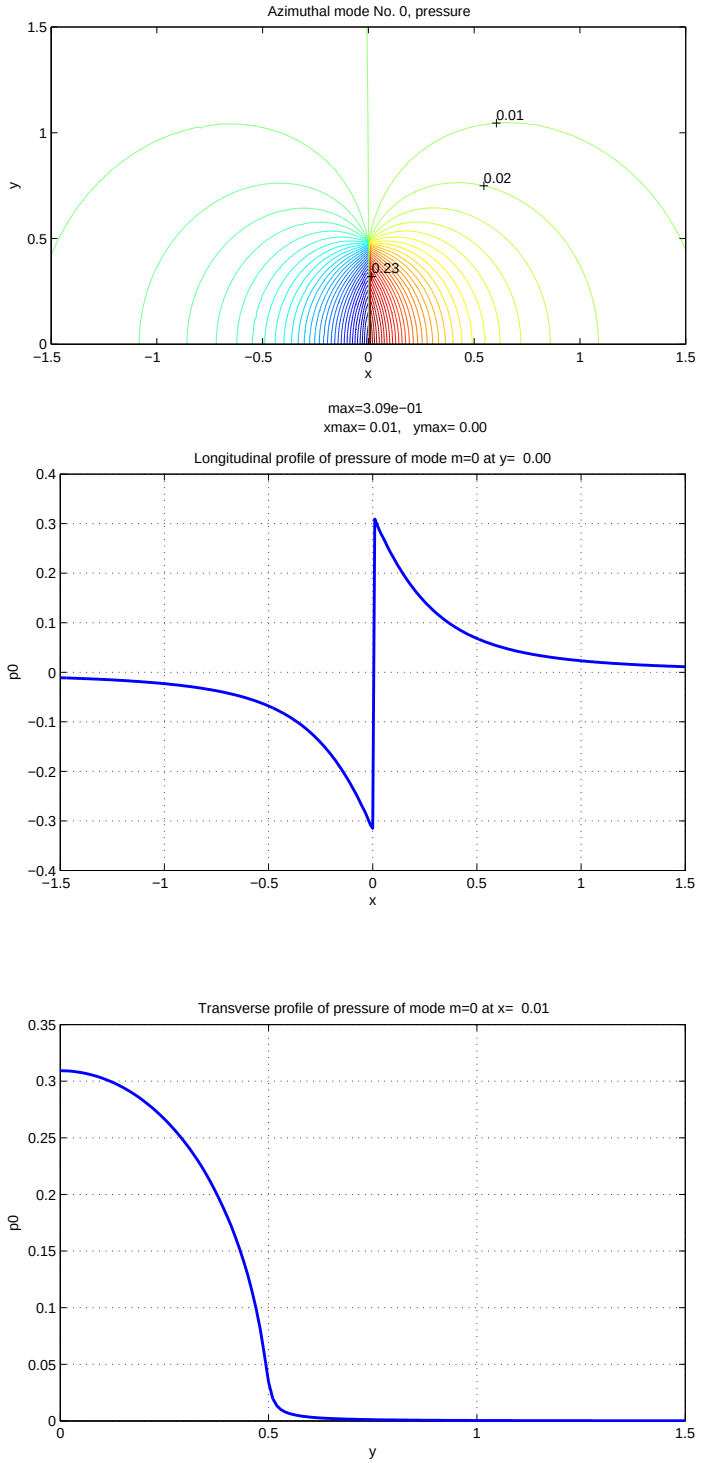

Figure 3.7: The pressure field generated by a unit acceleration of the disc in the right direction. Upper figure: iso-pressure lines, lower figures: streamwise and transverse profiles.

- Compute the advective terms accounting for the domain rotation according to Eq. (2.8). The computation of advective terms is performed in the frame of the previous time-step.

- Rotate the frame of the spherical sub-domain. The rotation is obtained using the angular velocity vector $\mathbf{\Omega}$ of the frame and the time step dt: $\mathbf{n}_j^{(n+1)} = \mathbf{n}_j^{(n)} + dt\mathbf{\Omega} \times \mathbf{n}_j^{(n)}$. This relation holds in the fixed frame and $\mathbf{n}_j$ are columns of the matrix $\mathbf{R}^T$. In the rotating frame, $\mathbf{n}'^{(n)}_j$ are columns of the matrix $\mathbf{R}$. They are rotated using the relation: $\mathbf{n}'^{(n+1)}_j = \mathbf{n}'^{(n)}_j - dt\mathbf{\Omega} \times \mathbf{n}'^{(n)}_j$. This relation corresponds to the linearization of the rotation. The resulting matrix $\mathbf{R}^T = [\mathbf{n}'_1, \mathbf{n}'_2, \mathbf{n}'_3]$ is thus not exactly orthogonal. The orthogonalization is obtained by the Gramm-Schmidt procedure. Then the Euler angles are computed from the matrix $\mathbf{R}$ and the rotation matrices in $\ell \leq \ell_{max}$ subspaces are updated.

- Solve for the velocity and pressure fields with boundary conditions given by the body velocities at the previous time step and compute the new velocities by solving the motion equations of the body as described in Sec. 3.10.1.

- Originally the new velocities were used to define new boundary conditions and the velocity and pressure fields were recomputed by solving the full Stokes problem in the same way as at the previous stage. This doubles, however, the computing costs and is not necessary to do. Instead, it is sufficient to use the fact that the sought solution differs only by the boundary conditions at the body surface. The field updates depend linearly on the updates of the velocities. The relation can be written as (see Jenny & Dušek (2004)): $\Delta\mathbf{U}^{(n+1)} = \mathbf{SX}, \Delta\mathbf{P}^{(n+1)} = \mathbf{TX}$ where $\mathbf{X}$ is the array of six velocity updates ($\Delta\mathbf{U}$, $\Delta\mathbf{\Omega}$) and $\mathbf{S}$ and $\mathbf{T}$ are matrices of flow accelerations that are computed while generating the force matrix $\mathbf{A}$. The matrices $\mathbf{S}$ and $\mathbf{T}$ are stored and used to compute the velocity and pressure field updates directly. The latter are added to the intermediate fields obtained with previous body velocities which yields in updated fields with virtually no additional costs.

3.12 Numerical tests

3.12.1 Fixed disc placed perpendicularly to the flow

A parametric study of the transition scenario in the wake of flat cylinders and spheroids placed perpendicularly to the flow was given in Chrust *et al.* (2010) (see also chapter 4). The mesh represented in Figure 4.1 is practically the same as that used for an infinitely thin disc in Chrust *et al.* (2010), where the dependence on the size of the domain, on the breakup into spectral elements, on the number of collocation points per spatial direction and on the truncation of the azimuthal Fourier expansion were discussed. It was shown that the following parameters: number of spectral elements $N_{el} = 256$ for a disc, $N_{el} = 230$ for a cylinder $\chi = 1$, number of Gauss-Lobatto-Legendre collocation points in each direction (z, r) $N = 6$, number of azimuthal Fourier modes $m = 4$ and upstream, downstream extension as well as the radius

of the cylindrical domain equal to $L_u = 12d$, $L_d = 25d$ and $R_c = 8d$, respectively, yield a precision better than 1% in the determination of the critical Reynolds numbers of the first two bifurcations. In this sub-section, we test the influence of the truncation of the spherical function expansion ℓ_{max} and of the radius of the spherical domain. We compare the critical Reynolds numbers of the primary, regular and of the secondary, Hopf bifurcations obtained with the domain decomposition with those found with the original code used in Chrust *et al.* (2010). The purpose is to show that the interface connecting the decomposed sub-domains does not perturb the computation. The primary bifurcation thresholds are summarized for an infinitely thin disc $\chi = \infty$ and for a thick cylinder $\chi = 1$ in Tables 3.3 and 3.4, respectively. The thresholds depend very weekly on the radius of the spherical sub-domain. It is seen that the truncation of the expansion into spherical functions at $\ell_{max} = 15$ is already sufficient to obtain a better than 1% precision for the infinitely thin disc. The sensitivity to the radius is very likely due to the presence of localized flow structures. This variation (at $\ell_{max} = 15$) is stronger for the thick cylinder. However, very rapidly, with moderately increased ℓ_{max}, virtually the same threshold is obtained independently of the spherical sub-domain radius. For the disc, the obtained critical Reynolds number lies within 0.03% from the value obtained in a computation without domain decomposition. For the thick cylinder of aspect ratio $\chi = 1$ the largest discrepancy for $\ell_{max} = 25$ does not exceed 0.6%. The agreement is even better for the secondary bifurcation threshold.

$R_s \diagdown \ell_{max}$	15	20	25
1.00	117.16	117.13	117.12
1.35	116.55	117.09	117.13
1.70	116.05	117.07	117.13
2.00	116.51	117.33	117.13

Table 3.3: Threshold of the primary bifurcation of an infinitely thin disc $\chi = \infty$ perpendicular to the flow. Influence of the radius R_s of the spherical domain and of the truncation ℓ_{max} of the spherical function expansion on the bifurcation threshold. The threshold of the primary bifurcation obtained with the original code is equal to $Re_I = 117.17$ (see Chrust *et al.* (2010) and chapter 4)

3.12.2 Fixed disc inclined by 30 degrees with respect to the flow direction

The capability of the numerical method to resolve a fully three-dimensional geometry was tested for a fixed disc with its axis inclined by 30 degrees with respect to the flow direction. Iso-lines of the streamwise component of the velocity field are represented in Figure 3.8 at $Re = 120$. The spherical interface (represented by the circle) has a radius of $1d$. At $Re = 120$, the flow oscillates periodically generating an oscillating lift force having a non-zero mean value. The order of the expansion into spherical functions given by $\ell_{max} = 15$ is sufficient to obtain iso-lines that are perfectly smooth across the interface. Figure 3.9 represents iso-surfaces of the streamwise component of the vorticity. Again, the interface

$R_s \diagdown \ell_{max}$	15	20	25	15	25
1.00	274.81	274.06	274.15	358.59	358.78
1.35	265.15	274.43	274.34	–	–
1.70	272.75	275.26	275.26	–	–
2.00	243.19	274.62	275.95	337.2	358.91

Table 3.4: Threshold of the primary (left of the vertical line) and secondary bifurcation of a cylinder $\chi = 1$ perpendicular to the flow. Influence of the radius R_s of the spherical domain and of ℓ_{max} on the bifurcation threshold. Threshold of the primary and secondary bifurcation obtained with the original code is equal to $Re_I = 274.16$ and $Re_{II} = 358.89$. "–" marks non considered cases.

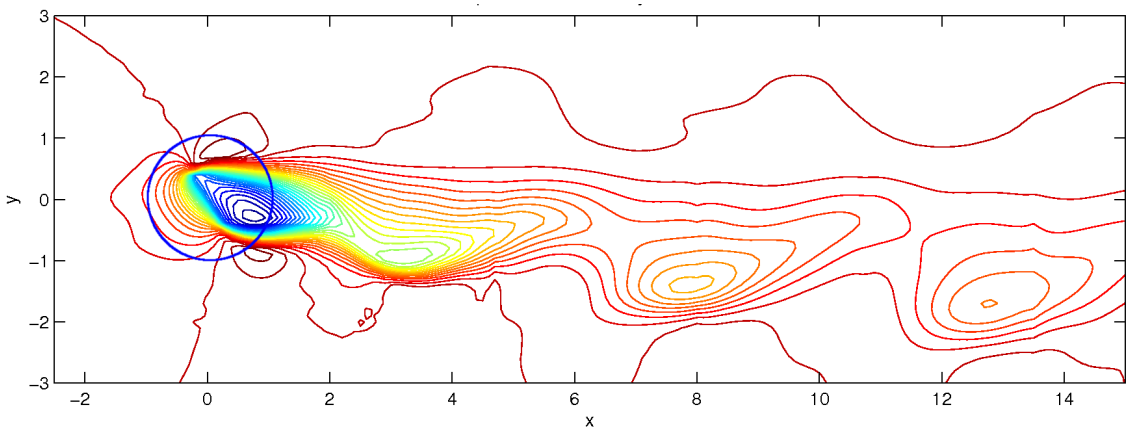

Figure 3.8: Disc $\chi = \infty$, $Re = 120$ inclined by $\varphi = 30^o$ w.r.t. the flow direction. Streamwise component of the velocity field. The circle marks the interface between the two sub-domains. $\ell_{max} = 15$, $R_s = 1$.

between the two sub-domains is not visible, indicating that it does not perturb the flow.

To provide a quantitative test of the numerical sensitivity to the presence of the interface, we report, in Table 3.5, the decay rate for several values of the radius R_s and for two truncations ℓ_{max} of the expansion into the spherical functions obtained close to the threshold of the Hopf bifurcation triggering the oscillations. The variation in the column $\ell_{max} = 25$ corresponds to a maximum error in the determination of the critical Reynolds of ≈ 0.06 as can be inferred from the value of the bifurcation threshold and from the decay rates.

3.12.3 Freely ascending sphere of density ratio $\rho_s/\rho = 0.5$.

In the case of spherical particles, it has become common to define the Galileo number $\widetilde{G} = \sqrt{|\rho_s/\rho - 1|gd^3}/\nu$, that differs by the factor of $\sqrt{\pi/6}$ from the Galileo number defined for discs (Eq. 2.58). In this subsection we mention the Galileo number $\widetilde{G}$ introduced in Jenny *et al.* (2004) with the value of G in parentheses. A sphere of density equal to half that of the

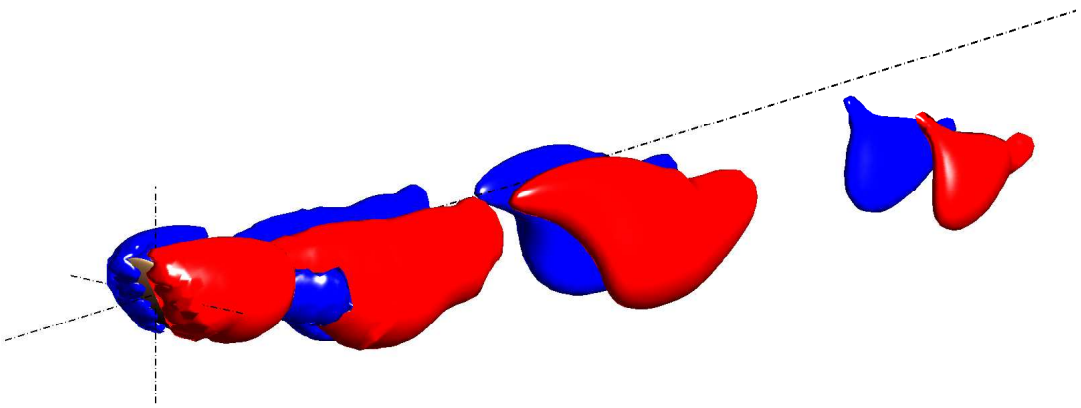

Figure 3.9: Disc $\chi = \infty$, $Re = 120$ inclined by $\varphi = 30^o$ w.r.t. the flow direction. Streamwise component of the vorticity. Isovalue level equal to 0.2. $\ell_{max} = 15$, $R_s = 1$.

$R_s \diagdown \ell_{max}$	15	25
1.00	-0.0346	-0.0339
1.35	-0.0348	-0.0347
1.70	-0.0371	-0.0341
2.00	-0.0362	-0.0343

Table 3.5: Decay rate of the oscillations of the fixed disc inclined by $\varphi = 30^o$ with respect to the free stream direction at $Re = 105$. The bifurcation threshold lies at $Re_{crit} = 110$.

fluid was shown in Jenny *et al.* (2004) to undergo a regular bifurcation at the Galileo number $\widetilde{G} = 156.1$ ($G = 113.0$) leading to a steady oblique regime. At $\widetilde{G} = 173.2$ ($G = 125.3$), a secondary, Hopf bifurcation triggers periodic oscillations and the oblique oscillating regime sets in. At $\widetilde{G} = 178$ ($G = 128.8$) the zig-zagging regime appears intermittently before becoming periodic at higher Galileo numbers. These three regimes were used for testing the new algorithm. The advantage of the spherical body for this purpose is that it can be simulated both in a fixed, non-decomposed domain, and in the decomposed domain. In the latter case, the spherical sub-domain can be considered fixed with an arbitrary orientation with respect to the cylindrical one or moving, following the sphere rotation. This enables a series of very severe tests. The sphere rotation is only due to shear effects. As the result, its time scale is much slower than that of the periodic oscillations, which makes it possible to see the effect of a monotonous rotation of the computational domain in oblique regimes. Moreover, the zig-zagging state was shown to be extremely sensitive to small perturbations (see Jenny *et al.* (2004)), the question is thus if it is faithfully reproduced by the new numerical method.

At the Galileo number $\widetilde{G} = 160$ ($G = 115.8$), the solid-fluid system is just above the

	no interface	$\psi = 0$, $\ell_{max} = 15$	$\psi = 0$, $\ell_{max} = 31$	$\psi = 90^o$, $\ell_{max} = 15$,	$\psi = 90^o$, $\ell_{max} = 31$
u_h	0.0880	0.0857	0.0875	0.0620	0.0892
Ω	0.0158	0.0146	0.0158	0.0112	0.0160

Table 3.6: Sphere $\tilde{G} = 160$ ($G = 115.8$). Fixed spherical sub-domain of radius $R_s = 2$ rotated by angle ψ with respect to the vertical. u_h – asymptotic horizontal velocity, Ω – asymptotic rotation velocity of the sphere.

threshold of the steady oblique regime. In Figure 3.10 (b) the black dashed line represents the settling of the horizontal velocity to its steady non-zero value starting from an initial condition corresponding to the (unstable) vertical ascension. This reference simulation is obtained without domain decomposition. After a short overshoot, the steady state is rapidly reached without practically any secondary oscillations. During the oblique ascension the sphere slowly turns in the plane of the trajectory. If we introduce the domain decomposition and let the spherical sub-domain rotate at the same angular velocity as the solid body itself to simulate a computation necessary for a non-spherical body, we notice a very high sensitivity to the radius for an insufficient spherical function expansion ($\ell_{max} = 15$). This sensitivity is easy to understand especially for the radius $R_s = 3$. In this case, when the rotation angle reaches 90 degrees (see the red full line in Figure 3.10a) the axisymmetry breaking instability decays and the sphere ceases to rotate before, eventually, starting to rotate and to drift in the opposite direction. The reason is the localized intersection of the wake with the interface, which is not sufficiently resolved if the spherical function expansion is truncated at $\ell_{max} = 15$. If the radius of the interface is taken equal to $1d$ (blue full line), the steady oblique regime is quite well captured with only a slight decrease of the horizontal velocity at the moment when the wake leaves the spherical sub-domain perpendicularly to the polar axis. This fact is confirmed in Table 3.6 showing the variation of the obtained value of the horizontal and rotation velocities depending on the orientation of the spherical sub-domain (taken fixed) and on the truncation of the spherical function expansion. The problem is overcome by taking $\ell_{max} = 31$. In Figure 3.10 c) the dashed black line representing the result without domain decomposition is still reported. The red full line, that corresponding to the problematic value of the radius $R_s = 3$, becomes very rapidly horizontal and is close to the value obtained without interface. Table 3.7 provides some quantitative information. It shows, that the initial amplification rates are well captured even for $\ell_{max} = 15$, which is explained by an initial small angle between the polar axis of spherical domain and the vertical direction.

Higher above the threshold, at $\tilde{G} = 170$ ($G = 123.0$), the effect of the domain rotation is still significant for $\ell_{max} = 15$ and $R_s = 3$ (see Figure 3.11 b). This Galileo number still corresponds to the steady oblique regime but it approaches the onset of the secondary – Hopf bifurcation, which makes the decaying oscillations well visible. The average rotation velocity of the sphere is slower (Figure 3.11 a) and when the rotation angle reaches 90 degrees the oscillations are re-excited. Again, the behavior is significantly better for $R_s = 1$. For

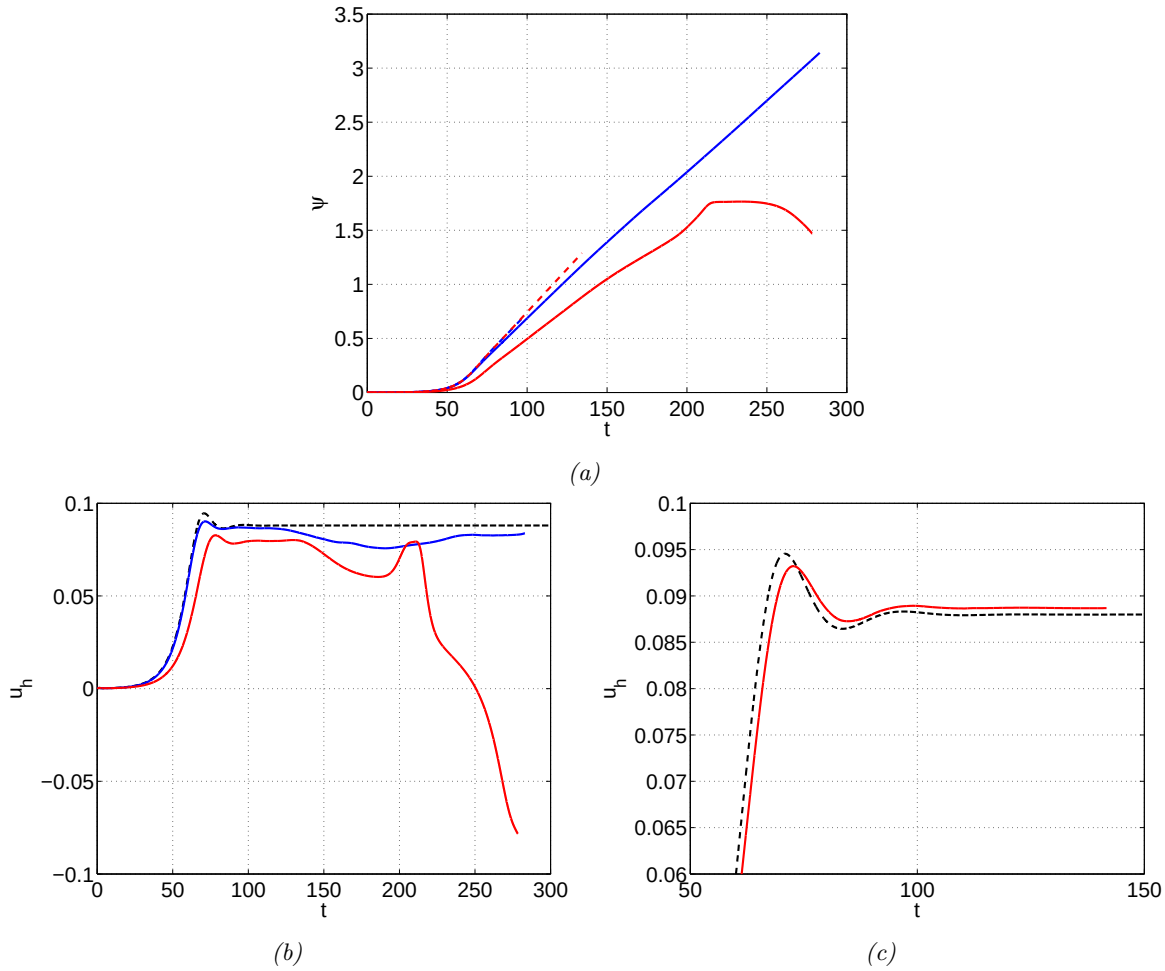

Figure 3.10: Sphere $\tilde{G} = 160$ ($G = 115.8$). a) The rotation angle as a function of time. Red full line: $\ell_{max} = 15, R_s = 3$, red dashed line: $\ell_{max} = 31, R_s = 3$, blue line: $\ell_{max} = 15, R_s = 1$. b) $\ell_{max} = 15$: red line - $R_s = 3$, blue line - $R_s = 1$. Black dashed line: computation without interface. c) $\ell_{max} = 31$, same meaning of lines as in b).

R_s	γ_1	u_h	Δu_h
1.00	0.1054	0.0847	0.0759
	0.1070	0.0858	< 0.0001
2.00	0.1115	0.0860	0.1675
	–	–	–
3.00	0.0990	0.0798	0.1611
	0.1068	0.0887	< 0.0001
no interface	0.1083	0.0880	0

Table 3.7: Sphere $\tilde{G} = 160$ ($G = 115.8$). γ_1 linear amplification rate of the axisymmetry breaking bifurcation, u_h - asymptotic value of the horizontal velocity, Δu_h fluctuation due to the domain rotation. First lines: $\ell_{max} = 15$, second lines $\ell_{max} = 31$.

$\ell_{max} = 31$ the lines corresponding to both $R_s = 3$ and $R_s = 1$ are superimposed on the result obtained without domain decomposition.

R_s	γ_1	γ_2	f_2	u_h	Δu_h
1.00	0.2723	-0.0414	0.0782	0.1425	0.0045
	0.2736	-0.0404	0.0765	0.1456	< 0.0001
2.00	0.2887	-0.0316	0.0811	0.1370	0.0050
	–	–	–	–	–
3.00	0.2739	-0.0283	0.0757	0.1340	0.0040
	0.2746	-0.0405	0.0799	0.1462	< 0.0001
no interface	0.2765	-0.0396	0.0786	0.1465	0

Table 3.8: Sphere $\tilde{G} = 170$ ($G = 123.0$). γ_1 linear amplification rate of the axisymmetry breaking bifurcation, γ_2 linear decay rate of the Hopf bifurcation, f_2 frequency of oscillations, u_h - asymptotic value of the horizontal velocity, Δu_h fluctuation due to the domain rotation. First lines: $\ell_{max} = 15$, second lines $\ell_{max} = 31$.

At $\tilde{G} = 175$ ($G = 126.6$) the regime is oblique oscillating. The insufficient accuracy of the discretization at the interface for $R_s = 3$ and $\ell_{max} = 15$ results in an overestimation of the amplitude and of the period of oscillations. A significant improvement is obtained for $\ell_{max} = 31$. The Tables 3.8 and 3.9 sum up the quantitative data.

The 'zig-zagging' regime is captured for all tested cases of discretization of the interface. Interestingly enough, the sensitivity to the truncation of the spherical function expansion and to the radius R_s is much weaker. This can be, at least partly, explained by the fact that the rotation angle does not exceed 0.23 radians, therefore the spherical sub-domain rotation is very limited.

The results of tests in the configuration of a freely ascending sphere show that ℓ_{max} is the decisive parameter for reaching a good accuracy. The variation of the radius R_s can serve

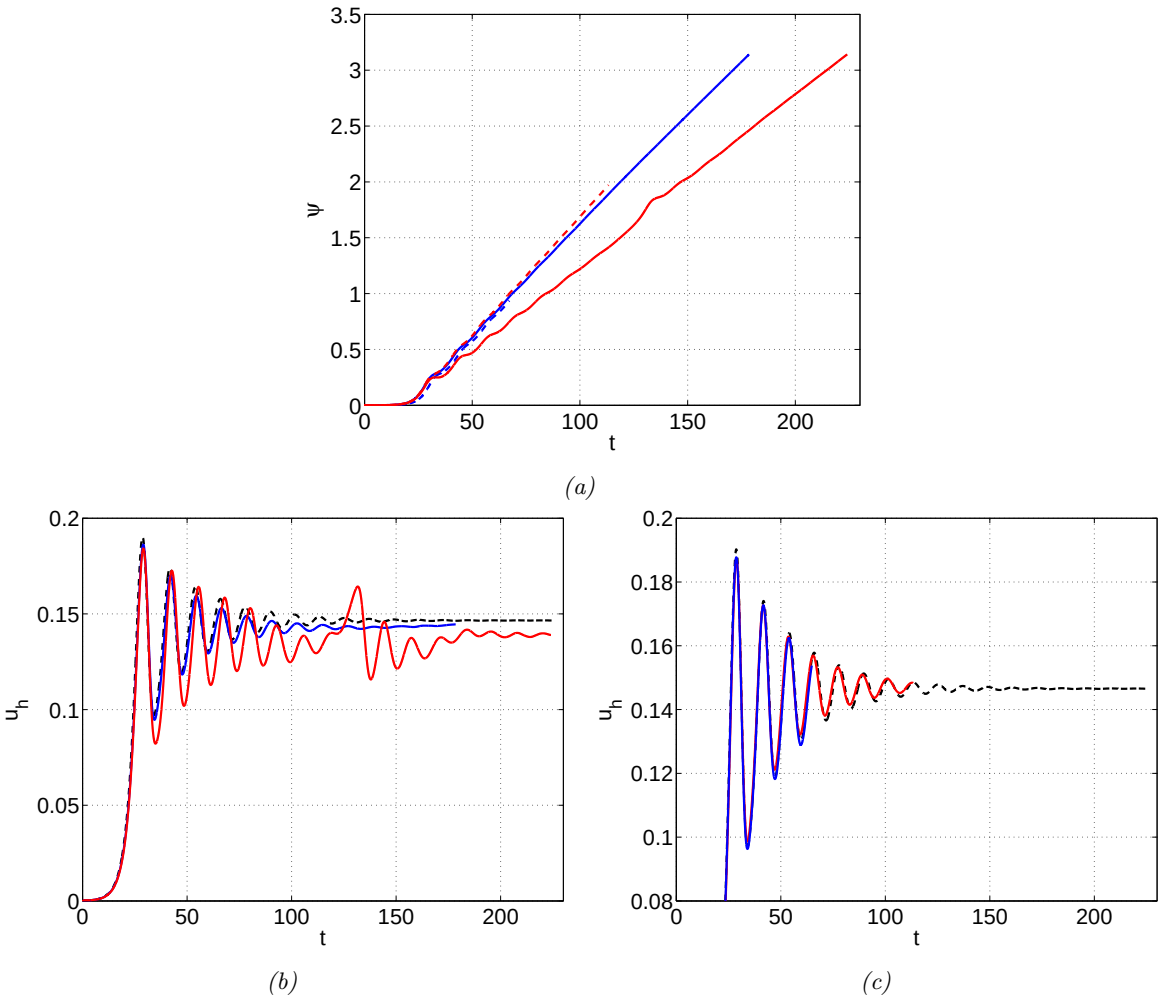

Figure 3.11: $\tilde{G} = 170$ ($G = 123.0$). The meaning of the lines is the same as in Figure 3.10. a) rotation angle, b) horizontal velocity, $\ell_{max} = 15$, c) horizontal velocity, $\ell_{max} = 31$.

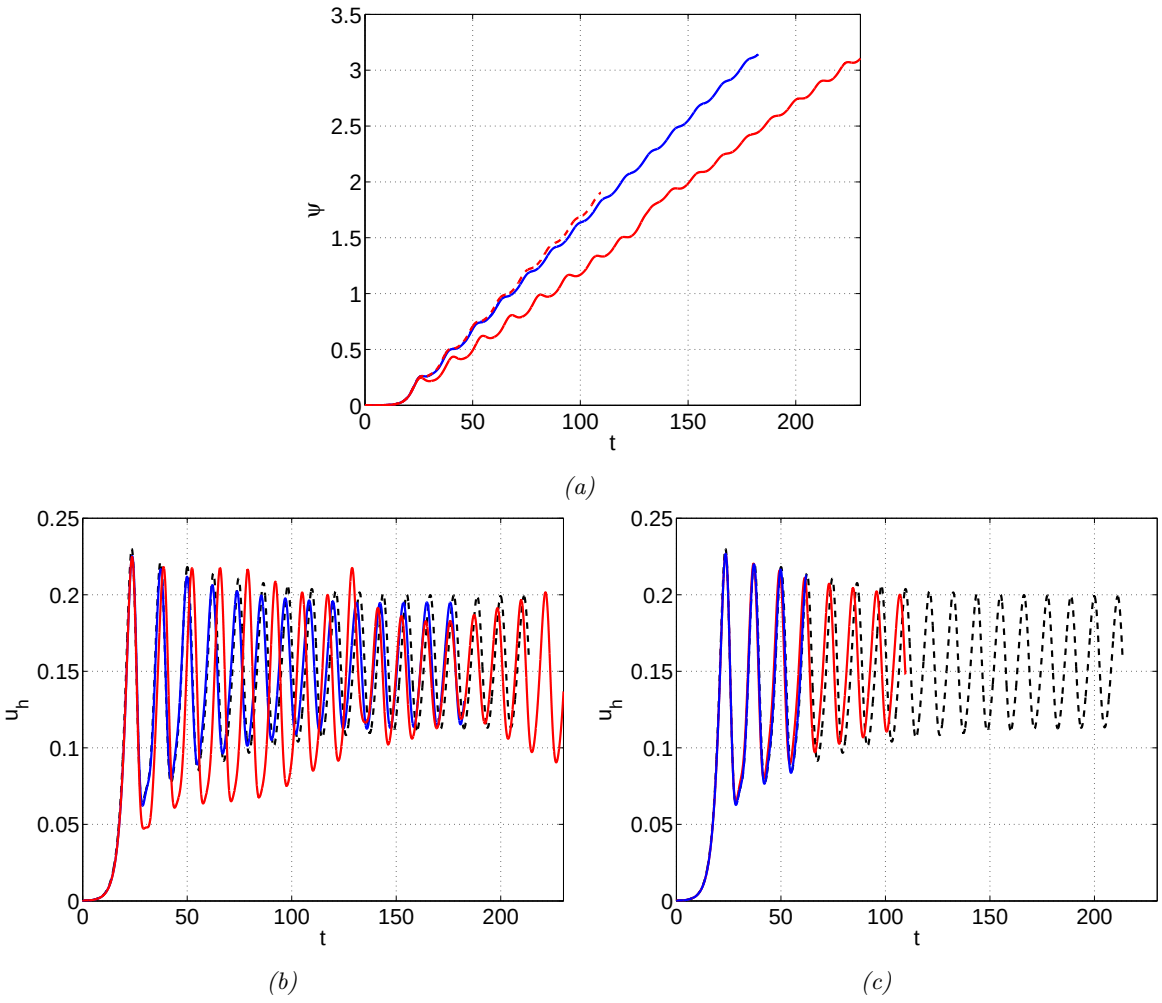

Figure 3.12: $\tilde{G} = 175$ ($G = 126.6$). The meaning of the lines is the same as in Figure 3.10. a) rotation angle, b) horizontal velocity, $\ell_{max} = 15$, c) horizontal velocity, $\ell_{max} = 31$.

R_s	f_2	$\overline{u}_h$	A_{u_h}
1.00	0.0809	0.1544	0.0408
	0.0797	0.1535	–
2.00	0.0791	0.1473	0.0418
	–	–	–
3.00	0.0770	0.1459	0.0539
	0.0818	0.1567	0.0370
no interface	0.0792	0.1560	0.0424

Table 3.9: Sphere $\tilde{G} = 175$ ($G = 126.6$). f_2 frequency of oscillations, $\overline{u}_h$ - mean value of the horizontal velocity, A_{u_h} amplitude of oscillations of the horizontal velocity. First lines: $\ell_{max} = 15$, second lines $\ell_{max} = 31$.

R_s	A_Ψ	A_{u_h}	A_Ω	f_3
1.00, $\ell_{max} = 15$	0.1586	0.3017	0.0577	0.0347
2.00, $\ell_{max} = 15$	0.1367	0.3022	0.0540	0.0354
3.00, $\ell_{max} = 15$	0.1611	0.2854	0.0503	0.0353
3.00, $\ell_{max} = 31$	0.1560	0.3010	0.0552	0.0356
no interface	0.1522	0.2982	0.0544	0.0346

Table 3.10: Sphere $\tilde{G} = 185$ ($G = 133.9$). A_Ψ - amplitude of the rotation angle, A_{u_h} - amplitude of the horizontal velocity oscillations, A_Ω - amplitude of the angular velocity oscillations, f_3 - frequency.

for testing whether ℓ_{max} is large enough for the results to be insensitive to the size of the radius (within reasonable limits, say between 1 and 3).

3.12.4 Freely falling discs and cylinders

The main purpose of the algorithm is to simulate the free movement of non-spherical bodies. The results of tests for a freely falling infinitely thin disc are presented in Tables 3.11 through 3.13. The primary bifurcation of a freely falling disc is of the Hopf type for all values of non-dimensionalized mass m^*. Table 3.11 checks if the domain extent, found sufficient for a fixed disc and for a free sphere, is still satisfactory for a freely falling disc by computing, close to the bifurcation threshold, the amplification rate and the frequency of the flutter of the disc for variable radius R_c of the cylindrical domain, upstream and downstream lengths L_u and L_d, while keeping the radius of the spherical domain and the truncation of the spherical function expansion at the interface fixed. As can be seen, the size of the domain defined by $R_c = 8$, $L_u = 12$ and $L_d = 25$ used already for the sphere is more than sufficient because the maximal difference of the found amplification rates corresponds to a maximal error in the determination of the critical Galileo number of less than 0.1.

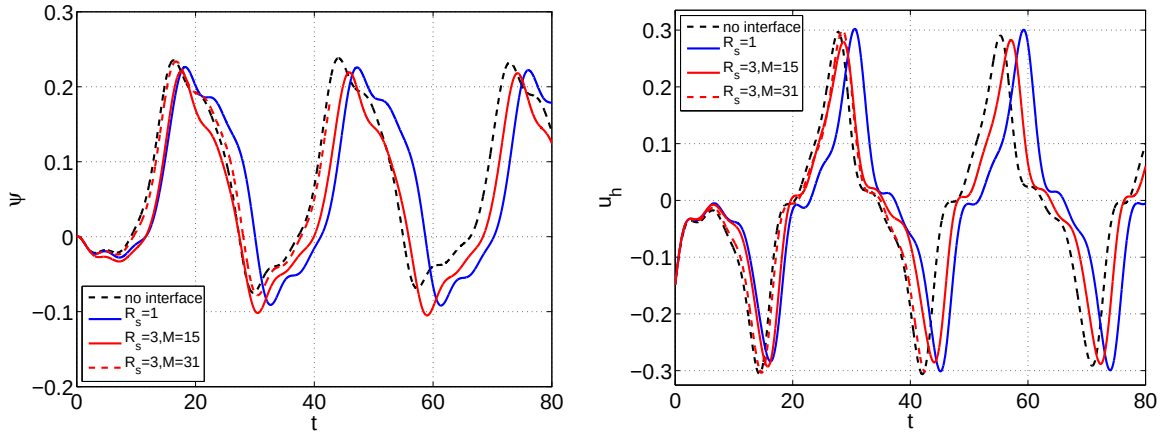

(a) *(b)*

Figure 3.13: Zig-zagging regime at $\tilde{G} = 185$ ($G = 133.9$). (a) Rotation angle as a function of time. (b) Horizontal velocity.

R_c	L_u	L_d	γ	f
8	12	25	0.0359	0.3376
10	12	25	0.0355	0.3375
12	12	25	0.0353	0.3375
8	12	30	0.0359	0.3376
8	12	35	0.0358	0.3376
8	24	25	0.0358	0.3375

Table 3.11: Test of the influence of the extent of the domain for a thin disc $\chi = \infty, m^* = 0.1$, $R_s = 1$, $\ell_{max} = 15$, $G = 70$. The bifurcation threshold lies at $G_{crit} = 64.2$.

Table 3.12 shows the sensitivity of the amplitude and of the frequency of the horizontal velocity of a fully saturated fluttering state to the variation of the radius of the spherical sub-domain and to the truncation of the spherical function expansion at the interface (similarly as for the sphere in the previous sub-section). The same table (last column) shows also their effect on the determination of the bifurcation threshold. Unlike for the sphere, the results are practically insensitive to these parameters, which means that the truncation at $\ell_{max} = 15$ ensures a very good accuracy.

For freely falling discs, very few data are available in the literature. A noteworthy exception is the PhD thesis Auguste (2010) reporting the thresholds for 5 different values of the non-dimensional moment of inertia I^* (i.e., for 5 values of m^*; recall the relation for thin discs: $I^* = m^*/16$). The numerical method of Auguste (2010) is completely different. It is based on a 3D finite volume discretization and uses no domain decomposition. A whole domain rotates with the disc (similarly as in Shenoy & Kleinstreuer (2010) where flat

R_s	$A_{u_h}(G=80)$	$f_{u_h}(G=80)$	G_{crit}
1.00	0.9921	0.3801	64.11
	0.9956	0.3796	64.19
2.00	0.9911	0.3799	64.41
	0.9934	0.3794	64.17
3.00	0.9919	0.3798	–
	0.9934	0.3795	–

Table 3.12: $A_{u_h}(G=80)$ and $f_{u_h}(G=80)$: amplitude and frequency of oscillations of horizontal velocity for a thin disc $\chi=\infty, M^*=0.1$ at $G=80$. G_{crit}: critical Galileo number. Upper lines: $\ell_{max}=15$, lower lines: $\ell_{max}=31$.

cylinders are considered). For this reason, the comparison with the results Auguste (2010) is particularly valuable. The agreement reported in Table 3.13 is very satisfactory.

I^*	Ar_{cr}	Ar_{cr} of Auguste (2010)
0.004	36.15	33
0.012	25.71	24
0.048	16.69	16
0.160	14.64	14
0.480	17.26	14–18

Table 3.13: Primary bifurcation thresholds expressed in terms of the Archimedes number $Ar=\sqrt{\frac{3}{4\pi}}G$ for a thin disc $\chi=\infty$. Third column: values reported in Auguste (2010).

Our method has the capability to simulate all three, experimentally observed Field *et al.* (1997), regimes as can be seen in Figure 3.14. We are able to run simulations up to $G=500$ without any problem of numerical stability for all values of m^*. The numerical performance of the method is very satisfactory. A relevant criterion is given by the computing costs of a physical period of oscillations. The simulation of a period of flutter of a thin disc with 15 azimuthal Fourier modes (and $\ell_{max}=15$) requires only 25% more CPU time than the simulation of a period of an oblique oscillating regime of a sphere with 7 azimuthal Fourier modes and without interface.

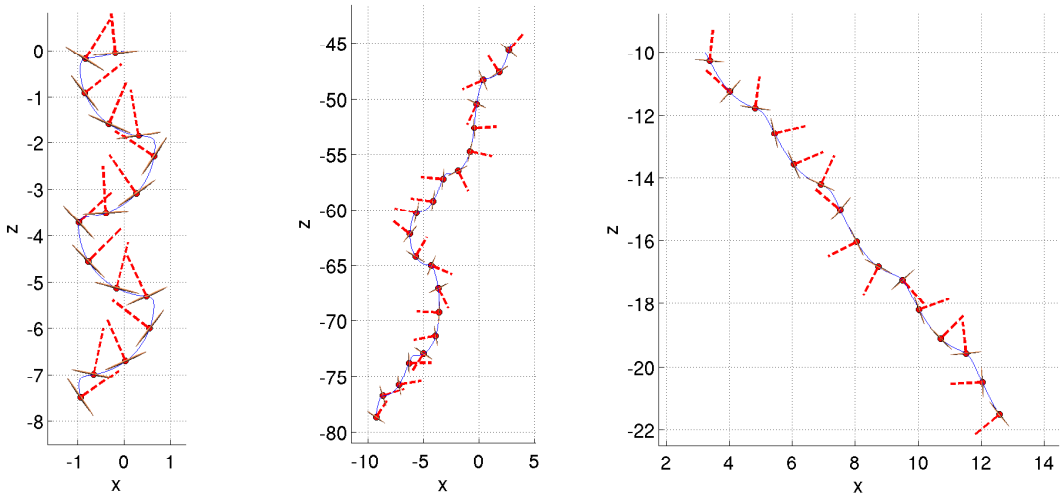

(a), $m^* = 0$, $G = 180$ *(b)*, $m^* = 0.25$, $G = 110$ *(c)*, $m^* = 0.5$, $G = 140$

Figure 3.14: Side view of plane trajectories of thin discs: (a) periodic zig-zag path, (b) intermittent regime, (c) tumbling (auto-rotation) of a disc. The red dashed line marks the direction of a half axis of the disc, which makes it possible to distinguish the tumbling from a flutter.

Chapter 4

Parametric study of the transition in the wake of oblate spheroids and flat cylinders

The content of this chapter was published in Chrust et al. *(2010).*

4.1 Known facts

The present section sums up bibliographic data already discussed in chapter 1 with special focus on the wakes of oblate spheroids and flat cylinders. Such rearrangement helps in understanding the motivation of the described investigation.

The pioneering linear analysis of the breaking of axisymmetry in wakes of axisymmetric bodies of Natarajan & Acrivos (1993) focused on two prototypical bodies: a sphere and a disc. While the wake of a sphere has been the topic of extensive experimental research, that of a thin disc and that of flat cylindrical bodies has been taken up only in a handful of recent, mostly numerical and theoretical papers presented in section 1.6 of the introduction chapter. Let us recall that the geometry of flat cylinders and oblate spheroids is characterized by a single dimensionless parameter - the aspect ratio χ. For a cylinder, it is defined as $\chi = d/h$ where d is the cylinder diameter and h the cylinder height. A 'thin disc' is considered to correspond to an infinite aspect ratio while if the body is cylindrical with non-zero height it will be called flat cylinder if $\chi > 1$. For an oblate spheroid, the aspect ratio is defined as $\chi = d/a$ (with d the diameter and a the length of the polar axis). For fixed bodies, the limit of infinite aspect ratio describes the same configuration, that of a thin disc, both for spheroids and cylinders.

The existing results have shown that the transition scenario in the wakes of discs and flat cylinders of a large aspect ratio differs considerably from that of the fixed sphere wake. The transition process involves several new states that do not exist in the sphere wake. While for the case of a sphere, the secondary Hopf bifurcation leading to a periodic state, conserves the symmetry plane selected at the primary bifurcation (see chapter 1.5), for the case of a disc the secondary bifurcation, also of the Hopf type, breaks the symmetry of the

flow (see Figure 1.9 representing the axial vorticity of the wake). The symmetry of the flow can be more simply understood by representing the lift vector in the plane normal to the flow direction. Although the mean lift lies in the symmetry plane chosen arbitrarily at the first bifurcation, the oscillating component is perpendicular (see Figure 4.9 below). We shall call this state *periodic state without planar symmetry*. In the literature, it has been called RSB (reflectional symmetry breaking) by Fabre *et al.* (2008), MM_π (mixed mode with phase π) state by Meliga *et al.* (2009), 'steady 3D periodic with regular rotation of the separation region' by Shenoy & Kleinstreuer (2008) or 'yin-yang' by Auguste *et al.* (2010). With increasing of the Reynolds number the mean value of the lift decreases until it vanishes. This leads to a periodic state with planar symmetry. This new *periodic state with a zero mean lift* has, however, a symmetry plane perpendicular to that selected at the first bifurcation (see Figure 1.10) unlike for the wake of a sphere. Subsequently the wake becomes chaotic. All these states are characterized by the absence of helicity explained (see Danaila *et al.* (1998), Meliga *et al.* (2009), Fabre *et al.* (2008) and section 1.4) by an equal amplitude of modes with positive and negative helicity. For cylinders of intermediate aspect ratio states with non-zero net helicity have also been reported. We shall call them *state with non-zero helicity*. They are absent both in the transition scenario of a sphere and of a thin disc. Auguste *et al.* (2010) finds them for a flat cylinder of aspect ratio $\chi = 3$. The state described by Auguste *et al.* (2010) is marked by the presence of two characteristic time scales. The helicity yields an elliptic path of the lift (on the time scale of the vortex shedding), which itself moves periodically in the plane perpendicular to the flow axis (on a slow time scale). Therefore the lift path can be described as a slowly oscillating ellipse (see Figure 4.15 below).

The theoretical works of Fabre *et al.* (2008) and Meliga *et al.* (2009) shed light on the underlying non-linear interactions explaining the transition scenario of flat axisymmetric bodies. As mentioned in section 1.6 this configuration is characterized by two parameters: the aspect ratio and the Reynolds number. The existing bibliography does not provide an exhaustive investigation of this parameter space for cylinders and the case of spheroids has never been studied excepting Zastawny *et al.* (2012) who have carried out Direct Numerical Simulations of oblate spheroids, perpendicular and inclined to the incoming uniform flow direction, of the aspect ratio $\chi = 5$, 2.5 and 1.25. However, they do not provide the details of the transition scenario, as their purpose was to derive the correlations for the lift, drag and torque coefficients. For flat cylinders the parametric study of the first two bifurcation thresholds of Fernandes *et al.* (2007) can be improved, extended and refined with account of the progress in identification of more complex regimes. The linear analysis of Natarajan & Acrivos (1993) takes up the thin disc and a sphere as two extreme cases. The link between them is represented rather by oblate spheroids than by flat cylinders.

4.2 Specificities of numerical implementation

We consider fixed cylinders and oblate spheroids, characterized by the aspect ratio χ defined in the previous section, placed with their rotation axis parallel to a uniform flow. The flow of an incompressible fluid past these bodies is governed by the non-dimensionalized three-

dimensional Navier-Stokes equations (2.3) and (2.4) depending on the Reynolds number (2.5).

The equations are solved in a cylindrical coordinate system (z, r, θ), with the z-axis parallel to the free-stream direction, r the distance to the axis and θ the azimuthal angle. The equations 2.3 and 2.4 are discretized using the spectral–spectral-element discretization of Ghidersa & Dušek (2000). (Its review is presented in chapter 3.1.) The method combines the Fourier expansion in the azimuthal direction with a spectral-element discretization in the axial-radial (z, r)-plane. The cylindrical computational domain of radius $R = 8d$ extends $12d$ upstream and $25d$ downstream of the considered objects. The extent of the domain has many times been tested in previous work. It must account for flow conditions depending on the considered Reynolds numbers. E.g. for low Reynolds numbers much larger domains must be used (see e.g. Kotouč *et al.*, 2009*a*). At Reynolds number exceeding 100 the mentioned domain dimensions together with no-stress boundary conditions at the outflow and lateral boundary were, however, always found to be sufficient. This was tested by determining the instability thresholds. The extent of the domain was shown to guarantee an error smaller than one percent of the obtained critical Reynolds numbers. The $(z - r)$-plane is broken up into spectral elements with N Gauss-Lobatto-Legendre collocation points in each direction (z, r). An example of the break up of the axial-radial plane into spectral elements is presented in Figure 4.1. The azimuthal direction is discretized by Fourier expansion. The flow is forced by a uniform Dirichlet boundary condition at the inflow basis of the cylindrical domain.

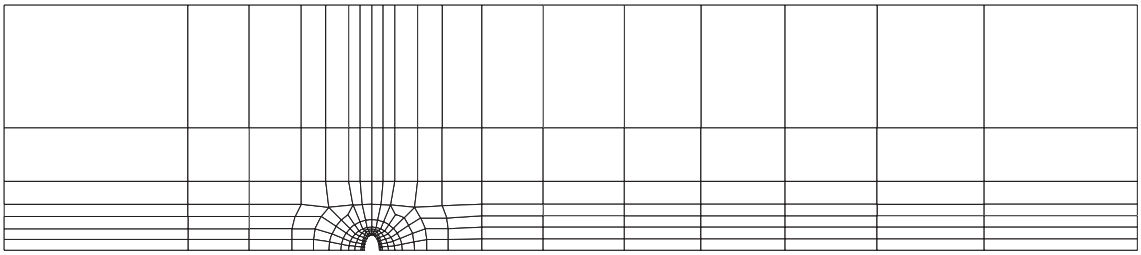

Figure 4.1: Spectral element discretization of the radial-axial plane of the computational domain of an oblate spheroid of χ=2. The inflow is situated at left. The cylindrical computational domain of radius $R = 8d$ extends $12d$ upstream and $25d$ downstream.

The spectral-element break-up of the $(z - r)$-plane had to be adapted to the new configuration. Especially for that of the thin disc and for the cylindrical bodies for which the flow conditions at the body surface differ from that of a sphere. The mesh had to be refined close to the sharp edges to accurately capture the sharp gradients. The mesh modifications as compared to the mesh presented in Ghidersa & Dušek (2000) are limited roughly to a domain of radius $1d$. Figure 4.2 presents the details of the mesh in the close surrounding of an infinitely thin disc. As can be noticed, the mesh is well refined in the vicinity of the tip of the disc in order to correctly resolve the resulting steep gradients. At the same time, it is to be noted that the time step, and therefore the simulation cost, depends directly on the size of the smallest mesh element. They are linked through the Courant–Friedrichs–Lévy condition

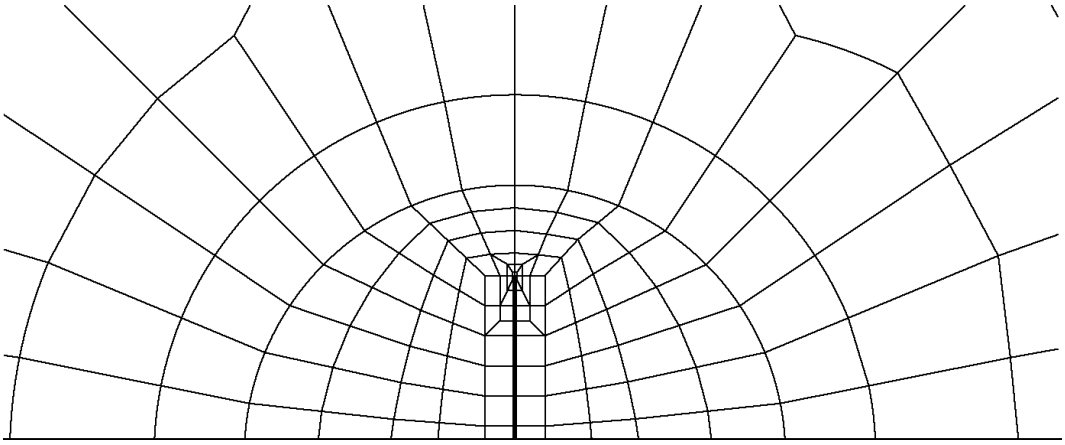

Figure 4.2: The details of the mesh for a disc ($\chi = \infty$). The disc is marked by a thick black line. The mesh is well refined in the proximity of the disc.

that has to be fulfilled to assure the stability of our time discretization scheme treating the advective terms explicitly using the third order Adams-Bashforth scheme. Figures 4.3 and 4.4 present the details of the mesh used for flat cylinders of the aspect ratio $\chi = 6$ and 1. Figure 4.5 shows the details of the mesh used for a thin, while figure 4.6 presents the mesh used for a thick oblate spheroid of the aspect ratio $\chi = 6$ and 1.25, respectively. Details of the meshes for intermediate aspect ratios are omitted due to their similarity to the cases presented above. For each considered configuration several meshes have been developed and tested for the dependence of the primary and secondary thresholds on the number of collocation points. A bad mesh yields a solution sensitive to the refinement within spectral elements. The retained meshes contain 199 – 241 elements. Table 4.1 indicates the number of spectral elements used to discretize the axial-radial plane of the computational domain for flat cylinders and oblate spheroids depending on their aspect ratios. Let us mention that the case of infinite aspect ratio is treated as an object of exactly zero thickness. For this purpose, a slight adaptation of the code was necessary to uncouple spectral elements separated by the line representing the solid object (see Figure 4.2).

The numerical tests consisted in determining the influence of the number of the Gauss-Lobatto-Legendre collocation points N on the first and second bifurcation threshold and the influence of the number of azimuthal modes m on the secondary instability threshold. The results for the thin disc are presented in Table 4.2. They show that 6 collocation points and an azimuthal expansion truncated at $m = 4$ provide values that are almost insensitive to further mesh refinement and that agree with bibliographic data. The precise thresholds of the primary and secondary bifurcations were obtained by post-treating the transients of the simulations carried out in their proximity. In particular, we extract the decay/growth rates immediately below/above the threshold and we subsequently estimate the threshold be the linear interpolation. Alternatively, the growth rates of the primary bifurcation were computed by solving the eigenvalue problem for the linearized Navier-Stokes

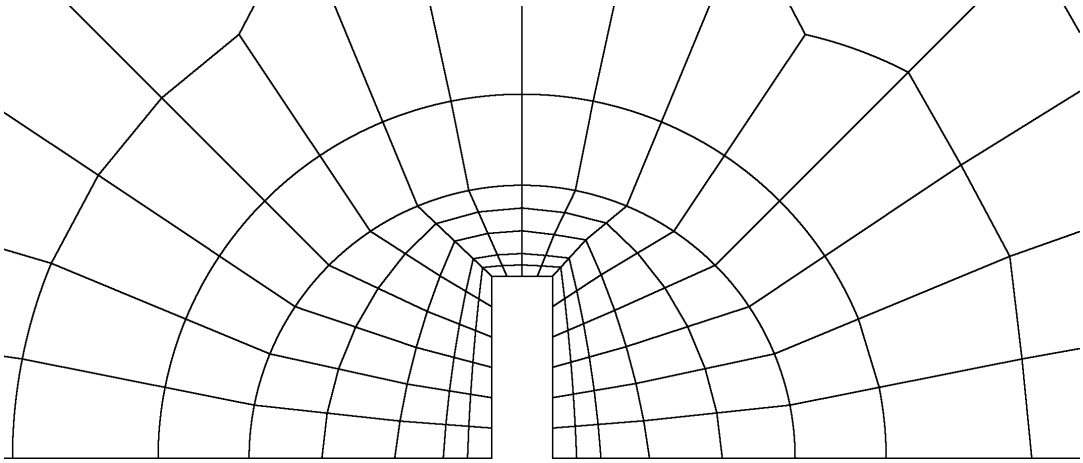

Figure 4.3: The details of the mesh for a flat cylinder of the aspect ratio ($\chi = 6$). The mesh is well refined in the proximity of the cylinder.

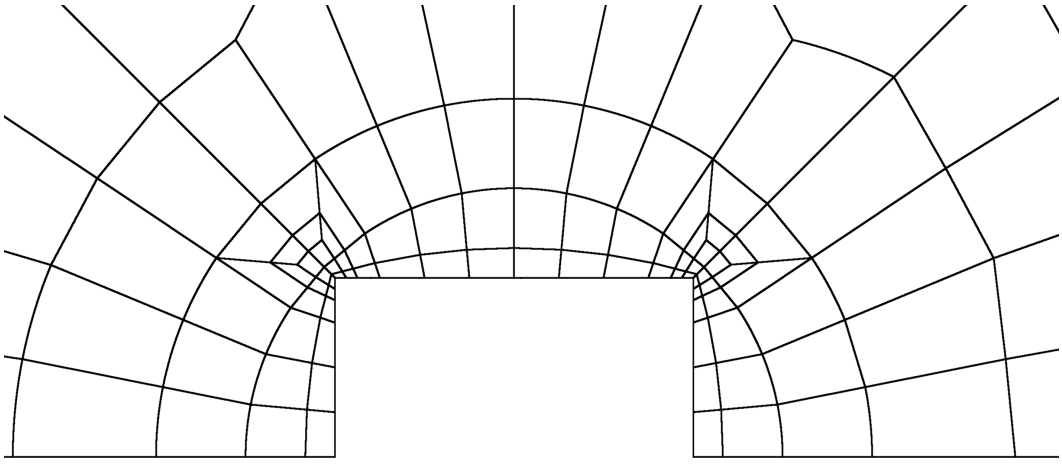

Figure 4.4: The details of the mesh for a thick flat cylinder of the aspect ratio ($\chi = 1$). The mesh is refined in the proximity of the corners of the cylinder.

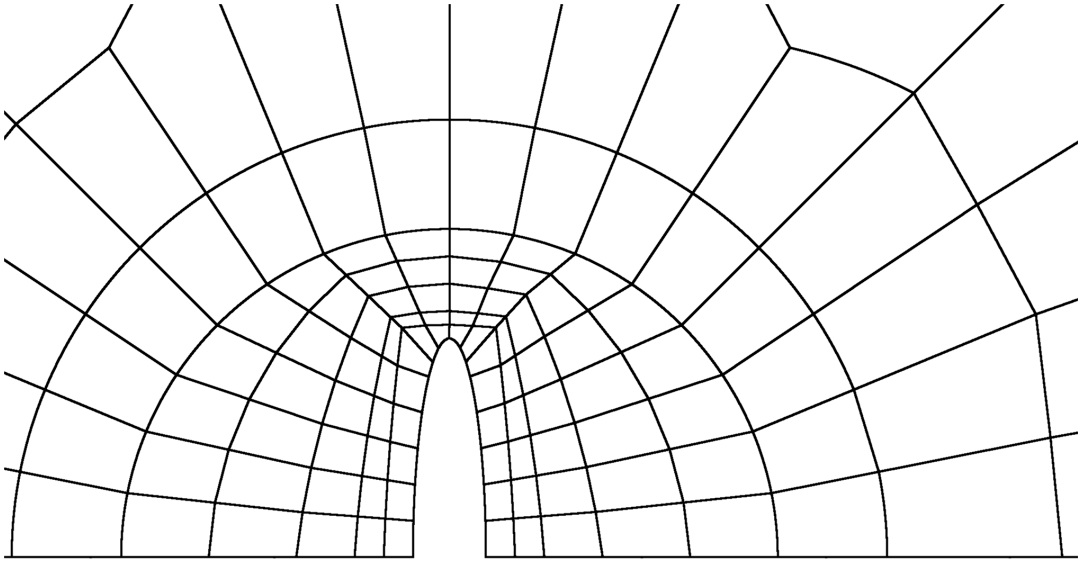

Figure 4.5: The details of the mesh for a thin oblate spheroid of the aspect ratio ($\chi = 6$). The mesh is refined close to the equator of the spheroid.

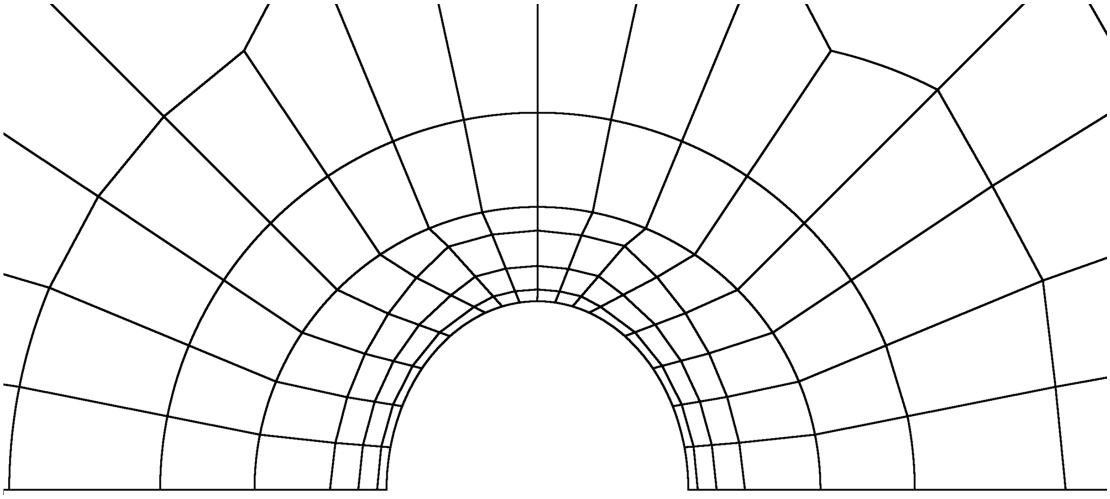

Figure 4.6: The details of the mesh for a thin oblate spheroid of the aspect ratio ($\chi = 1.25$). The mesh is refined at the surface of the spheroid to resolve the boundary layer and its detachment.

χ	cylinders	oblate spheroids
∞	249	249
6	231	231
4	223	–
3	227	215
2.25	223	215
2	231	215
1.92	–	215
1.85	–	215
1.8	219	215
1.5	227	199
1.25	–	215
1	215	215

Table 4.1: Number of spectral elements used for the discretization of the axial-radial plane of the computational domain for flat cylinders and oblate spheroids depending on their aspect ratios.

	N=6		N=8	
Re_1	117.17		116.92	
Re_2	125.18 (4)	125.15 (6)	125.12 (4)	125.11 (6)

Table 4.2: Mesh test results for a thin disc. The values in brackets indicate the number of azimuthal modes of a Fourier expansion. (N stands for the number of collocation points in spectral elements.) Re_1 denotes the critical Reynolds number of the primary bifurcation, Re_2 that of the secondary bifurcation.

equations obtained by limiting simply the azimuthal expansion to the mode $m = 1$ as explained in Ghidersa & Dušek (2000). The matrix of the problem is stored in sparse form and the least stable eigenvalue is determined by the shift-invert Arnoldi method in Matlab. Both approaches, that of monitoring the transients and the eigenvalue computation, yield exactly the same result but the eigenvalue computation is much more efficient.

4.3 Results

4.3.1 Transition states

In chapter 1.6 we listed seven states (*(a)* through *(g)*) that have been described in the bibliography as representing the stages of transition in the wake of thin discs. The transition stages we observed in the wake of oblate spheroids are very similar. The parametric investigation presented below (see the two following subsections) shows that the classification of chapter 1.6 is valid for the whole parameter domain investigated for oblate spheroids, namely $\chi \geq 1$.

We provide sample illustrations of analogs of the states reported in the bibliography on cylindrical bodies in the case of oblate spheroids. Converged states obtained after the decay of transients are represented. The time evolution (including the transients) was monitored by plotting the three components of the hydrodynamic force and the flow field at several points of the wake. The lift coefficient is represented in the figures as best illustrating the nature of the states.

Figure 4.7 presents the iso-contours of the streamwise component of the vorticity for an oblate spheroid of the aspect ratio $\chi = 1.25$ at the Reynolds number $Re = 225$. The wake is steady and planar symmetric. It resembles the *steady non-axisymmetric* state found for a sphere, discs and cylinders. The symmetry plane is selected by an initial condition. The breaking of initial axisymmetry yields a non-zero lift oriented in the plane of symmetry. The wake is characterized by the presence of the two counter-rotating vortices.

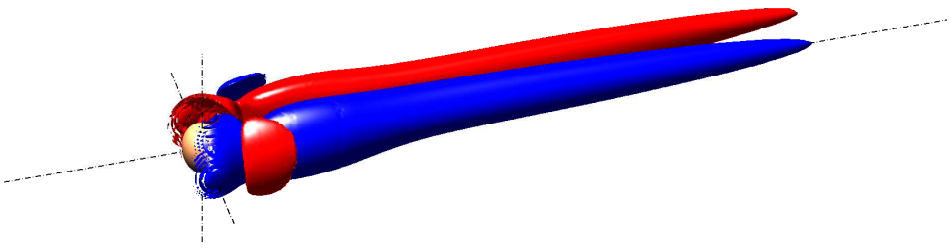

Figure 4.7: Steady asymmetric state *(a)*. Iso-contours of the streamwise component of the vorticity. Oblate spheroid $\chi = 1.25$, $Re = 225$.

Similarly as for a disc and thin cylinders, the *periodic state without planar symmetry - (b)* was found for thin oblate spheroids. Figure 4.8 presents the iso-contours of the streamwise component of the vorticity for an oblate spheroid of the aspect ratio $\chi = 6$ and the Reynolds number $Re = 145$. The steady asymmetric state is replaced via a Hopf bifurcation, by the unsteady state without the plane of symmetry. The mean lift lies in the symmetry plane selected at the first bifurcation but oscillates in the perpendicular plane, as shown in Figure 4.9.

For thick spheroids, we found the *periodic state with a planar symmetry - (c)* characterized by the lift force oscillating with a non-zero mean value in the symmetry plane selected at the first bifurcation as was observed many times in the sphere wake (Johnson & Patel, 1999) and more recently for a cylinder of aspect ratio $\chi = 3$ by Auguste *et al.* (2010). The axial vorticity of the wake of this state is represented in Figure 4.10. Note that the vortical structures in Figure 4.10 are shifted upward with respect to the flow axis. This yields a non-zero mean lift in the plane of the figure. The projection of the lift coefficient on the plane perpendicular to the free stream direction is plotted in Figure 4.11.

Similarly as for thin cylinders, for thin oblate spheroids, we found that the mean lift of the *periodic state without planar symmetry - (c)* decreases with the increase of the Reynolds

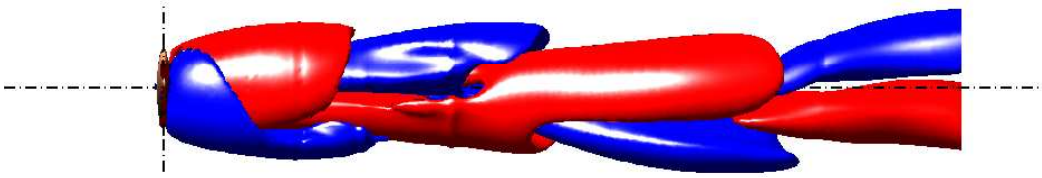

Figure 4.8: Periodic state without planar symmetry *(b)*. Iso-contours of the streamwise component of the vorticity. Oblate spheroid $\chi = 6$, $Re = 145$.

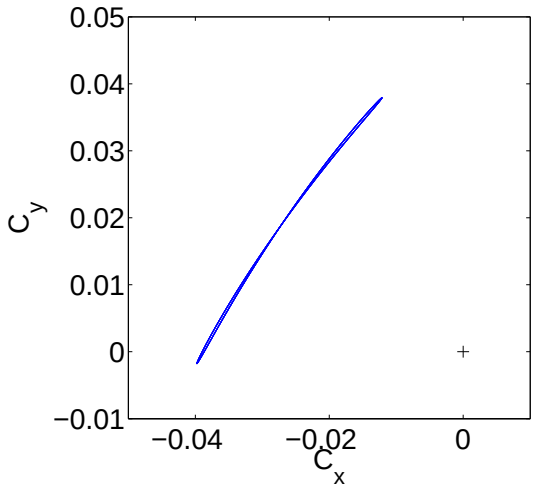

Figure 4.9: Periodic state without planar symmetry *(b)*. Projection of the lift coefficient on the plane perpendicular the the body symmetry axis. The mean lift has a non-zero value. The lift oscillations are in the plane perpendicular to the symmetry plane selected at the primary bifurcation. Oblate spheroid $\chi = 6$, $Re = 145$. The cross marks the point of the zero lift.

number until the *periodic state with a zero mean lift - (d)* is reached. The new state has a plane of symmetry, however, this plane is perpendicular to the symmetry plane selected at the primary bifurcation. The wake oscillates with a zero mean lift. The axial vorticity of the wake is visualized in Figure 4.12. The vortical structures are shedded symmetrically below and above the flow axis represented by the dashed line. The projection of the lift coefficient on the plane perpendicular to the free stream direction is plotted in Figure 4.13. The simulation was obtained by letting the state represented in Figure 4.9 evolve from $Re = 145$ to $Re = 183$. In figure 4.14 we represent these two states, the *periodic state without planar symmetry* at $Re = 145$ and the *periodic state with a zero mean lift* at $Re = 183$ as well as

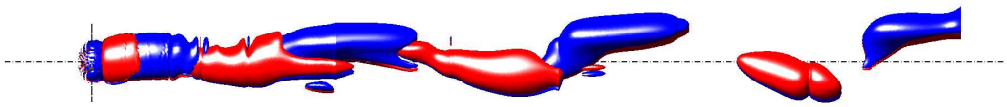

Figure 4.10: Periodic state with planar symmetry *(c)*. Iso-contours of the streamwise component of the vorticity. Oblate spheroid $\chi = 1.25$, $Re = 268$.

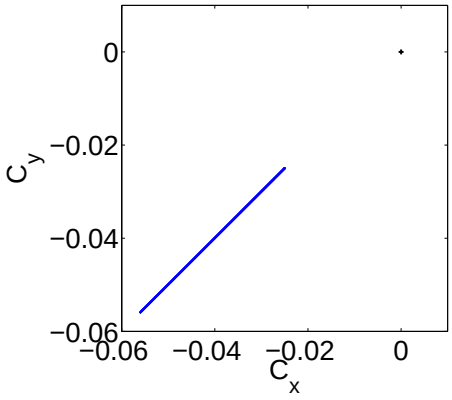

Figure 4.11: Periodic state with planar symmetry *(c)*. Projection of the lift coefficient on the plane perpendicular to the body symmetry axis. The mean lift has a non-zero value. The symmetry plane selected at the first bifurcation is conserved. Oblate spheroid $\chi = 1.25$, $Re = 268$.

the *steady asymmetric* state at $Re = 135$. While, the symmetry plane was oriented roughly -45 degrees with respect to the horizontal axis at $Re = 135$, its position is given by an angle of +45 degrees at $Re = 183$.

We also evidenced the *state with non-zero helicity - (e)* for oblate spheroids of intermediate aspect ratios $1.1 < \chi < 2.2$. As already mentioned, the state with non-zero helicity was reported only once as the 'knit-knot' mode at $\chi = 3$ and $Re = 187$ in the wake of a cylinder (Auguste *et al.*, 2010). Many cases of similar states have, however, been evidenced in the opposing flow past a heated sphere at moderate Richardson numbers by Kotouč *et al.* (2009*b*). As a rule, the domain of stability of purely bi-periodic states is very restricted. The main period is the 'leading frequency' of vortex shedding linked to the Hopf bifurcation and the secondary one the (sometimes very slow) frequency characteristic for the 'migration' of

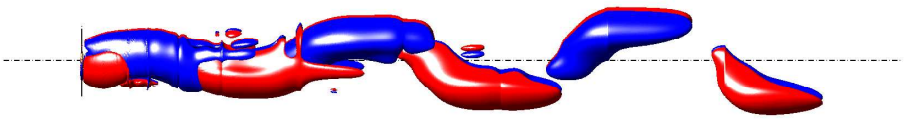

Figure 4.12: Periodic state with a zero mean lift *(d)*. Iso-contours of the streamwise component of the vorticity. Oblate spheroid $\chi = 6$, $Re = 183$.

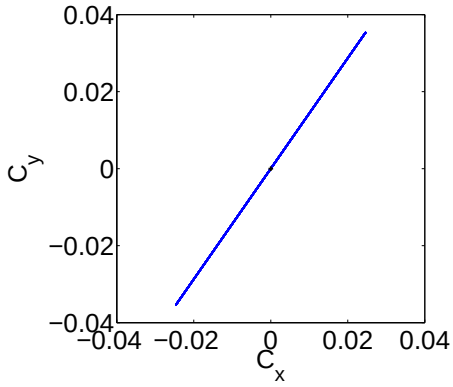

Figure 4.13: Periodic state with a zero mean lift *(d)*. Projection of the lift coefficient on the plane perpendicular to the body symmetry axis. The mean lift has a zero value. The symmetry plane is perpendicular to the symmetry plane selected at the first bifurcation. Oblate spheroid $\chi = 6$, $Re = 183$.

the ellipse representing the projection of the lift onto the plane perpendicular to flow axis at the scale of one vortex shedding period. The states of non-zero helicity have usually more complicated quasi-periodic dynamics before becoming chaotic. Very often, at least in the opposing flow past a sphere, the ellipse is very flat which means that there still remains a slightly distorted symmetry plane of the wake. The latter either slowly oscillates or rotates (see Figure 19 of Kotouč *et al.* (2009*b*)). In the case of oblate spheroids we evidenced both a rotating (see Figure 4.16 for $\chi = 1.25$ $Re = 283$) and oscillating version (see Figure 4.17 for $\chi = 1.85$ $Re = 190$) of the state with non-zero net helicity. In the 'rotating' case the path of the lift describes an ellipse slowly rotating with constant angular velocity in one direction, in the 'oscillating' case, its rotation stops and reverses back so that the ellipse axis oscillates only within a limited angle. The main difference between figure 19 of Kotouč *et al.* (2009*b*)

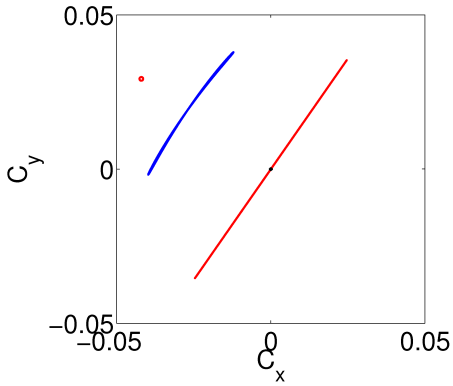

Figure 4.14: Projection of the lift coefficient on the plane perpendicular to the body symmetry axis for an oblate spheroid of aspect ratio $\chi = 6$ at $Re = 135$ (red circle), $Re = 145$ (blue line) and $Re = 183$ (red line). The cross marks the point of zero lift.

and the present figure 4.16 consists of the non-zero mean lift taken over one short vortex shedding period. Such a state was also evidenced in opposing flow but only in its rotating version.

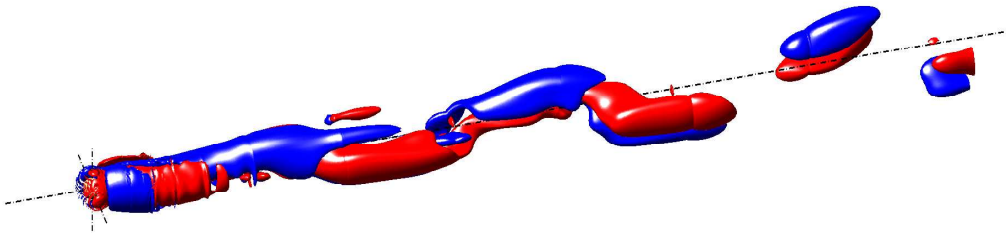

Figure 4.15: State with a non-zero helicity *(e)*. Iso-contours of the streamwise component of the vorticity. Oblate spheroid $\chi = 1.25$, $Re = 283$.

The onset of chaos is not always quite clear cut. If states with well defined symmetry, *(c)* and *(d)*, become chaotic, the onset of chaos is associated to the loss of this symmetry. The chaotic state described by Shenoy & Kleinstreuer (2008) arises from state *(d)* and that of Auguste *et al.* (2010) from state *(c)*. Auguste *et al.* (2010) demonstrate clearly that a quasi-(multi-) periodicity (with a possible subharmonic lock-in) precedes the onset of chaos. The same observation has been made for a sphere (Bouchet *et al.*, 2006). The exact limit between a multi-periodic and a chaotic state is difficult to set, which makes the onset of chaos difficult to identify in helical states *(e)* in which the symmetry is already absent. Nevertheless we observe again a characteristic subharmonic that distorts the traveling 'ellipse' of the lift path.

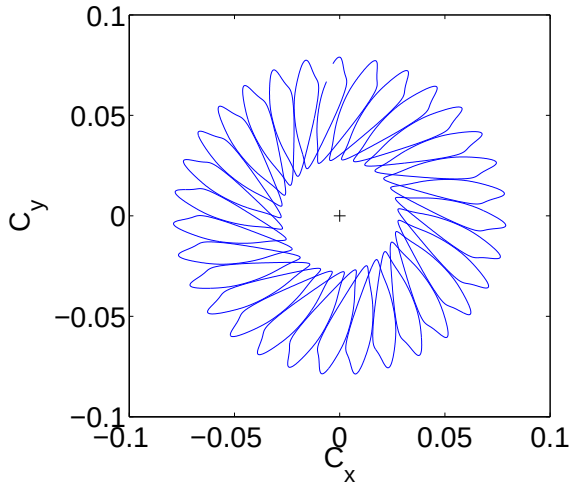

Figure 4.16: State with a non-zero helicity *(e)*. Projection of the lift coefficient on the plane perpendicular to the body symmetry axis. The lift vector describes a rotating ellipse. Oblate spheroid $\chi = 1.25$, $Re = 283$.

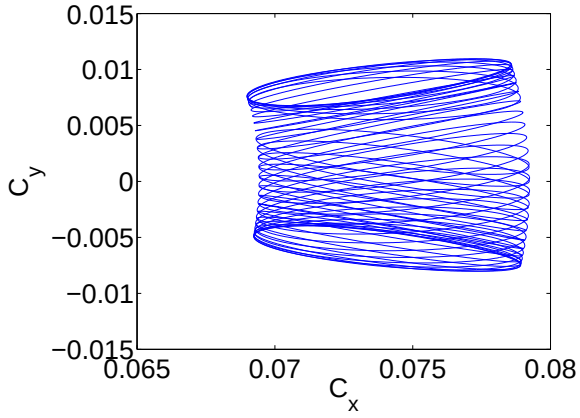

Figure 4.17: State with a non-zero helicity *(e)*. Projection of the lift coefficient on the plane perpendicular to the body symmetry axis. The lift vector describes an oscillating ellipse. Oblate spheroid $\chi = 1.85$, $Re = 190$.

The latter becomes more and more complicated as large time scale modulations set in until both the time plots and the lift path become completely disorganized. To sum up, unlike for other thresholds that can be determined potentially with arbitrary precision, the line delimiting the onset of chaos in the state diagrams presented below is to be understood as approximate. Figure 4.18 presents a plot of the projection of the lift coefficient on the plane

perpendicular to the body symmetry axis for the case of an oblate spheroid of the aspect ratio $\chi = 1.5$ at the Reynolds number $Re = 310$. It describes a chaotic path.

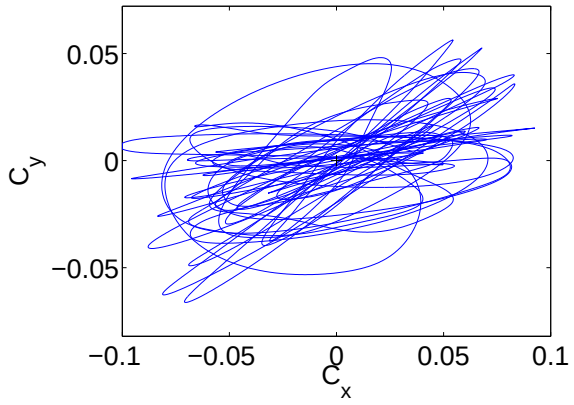

Figure 4.18: Chaotic state *(g)*. Projection of the lift coefficient on the plane perpendicular the the body symmetry axis describing a chaotic path. Oblate spheroid $\chi = 1.5$, $Re = 310$.

4.3.2 State diagram for oblate spheroids

To obtain the state diagram in the $Re - \chi$ parameter plane we investigated around three hundreds of regimes. The transition scenario for oblate spheroids (see Figure 4.20) can be roughly divided into a sphere-like and a thin-disc-like one. The difference starts to appear at the secondary bifurcation, the primary steady non-axisymmetric state *(a)* being present in the qualitatively same form for all aspect ratios. The sphere-like and thin-disc-like states are separated by the sub-domain of states *(e)* with non-zero helicity extending from the secondary bifurcation threshold at $\chi \approx 2$ almost to the sphere case $\chi = 1$. We have taken a special care to see why the states of non-zero helicity have never been evidenced in the sphere wake. It appears that the corresponding *(e)*-sub-domain is cut off between $1/\chi = 0.9$ and 0.95. The most striking feature of the thin-disc-like scenario is that the secondary bifurcation leading to the periodic state without planar symmetry *(b)* appears to be subcritical. Any subcritical bifurcation has two characteristic features (Strogatz, 1994, ch. 8.2): a bistability interval below the linear instability threshold and a super-exponential growth above the threshold. An example of super-exponential growth is presented in Fig. 4.19. The bi-stability band is represented by the red filled area in fig. 4.20. The subcriticality seems to be closely linked to the Hopf bifurcation to the *(b)*-state. It is, however, difficult to trace it to the point at which the bifurcation to the non symmetric state meets that to the symmetric one (slightly above $\chi = 2$ for spheroids and close to $\chi = 4$ for cylinders) because the bi-stability interval becomes very narrow. At $\chi = 2.25$ it either no longer exists or is narrower than one Reynolds number unit. The bi-stability interval is represented graphically for several aspect ratios of spheroids and a cylinder of $\chi = 6$ in Figure 4.21. The amplitudes of oscillations of the lift coefficient are plotted. A non-zero amplitude is synonymous of the state *(b)*. The

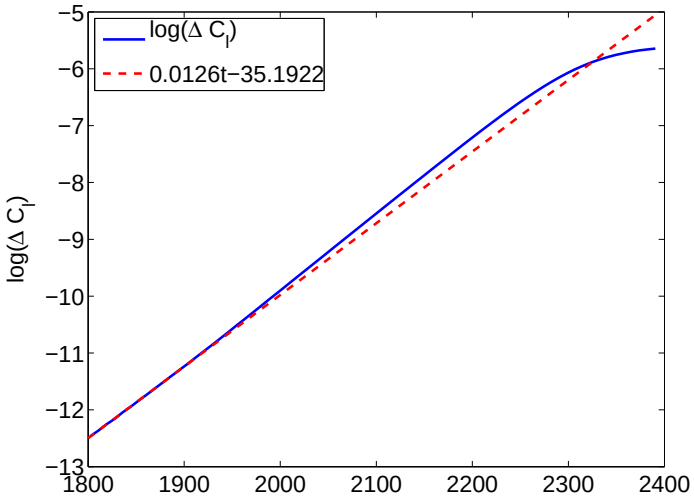

Figure 4.19: Logarithmic plot of the amplitude of the oscillation of the lift coefficient of a thin disc ($\chi = \infty$) at $Re = 126$ (full line) compared to the purely exponential growth (dashed line obtained by a linear fit of the initial stage of growth). Note the super-exponential growth in the time interval $t \in [1950, 2350]$ time units.

interval of stability of the steady state *(a)* is represented by dashed lines traced along the horizontal axis (zero amplitude). The same bi-stability can also clearly be seen in the plot of the mean lift as a function of the Reynolds number. The curves of the steady lift in the state *(a)* do not connect continuously to that of the mean lift in the unsteady periodic state *(b)* and the intervals of existence of both states overlap (see Figure 4.22). The limits of the bistability interval are also provided in Table 4.3. The upper bistability limits were traced in the following way. First an established steady asymmetric state *(a)* was computed. Subsequently we increased the Reynolds number by $\Delta Re = 1$ using the converged steady state as an initial condition and waited until the transients disappear. Next, the Reynolds number was incremented and the previous computation was used an initial condition for the new one. We had to pay attention for the initial condition to be only very weakly perturbed. We continued the procedure until the oscillations appeared. In the proximity of the threshold we were able to extract the decay/growth rates. This made it possible to find it precisely by interpolation. The lower threshold limit was found in a similar way. We decreased the Reynolds number by one each time using as an initial condition an established oscillating state until the oscillations disappeared. The values in brackets reported in Table 4.3 are the last Reynolds number values at which the oscillations were maintained.

4.3.3 State diagram for flat cylinders

The state diagram for flat cylinders of aspect ratio $\chi \geq 1$ is represented in Figure 4.23. It can be seen that the intermediate scenario involving states with non-zero helicity does not extend beyond $\chi = 1.8$ and that the thin-disc-like scenario is limited by an aspect ratio

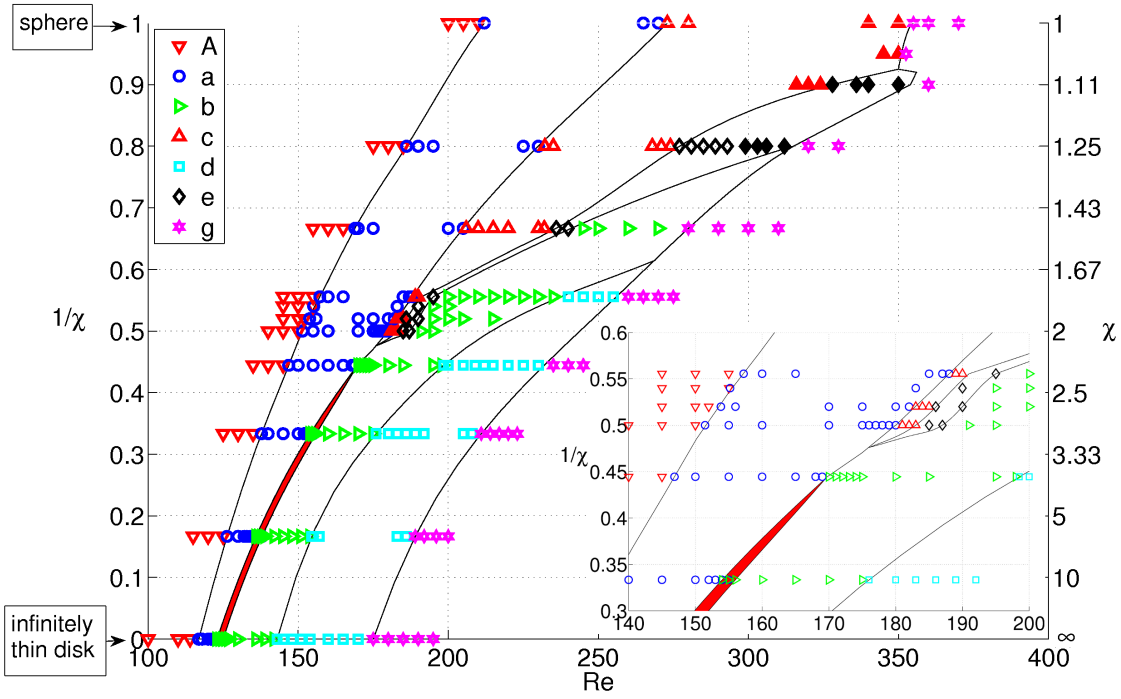

Figure 4.20: State diagram for oblate spheroids. *A* stands for axisymmetric state. The letters a through g in the legend refer to the same states as in chapter 1.6. The filled triangles (c), and diamonds (e) represent pre-chaotic states with a subharmonic modulation. They can be either with non-zero helicity (diamonds) or with planar symmetry (triangles). The narrow filled band represents the domain of bi-stability at the subcritical bifurcation.

spheroids			cylinders		
χ	Re_2'	Re_2	χ	Re_2'	Re_2
∞	[124]	125.2	∞	[124]	125.2
6	[136]	137.7	6	[148]	150.1
3	[154]	155.7	4	[164]	165.6

Table 4.3: Linear stability thresholds Re_2 and lower bounds of bi-stability Re_2' ($Re_2' < Re_2$) of the subcritical Hopf bifurcation for oblate spheroids and flat cylinders. (The values in brackets are closest integer upper bounds, i.e. the bistability interval starts at least at these values.)

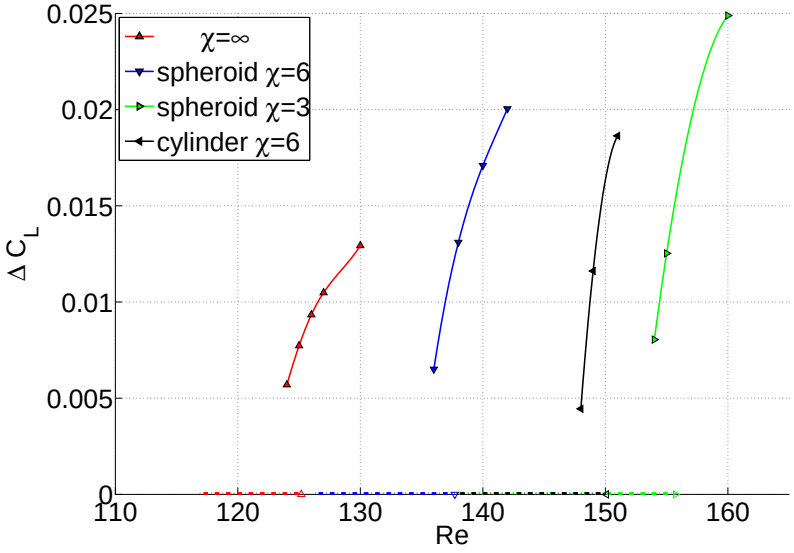

Figure 4.21: Oscillation amplitude ΔC_L of the lift coefficient as a function of the Reynolds number for oblate spheroids of $\chi = \infty, 6, 3$ and a flat cylinder of $\chi = 6$ (see the legend). The stability interval of the steady non-axisymmetric state is represented by dashed lines along the horizontal axis. Their linear instability thresholds are plotted as empty triangles.

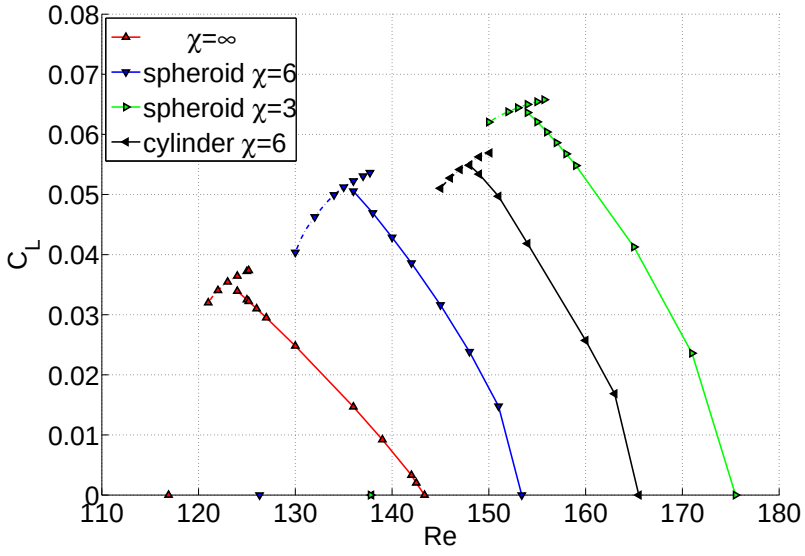

Figure 4.22: Mean lift as a function of Reynolds number for oblate spheroids of $\chi = \infty, 6, 3$ and a flat cylinder of $\chi = 6$ (see the legend).

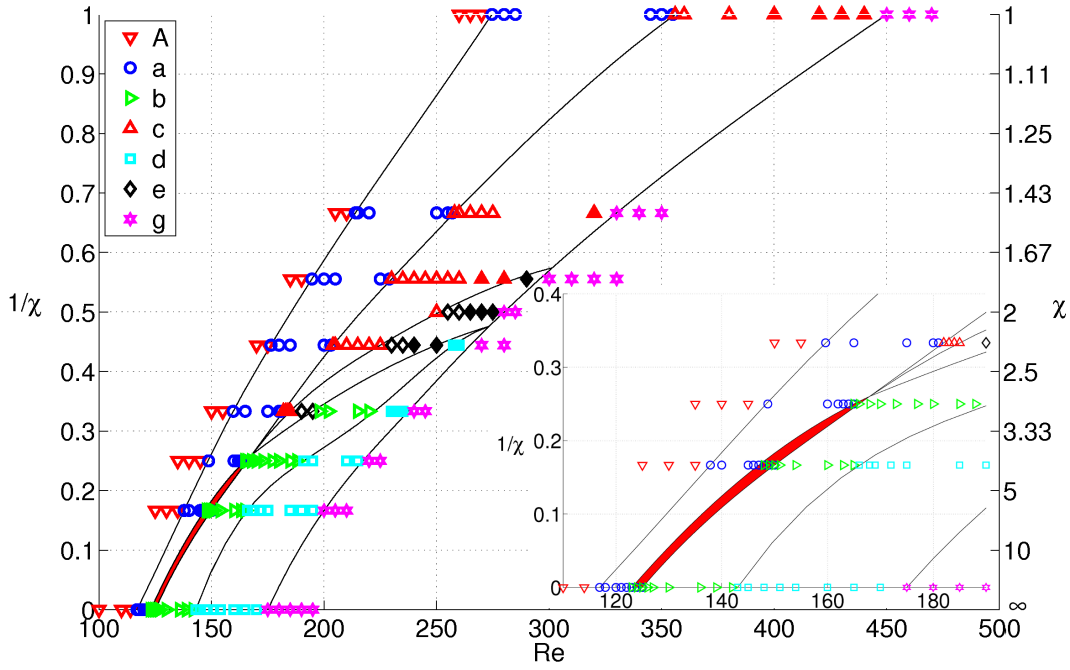

Figure 4.23: State diagram for cylinders. The meaning of the symbols is the same as in the caption of Figure 4.20. The band of bi-stability at the subcritical bifurcation is still present for $1/\chi \leq 0.25$.

slightly smaller than 4. The first two thresholds, fitted by Fernandes *et al.* (2007) to straight lines in terms of $1/\chi$, are in agreement with our data close to $\chi = \infty$ but deviate from the thresholds evidenced in Figure 4.23 at $\chi = 2$. However, a closer look on Figure 13 of Fernandes *et al.* (2007) shows that the really computed values at $\chi = 2$ lie clearly above the fit. There is a very good agreement of the thresholds of all described states in the papers by Fabre *et al.* (2008) and Meliga *et al.* (2009). The thresholds of Shenoy & Kleinstreuer (2008) are systematically above those of Figure 4.23. The difference grows considerably with the Reynolds number. The comparison of our results with those reported in the literature is provided in Table 4.4.

4.4 Conclusions

We presented an exhaustive parametric study of the transition scenario in the wake of oblate spheroids and of flat cylinders placed with their rotation axis parallel to the uniform flow. We find a significant qualitative similarity between both configurations. At large aspect ratios ($\chi > 2.3$ for spheroids and $\chi \geq 4$ for cylinders), the secondary bifurcation giving rise to a periodic state without planar symmetry is subcritical with a hysteresis interval

χ	Re_1	Re_2 / St_2	Re_3 / St_3	Re_4 / St_4	Re_5 / St_5	Re_6
∞ [1]	≈115	≈121	≈140			
		0.119				
∞ [2]	116.9	125.3	143.7*			
		0.121	*0.118*			
∞ [3]	116.92	([124],125.2)	[142,143]	[165,170]		
		0.120	*0.118*			
10 [4]	135	155	172	280		
		0.113				
10 [3]	129.6	(136.3,138.7)	154.4	188.8		
		0.115	*0.114*			
3 [5]	≈159.4	≈179.8	[184,185]	[190,191]	≈215	≈240
		0.109				
3 [3]	159.65	[181,182]	[185,190]	[195,198]	[220,230]	[235,240]
		0.112	*0.112*	*0.112*	*0.111*	

Table 4.4: Bifurcation thresholds. Numbers in brackets indicate authors: [1] Fabre *et al.* (2008), [2] Meliga *et al.* (2009), [3] present study, [4] Shenoy & Kleinstreuer (2008), [5] Auguste *et al.* (2010). * result obtained using asymptotic expansion. At $\chi = 10$, the values of the present study are obtained by interpolation between $\chi = \infty$ and $\chi = 6$. Re_2 is understood as the critical Reynolds number for the loss of stability of the steady non-axisymmetric state. Values in italics below the critical Reynolds numbers: Strouhal numbers of the oscillations at the corresponding threshold. For the quasi-periodic state at $\chi = 3$, $Re = Re_4$ the dominant frequency is indicated.

of about two Reynolds number units. For small aspect ratios ($\chi \geq 1$ are considered), the sphere-like scenario is recovered only at aspect ratios very close to one for spheroids, while for cylindrical bodies the same holds for $\chi \leq 1.7$. For intermediate aspect ratios, a domain of states with non-zero net helicity separates states typical for the sphere wake from those of an infinitely thin disc. The presented state diagrams sum up the stability domains of all observed transitional states and may thus serve as a tool for determining the expected asymptotic state for any numerical or experimental configuration involving oblate spheroids and flat cylinders. Beyond this practical aspect they may provide a basis for theoretical reflection that has already been developed for thin discs in the papers by Fabre *et al.* (2008) and Meliga *et al.* (2009). The subcriticality of the secondary Hopf bifurcation can to some extend be neglected but, if it is to be taken into account, the weakly non-linear models must be developed to a higher order. It is very likely unobservable experimentally. But, as we argue in the next chapter, the whole 'thin-disc-like' scenario is difficult, if not impossible, to evidence experimentally. Finally, the detailed knowledge of the transition scenario of fixed objects provides an indispensable reference for simulations of freely falling discs. This topic has gained a significant attention of the scientific community since the experimental paper by Field *et al.* (1997). It will be considered in next chapters.

The results of this chapter have been published in the paper by Chrust *et al.* (2010).

Chapter 5

Effect of the inclination on the transition scenario in the wake of fixed discs and flat cylinders

5.1 Existing background

It is remarkable that the transition in the wakes of a fixed disc and thin flat cylinder of the aspect ratio $\chi = 10$, placed in a uniform flow, differs significantly in Direct Numerical Simulations (DNS) of Fabre *et al.* (2008) and Shenoy & Kleinstreuer (2008), respectively, from that observed for a sphere (see Johnson & Patel, 1999). The results of the previous chapter (see also Chrust *et al.*, 2010) revealed that the transition scenario of a thin disc applies to flat cylinders of the aspect ratio $\chi \geq 4$. However, at the same time, the experimental results obtained by Szaltys *et al.* (2011) for a fixed flat cylinder of the aspect ratio $\chi = 6$, which we shall call in what follows a flat cylinder did not confirm the numerical predictions and showed rather a transition scenario qualitatively similar to that observed for a sphere.

Direct Numerical Simulation of Chrust *et al.* (2010) carried out for a flat cylinder of the aspect ratio $\chi = 6$ showed that the initial axisymmetric state is replaced by a steady planar symmetric state via a regular bifurcation in the $m = 1$ azimuthal subspace at the Reynolds number $Re^I_{num} = 137.86$. The orientation of the symmetry plane is arbitrary and is selected by the initial conditions. The flow is characterized by the appearance of two counter-rotating vortices. The breaking of axisymmetry yields a steady lift oriented in the symmetry plane. This state is denoted as SS (steady state) by Fabre *et al.* (2008) and Meliga *et al.* (2009) and 'steady asymmetric' by Shenoy & Kleinstreuer (2008). The threshold of the primary bifurcation has been given by Fernandes *et al.* (2007) as a function of χ for cylinders of finite aspect ratio. Szaltys *et al.* (2011) found experimentally the threshold for a flat cylinder of the aspect ratio $\chi = 6$ slightly lower than that predicted by DNS - at the Reynolds number $Re^I_{exp} = 125$.

While the steady asymmetric state is found both experimentally and numerically for the case of a thin flat cylinder, the secondary bifurcation, albeit of the Hopf type in the two cases, has been found to lead to two qualitatively different states. DNS of Chrust

et al. (2010) revealed a specific *periodic state without planar symmetry*, which was reported for the first time for a thin disc by Fabre *et al.* (2008) and a cylinder of the aspect ratio $\chi = 10$ by Shenoy & Kleinstreuer (2008). This state is characterized by a 'kinking of trailing vortices' past the body generating an oscillating component of the lift. While the mean lift lies in the symmetry plane selected at the primary bifurcation, the oscillating component is perpendicular. As a consequence, it has been called RSB (reflectional symmetry breaking) by Fabre *et al.* (2008), MM_π (mixed mode with phase π) state by Meliga *et al.* (2009), 'steady 3D periodic with regular rotation of the separation region' by Shenoy & Kleinstreuer (2008) or 'yin-yang' by Auguste *et al.* (2010). For a thin disc, this state appears at $Re^{II}_{num} = 125.18$ (see Chrust *et al.* (2010)) and persists up to $Re^{3}_{num} \approx 143$. Figure 5.1 represents this state for the case of a disc at $Re = 135$. The plot of the projection of the lift coefficient on the plane perpendicular to the free stream direction at the same Reynolds number is shown in Figure 5.2. For the mentioned flat cylinder ($\chi = 6$) the bifurcation threshold was found at $Re^{II}_{num} = 150.0$. Chrust *et al.* (2010) reported the Strouhal number, $St = fd/U$, where f is the characteristic frequency and U the free stream velocity, at the onset of oscillations $St^{II}_{num} = 0.112$. On the other side, Szaltys *et al.* (2011) evidenced in experiments that the Hopf bifurcation leads to a periodic state with planar symmetry observed many times in the wake of a sphere (see e.g. Johnson & Patel, 1999). They found the Strouhal number at the onset of oscillations of $St^{II}_{exp} = 0.16$. In this state, the lift has a non-zero mean value and oscillates in the symmetry plane. It is the RSP state of Fabre *et al.* (2008), MM_0 state of Meliga *et al.* (2009) or 'zig-zig' state of Auguste *et al.* (2010). The reflectional symmetry preserving state observed experimentally for a cylinder $\chi = 6$ is presented in Figure 5.3.

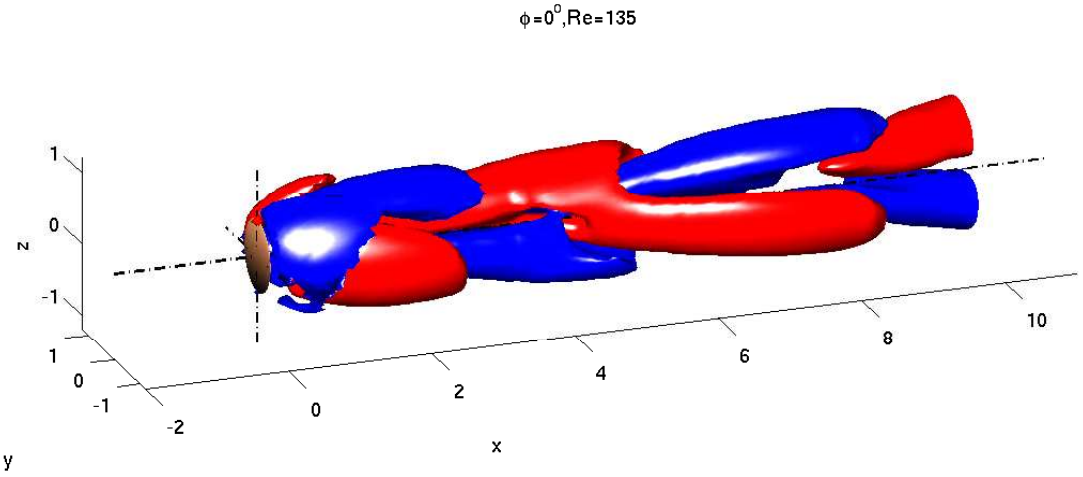

Figure 5.1: Thin disc perpendicular to the free stream direction, $\chi = \infty$, $Re = 135$. Periodic state without planar symmetry. Iso-contours of the streamwise component of vorticity.

Direct Numerical Simulation (Chrust *et al.*, 2010) for a thin cylinder predict, upon a further increase of the Reynolds number, the appearance of the periodic state with zero mean lift, which is not present in the scenario of a sphere, nor in the scenario found experimentally for this configuration by Szaltys *et al.* (2011). The mean value of the lift in periodic state

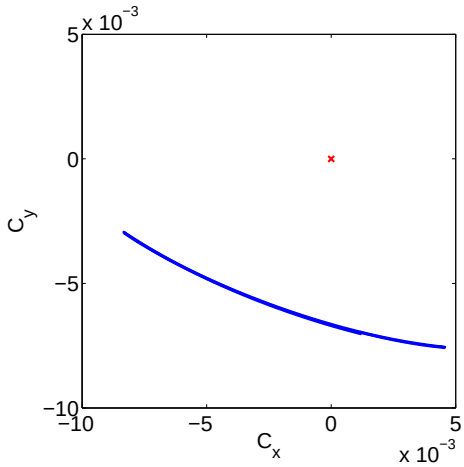

Figure 5.2: Thin disc perpendicular to the free stream direction, $\chi = \infty$, $Re = 135$. Periodic state without planar symmetry. Projection of the lift coefficient on the plane perpendicular to the body symmetry axis. The mean lift has a non-zero value. The lift oscillations are perpendicular to the symmetry plane selected at the primary bifurcation.

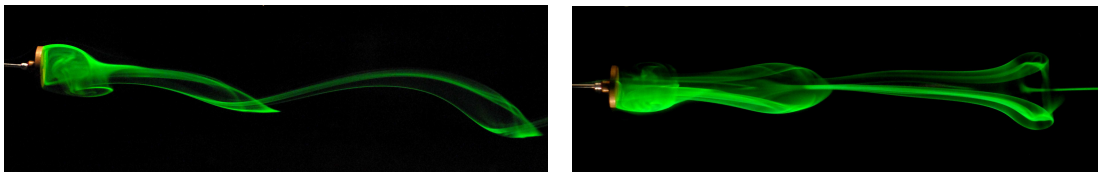

Figure 5.3: Flat cylinder $\chi = 6$. Periodic state with planar symmetry and non-zero mean lift observed experimentally. The wake is visualized using a fluoresceine dye. Left: side view, right: top view.

without planar symmetry progressively decreases to finally disappear. The wake recovers the symmetry plane, that is oriented perpendicularly to that chosen at the primary bifurcation. This periodic state with a zero mean lift has already been observed for a disc and a cylinder of the aspect ratio $\chi = 10$ by Fabre *et al.* (2008) and Shenoy & Kleinstreuer (2008), respectively. This state is called SW (standing wave) mode (Fabre *et al.*, 2008; Meliga *et al.*, 2009) or 'unsteady with plane of symmetry and zero lift force' (Shenoy & Kleinstreuer, 2008). Chrust *et al.* (2010) found its threshold (for the mentioned flat cylinder of aspect ration 6) at the Reynolds number $Re^3_{num} = 166.0$.

Szaltys *et al.* (2011) observed the periodic state with a non-zero mean lift up to a Reynolds number $Re^{qp}_{exp} = 185$, above which a second frequency equal to about a half of the base frequency appeared. They noticed a regular hairpin shedding with irregularities midway between hairpin heads. For the case of a disc, Fabre *et al.* (2008) demonstrated that the transition to chaos is preceded by a *quasi-periodicity* characterized by the presence of a slower frequency close to 1/3 of the 'leading frequency' of the previous regimes. Auguste

et al. (2010) showed clearly that a quasi- (multi-) periodicity (with a possible subharmonic lock-in) precedes the onset of chaos for a case of a flat cylinder $\chi = 3$. Identical observation has been made for a sphere by Bouchet *et al.* (2006). The exact limit between a multi-periodic and a chaotic state is difficult to set. Chrust *et al.* (2010) provide for a cylinder of the aspect ratio $\chi = 6$ approximate threshold of the appearance of chaos at the Reynolds number $Re_{num}^{chaos} \approx 200$.

The purpose of this chapter is to present a joint experimental and numerical study that shall elucidate the reasons of the disagreement in the transition scenario predicted by DNS and observed experimentally for a flat cylinder $\chi = 6$. We presume that the impossibility to observe experimentally the periodic state without planar symmetry, as evidenced by DNS, stems from the difficulty of realization of a perfectly axisymmetric configuration in experiments. In other words, we suspect that the holding of the cylinder artificially maintains a given plane of symmetry of the wake. It is to be noted, that the cylinder axis is never perfectly parallel to the free stream direction, as it is the case in numerical simulations and the fixing tube enhances this effect. Therefore we shall study the influence of the inclination angle on the observed transition scenario. According to our knowledge, such study has never been done before. Two cases are studied numerically: a disc $\chi = \infty$ and a flat cylinder $\chi = 6$. In the experiments, we consider only the case of the cylinder of aspect ratio $\chi = 6$.

A similar configuration has already been investigated experimentally by Calvert (1967) who studied thin discs inclined to the flow, so that their symmetry axis made an angle between 10^o and 50^o with the free stream direction. However, the considered Reynolds numbers between 500 and 1000 are significantly higher than those corresponding to transitional regimes, which are of our interest. He observed strong vortex shedding at angles of incidence exceeding 20^o. As the angle was increased, the vortex shedding frequency rose. The vortices were shed always from the same location on the disc - the trailing edge, and their orientation did not change. This was not the case for a disc placed perpendicularly, for which the flow was already turbulent.

The experimental part of this work was carried out at the École Supérieure de Physique et de Chimie Industrielles (ESPCI) in the Laboratoire de Physique et Mécanique des Milieux Hétérogènes (PMMH) in Paris by Lukasz Klotz and Tomasz Bobiński under the supervision of Sophie Goujon-Durand and José Eduardo Wesfreid. The origins of this cooperation date back to my internship at ESPCI that I did during my master studies. My internship was dedicated to development of the algorithm of the decomposition of the streamwise component of the vorticity field obtained from the Particle Image Velocimetry (PIV) measurements into Fourier modes. The analysis of amplitudes of Fourier modes proved to be useful in determining the transition thresholds and, moreover, shed light on the transition scenarios of a sphere and of a flat cylinder as demonstrated by Szaltys *et al.* (2011). At the same time, our study of the thin cylinder revealed the differences in the transition scenario compared to the one predicted by DNS. I am thankful to Sophie Goujon-Durand and José Eduardo Wesfreid for inviting me several times to Paris to carry out this joint work.

5.2 Numerical implementation

We consider fixed axisymmetric flat cylinders and a thin disc with their axis of revolution inclined by an arbitrary angle ϕ with respect to the direction of the asymptotic uniform flow. The flow of an incompressible fluid past these bodies is governed by the same Navier Stokes equations (2.3) and (2.4) non-dimensionalized with respect to the inflow velocity U and the diameter d.

The Reynolds number Re is defined as $Re = Ud/\nu$. The second dimensionless parameter, the aspect ratio introduced in the previous section, completely defines the geometry of the cylinder. We closely adapt the numerical method used by Ghidersa & Dušek (2000) for the case of a sphere and, more recently, by Chrust *et al.* (2010) for the study of the transition in the wake of fixed flat cylinders and oblate spheroids placed with their rotation axis parallel to the uniform flow.

In the previous chapter the geometrical configuration was axisymmetric which made it possible to use the code of Ghidersa & Dušek (2000) and Jenny & Dušek (2004) without modification. The inclination of the cylinder with respect to the uniform flow direction breaks, however, the axisymmetry of the configuration. The cylindrical domain is therefore decomposed into a spherical sub-domain with center O and radius R_s ($d/2 < R_s < R_c$) containing the body and the remaining volume of the cylinder and the domain decomposition described in chapter 3, albeit in its static version, is used. The new version of the code was tested in the intended configuration in several ways described in the next sub-sections.

5.2.1 Test of the influence of the spherical function expansion order ℓ_{max} and of the radius of the spherical sub-domain R_s on the thresholds in the transition of a fixed disc and thick cylinder $\chi = 1$ perpendicular to the flow

Two new numerical parameters arise from the domain decomposition, namely, the radius of the spherical sub-domain R_s and the order of expansion in spherical harmonic functions on the interface ℓ_{max}. The later is responsible for the accuracy of the connection at the spherical interface. We closely adapt the mesh used for an infinitely thin disc by Chrust *et al.* (2010) limiting the modifications to a relatively small region in the proximity of the disc. The new mesh for a thin disc and its details in the proximity of the body are presented in Figures 5.4 and 5.5, respectively. Figure 5.6 shows the details of the mesh for the flat cylinder $\chi = 6$, that was used in the present study. The mesh for a thick cylinder $\chi = 1$ is essentially the same as the one presented in chapter 4.2 (see Figure 4.4). Its modification was limited to the addition of the concentric layers of elements in the proximity of the object. Note the thick dark line that marks the interface between the two sub-domains. In the paper Chrust *et al.* (2010) we tested the meshes for the dependence on the size of the domain, on the breakup into spectral elements, on the number of collocation points per spatial direction and on the truncation of the azimuthal Fourier expansion. It was demonstrated that the choice of the following parameters: number of spectral elements $N_{el} = 256$ for a thin disc and $N_{el} = 230$ for a thick cylinder $\chi = 1$, number of Gauss-Lobatto-Legendre collocation points in each direction (z, r) $N = 6$, number of azimuthal Fourier modes $m = 4$ and upstream,

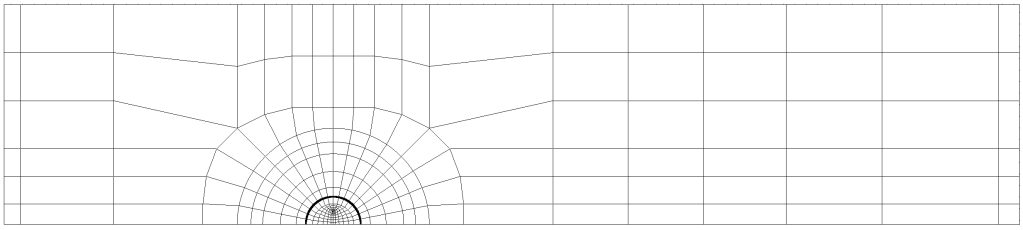

Figure 5.4: Thin disc $\chi = \infty$. Spectral element discretization of the radial-axial plane of the computational domain. The inflow is situated on the left. The cylindrical computational domain of radius $R = 8d$ extends $12d$ upstream and $25d$ downstream. The mesh contains $N_{el} = 278$ spectral elements. The interface at $R_s = d$ is marked by a thick line.

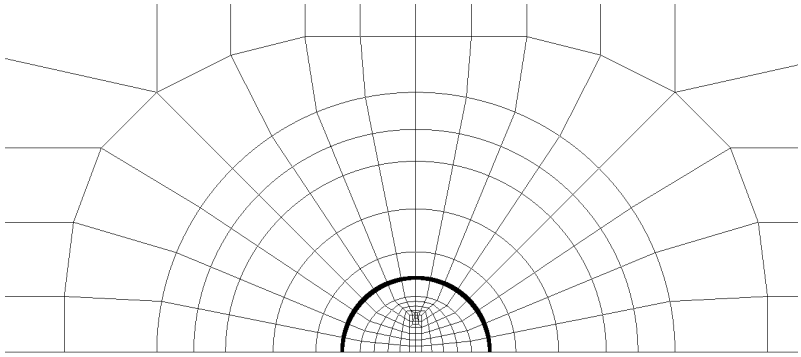

Figure 5.5: Thin disc $\chi = \infty$. Details of the spectral element discretization of the radial-axial plane of the computational domain. The interface at $R_s = d$ is marked by a thick line.

downstream extension as well as the radius of the cylindrical domain equal to $L_u = 12d$, $L_d = 25d$ and $R_c = 8d$, respectively, yield a precision better than 1% in the determination of the critical Reynolds numbers of the first two bifurcations.

Our present concern is to show that the spherical interface reconnecting the two sub-domains does not perturb the computation. Therefore, we tested the influence of the truncation of the spherical harmonic function expansion order ℓ_{max} and of the radius of the spherical sub-domain on the thresholds of the primary, regular and of the secondary, Hopf bifurcations in the case of a thin disc and a thick cylinder $\chi = 1$. The results found with the domain decomposition were compared to those obtained with the original code used in the paper Chrust *et al.* (2010) already in chapter 3. Tables 3.3 and 3.4 summarize the primary bifurcation thresholds for a thin disc $\chi = \infty$ and for a thick cylinder $\chi = 1$, respectively. It can be inferred that the truncation of the expansion into spherical functions at $\ell_{max} = 15$ is already sufficient to obtain the precision better than 1% for the thin disc. The thresholds depend only very weakly on the radius of the spherical sub-domain R_s. This sensitivity to the radius can be explained very likely by the presence of localized flow structures in the vicinity of the body. At $\ell_{max} = 15$, this variation is much stronger for the thick cylinder the surface of which is closer to the spherical interface. Nevertheless, with moderately increased

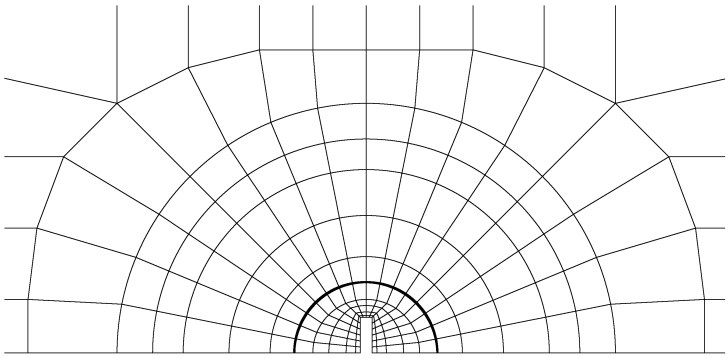

Figure 5.6: Cylinder $\chi = 1$. Details of the spectral element discretization of the radial-axial plane of the computational domain. The mesh contains $N_{el} = 252$ spectral elements. The interface at $R_s = d$ is marked by a thick line.

ℓ_{max}, virtually the same threshold is obtained independently of the spherical sub-domain radius. For the disc, the obtained critical Reynolds number lies within 0.03% from the value obtained in a computation without domain decomposition. For the thick cylinder of aspect ratio $\chi = 1$ the largest discrepancy for $\ell_{max} = 25$ does not exceed 0.6%. The agreement is even better for the secondary bifurcation threshold.

5.2.2 Fixed disc inclined by 30 degrees with respect to the flow direction

As a next test the configuration of the fixed disc inclined by 30 degrees with respect to the flow direction described in section 3.12.2 was considered. We computed the flow field above the Hopf bifurcation threshold at $Re = 120$ and we investigated the sensitivity of the decay rate just below the threshold at $Re = 105$, the critical Reynolds number being 110. The results showed that the numerical interface et $R_s = 1$ is invisible in flow visualizations at $Re = 120$ and that a truncation of the spherical function decomposition at interface at $\ell_{max} = 15$ assures a precision better than 1% in the determination of the critical Reynolds number.

5.3 Experimental setup

The experiments were carried out in a low velocity horizontal water channel with a square test cross-section 100x100 [mm] and a length of 860 [mm]. A typical free stream velocity ranged from 4 to 40 [mm/s], which in the case of the considered cylinder, corresponded to the Reynolds number range $50 - 500$ (for ambient temperature T=20 [^{0}C]). The precise calibration of the flow meter allowed for the determination of the Reynolds number with a precision of $\pm 5\%$. The investigated cylinder had a diameter of $d = 12$ [mm] and a thickness of $h = 2$ [mm] resulting in the aspect ratio of $\chi = 6$. It was mounted in the central part of the test section cross section by rigid tubes that supplied fluoresceine dye used for the flow visualization. The dye was ejected through a horizontal slit on the downstream face of

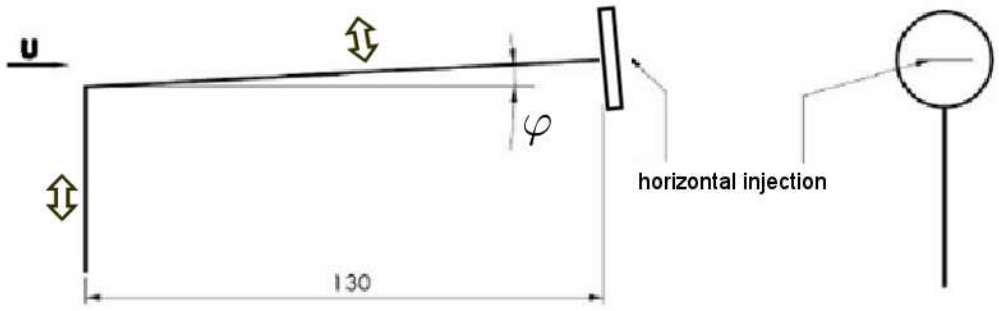

Figure 5.7: Holding details. Cylinder diameter $d = 12$ [mm], thickness $h = 2$ [mm]. The arrows indicate the possible adjustment directions of the holding tubes. The cylinder is inclined to the flow by the angle ϕ. The length of the vertical tube was adjusted to keep the cylinder in the middle of the cross section of the test section for all tested inclination angles.

the cylinder. The blockage ratio (defined as area of the cross-section of the cylinder/area of the cross-section of the channel) was below Br=1.2% in the perpendicular configuration. To account for the inclination of the cylinder, the rigid tubes were bent appropriately. The maximum inclination of 15^0 was allowed by the used holding set-up. The details of the mounting are presented in Figure 5.7. The velocity measurements were carried out using Particle Image Velocimetry.

5.4 Results

We have carried out a series of Direct Numerical Simulations for a thin disc $\chi = \infty$ and a flat cylinder $\chi = 6$ for the Reynolds numbers corresponding to the transitional regimes. We investigated the influence of the inclination ϕ (rotation around x-axis), measured as the angle between the axis of symmetry of the body and the uniform flow direction, on the transition scenario and bifurcation thresholds. We considered the angles of inclination in the range $0^o - 50^o$ for a disc and $0^o - 60^o$ for a thin cylinder. Simultaneously we carried out experiments for a flat cylinder $\chi = 6$ and angles of inclination going from 0^o to 15^o degrees. In the next subsection we present the numerical results obtained for a thin disc. Subsequently, we compare the numerical and experimental results found for a thin cylinder.

For the thin disc we investigated the effect of a slight inclination on the scenario observed for a disc placed exactly perpendicularly to the flow direction.

5.4.1 Infinitely thin disc very slightly inclined with respect to the free stream direction

We have mentioned that the intriguing scenario predicted by direct numerical simulation has never been observed experimentally. It is thus, in particular, interest to consider very small inclination angles and see if there is a the critical inclination angle ϕ^* above which the the periodic state without planar symmetry, observed for the disc perpendicular to the free stream direction (see Figs. 5.1 and 5.2), is suppressed.

We examined small angles of inclination of 0.0057^o, 0.057^o, 0.57^o ($1e-04$, $1e-03$ and $1e-02$ radian, respectively), 2^o and 4^o. We chose to rotate the disc about the x-axis. Even the smallest inclination results in a non-zero lift but it does not mean that the effects comparable to those of the primary (regular) bifurcation disappear. The inclination removes only the arbitrariness of the selection of the symmetry plane of the resulting flow. The instability enhances the lift and makes it approach progressively the same curve as for the perfectly axisymmetric geometry. In our configuration the lift was positive in the direction of y-axis for Reynolds numbers below the threshold of unsteadiness. In figure 5.8 we represent the values of the lift coefficients obtained at 4 values of the Reynolds number for three small values of inclination angle close to the first two critical Reynolds numbers corresponding of a disc placed exactly perpendicularly to the flow direction. At a $Re = 115 < Re_1$ the lift is essentially due to the inclination as can be from the proportionality of the lift to the inclination angle. This contrasts with what happens at $Re = 125$ when all the three values are practically superimposed on that corresponding to $\phi = 0^o$. The lift is virtually independent of the (small) inclination. (At the $Re = 120$ we obtained the saturated value only at $\chi = 1e-02$ radian.) The same is true at $Re = 135$ for the mean value of the lift of the oscillating state (only one converged state was obtained).

It can be considered that if the inclination is sufficiently small the effects of the regular bifurcation are dominant and the role of the inclination is reduced to the selection of the symmetry plane. The question is what happens at the onset of the Hopf bifurcation. As will be seen in the next section, for larger angles ($\phi \geq 4^o$) the oscillating state keeps the planar symmetry defined by the inclination. The mean lift (due mainly to the inclination itself) is non-zero and the lift oscillates in the symmetry plane as is the case in what we called 'periodic oscillating state with planar symmetry and non-zero mean lift' in the case of the fixed sphere wake. How does the 'periodic state without planar symmetry' characteristic for the disc placed perpendicularly to the flow become 'periodic with planar symmetry and non-zero mean lift' when the disc is slightly inclined? The answer is given by Figures 5.9 and 5.10 obtained for the smallest considered inclination of 0.0001 radian (0.006^o) by running a simulation at $Re = 135$ starting from the initial condition corresponding to the steady state at $Re = 125$ (blue circle at $Re = 125$ in Figure 5.8). The most striking feature is that, in spite of the tiny value of the inclination angle, the oscillations set in in the symmetry plane (along the $y-axis$) which contrasts with the case of an exactly zero inclination, when the lift starts immediately to oscillate perpendicularly to its steady value. The symmetry plane seems to be sufficiently stable to allow the Hopf bifurcation to saturate. This occurs after about 200 time units. At the same time the oscillations wipe out, through non-linear interaction, the initially non-zero mean lift. The state becomes periodic with planar symmetry and zero

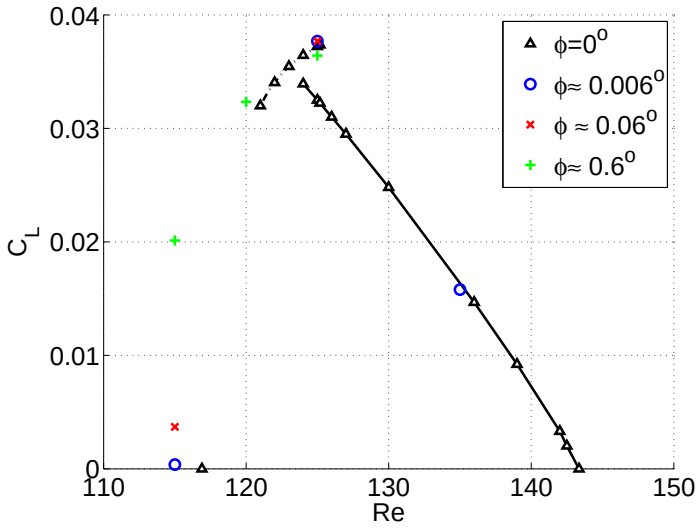

Figure 5.8: Lift coefficient for varying inclination close to the onset of instabilities. Mean value above the threshold of unsteadiness. (Critical Reynolds numbers of the first two bifurcations in the wake of a perpendicularly placed disc: $Re_1 = 117$, $Re_2 = 125$.)

mean lift. However, as the oscillations develop, the symmetry of the state becomes unstable as can be seen on the C_x-component of the lift represented in the right Figure 5.9. The growth rate in the x-direction is clearly driven by the amplitude of the oscillating mode as can be seen from the fact that it becomes constant at the same time as the amplitude of C_y. Due to too perfect initial symmetry (initial value of C_x of the order of 10^{-14}) it was time consuming to obtain a saturation of the amplification of the C_x component. It has, nevertheless been approximately obtained. The plane of the oscillations remains conserved but it is progressively shifted in the direction of the x axis which yields a non-zero mean value of C_x. The finally obtained state is thus again without symmetry and with a non-zero mean lift as it is the case for a perfectly perpendicularly placed disc.

The instability of the symmetric state was monitored by evaluating the growth rate of the x component of the lift as a function of the inclination angle (without attempting to reach the saturation). The growth rate only slightly decreases from 0.023 at 10^{-4} (0.006^o) radian to 0.022 at 10^{-2} radian (0.6^o). At 2^o we could not yet decide whether a growth was present but at 4^o the x-component of the lift remained of the order of 10^{-14} while the oscillations of the y component had reached saturation. It can be admitted that starting form an inclination of 4^o the Hopf bifurcation conserves the symmetry plane and a state with non-zero mean lift and oscillations in the symmetry plane arises.

The scenario of exactly perpendicular disc being limited to small inclinations it is not surprising that it can hardly be confirmed in experiments where the disc holding modifies the flow and the disc inclination is not controlled with enough accuracy.

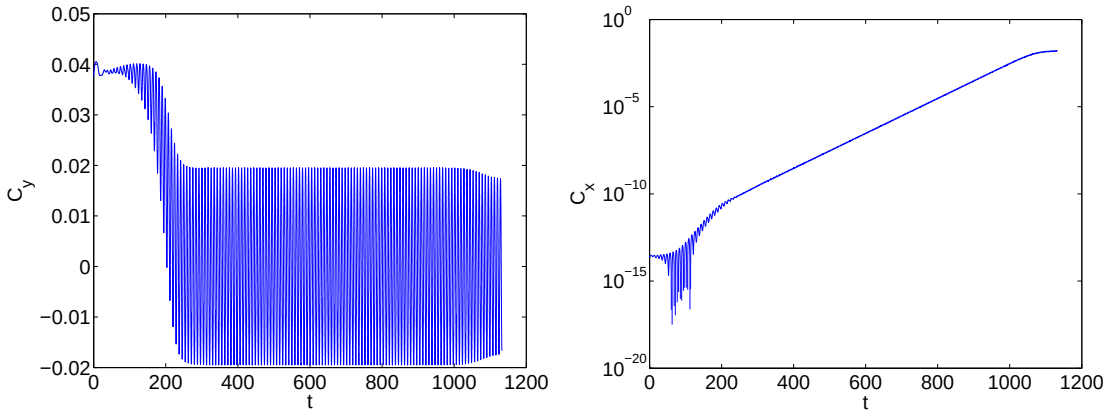

Figure 5.9: Thin disc inclined by $\phi = 0.006^o$ at $Re = 135$. y- (left figure) and x- (right figure) component of the lift coefficient as a function of time. Note the linear scale of the left figure and the semi-logarithmic scale of the right figure.

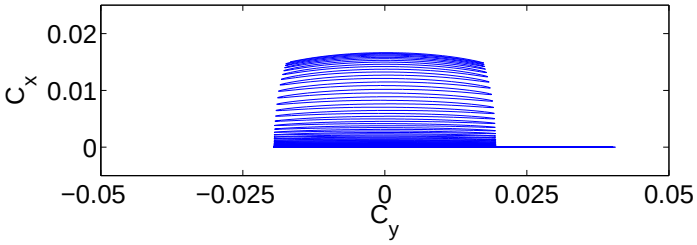

Figure 5.10: Thin disc inclined by $\phi = 0.006^o$ at $Re = 135$. Projection of the lift coefficient on the plane perpendicular to the free stream direction. The oscillations leave the initial symmetry plane and settle with a mean value perpendicular to the initial steady value. (The x-component is plotted along the vertical axis.)

5.4.2 Infinitely thin disc inclined with respect to the free stream direction by more than 4^o.

As we have already seen, starting form an inclination of about 4 degrees the symmetry with respect to the plane selected by the direction of the inclination is conserved. The first bifurcation is of the Hopf type. The transition is from the steady planar symmetric state, represented in Figure 5.11 for a disc inclined by $\phi = 4^o$, characterized by two counter-rotating vortices, to the periodic state with a non-zero mean lift conserving the initial plane of symmetry. The vorticity in the wake in this state is represented for the same angle of inclination of the disc in Figure 5.12. The inclination influences the critical Reynolds number of the onset of oscillations.

The threshold of the Hopf bifurcation is not a monotonic function of the inclination angle of the disc. Figure 5.13 represents the instability threshold as a function of ϕ. At first, the threshold decreases with the inclination angle before reaching a minimum for $\phi^{min} \approx 20^o$.

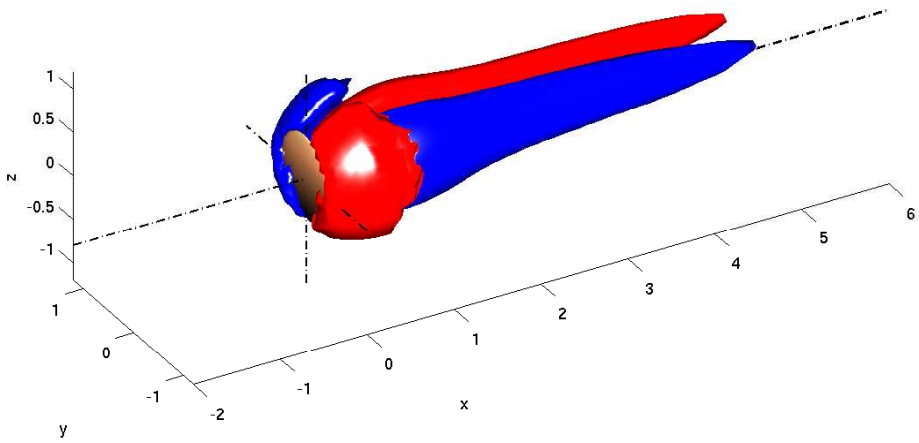

Figure 5.11: Disc inclined with respect to the free stream direction by $\phi = 4^o$ at $Re = 120$. Axial vorticity iso-surfaces at levels 0.2. Steady asymmetric state.

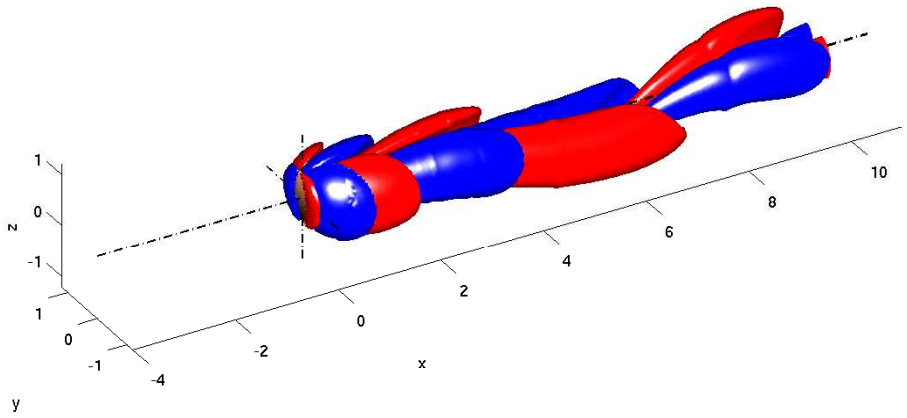

Figure 5.12: Disc inclined to the free stream direction by $\phi = 4^o$ at $Re = 135$. Axial vorticity iso-surfaces at levels 0.1. Periodic state with a non-zero mean lift. The initial plane of symmetry is conserved. The first bifurcation is of the Hopf type.

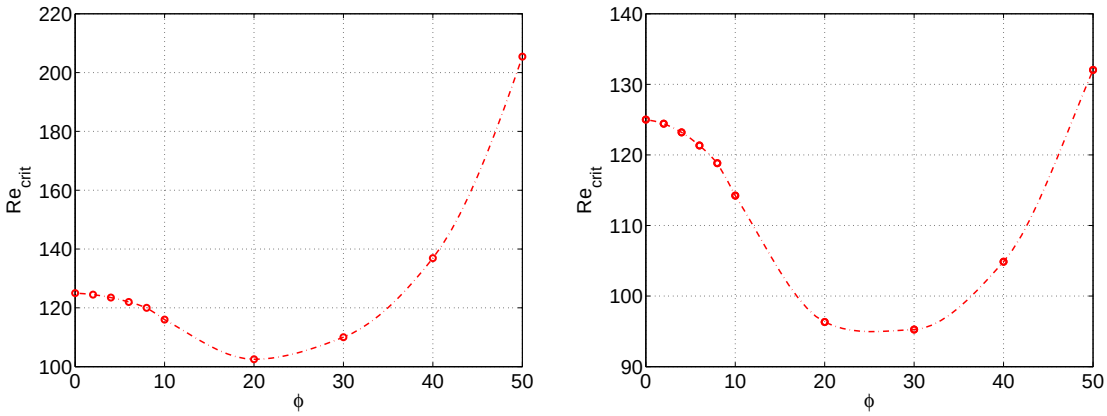

Figure 5.13: Thin disc $\chi = \infty$. Threshold of the Hopf instability as a function of the inclination angle ϕ. Left figure: $Re = Ud/\nu$, right figure: $Re = Ud\cos(\phi)/\nu$.

Afterwords, the threshold starts to grow rapidly. The growth is partly due to the definition of the Reynolds, which does not account for the decreasing perpendicular cross section of the disc. Nevertheless a qualitatively similar curve is obtained if the Reynolds is based on $d\cos(\phi)$.

Table 5.1 reports the values of the Strouhal number at the threshold of unsteadiness. In calculation of the Strouhal numbers the diameter of the disc was chosen as the characteristic length scale (not its projection on the plane perpendicular to the flow). As can be inferred from the table, the Strouhal number at the threshold of instability triggering the periodic state after initial decrease observed for $\phi = 10^o$, grows with the inclination angle. In agreement with the observation of Calvert (1967), we noticed the increase of the strength of the vortex structures (level of vorticity) with the inclination ϕ. The Strouhal number varies significantly only in the close proximity of the onset of unsteadiness (see Figure 5.14). We therefore compare the Strouhal numbers obtained relatively far from the threshold, at $Re = 250$, for inclination angles varying from 0^o to 40^o with the values obtained by Calvert (1967) at Reynolds numbers between 3500 and 5000, assuming that the Strouhal number no longer varies in the turbulent domain. As can be seen in Figure 5.15, our data is in good agreement with the experimental results.

The periodic state with planar symmetry was observed to persist upon the increase of the Reynolds number for all considered angles of inclination $\phi > \phi^*$ until the transition to chaos.

As already mentioned in the caption of Figure 5.14, we evidenced chaotic states for disc inclinations of 10^o and 20^o starting from $Re = 250$. As can be seen in Figure 5.16 the transition to chaos breaks both the periodicity and the planar symmetry of the wake.

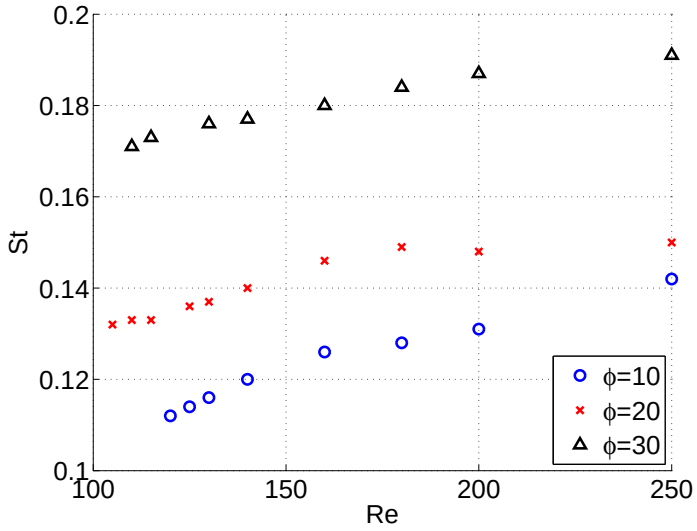

Figure 5.14: Strouhal number as a function of the Reynolds number. For $Re > 150$ the Strouhal number varies slowly with the Reynolds number. For $\phi = 10^o$ and 20^o the flow is already chaotic and $Re = 250$. The represented Strouhal number corresponds to one of the two dominant peaks of the frequency spectrum.

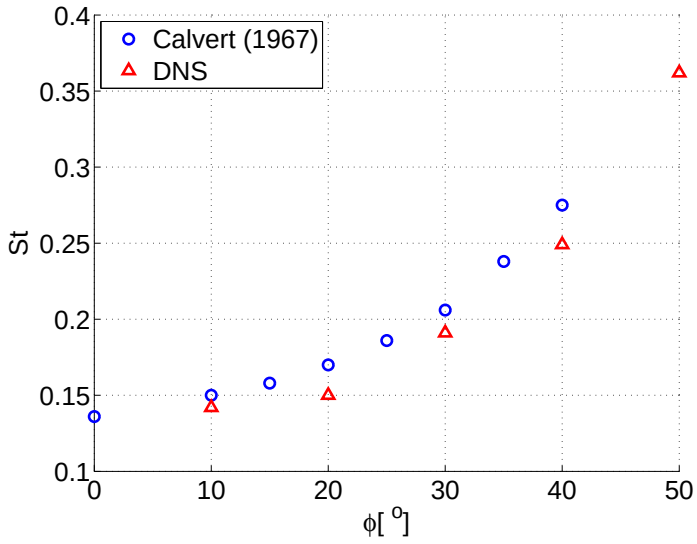

Figure 5.15: Strouhal number as a function of the inclination angle ϕ. Comparison of numerical results obtained at $Re = 250$ with the values given by Calvert (1967) obtained at Reynolds numbers between 3500 and 5000.

ϕ [^{o}]	Re_{crit}	St
0	125.2	0.120
10	116.1	0.113
20	102.6	0.132
30	110.0	0.171
40	136.9	0.239
50	205.4	0.352

Table 5.1: Critical Reynolds and Strouhal number at the onset of the periodic state as a function of the inclination angle ϕ.

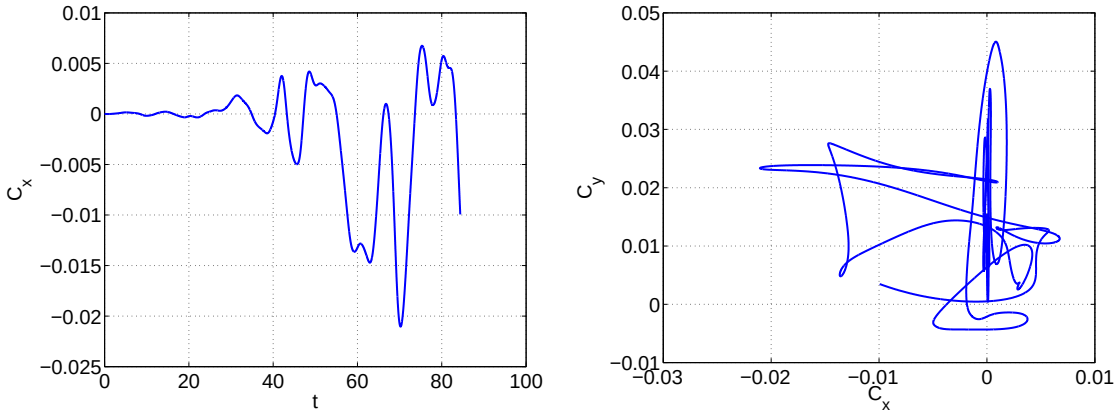

Figure 5.16: Thin disc $\chi = \infty$ inclined by $\phi = 10^o$. Chaotic state at $Re = 300$. Left figure: x- component of the lift coefficient as a function of time, right: x versus y- component of the lift coefficient.

5.4.3 Flat cylinder of the aspect ratio $\chi = 6$ inclined to the free stream direction

The thresholds of the Hopf bifurcation were determined by experimental measurement in the wake of a flat cylinder $\chi = 6$. The angle of inclination of the cylinder, measured as the angle between its axis of symmetry and the free stream direction, was varied from 0^o to 15^o. We estimate the precision with which we could set the inclination of the cylinder to be $\pm 2^o$. At the same time, these thresholds were computed by direct numerical simulation of a cylinder of the same aspect ratio for an extended range of inclinations going from 0^o to 60^o in the same as for the disc in the previous section.

The transition scenario, found numerically (see Chrust *et al.*, 2010) and experimentally (see Szaltys *et al.*, 2011), for the considered flat cylinder placed perpendicularly in a uniform flow was discussed in chapter 5.1. It is qualitatively the same as for a thin disc. Theoretically, the symmetry plane selected by the first bifurcation in numerical simulations is arbitrary and depends only on initial conditions. This is not the case in experiments. The mounting (see

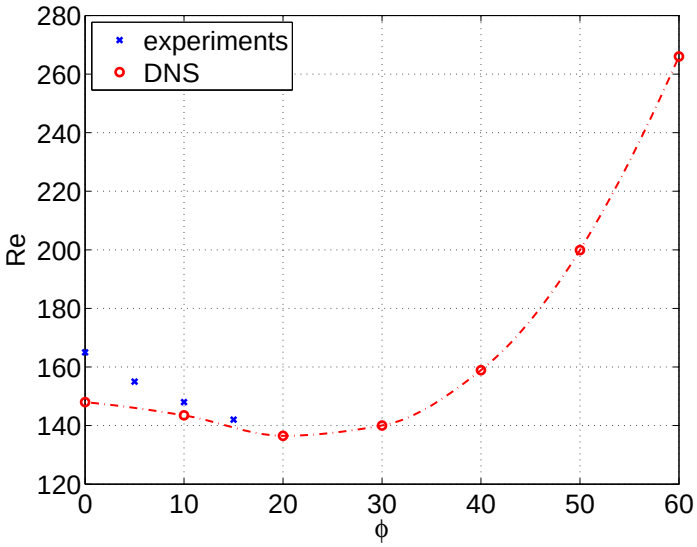

Figure 5.17: Flat cylinder $\chi = 6$. Threshold of the Hopf bifurcation as a function of the inclination angle ϕ. ($Re = Ud/\nu$.)

Figure 5.7) selects the symmetry plane. In our case, the tubes holding the cylinder lay in a vertical plane aligned with the free stream direction. Their influence forced the symmetry plane to lie in this plane (see Figure 5.3). Gumowski *et al.* (2008) demonstrated for the case of a sphere, that if the plane defined by the holding is not aligned with the free stream direction, the symmetry plane selected at the primary bifurcation is distorted. Moreover, this distortion is conserved by the secondary Hopf bifurcation. Szaltys *et al.* (2011) found that the same occurs for the flat cylinder. The orientation of the symmetry plane selected by the mounting remains unaltered until the transition to chaos.

The thresholds of the Hopf bifurcation obtained numerically and experimentally are compared in Figure 5.17. In experiments, the thresholds were found basing on the fluorescein dye visualization. The results are in acceptable agreement, namely, at $\phi = 15^o$ the agreement is very good. As the angle of inclination is increased, the intensity of the vortex shedding rose facilitating the determination of the thresholds. For the case of a cylinder perpendicular to the free stream direction, the onset of visible shedding of vortex structures was preceded by the ondulation of the two counter-rotating vortices. The difference with the numerical result might stem from the fact that it was difficult to precisely capture their onset. Also the stabilizing effect of the holding was probably stronger. We could not perform experiments for inclination angles exceeding 15^o due the limitations of our holding. However, as can be inferred from the numerical results, thresholds of the Hopf bifurcation follow a similar trend as for thin discs. The threshold initially decreases and reaches the minimum for $\phi^{min} \approx 20^o$ before it starts to grow rapidly. The Strouhal numbers found numerically at the instability thresholds are given, along with the critical Reynolds numbers, in Table 5.2.

ϕ [^{o}]	Re_{crit}	St	St^{exp}
0	150.0	0.120	0.158
5	–	–	0.177
10	143.5	0.117	0.179
15	–	–	0.172
20	136.5	0.130	–
30	140.0	0.154	–
40	158.9	0.205	–

Table 5.2: Strouhal number at the onset Re_{crit} of the periodic state as a function of the inclination angle ϕ for a cylinder of the aspect ratio $\chi = 6$. St indicate numerical and St^{exp} experimental results, respectively. Strouhal numbers found experimentally are higher than those predicted by our DNS. Similar overestimation of Strouhal numbers was observed for a sphere. It is related to the blockage effect of the water tunnel.

5.5 Conclusions

We have demonstrated that the transition scenario predicted by DNS for flat cylinders of aspect ratio $\chi \geq 4$ is purely theoretical. As evidenced for the case of a disc, a slight disturbance of the axisymmetry of the problem, results in a significant change. Above the Hopf bifurcation threshold, the inclination of the disc does not select the direction of the mean lift but of the plane of its oscillations. The long transients of the phenomenon indicate a weak stability of the resulting state making it unlikely to resist experimental disturbances. Moreover, for the inclination angles exceeding about 4 degrees, the periodic state without planar symmetry, characteristic for a disc placed perpendicularly to the free stream direction, is suppressed even in numerical simulations. It is replaced by a periodic state with a planar symmetry qualitatively similar to the one observed in the wake of a sphere. We thus infer that the impossibility to observe experimentally the theoretical scenario for the considered geometries (see Fabre *et al.*, 2008) stems from the influence of the holding and of a small uncontrolled inclination of the cylinder in the realized experiments. Their effect is to force the symmetry plane of the wake for all states present in the transition scenario until the appearance of chaos.

At the same time, we investigated the effect of the inclination on the Hopf bifurcation threshold in the wake of a disc and a cylinder of the aspect ratio $\chi = 6$. Our numerical and experimental results are in good agreement for an inclined flat cylinder. The dependence of the transition thresholds on the Reynolds number is a non-monotonic function of the inclination angle. Both for a disc and a flat cylinder, a small inclination initially promotes the transition to the periodic state. However, beyond a certain inclination, which for both configurations was found to be the same, $\phi^* \approx 20^o$ the trend reverses as the inclination tends to have a stabilizing effect.

Chapter 6

Numerical simulation of the dynamics of freely moving discs

The content of this chapter was submitted to the Physical Review Letters.

6.1 Present status of knowledge

An efficient numerical method has allowed recently Jenny & Dušek (2004) to identify the complete scenario of the transition of freely falling spherical particles. It was demonstrated, that a sequence of well defined ordered states, depending on two dimensionless parameters, the Galileo number (see Eq. 2.24) and the solid to fluid density ratio, and changing through bifurcations, lead to deterministic chaos. The predicted scenario was confirmed to a large extent by experiments of Veldhuis & Biesheuvel (2007), who evidenced qualitatively similar transitional regimes (see chapter 1.7). In contrast with spherical particles, few numerical results exist for non-spherical bodies. In this chapter, we focus our attention on freely falling infinitely thin discs (we recall that a disc is defined as a flat cylinder of infinite aspect ratio $\chi = \infty$). Examples of motion of such bodies can be found in a daily life. Everybody has observed the fluttering or tumbling motion of confetti falling in the air or of a coin dropped in water. It is intriguing in its own right, but also important for the understanding of particle dispersion in many practical applications. Field *et al.* (1997) interpreted the variety of motion regimes of falling discs, observed in their own and earlier (Willmarth *et al.*, 1964; Stringham *et al.*, 1969) experiments, from the viewpoint of the theory of deterministic chaos (Strogatz, 1994). They identified four distinct states depending on two dimensionless parameters, the non-dimensionalized moment of inertia I^* (see Eq. 2.28) and the Reynolds number based on the mean vertical velocity and presented a state diagram identifying the stability regions of these states in the $Re-I^*$ parameter plane. For low Reynolds numbers the fall was found to be steady and vertical. The wake remained axisymmetric. Depending on I^*, for small values, a periodic fluttering or, for higher, a tumbling state was observed. Both were found to be planar. The fluttering state was characterized by the authors as periodic oscillations, with the disc inclination angle ϕ, defined as an angle between its normal and the vertical direction, never exceeding $\pi/2$. The tumbling motion was described as a side-way

drifting of a disc rotating in a given direction. The authors couldn't determine if this state is periodic. The two mentioned states were found to be separated by a region of 'chaotic' states characterized by an intermittent switching between flutter and tumbling. More recently, Fernandes *et al.* (2007) found experimentally small amplitude states, that were described later by Ern *et al.* (2012) as "possibly irregular or even chaotic". The observed amplitudes were so small that, initially, these states were considered as vertical (see Fernandes *et al.*, 2007). The more recent identification as chaotic states stems from the results of Direct Numerical Simulations carried out by Auguste (2010), who reported the existence of small amplitude non-vertical regimes preceding the appearance of large planar oscillations. Zhong *et al.* (2011) identified, experimentally, a new type of motion. They observed that, for discs with very small inertia I^*, the initial planar zigzag motion (flutter) is not stable and that non-planar, spiral trajectories develop instead. To sum up, four different ordered regimes have been identified so far, but a systematic investigation of their stability and of the transitions between them is still missing.

Numerical simulations allow an exact control of boundary conditions and provide very detailed mathematical solutions. In experiments, it is difficult to precisely control the physical properties of the system and the initial and boundary conditions. For instance, the fluid remains non-quiescent unless it was left to settle down for a sufficiently long time in between two observations. Moreover, measurements of physical quantities in a non intrusive manner are far from being trivial in most cases. As a result, experimental observations reflect a much more complex reality. They are less reproducible and less suited for theoretical analysis than Direct Numerical Simulation. For this reason, experiments and simulations are complementary and both are needed for a perfect understanding of the phenomena (see Jenny & Dušek, 2004; Veldhuis & Biesheuvel, 2007; Horowitz & Williamson, 2010*b*, for the case of a sphere). While in the case of a spherical body numerical results preceded the experiment, the above cited work of Willmarth *et al.* (1964); Stringham *et al.* (1969); Field *et al.* (1997) and Zhong *et al.* (2011) opened the way for the investigation of the behavior of discs. The problem of both accurate and efficient, three-dimensional, simulation of falling discs and, more generally, flat bodies turned out to be a real numerical challenge (Ern *et al.*, 2012). In this chapter, we fill this gap by employing our spectral–spectral-element method described in chapters 2 and 3 to systematically explore the transition scenario of infinitely thin discs freely moving in an initially quiescent Newtonian fluid.

6.2 Specific mathematical formulation and implementation of the numerical method

In this section we briefly specify the general mathematical formulation and the numerical implementation described in chapters 2 and 3. An infinitely thin disc of finite mass m can be considered to be made of an infinitely dense material and to have a zero volume. From this viewpoint the buoyancy effects would be negligible as it is the case for experiments in the air. In water, however, the solid/fluid density ratio of usual materials remains small and buoyancy cannot be neglected. A more general interpretation of the formula (2.54) thus consists in writing

$$U_{ref} = \sqrt{m^* g_{eff\,disc} d}, \tag{6.1}$$

where the effective gravitational acceleration is defined as

$$g_{eff\,disc} = \left| 1 - \frac{\rho}{\rho_s} \right| g. \tag{6.2}$$

Note that this definition is not the same as the one given Eq. (2.6) which is that used for spheres in Jenny *et al.* (2004) where, specifically, very light spheres of density much smaller than that of the fluid were focused on and which can be applied to objects made of very light materials. In the present case, thin discs made of a considerably lighter material than the fluid are to be considered as objects of zero non-dimensionalized mass and only solid density starting from ρ_s slightly smaller than ρ to $\rho_s \gg \rho$ is of interest. Such a definition makes it possible to account for experimental implementations using materials of comparable density to that of the fluid allowing larger spatial scales for the same Galileo numbers.

The solved equations are Eqs. (2.56, 2.57) where the Galileo number is

$$G = \frac{\sqrt{m^* g_{eff\,disc} d^3}}{\nu}. \tag{6.3}$$

and the movement equations of the solid body (2.51) through (2.53). Here we consider homogeneous discs for which Eq. (2.29) applies and $\alpha = 2$.

The numerical method has been described in chapter 3. For the simulation of discs the spectral element decomposition of the axial - radial plane represented in Figure 4.1 was used. The detail of the mesh close to the disc is given in Figure 6.1. A still larger zoom on the elements at the edge of the disc is in Figure 4.2. The mesh 4.1 has, however, been modified, as compared to that in Figure 4.2 in order to allow for a variation of the radius of the spherical interface up to 3. Recall that the treatment of the interface requires that there are two concentric layers of spectral elements on both sides. The results of tests of the sensitivity of the simulation to the choice of the values of numerical parameters were given in section 3.12.4 (see Tables 3.11 and 3.12). They led us to the following choice of numerical parameters (see Figure 2.1 for the meaning of symbols): $L_u = 12d$, $L_d = 25d$ and $R_c = 8d$, 6 collocations points per spatial direction in spectral elements, $M = 15$ azimuthal modes and equal to the truncation of the spherical function expansion ℓ_{max}. For all the simulations the radius of the spherical interface was set equal to $1d$ as also indicated in Figure 6.1.

The two parameters, the Galileo number G and the dimensionless mass m^* define a two-parameter plane that was investigated in the domain $G \leq 500$ and $0 \leq m^* \leq 10$.

6.3 Results

DNS takes all physically relevant degrees of freedom into account, including those of the fluid flow, with a controlled accuracy. In spite of that, the numerical solution behaves like a low-dimensional dynamic system obeying bifurcation theory. This makes it possible to characterize its dynamics by a set of bifurcating asymptotic states. However, some caution is needed in their physical interpretation. They correspond to stable asymptotic regimes

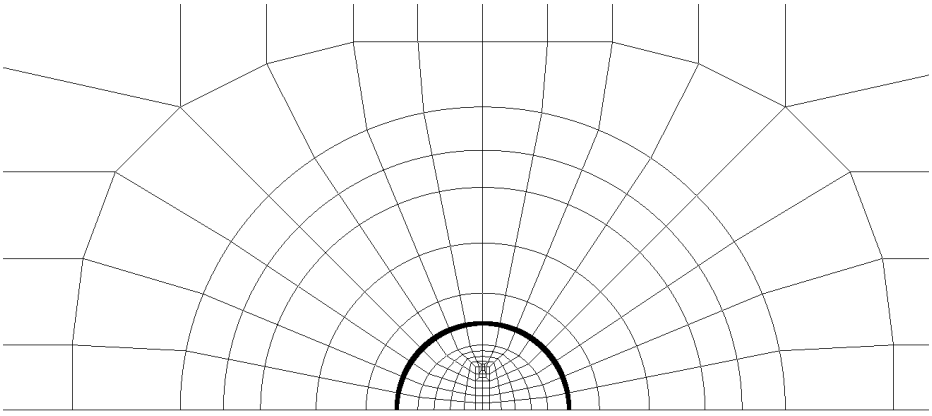

Figure 6.1: Thin disc $\chi = \infty$. Details of the spectral element discretization of the radial-axial plane of the computational domain. The interface at $R_s = d$ is marked by a thick line.

reached in an infinite time horizon by a system for a fixed set of state parameters. In practical situations "infinite" means extremely diverse time scales given by the stability of the state. The latter decreasing dramatically close to bifurcations and at the onset of chaos, not all bifurcating states are really observable in laboratory experiments.

This section is organized as follows. In the next sub-section 6.3.1 we present the morphology of the states identified in the investigated domain $25 \leq G \leq 500$ and $0 \leq m^* \leq 10$ of the parameter plane.In the section 6.3.2 we discuss the state diagram characterizing the transition scenario in the (m^*, G) plane. Finally we discuss the found transition scenario in section 6.3.3.

6.3.1 States present in the scenario of the transition to chaos

The scenario is characterized by a limited number of bifurcating states for which we attempt to provide a quantitative description in terms of the following quantities wherever they apply: the amplitude of the path oscillations in the horizontal direction Δs, the mean horizontal and vertical velocities u_h and u_z, and their amplitudes of oscillations A_{u_h} and A_{u_v}, respectively, the inclination angle ϕ, defined as the angle between the axis of the disc and the vertical direction and its maximum value ϕ_{max}, the angular velocity of rotation (about a horizontal axis) ω_h, the Strouhal number $St = fd/u_z$, where f is the oscillation frequency (obtained mostly from the horizontal velocity). The Reynolds number used by other authors (see Field *et al.*, 1997; Fernandes *et al.*, 2007) is obtained simply by multiplying the Galileo number by u_z.

The simplest state - steady vertical fall requires no further comments. It is characterized by $u_h = A_{u_h} = A_{u_z} = \phi_{max} = \omega_h = \Delta s = St = 0$. The terminal velocity $u_\infty = u_z$ equivalent to a constant terminal Reynolds number depends only on the Galileo number and can be obtained by a simple axisymmetric computation by determining the drag compensating the weight and buoyancy of the disc.

Periodic fluttering state

The trajectory of the fluttering state lies in a plane arbitrarily selected by initial conditions. The average direction of the trajectory is vertical and the disc center describes a zig-zagging path about the vertical direction. Its symmetry axis rotates with an angular velocity normal to the plane of the trajectory and oscillates about zero with values not exceeding 90 degrees. The period of oscillations of u_h, ω_h and ϕ is the same, while the vertical velocity u_z oscillates with a double frequency. The onset of this state was tracked by observing one of these parameters, usually the horizontal velocity u_h. Figure 6.2 shows the saturated fluttering state by representing u_h (top), u_z (middle) and ϕ (bottom) for $m^* = 0.1$ at $G = 90$. Both A_{u_h} and A_{u_z} in the saturated state have a constant non-zero value. The period of oscillations of u_h and ϕ is 2.606 (in units given by the non-dimensionalization described in chapter 2). This corresponds to a non-dimensional frequency of 0.384 and, with account of the mean value -1.241 of the vertical velocity, to a Strouhal number equal to $St = 0.309$. The vertical component of the velocity oscillates at twice the frequency of the horizontal component.

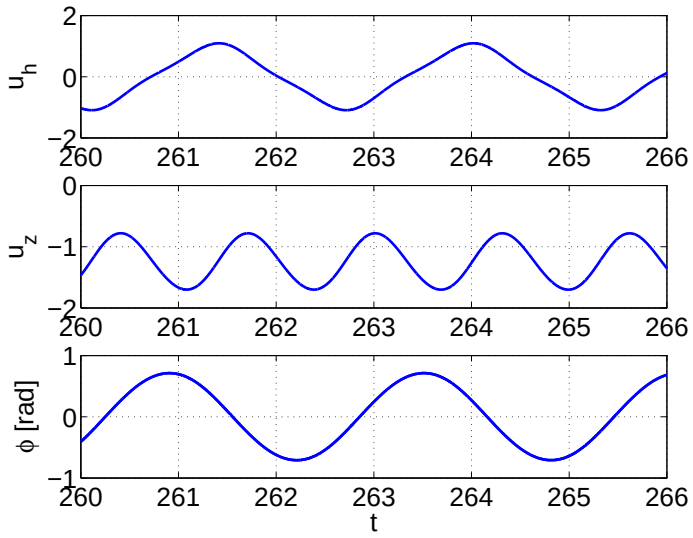

Figure 6.2: $m^* = 0.1$, $G = 90$. *(top)* Horizontal component of the velocity; *(middle)* vertical component of the velocity; *(bottom)* inclination of the disc defined as an angle between the disc axis and the vertical direction.

Figure 6.3 shows a typical trajectory. A disc oscillates periodically back and forth. The maximum angle of rotation ϕ_{max} does not exceed $\pi/2$. Otherwise, the disc flips over the edge and starts to tumble. It is interesting to note that the amplitude of the vertical velocity oscillations can exceed the mean value. E.g., for $m^* = 0.1$ and $G > 200$ we observed that, as the disc approached its extreme lateral position, it began to climb.

For small m^* ($m^* \leq 0.1$) the maximum inclination angle of the disc ϕ_{max} never exceeds $\pi/2$. E.g., for $m^* = 0$ it reaches a maximum value of slightly less than 24^o at $G = 200$ and decreases to 22^o at $G = 500$ (see Figure 6.5 a)). In contrast when the fluttering state gives way to tumbling (intermittent) the maximum angle grows to $\pi/2$ when the disc starts to

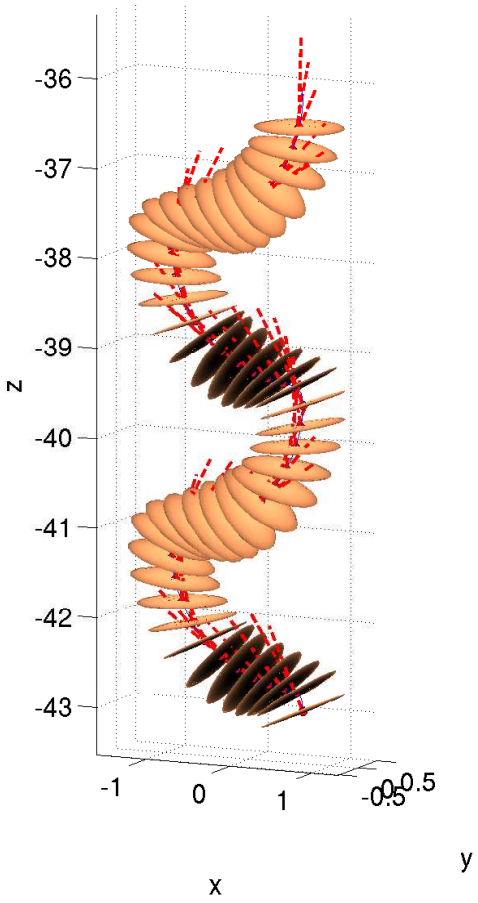

Figure 6.3: Fluttering periodic state, $m^* = 0.1$, $G = 200$, z – vertical position, x, y – horizontal positions as multiples of d. The red dashed line represents a half-axis of the disc.

tumble. This provides a useful method for delimiting precisely the stability of the fluttering state (see Figures 6.5 a) and c)).

Figure 6.4 shows the wake of a disc in a saturated periodic fluttering regime for $m^* = 0.1$ at $G = 200$ by representing the axial vorticity iso-surfaces at levels 0.9. In one oscillation period a pair of vortices is shedded from the disc, each with the opposite orientation.

Tumbling state

The flutter does not usually transits directly to a stable tumbling state but switches intermittently from flutter to tumbling which results in an intermittent chaos described in the next section. The exactly periodic tumbling state is characterized by the rotation of the disc over edge in one direction. This results in an oblique trajectory. The angular velocity ω_h and the horizontal velocity u_h are oscillating functions of time with a non-zero mean value characterizing the rotation direction and the horizontal drift. Two typical situations are

m^*	G	u_z	Δu_z	Δu_h	$\Delta\omega_h$	$\Delta s/d$	St	$\phi_{max}[rad]$
0	140	-1.376	0.271	1.024	1.381	0.271	0.426	0.380
0	150	-1.374	0.307	1.109	1.467	0.287	0.437	0.392
0	160	-1.362	0.333	1.177	1.526	0.298	0.446	0.401
0	170	-1.371	0.356	1.237	1.570	0.308	0.454	0.408
0	180	-1.367	0.377	1.296	1.608	0.317	0.464	0.414
0	200	-1.363	0.401	1.380	1.649	0.328	0.477	0.415
0	300	-1.343	0.476	1.682	1.712	0.370	0.528	0.407
0	400	-1.328	0.530	1.885	1.709	0.399	0.562	0.390
0	500	-1.292	0.546	2.035	1.693	0.411	0.598	0.380
0.05	75	-1.316	0.225	0.733	1.240	0.266	0.317	0.466
0.05	80	-1.307	0.292	0.854	1.420	0.299	0.326	0.523
0.05	90	-1.301	0.370	1.001	1.588	0.338	0.330	0.578
0.05	100	-1.285	0.423	1.108	1.6781	0.366	0.345	0.599
0.1	80	-1.250	0.408	0.991	1.648	0.370	0.304	0.685
0.1	90	-1.241	0.460	1.093	1.718	0.400	0.310	0.711
0.1	100	-1.232	0.502	1.181	1.759	0.427	0.306	0.731
0.1	200	-1.199	0.972	2.097	1.863	0.797	0.292	0.962
0.1	300	-1.255	1.333	2.778	1.876	1.199	0.246	1.102
0.1	400	-1.291	1.601	3.297	1.855	1.578	0.216	1.174
0.1	500	-1.339	1.839	3.759	1.826	1.974	0.190	1.227
0.25	90	-1.347	0.924	1.602	2.213	0.749	0.182	1.362
0.5	38	-1.166	0.106	0.343	0.865	0.209	0.208	0.555
0.5	50	-1.254	0.365	0.737	1.626	0.410	0.184	1.057
0.75	45	-1.271	0.284	0.595	1.482	0.379	0.154	1.040
0.75	50	-1.377	0.432	0.774	1.791	0.527	0.131	1.340
1	40	-1.222	0.160	0.396	1.107	0.287	0.160	0.867
2	34	-1.165	0.043	0.173	0.568	0.165	0.137	0.532
2	38	-1.243	0.095	0.267	0.856	0.251	0.123	0.822
10	45	-1.250	0.006	0.050	0.173	0.094	0.067	0.332

Table 6.1: Some quantitative data for selected periodic fluttering states. Meaning of symbols: u_z - mean vertical velocity, Δu_z, Δu_h, $\Delta\omega_h$ - amplitude of oscillations of the vertical and horizontal component of velocity and of the angular velocity, respectively, $\Delta s = \sqrt{(s_x^2 + s_y^2)}$ - maximum horizontal displacement, where s_x and s_y are displacements in the $x-$ and $y-$ direction, respectively, St - the Strouhal number and ϕ_{max} is the maximal inclination of the disc.

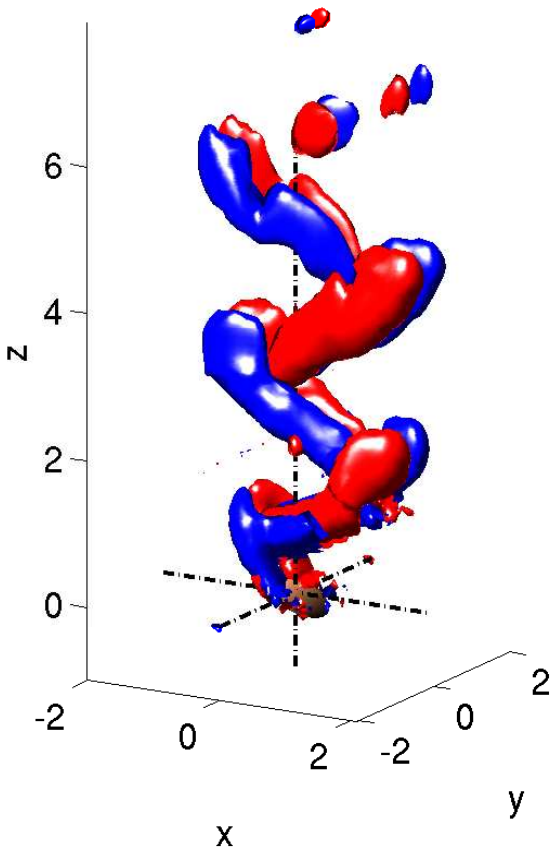

Figure 6.4: Fluttering periodic state, $m^* = 0.1$, $G = 200$. Axial vorticity iso-surfaces at levels 0.9.

encountered. For small values of $m^* < 0.75$ the disc go through distinct phases of a rotation and a flight over edge (see Figure 6.6). Figure 6.7 shows u_h (top), u_z (upper-middle), ω_h (bottom-middle) and ϕ (bottom) for $m^* = 0.5$ at $G = 160$. As can be seen from the figure, two (negative) peaks (a larger followed by a smaller one) correspond each to a half turn. During this phase, the disc does not practically fall and, during the first half turn, it reaches the maximal horizontal velocity. After completion of the turn, the angular velocity reaches a zero value. The horizontal velocity passes through a minimum before starting to increase gradually while the vertical velocity strongly accelerates. The rotation angle lies clearly midway between the dotted lines marking the vertical position of the disc axis, i.e. the disc axis is horizontal. For disc with substantial inertia the oscillations of the above mentioned quantities, that is u_h, u_z and ω_h, are practically harmonic (see Figure 6.8) and the ampli-

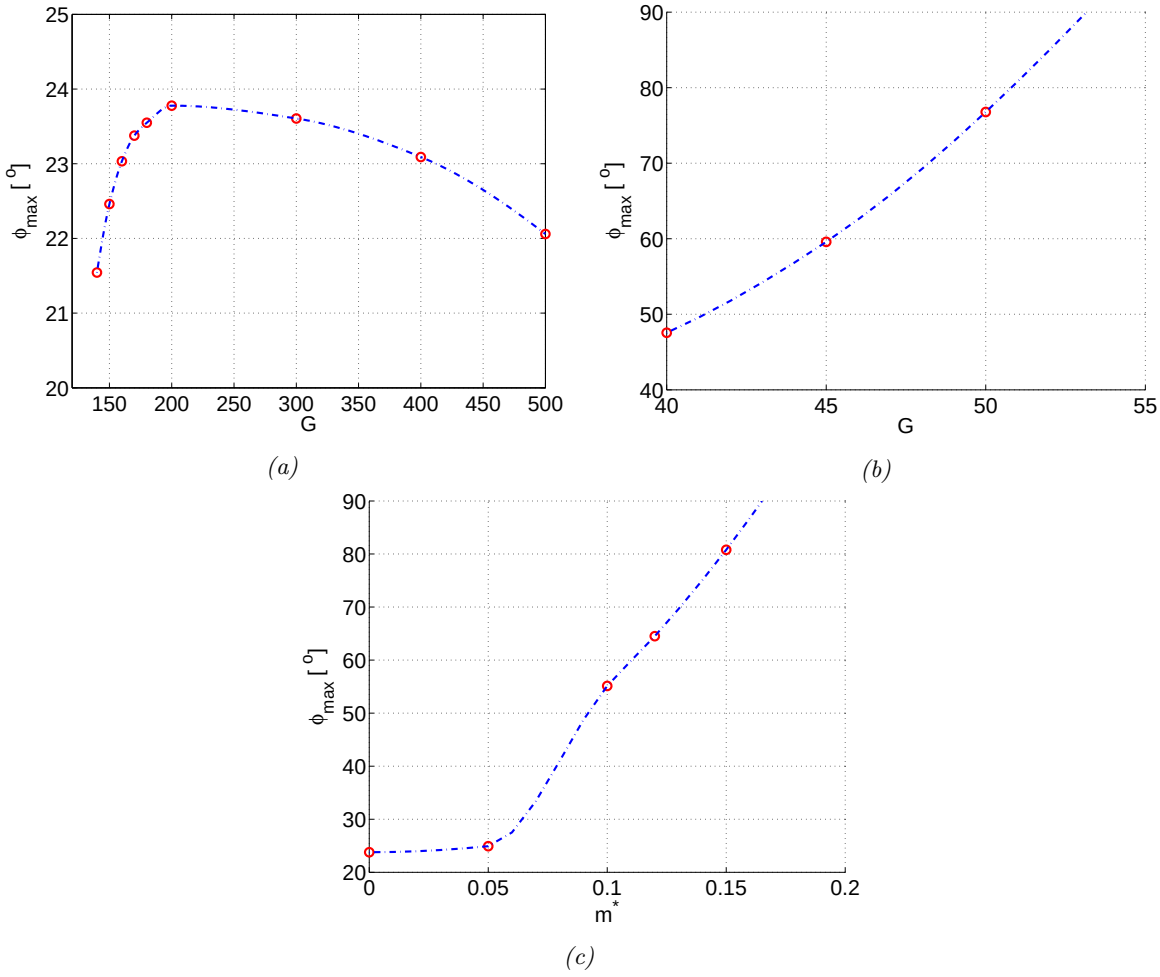

Figure 6.5: a) Fluttering periodic state, $m^* = 0$. Maximum inclination of the disc ϕ_{max} as a function of the Galileo number. b) Same as in Figure a) for $m^* = 0.75$. The limit of stability of the fluttering state can be estimated at $G \approx 53.5$. c) $G = 200$, maximum inclination angle as a function of m^*. The disc starts to tumble at $m^* \approx 0.163$.

m^*	G	u_z	Δu_z	u_h	Δu_h	ω_h	$\Delta\omega_h$	St
0.75	90	-1.224	0.504	-0.929	0.351	1.292	0.721	0.315
0.75	100	-1.202	0.534	-0.929	0.349	1.317	0.689	0.333
0.75	120	-1.159	0.485	-0.940	0.349	1.393	0.632	0.366
0.75	140	-1.126	0.472	-0.941	0.347	1.442	0.592	0.392
0.75	160	-1.101	0.466	-0.943	0.346	1.480	0.567	0.412
0.75	200	-1.067	0.461	-0.941	0.347	1.533	0.538	0.443
0.75	300	-1.014	0.451	-0.939	0.343	1.599	0.502	0.490
0.75	400	-0.987	0.449	-0.937	0.344	1.626	0.487	0.515
1	80	-1.267	0.424	-0.631	0.203	0.875	0.477	0.283
1	100	-1.213	0.397	-0.858	0.270	1.259	0.570	0.320
1	150	-1.139	0.367	-0.863	0.264	1.389	0.479	0.381
1	200	-1.099	0.359	-0.861	0.259	1.463	0.441	0.418
1	300	-1.059	0.352	-0.858	0.257	1.529	0.423	0.458
1	400	-1.035	0.353	-0.859	0.258	1.552	0.418	0.476
2	50	-1.412	0.283	-0.690	0.167	0.865	0.595	0.176
2	54	-1.399	0.280	-0.702	0.165	0.894	0.563	0.187
2	58	-1.374	0.264	-0.712	0.163	0.921	0.534	0.199
5	40	-1.497	0.158	-0.499	0.104	0.600	0.421	0.113
10	50	-1.474	0.079	-0.459	0.056	0.565	0.219	0.118
10	80	-1.419	0.061	-0.538	0.044	0.765	0.141	0.170
10	150	-1.330	0.047	-0.584	0.035	1.035	0.088	0.246
10	200	-1.297	0.045	-0.594	0.033	1.143	0.076	0.279

Table 6.2: Some quantitative data for selected tumbling states from the state diagram of Figure 6.20. Meaning of symbols: u_z, u_h and ω_h - mean vertical, horizontal and angular velocity, Δu_z, Δu_h, $\Delta\omega_h$ - amplitude of oscillations of the vertical and horizontal component of velocity and of the angular velocity, respectively, St - the Strouhal number.

tude of oscillations of the velocities is small compared to mean values. The disc describes a practically rectilinear oblique trajectory while rotating regularly about a horizontal axis.

Figure 6.9 shows the vortical structures in the wake of a disc in a tumbling regime for $m^* = 0.5$ at $G = 160$ by representing the axial vorticity iso-surfaces at levels 1.1.

Intermittent and tumbling - zigzagging regimes

For $m^* < 2$, the tumbling and periodic fluttering states are separated by a region of intermittent states. In this region none of both states is stable. The flutter is no longer limited to an amplitude smaller than 90^o and the tumbling is not yet stable enough to persist in a periodic regime. The rotation stops at irregular intervals and changes the direction. The duration of tumbling stages is clearly random in Figure 6.10 showing the horizontal velocity u_h (top) and angular velocity ω_h (bottom) for $m^* = 0.25$ at $G = 110$. As can be seen, the disc switches randomly the direction of the rotation and of the side-wise motion. The

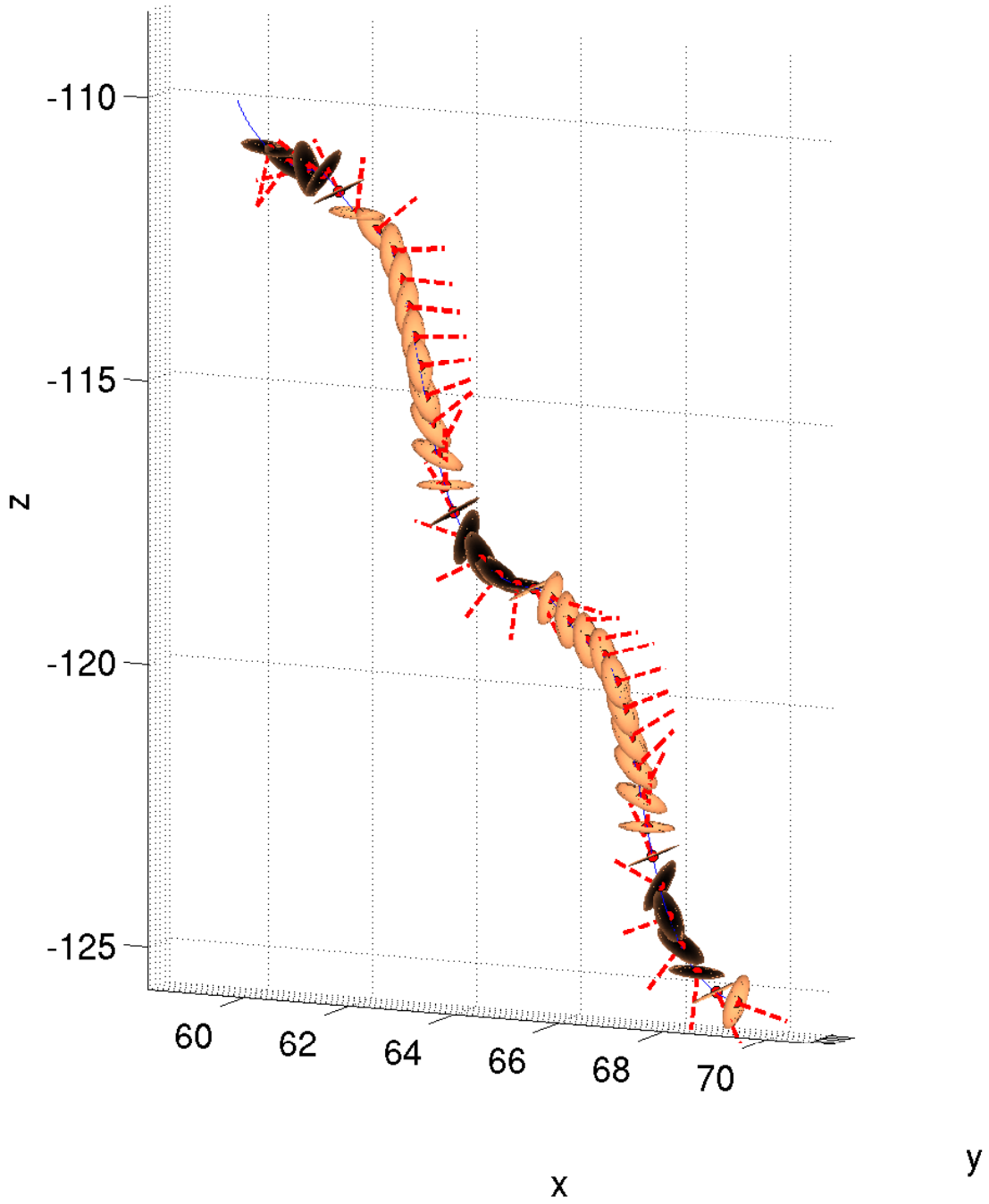

Figure 6.6: Tumbling state, $m^* = 0.5$, $G = 160$, z – vertical position, x, y – horizontal positions as multiples of d. The red dashed line represents a half-axis of the disc.

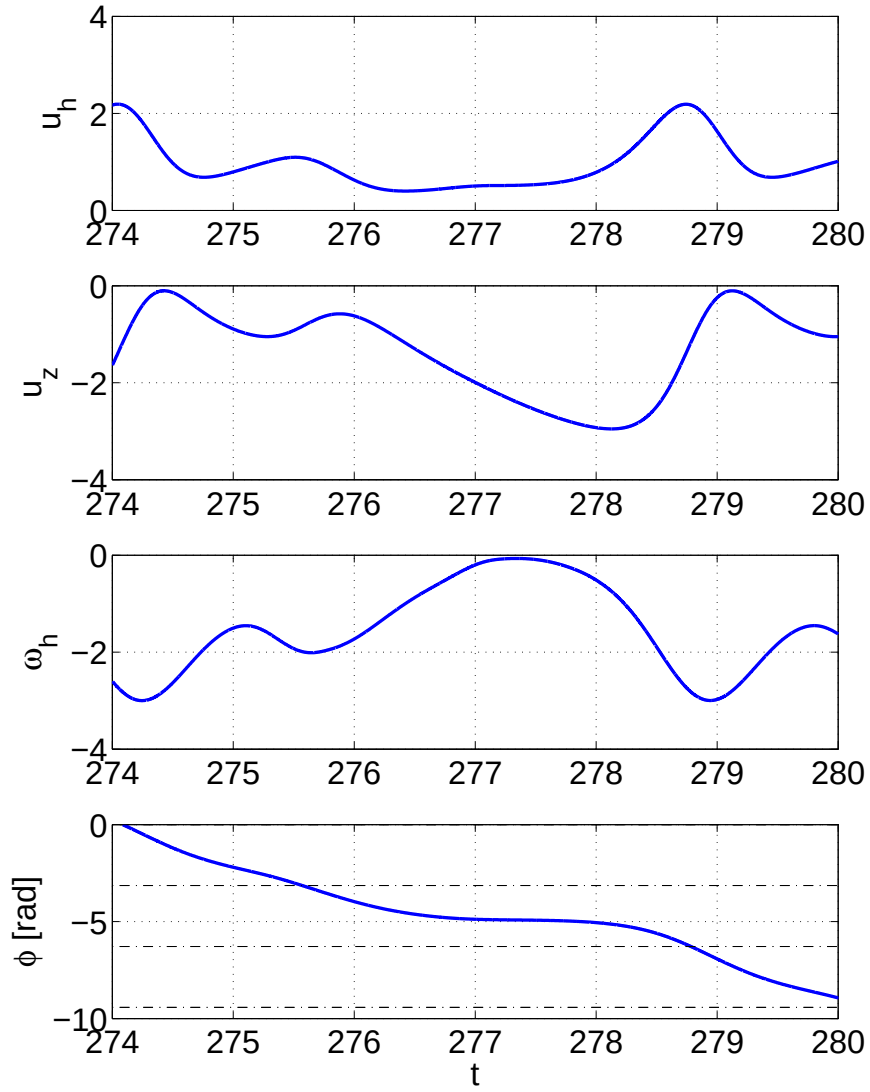

Figure 6.7: $m^* = 0.5$, $G = 160$. u_h: Horizontal component of the velocity; u_z: vertical component of the velocity; ω_h: angular velocity; ϕ: inclination of the disc defined as the angle between the disc axis and the vertical direction as functions of time. The dotted lines in the bottom graph mark the rotation by $k\pi$, where $k = 1, 2, ...$

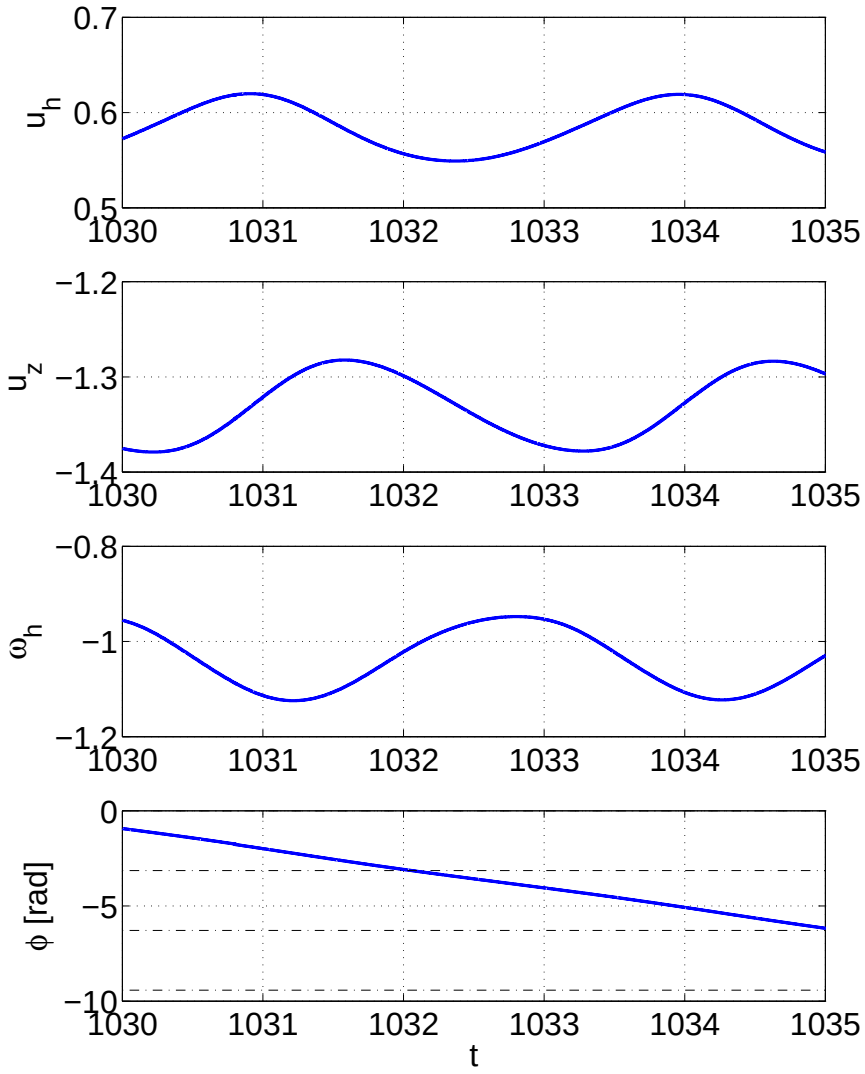

Figure 6.8: $m^* = 10$, $G = 150$. For the meaning of symbols, see caption of Figure 6.7.

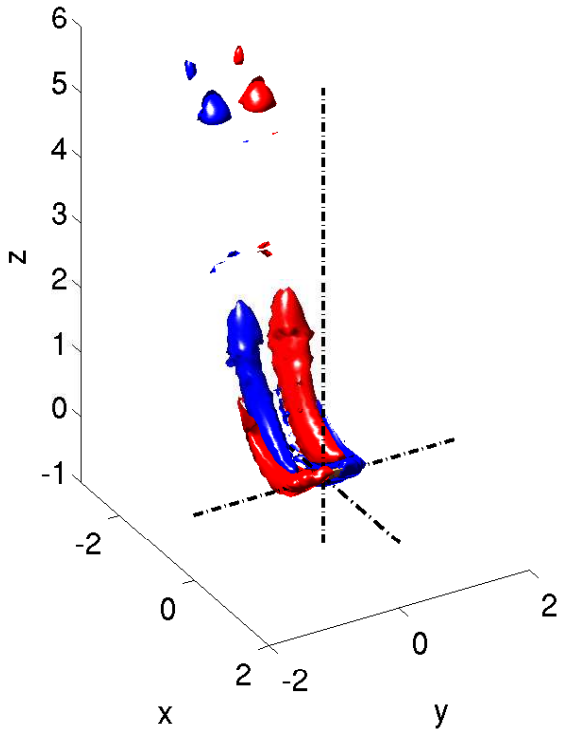

Figure 6.9: Tumbling state, $m^* = 0.5$, $G = 160$. Axial vorticity iso-surfaces at levels 1.1.

random trajectory of the disc is presented in Figure 6.13. It can be seen that at some point the disc has not enough inertia to continue turning in a given direction and therefore begins to turn in the opposite one.

At the same value of $m^* = 0.25$, but at higher Galileo number $G = 300$, we evidenced a periodic version of the same behavior. The switching of the sign of the angular and horizontal velocity occurs periodically. The simulation of Figure 6.12 was restarted using a periodic tumbling state as an initial condition. It shows that the disc tumbles by 2π periodically in opposite directions. This results again in a zig-zagging trajectory.

Quasi-vertical states

We found two distinct states characterized by a very small amplitude A_{u_h} of the horizontal velocity component and of other characteristics distinguishing them from a vertical fall (ω_h and ϕ), namely a periodic and a chaotic state. We call them the quasi-vertical periodic (QVP) and chaotic (QVC) states, respectively. A quasi-vertical periodic state resembles the periodic flutter. It is also planar. However, the Strouhal numbers are equal to about 1/3

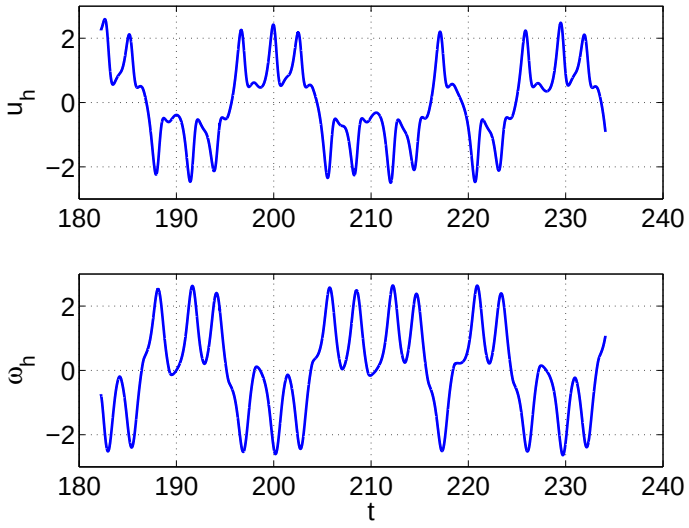

Figure 6.10: Intermittent state, $m^* = 0.25$, $G = 110$. *(top)* Horizontal component of the velocity; *(bottom)* the angular velocity ω_h.

the Strouhal numbers of the large amplitude flutter and the amplitude of the horizontal component of the velocity is small and its maximum observed value was $A_{u_h} < 0.05$. As a consequence the amplitude of the horizontal displacement of the disc was also very weak $\Delta s < 0.07d$. The maximum inclination ϕ_{max} of the disc never exceeded 3^o for all observed cases.

Figure 6.14 shows u_h (top), u_z (middle) and ϕ (bottom) for $m^* = 0.05$ at $G = 80$ as functions of the time. The linear growth rate of the amplification is $\gamma = 0.0228$. The amplitudes of the horizontal component of the velocity, as well as of the inclination angle begin to saturate to small asymptotic values $u_h \approx 0.022$ and $\phi_{max} \approx 0.009$ [rad] ($\approx 0.5^o$). The Strouhal number is equal to $St = 0.107$.

Very weak oscillations of the disc are hard to distinguish from disturbances caused by the initial perturbation of the surrounding fluid in experiments. For $m^* = 0$, the interval of periodic quasi-vertical regimes is very limited and the trajectories become chaotic and fully three dimensional. Figure 6.15 shows the onset of a typical chaotic quasi-vertical trajectory. For all the investigated cases, the trajectories displayed only a weak departure from the vertical trajectory ($< 0.1d$ for a vertical distance of $100d$). The maximum inclination angle was always $\phi_{max} < 5^o$ and the horizontal component of velocity was $u_{h_{max}} < 0.08$. Subsequently, for higher Galileo numbers the periodic flutter, described above, appears. It was demonstrated that for $m^* = 0$ this state co-exists with the quasi-vertical chaotic state for $G \approx 130 - 180$ and for $m^* = 0.05$ it co-exists with the quasi-vertical periodic and the steady vertical state. It can be conjectured that the competition of two pairs of complex conjugate eigenvalues related to the frequency of quasi-vertical periodic and of the periodic fluttering state might explain the early onset the quasi-vertical chaotic state.

The Strouhal numbers based on the frequency of oscillations of u_h for the quasi-vertical

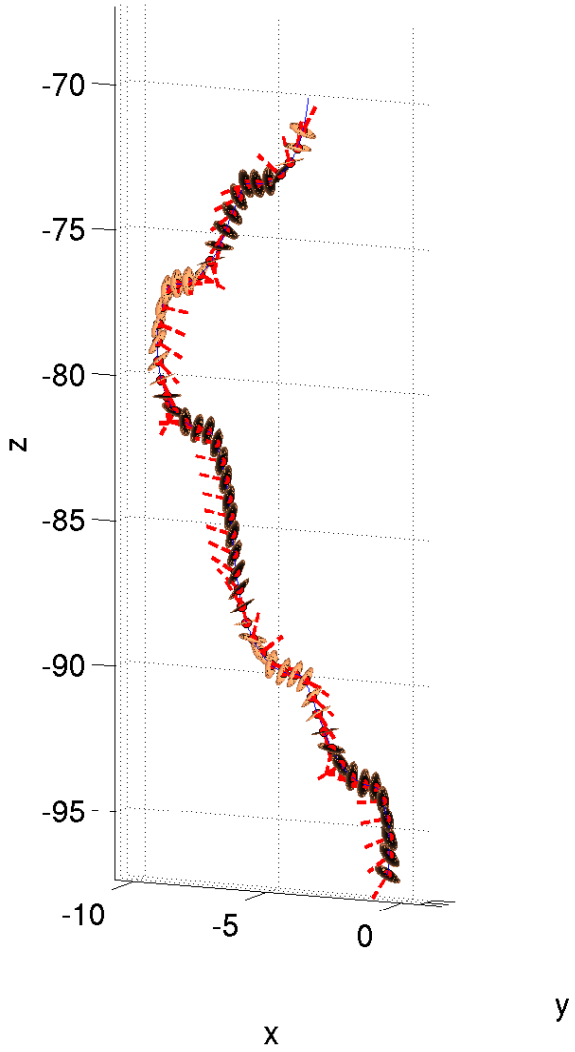

Figure 6.11: Intermittent state, $m^* = 0.25$, $G = 110$, z – vertical position, x, y – horizontal positions as multiples of d. The red dashed line represents a half-axis of the disc.

periodic states and the periodic flutter as a function of the Galileo number for $m^* = 0$ are represented in Figure 6.16. For infinitely light discs, both states are present. Two dash-dotted lines delimit the quasi-vertical chaotic region. The blue dashed line marks the lower limit of the appearance of the periodic flutter.

Three-dimensional states

Zhong *et al.* (2011) evidenced experimentally the existence of 'spiral' states in the transition scenario of thin discs. They identified two new types of motion, which they call spiral and transitional states, for discs having small moments of inertia I^*. They observed that the

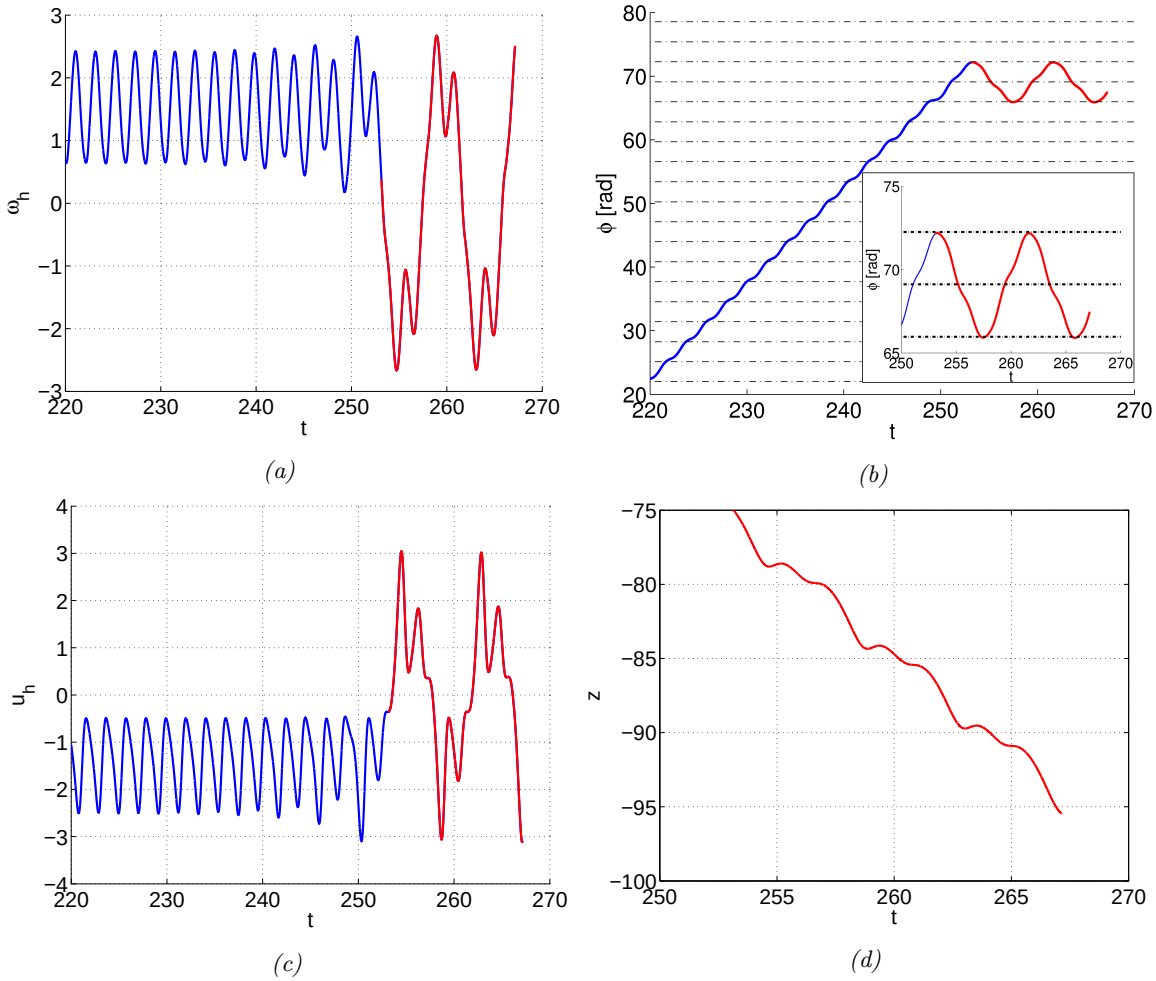

Figure 6.12: $m^* = 0.25$, $G = 300$. Subharmonic transition from the tumbling to the tumbling-zigzagging state. a) angular velocity ω_h; b) inclination angle ϕ in radians; c) horizontal component of the velocity u_h; d) vertical position z. The dotted lines in the graph b) mark the rotation by $k\pi$, where $k = 1, 2, ...$

m^*	G	u_z	Δu_z	Δu_h	$\Delta\omega_h$	Δs	St	$\phi_{max}[rad]$
0	90	-1.439	0.003	0.046	0.019	0.043	0.105	0.019
0	100	-1.444	0.004	0.055	0.030	0.061	0.100	0.022
0.05	85	-1.436	0.002	0.036	0.014	0.037	0.107	0.015

Table 6.3: Some quantitative data for selected quasi-vertical periodic states. For the meaning of the symbols see caption of Table 6.1.

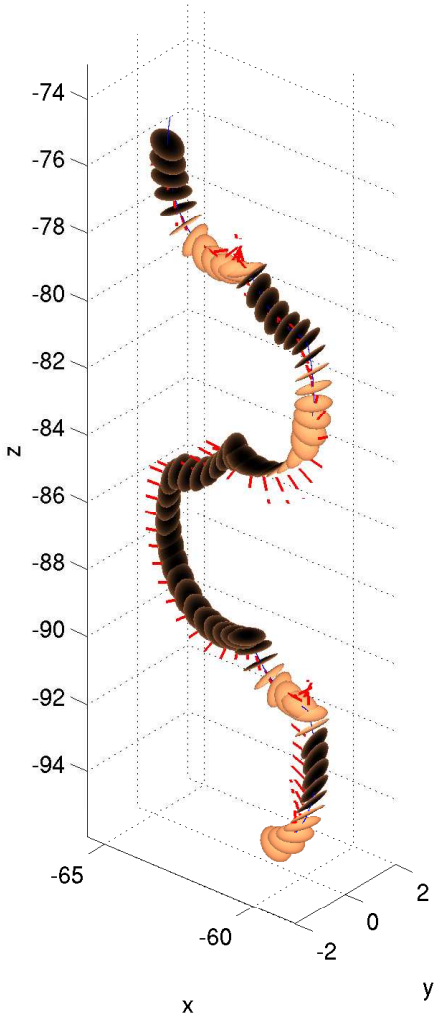

Figure 6.13: Tumbling-zigzagging state, $m^* = 0.25$, $G = 300$, z – vertical position, x, y – horizontal positions as multiples of d. The red dashed line represents a half-axis of the disc.

initial planar zigzag motion is destabilized by the growth of a secondary oscillation in the normal direction. The disc starts to rotate about its symmetry axis which leads eventually to a spiral motion. They characterize the found states using a factor ϵ expressing the ratio of the short axis to long axis of an ellipse resulting from the projection of trajectories on a horizontal plane described during one period. The planar motion corresponds to $\epsilon = 0$ and the spiral motion corresponds to $\epsilon = 1$. The transitional states correspond to intermediate values of ϵ.

We also evidenced similar states in our DNS. For $m^* = 0.05$ (which corresponds to $I^* = 3.125E - 03$) we observed that the planar zig-zag state quickly becomes unstable and

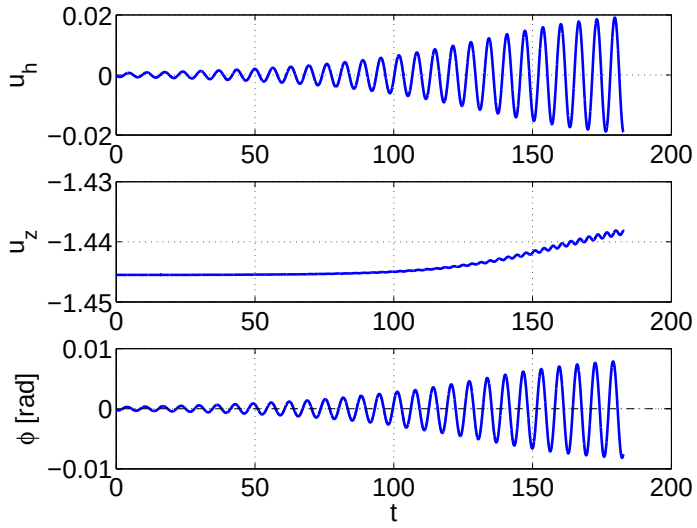

Figure 6.14: $m^* = 0.05$, $G = 80$. u_h: horizontal component; u_z vertical component of the non-dimensionalized velocity; ϕ inclination of the disc defined as the angle between the disc axis and the vertical direction in radians

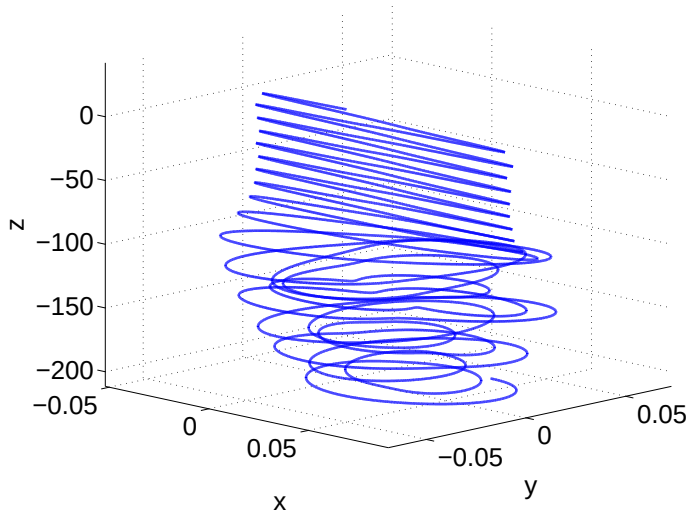

Figure 6.15: $m^* = 0.0$, $G = 120$. Quasi-vertical chaotic trajectory of the disc. z – vertical position, x, y – horizontal positions as multiples of d.

a transition to the spiral state takes place. Figure 6.17 shows the spiral trajectory found for $m^* = 0.05$ at $G = 300$. It is characterized by a constant angle of inclination of the disc equal to $\phi \approx 25^o$. The disc rotates about its axis with a constant angular velocity $\omega_z = 0.635$. The projection of the trajectory on the horizontal plane is a circle of radius $r/d = 0.37$. The vertical component of velocity is equal to $u_z = -1.07$. The Strouhal number

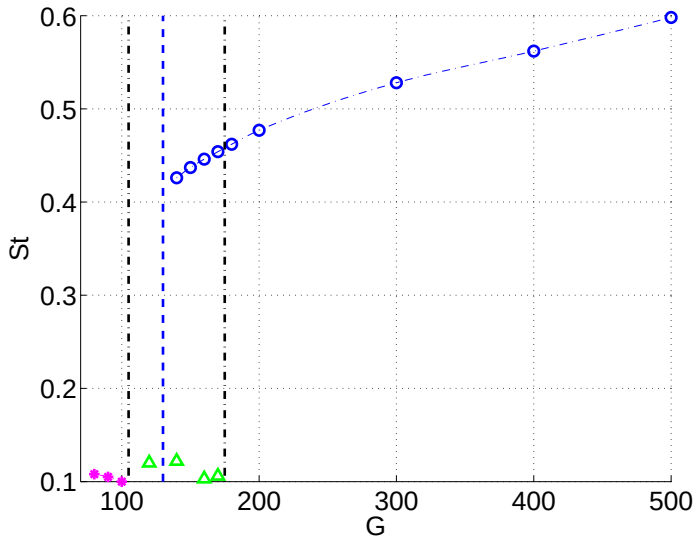

Figure 6.16: Strouhal number as a function of the Galileo number. Magenta markers - quasi-vertical periodic state; green markers - quasi vertical chaotic state, the Strouhal number was estimated using the main peak of the frequency spectrum and the mean vertical velocity; blue markers - periodic flutter state. The dash dotted lines delimit the interval of quasi-vertical chaotic states, the dashed line represents the lower limit of stability of the flutter.

based on the frequency of oscillations of the horizontal component of the velocity and on the vertical velocity is $St = 0.533$. Figure 6.18 shows the wake by representing the axial vorticity iso-surfaces at levels 0.35.

For other investigated values of $m^* < 0.5$ the departure of trajectories from the plane was extremely slow especially for low values of Galileo numbers and led to transitional states, which can all be expected to reach the established spiral motion. Zhong *et al.* (2011) reported the existence of three dimensional states only for $m^* < 0.13$. We found that for a sufficiently high Galileo number the planar trajectories become unstable whatever the non-dimensionalized mass $0 \leq m^* \leq 10$. In particular, we found that the tumbling state has its spiral counter-part, which can be called spiral tumbling state (ST). Its trajectory, found for $m^* = 0.5$ at $G = 400$, is represented in Figure 6.19. The projection of the trajectory on the horizontal plane describes a large circle of radius $r/d = 13$. The pitch angle of the spiral is equal to $\alpha = 42.5^o$. Other characteristics are summed up, together with those of the spiral state described above in Table 6.4.

6.3.2 State diagram

We swept the whole (m^*, G) parameter space in the range represented in the state diagram of Figure 6.20. The simplest state, stable at low values of G, is the vertical fall at a constant terminal velocity. The disc axis remains parallel to the vertical direction and all flow characteristics are steady. The state is a fixed point in terms of bifurcation theory. It is

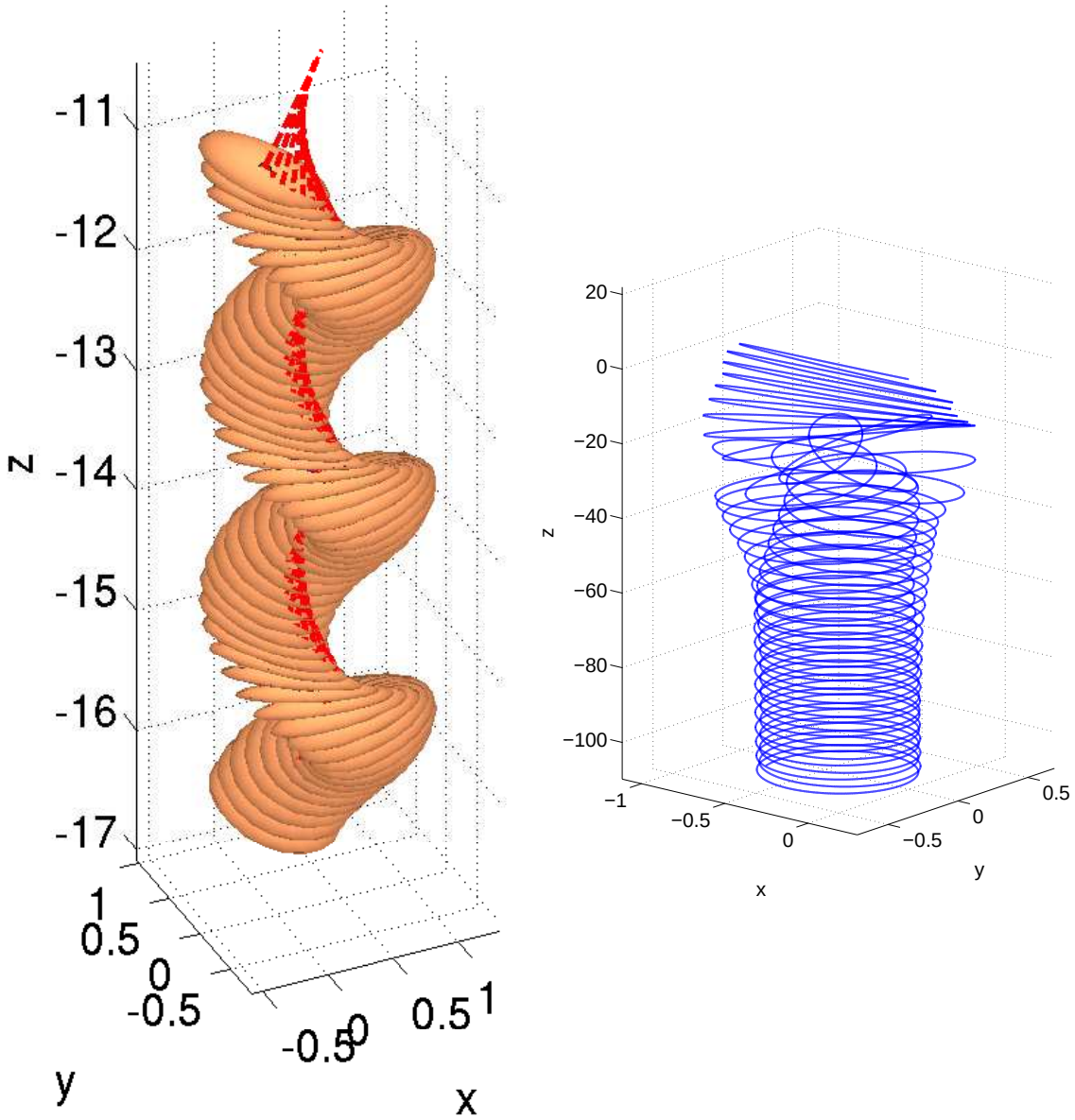

Figure 6.17: $m^* = 0.05$, $G = 300$; Left: spiral state; Right: trajectory showing transition from planar periodic fluttering state to a spiral state.

regime	m^*	G	Re	$\Delta Re/Re$	f	$\phi[^o]$	$\alpha[^o]$	r/d
spiral	0.05	300	320	0	0.57	24.9	0	0.37
ST	0.5	400	425	0.99	0.26	–	42.5**	13

Table 6.4: Some quantitative data for selected three dimensional regimes in diagram 6.20. ST: spiral tumbling; spiral: spiral state. Re: mean Reynolds number, $\Delta Re/Re$ relative amplitude of fluctuations of vertical velocity, f: non-dimensional frequency (in units $\sqrt{|m^* - V^*|g/d)}$, ϕ inclination angle of the axis (maximum for periodic variation), α mean angle w.r.t. vertical direction , r/d: horizontal deviation from the vertical direction: maximum for flutter, constant horizontal radius of trajectory for spiral regimes, ** pitch angle of a spiral trajectory).

characterized by a zero horizontal velocity, a zero angular velocity and a zero angle of the disc axis with respect to the vertical direction. Any of these quantities can be used for monitoring the stability of this state. For the case of a disc even the primary instability presents complex features, in contrast to a spherical body (for which it was of a regular type). This instability was investigated for increasing G for 10 values of m^* ranging from zero to 10.

The bifurcation responsible for the loss of stability of the steady state is of the Hopf type for all m^*. It is sub-critical for m^* between 0.1 and 1, which implies co-existence of the vertical fall and of the next, fluttering, periodic state in a finite region of the phase space. The fluttering state conserves a planar symmetry with a symmetry plane arbitrarily selected by initial conditions. The bistability poses the problem of dependence of the final state on the initial conditions or, in other words, on the attraction basin. It was tracked by increasing and then decreasing the Galileo number while using one simulation as the initial condition for the next one. The stability of asymptotic states was monitored using one of the above-mentioned quantities, mostly the horizontal velocity.

As can be seen in the state diagram (ser Figure 6.20) the case of $m^* = 10$ is peculiar. The primary bifurcation is supercritical and also leads to the periodic fluttering state. However, the next bifurcation, yielding the tumbling state, is strongly subcritical. As the result, the tumbling states coexists with both the fluttering and the vertical state in a very significant interval of Galileo numbers. The region of co-existence of the periodic flutter and of the tumbling state extends for $2 < m^* \leq 10$. Its lower and upper limits are marked by the red and blue lines in the diagram, respectively.

For $m^* < 0.1$ the primary bifurcation is also super-critical but yields completely different dynamics than for $m^* \leq 0.1$. A very weakly oscillating fluttering state sets in and rapidly becomes chaotic. The very small periodic and chaotic oscillations make the movement of the disc practically indistinguishable from vertical motion. We called these states quasi-vertical periodic and quasi-vertical chaotic (QVP, QVC). The data in Table 6.3 show that they are virtually unobservable experimentally because the trajectory deviates from a straight vertical at most by a few percent of the disc diameter and the amplitude of the disc oscillations barely exceeds 1 degree. The domain of quasi-vertical states significantly delays the onset of a visible flutter. For $m^* = 0$, we evidenced that the quasi-chaotic state persists until $G \approx 180$, above

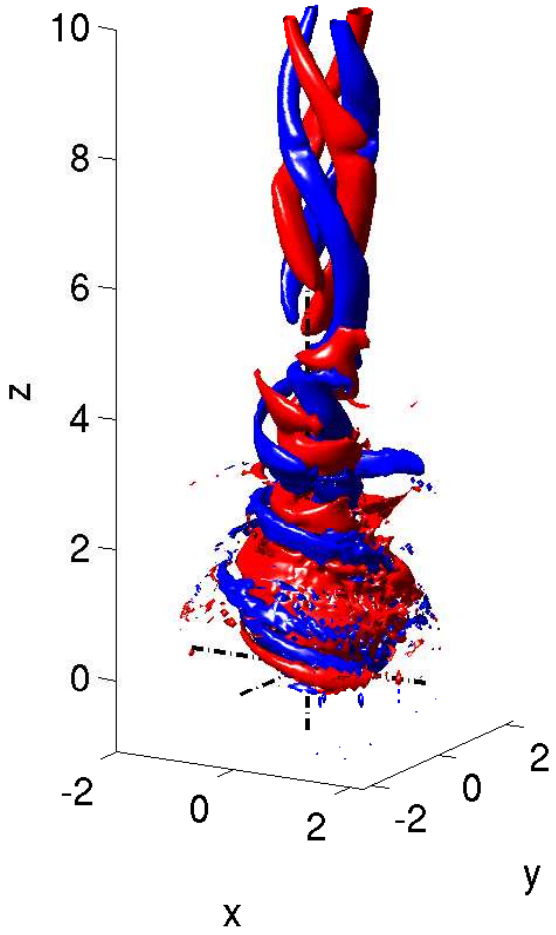

Figure 6.18: Spiral state, $m^* = 0.05$, $G = 300$. Axial vorticity iso-surfaces at levels 0.35.

which higher frequency, strong amplitude oscillations set in. This experimentally observable flutter co-exists with quasi-vertical chaotic states. The lower limit of the interval of bistability of these two states is equal to $G \approx 130$, which agrees very well with the threshold found by Fernandes *et al.* (2007) for thin discs $\chi > 20$ for small values of I^*. It can be assumed that the quasi-vertical state is responsible for the delay of the onset of oscillations observed in experiments. It can also be expected that the experimentally observed threshold will be sensitive to experimental noise. For $m^* = 0.05$ the scenario is similar to that observed for $m^* = 0$. The first bifurcation leads to the quasi-vertical periodic state, characterized by a low frequency and a small amplitude. This state is than directly replaced by a regular periodic flutter (higher frequency, significant amplitude). The quasi-vertical chaotic state was not

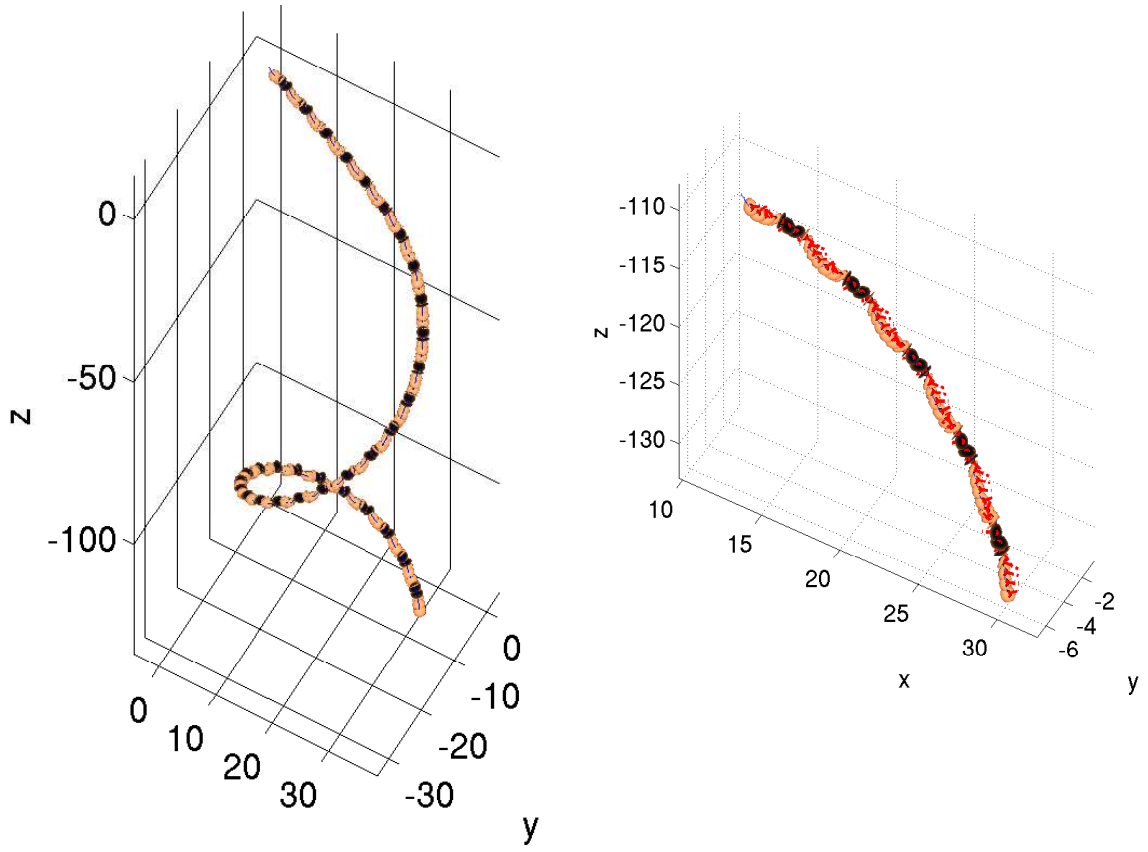

Figure 6.19: $m^* = 0.5$, $G = 400$; Spiral tumbling state. The disc is enlarged by a factor of 2 in the left figure, but it is on scale in the zoom of the right figure.

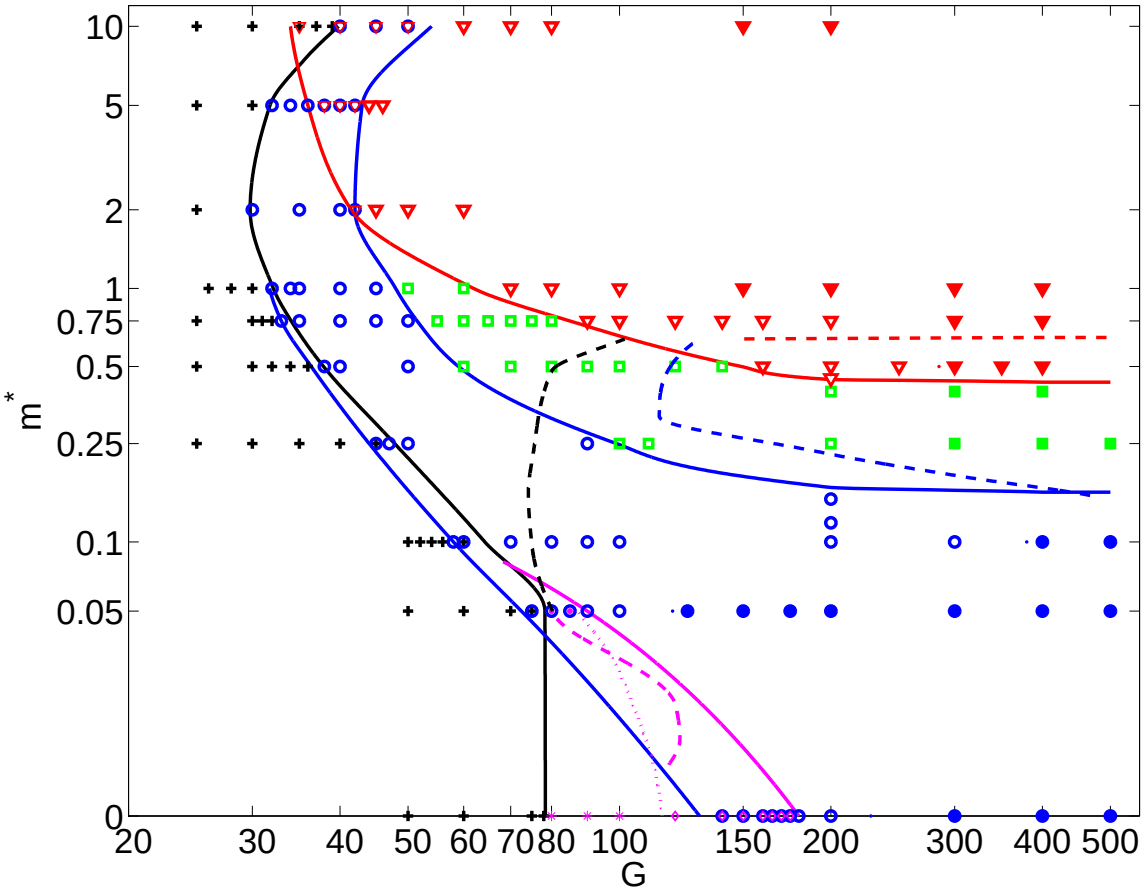

Figure 6.20: State diagram in the $G-m^*$ plane. The symbols denote regimes investigated by simulations. The full lines delimit the stability domains. Black color: vertical fall (crosses) and limit of stability of the vertical fall. Blue circles and blue lines: fluttering state, red triangles and lines: tumbling state. Green squares: intermittent state. Magenta (triangular domain at $m^* < 0.1$) - quasi-vertical states: asterisks - slow periodic, diamonds - chaotic. Three-dimensional (helical) trajectories are represented by filled symbols. Dashed lines are those Field *et al.* (1997) and Willmarth *et al.* (1964). Their colors establish the correspondence with the full lines resulting from the present numerical simulations. For $m^* < 0.1$ we associate the experimentally observed onset of flutter with a transition from a quasi-vertical regime, which explains the magenta color of the dashed line. The horizontal scale is logarithmic and the vertical one is given by $\log(m^* + 0.01)$ so as to allow $m^* = 0$ to be plotted.

observed at this value of m^*. By decreasing the Galileo number, we found this periodic state to co-exist with the quasi-vertical periodic and with the steady vertical states.

The state diagram (Fig. 6.20) shows that the dynamics of the discs is dominated by three ordered states: steady vertical fall and two periodic states (limit cycles), the fluttering state and the tumbling state. DNS makes it possible to dissipate all doubts about the periodicity of the tumbling state. The three dominant stability domains mentioned present overlaps related to sub-critical bifurcations and, at the same time, leave a significant domain, that of intermittency, uncovered. Such a situation has not been observed for a spherical body. This requires a different representation of the stability domains in the state diagram as compared to the case when only super-critical bifurcations are present and the states cannot co-exist. In Figure 6.20, the boundaries of the stability domains are represented by the solid colored lines delimiting them on two sides. For example, the fluttering state is stable in the whole domain delimited by the two blue lines. Only for $m^* \geq 1$ where the primary bifurcation is super-critical the blue line is superimposed to the upper limit of stability of the vertical state and is thus not represented. The red line delimits the region where the tumbling state is stable. The separation lines have not been traced arbitrarily, their position was deduced through interpolation of the decay or amplification rates of neighboring states. Only ordered states are represented in this manner. As a consequence, the domain of the intermittent state, considered as resulting from the absence of stability of both the flutter and the tumbling, is delimited by the blue and red lines. At lower Galileo numbers, all trajectories except those of the quasi-vertical chaotic state found for $m^* = 0$, are plane. At higher Galileo numbers, two types of helical trajectories (descrption is given in the previous sub-section) arise. They are closely related to the neighboring plane trajectories: the spiral trajectories described by Zhong *et al.* (2011) result form the destabilization of the flutter and the new helical tumbling results from the planar tumbling state. They are represented by filled symbols of the same shape as that used for the corresponding plane trajectory.

The figure of the state diagram 6.20 also features the stability limits of Field *et al.* (1997). For the transformation of the Reynolds numbers of the diagram of Field *et al.* (1997) to the Galileo numbers, the Reynolds - Galileo number dependence of the numerical simulation has been used. Due to the difficulty of controlling the initial condition in experiments, the sub-critical features escaped so far experimental observation. In particular, the upward shift of the onset of flutter for light discs (small m^*) can now be explained by the quasi-vertical, experimentally unobservable, regimes. Note that the dashed magenta line in Figure 6.20 falls well inside the bistability region of quasi-vertical and fluttering states. At $G > 100$, note the very good agreement of the lines delimiting the intermittent state from the side of both lower and higher non-dimensionalized masses. The fact that no unsteady states have been found experimentally below $G = 80$ is intriguing. We tried to find an explanation by comparing the characteristic vertical scale of amplification rates of the instabilities leading from the vertical fall to unsteady states to the vertical height of experimental set up of Field *et al.* (1997) but the amplification rates become large enough even at low Galileo numbers for the observation of the unsteady states to be expected even on limited vertical distances. The question has to be clarified in the future by a campaign of simultaneous experiments and simulations. Discs with high inertia ($m^* > 1$) have not been investigated previously but the trend towards tumbling has been reported.

6.3.3 Remarks

DNS provides more complete information on the transition scenario than can be obtained by experimental observations. The agreement between the numerical and experimental data is not perfect but is quite reasonable, especially as far as stability limits of fluttering and tumbling states at higher Galileo numbers are concerned. However, the absence of experimental observations of non-vertical states at small Galileo numbers ($G < 80$) and at larger values of m^* ($m^* > 0.1$) needs to be clarified. The state diagram does not provide all the relevant information. We have already mentioned the difficulty of observing the weakly oscillating chaotic regime for light discs. An explanation cannot be given without quantitative indication of the amplitudes of the oscillations of such states. Table 6.3 shows that the trajectories of the quasi-vertical states actually deviate from a vertical line by only a few percent of the disc diameter and the amplitude of disc rotation remains of the order of a degree. Laboratory observations of falling discs are limited by the vertical height of the experimental set up, as a consequence, slowly growing instabilities remain unnoticed. Therefore, amplification rates may represent valuable information. The experimental literature (see Ern *et al.*, 2012, for a complete review) does not report the existence of bistable states. This can be explained by the fact that in experiments it is difficult to control precisely the initial and boundary conditions. Moreover, the fluid medium is not perfectly quiescent, which perturbs the system and promotes the development of instabilities.

6.4 Conclusions

We revisited, completed and extended the widely known phase diagram of Field *et al.* (1997) by data concerning very light and very dense discs. We found the four states reported therein. Our instability thresholds are to a large extent in good agreement with the experimental data. For $m^* < 0.1$ we found a domain of co-existence of quasi-periodic and fluttering states. Its lower limit agrees very well with the experimental data. The appearance of the weakly oscillating states, which are unobservable in experiments, explains the delay of the transition observed for small m^* by Willmarth *et al.* (1964) for discs and recently by Fernandes *et al.* (2007) for flat cylinders of the aspect ratio $\chi \geq 10$. We report also a similar trend to observe tumbling states for higher values of m^*. However, we found significant differences in the onsets of instabilities for intermediate values of m^*. Our DNS indicate that the transition to the periodic fluttering and to the intermittent states occurs earlier than in experiments. This delay of onset of instabilities in experiments requires further explanation. We dissipated all doubts concerning the periodicity of the tumbling state. Finally we evidenced non-planar states reported by Zhong *et al.* (2011) and showed that at high Galileo numbers all trajectories become three-dimensional. In particular we discovered a new spiral tumbling state characterized by a regular helical trajectory of a very large diameter followed by the tumbling disc.

DNS yields details not only on the dynamics of the solid body but, as we have shown on examples of fluttering and tumbling regimes, also on that of the wake and its structure. The complete information thus obtained is of fundamental importance for the understanding of complex multi-particle flows. Accurate single particle simulations provide also a useful tool

for the benchmarking of numerical codes designed for multi-particle flow simulations.

Chapter 7

Oscillatory motion and wake instability of freely rising cylinders

In spite of the fact that the considered cylinders are rising, we retain the downward orientation of the vertical axis in the same way as in previous chapter.

7.1 History of the topic

Recent focus of the scientific community on freely falling particles was triggered to a large extent by the experimental paper of Field *et al.* (1997) (comprising the results of their own and earlier experiments: Willmarth *et al.* (1964); Stringham *et al.* (1969)). They demonstrated for the case of thin discs that, in spite of complicated mutual interactions of the solid and fluid degrees of freedom, the whole two-phase configuration behaves like a low-dimensional dynamical system obeying bifurcation theory. Four distinct states: steady fall, periodic fluttering, chaotic and tumbling (see chapter 6 for review) were shown to cover in non-overlapping manner the phase space spanned by two characteristic, dimensionless parameters: the non-dimensional moment of inertia I^* and the Reynolds number based on the mean vertical velocity u_m. One of the intriguing features of the presented scenario was the upward shift of the threshold of the primary bifurcation leading to a fluttering periodic state for low values of I^*. Namely for $I^* < 5e-03$, the onset of flutter is situated above the threshold of the onset of oscillations in the wake of a fixed disc. In the previous chapter, it was shown that the explanation is given by the existence of a regime characterized by oscillations of small amplitude (we called these regimes quasi-vertical states) shifting the onset of large, experimentally detectable oscillations to higher Galileo number. The threshold of the quasi-vertical regime lies well below the threshold of the oscillations of the wake of a fixed disc, which is in agreement with the observation made for a free sphere (see Jenny *et al.*, 2003) where the additional degrees of freedom of the body destabilize the system.

Investigation of bubbly flows (Magnaudet & Eames, 2000) and the problem of the specific behavior of light spheres (Karamanev & Nikolov, 1992) brought the study of rising bodies in the spotlight. The simulations of the light spheres, proved, however, to be difficult to reproduce experimentally because of the high sensitivity of the transition scenario to experimental

disturbances and imperfections, e.g. those of the mass distribution of the body (see Jenny *et al.*, 2004). A comparative experimental (Ellingsen & Risso, 2001) and numerical (Mougin & Magnaudet, 2002) investigation of deformable bubbles presents, in its turn, the difficulty of simulation of the moving geometry. As a convenient configuration, allowing, moreover, the choice of convenient spatial scales, marginally buoyant rigid flat cylinders have been considered by Fernandes *et al.* (2007). Fernandes *et al.* (2007) carried out experiments with freely rising cylinders of aspect ratio (defined as diameter to thickness ratio) χ ranging from 1.5 to 20 immersed in salt water of a density slightly higher than that of the solid body. They worked with a solid/fluid density ratio $\rho_s/\rho \approx 0.99$, where ρ is the fluid and ρ_s the solid density, respectively. They investigated the effect of the aspect ratio χ and of the mean terminal rise velocity, measured in terms of the terminal Reynolds numbers, on the dynamics of rising cylinders. The range of observed terminal Reynolds numbers was $80 \leq Re \leq 330$. They found for all considered aspect ratios that the first bifurcation replaced the steady vertical fall by a periodic oscillatory motion along plane zig-zagging trajectory called periodic fluttering state in chapter 6. For $\chi > 5$, the threshold Re_c of the periodic oscillations was found to lie, in agreement, with expectations, below the primary bifurcation threshold Re_{cf1} (that of the regular bifurcation leading to a steady non-axisymmetric state) of a fixed cylinder of the same aspect ratio. Similarly, the observed Strouhal numbers, defined as $St = fd/u_m$, where f is the frequency of oscillations and u_m the mean terminal velocity, were found in good agreement with the Strouhal number obtained numerically above the threshold of the secondary, Hopf, bifurcation in the wake of fixed cylinder: $St_c \approx St_{cf2}$. In contrast, the results obtained for higher aspect ratios were highly intriguing. They observed that the threshold Re_c was shifted considerably upwards (namely for $\chi \geq 10$) which led to the surprising conclusion that the degrees of freedom of the free body delay the onset of instability. Recently, Direct Numerical Simulation (Auguste *et al.*, 2010) of a free flat cylinder $\chi = 10$ revealed a series of low amplitude states preceding the onset of large regular oscillations. On the other hand, Fabre *et al.* (2012) showed, under the assumption that a regular bifurcation destabilizes the vertical path of a flat disc of aspect ratio 3 and 10 and ∞, that the additional degrees of freedom can have, indeed, a stabilizing effect. The threshold of the steady oblique state are independent of the density ratio of the cylinder and are higher (in terms of, equivalently, the Reynolds, Archimedes or Galileo number) than those of the regular bifurcation of the same cylinder held fixed.

In this chapter we investigate the configuration of the experiments of Fernandes *et al.* (2007) by Direct Numerical Simulations. We consider flat cylinders of density ratio ($\rho_s/\rho = 0.99$) for the range of aspect ratios $2 < \chi < \infty$. In particular, we attempt to explain the delay of the transition to the periodic fluttering state observed for large χ. We determine the domain of stability of the quasi-vertical states evidenced for thin discs in the previous chapter and we look for aspect ratios for which the theory of Fabre *et al.* (2012) can be practically applied, i.e. those at which the primary bifurcation leads to the steady oblique state.

7.2 Mathematical formulation and numerical implementation

We consider the cylinders as bodies of finite volume. Their mathematical characteristics are given by Eqs. (2.39) through (2.41) in section 2.2. The formulas of Eqs. (2.39) through (2.41) are used in Eqs. (2.48) through (2.50) which are solved together with the Navier-Stokes equations (2.56, 2.57), where the Galileo number is defined as:

$$G_{body} = \frac{\sqrt{V^* g_{eff} d^3}}{\nu} \tag{7.1}$$

with V^* the non-dimensionalized volume (2.39) and g_{eff} the modulus of the effective gravitational acceleration (2.6).

In section 3.12 we demonstrated for the case of a sphere and of a thin disc, as extreme cases, that the upstream and downstream extension as well as the radius of the cylindrical domain $L_u = 12d$, $L_d = 25d$ and $R_c = 8d$ are sufficient for obtaining a very satisfactory mesh independence. In the same section, the effect of all other numerical parameters has been tested and the results were transposed to the present situation. The radial-axial plane was broken up into spectral elements by modifying only the subdomain of radius 1 around the cylinder represented by a rectangle of height $d/2 = 0.5$ and of width d/χ. An example (represented for $\chi = 2$ is given in Figure 7.1. The number of spectral elements varies from 252 to 278 depending on the aspect ratio. The number of Gauss-Lobatto-Legendre collocation points in each direction (z, r) was taken $N = 6$. For discs, a maximal number of azimuthal Fourier modes of $m = 15$ was shown to provide a satisfactory truncation both inside the subdomains and at the connecting interface where it was used to truncate the spherical function expansion at $\ell_{max} = 15$. The radius of the spherical sub-domain was taken $R_s = 1$. The considered aspect ratios are summed up in Table 7.1 along with the used number of spectral elements and the corresponding non-dimensionalized mass and moment of inertia specified for the density ratio of 0.99. To avoid errors, the determination of the non-dimensionalized mass and moment of inertia was automatically coupled to the mesh geometry fixing the aspect ratio.

7.3 Results

We investigated the transition scenario of freely rising rigid flat cylinders immersed in a fluid of density close to that of the solid body ($\rho_s/\rho = 0.99$) similarly as in the experiment of Fernandes *et al.* (2007) for aspect ratios listed in Table 7.1. We swept the two-parameter $\chi - G$ space by varying the Galileo number for fixed values of χ. Figure 7.10 sums up the results in the form of a state diagram.

7.3.1 Evidenced regimes

Periodic flutter (PF)

The periodic flutter does not qualitatively differ from the regime already described in chapter 6. The trajectory is plane, vertical in the average and oscillates about the vertical direction.

χ	N_{el}	$m^*(\rho_s/\rho = 0.99)$	$I^*(\rho_s/\rho = 0.99)$
2	252	3.8877e-01	3.2398e-02
4	252	1.9439e-01	1.3162e-02
6	252	1.2959e-01	8.3994e-03
8	252	9.7193e-02	6.2011e-03
8.5	252	9.1476e-02	5.8227e-03
9	252	8.6394e-02	5.4885e-03
9.5	252	8.1847e-02	5.1910e-03
10	246	7.7754e-02	4.9244e-03
∞	278	0	0

Table 7.1: Considered aspect ratios χ, number of spectral elements of the break up of the radial-axial plane (N_{el}), non-dimensionalized mass m^* and non-dimensionalized moment of inertia I^* for the density ratio $\rho_s/\rho = 0.99$.

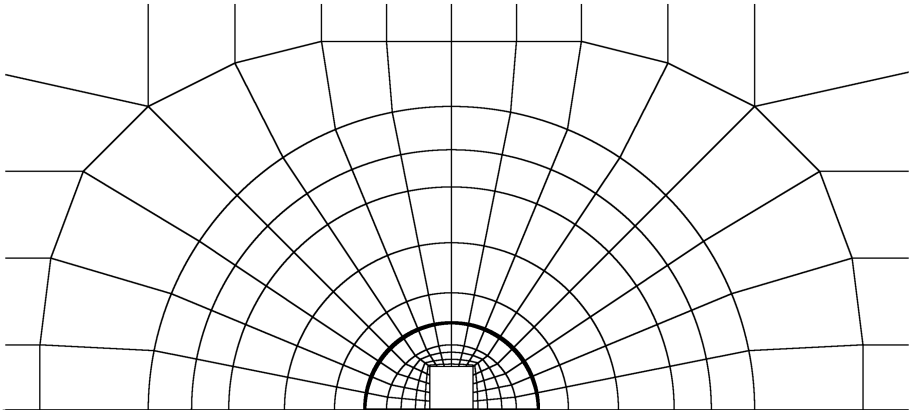

Figure 7.1: Thick flat cylinder $\chi = 2$. Details of the spectral element discretization of the radial-axial plane of the computational domain. The interface at $R_s = d$ is marked by a thick line.

It can be described as a zig-zagging path. The vortical structures of the wake (see Figure 7.2) are shedded with a symmetry plane corresponding to the plane of the trajectory. The fluttering state is characterized by strong oscillations of the cylinder axis with respect to the vertical direction. All other characteristics of the body dynamics (the horizontal and vertical velocity components and the horizontal angular velocity) oscillate with the same frequency (see Figure 7.3).

Weakly oblique steady and oscillating states

For aspect ratios varying from 9 to 10 the primary bifurcation is a regular supercritical bifurcation in similarly as for a sphere. The first bifurcating state is thus steady oblique. Its domain of stability is, however, very limited and the oblique trajectories are mostly oscillating in more or less complicated ways: periodic, quasi-periodic, intermittent. Their common feature is their planarity. Moreover, the horizontal drift is extremely weak and the oscillations are small. We shall call all such regimes as weakly oblique. Figure 7.4 represents the onset of a typical weakly oblique trajectory, periodic in the selected case $\chi = 8.5$, $G = 100$. In this case, the Hopf bifurcation sets in before the regular one. The regular bifurcation generates a non-zero mean value of the asymptotic regime. This results in an oblique trajectory. However, note the horizontal scale in Figure 7.5. The angle with respect to the vertical direction is actually only about 0.001 radian. The most visible feature of the instability is the direction of the axis of the cylinder. Its mean inclination and amplitude is about 0.03 radians (less than 2 degrees). As the result, this regime can be classified in the same category as the quasi-vertical regimes described in chapter 6 and in the next paragraph. The weakly oblique regimes can also practically periodically switch between an oblique steady and oblique oscillating trajectory (see Figure 7.6) or they can be chaotic intermittently oblique (see Figure 7.8). The randomness of the switching of the drift direction makes the trajectory vertical on the large time scales.

Quasi-vertical periodic and chaotic regimes (QVP,QVC)

With increasing Galileo number, the oscillation amplitude (slightly) grows and the mean value completely disappears. In this category we classify all quasi-vertical states with no mean horizontal drift. A modulation appears before the onset of chaos. The resulting states are of the same nature as those evidenced for a thin disc and called quasi-vertical (periodic and chaotic). In Figure 7.7 we show a quasi-periodic case of a quasi-vertical state. The already mentioned intermittent state (see Figure 7.8) has also no mean drift. The chaotic trajectories are fully three-dimensional (see Figure 7.9).

7.3.2 State diagram

Figure 7.10 sums up all the simulated regimes in the $\chi - G$ two-parameter plane. The different states described in section 7.3.1 are marked by different symbols. The limits of stability of these states were determined using the transients at the neighboring points yielding a more accurate estimation of their position.

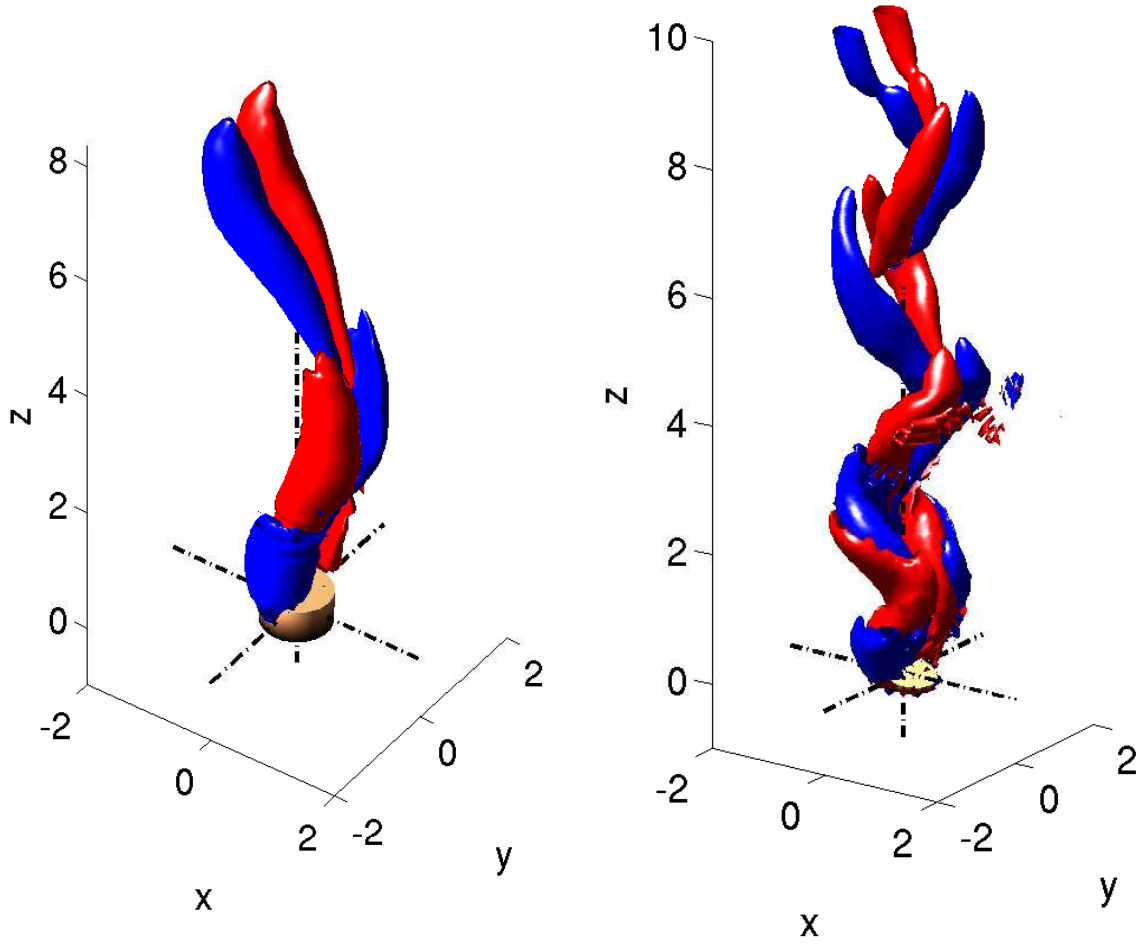

Figure 7.2: Periodic fluttering state. Left: $\chi = 2$, $G = 130$, axial vorticity iso-surfaces at levels 0.75. Right: $\chi = 9$, $G = 160$, axial vorticity iso-surfaces at levels 0.8.

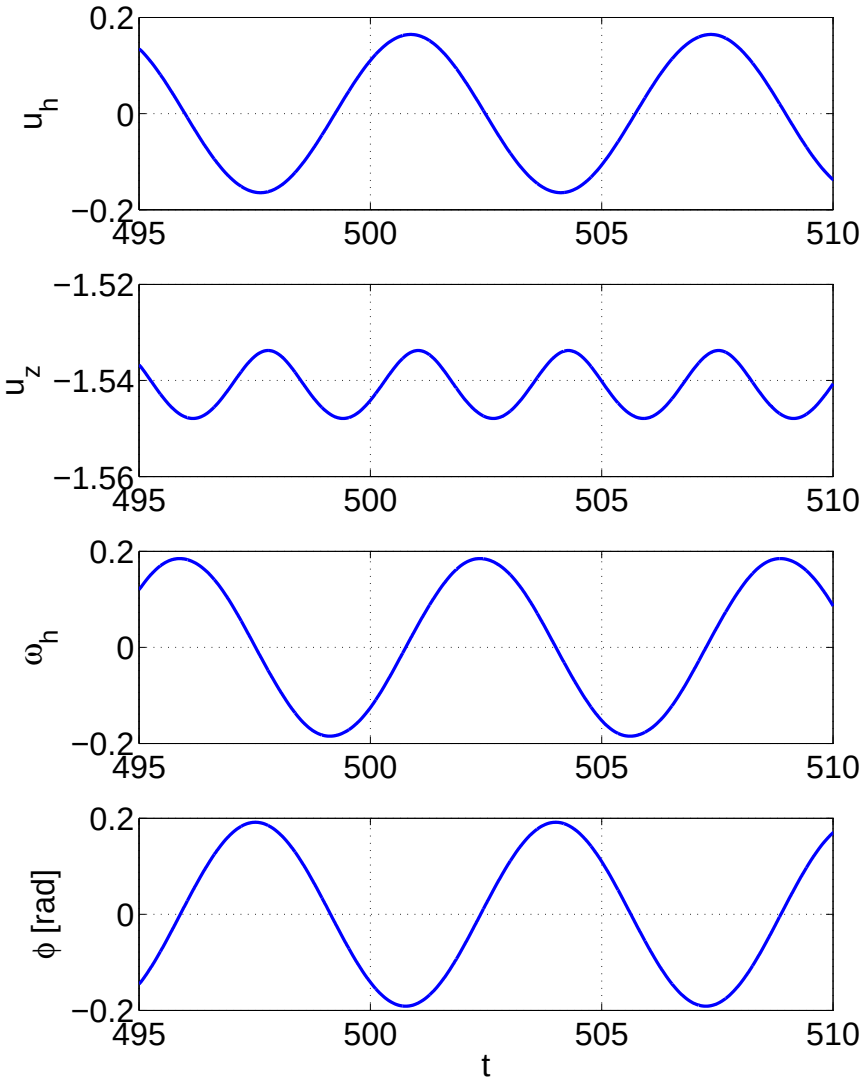

Figure 7.3: Periodic fluttering state: $\chi = 2$, $G = 130$. u_h: Horizontal component of the velocity; vertical u_z: component of the velocity; ω_h: angular velocity; ϕ: inclination of the disc defined as the angle between the disc axis and the vertical direction as functions of time.

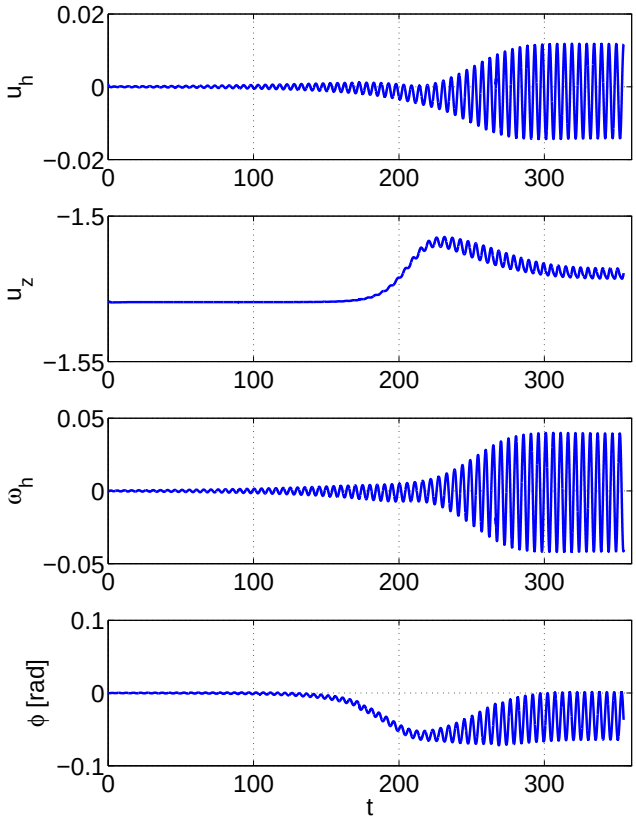

Figure 7.4: Weakly oblique oscillating state: $\chi = 8.5$, $G = 100$. For the meaning of symbols see caption of Figure 7.3.

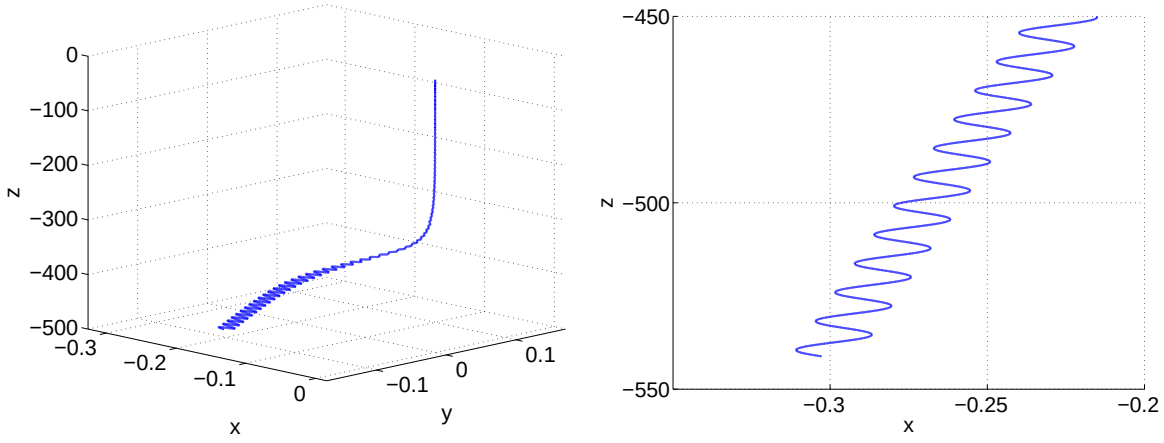

Figure 7.5: Weakly oblique oscillating state: $\chi = 8.5$, $G = 100$. Left: trajectory corresponding to the time interval represented in Figure 7.4. Right: zoom on the end.

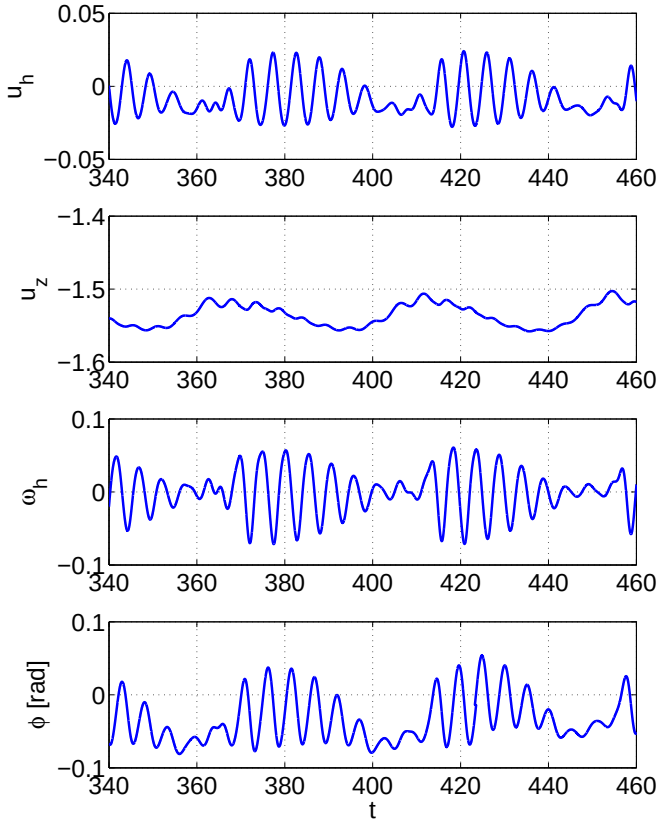

(Top)

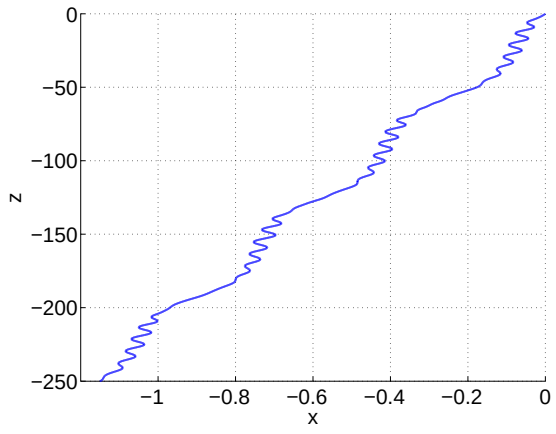

(Bottom)

Figure 7.6: Weakly oblique state with slow beatings: $\chi = 9.5$, $G = 110$. Top: for the meaning of symbols see caption of Figure 7.3. Bottom: trajectory.

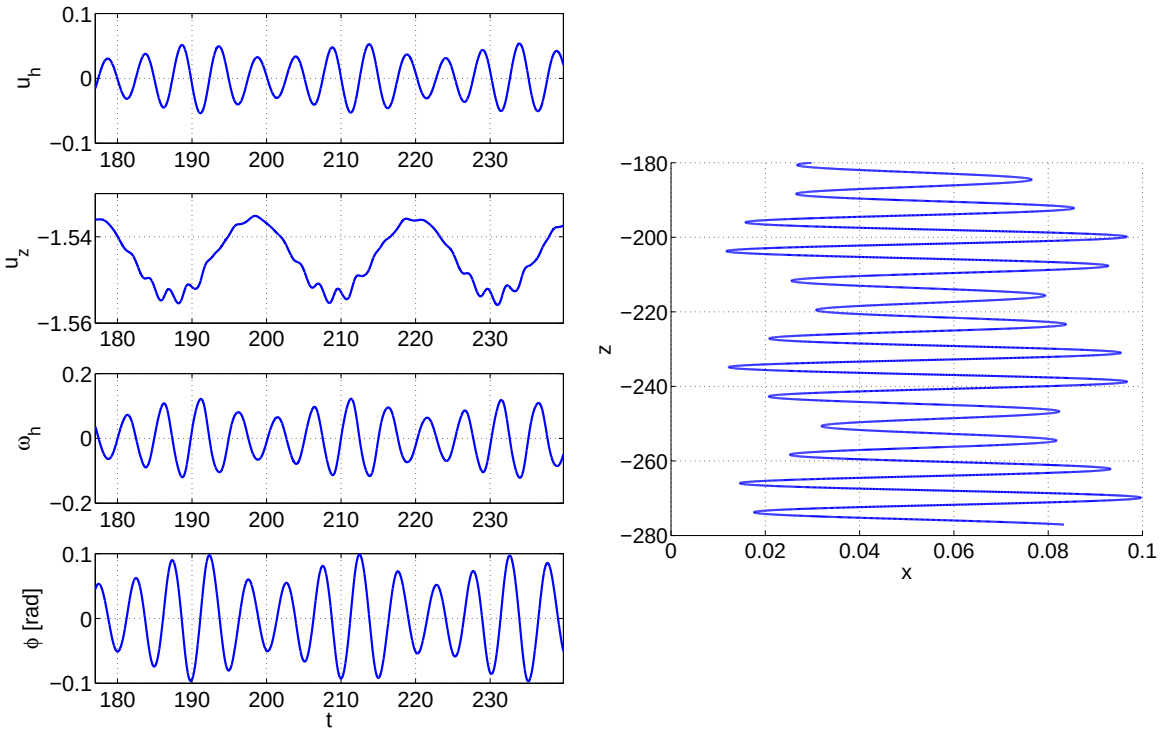

Figure 7.7: Quasi-vertical quasi-periodic state: $\chi = 8.5$, $G = 120$. Left: for the meaning of symbols see caption of Figure 7.3. Right: trajectory.

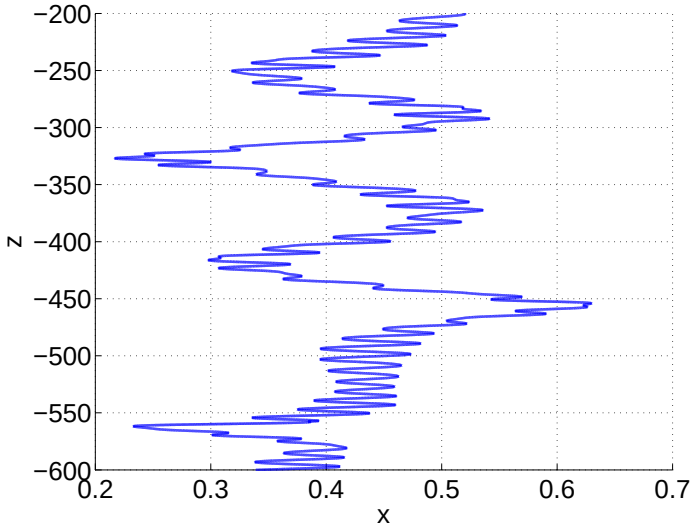

Figure 7.8: Quasi-vertical planar intermittent state: $\chi = 9.5$, $G = 130$. Trajectory.

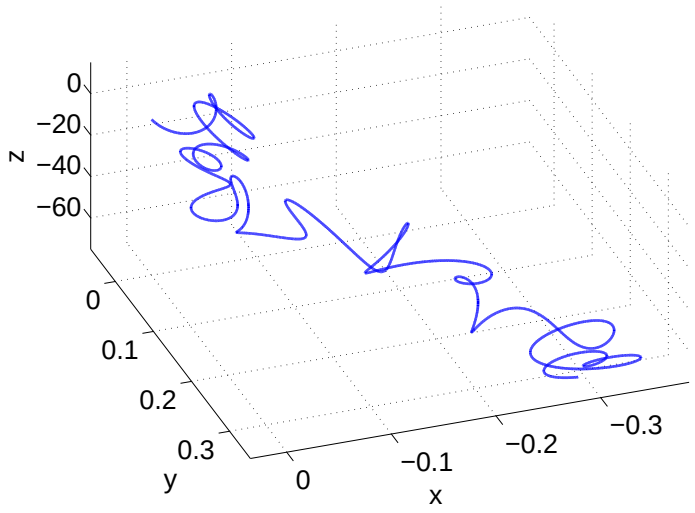

Figure 7.9: Quasi-vertical chaotic state: $\chi = 10$, $G = 150$. Trajectory.

For aspect ratios $\chi < 8$ the primary bifurcation is a Hopf one yielding directly a flutter (periodic oscillating state with large amplitude of oscillations) from a steady vertical state (steady vertical ascension). The lowest critical Galileo number is reached between $\chi = 4$ and $\chi = 6$ (see Table 7.2). Using the computed vertical velocity at the bifurcation threshold, critical Reynolds numbers were also determined. For $\chi = 8$ the stabilizing effects of the additional degrees of freedom of the free body shift the onset of flutter to the threshold of the secondary instability in the wake of a fixed cylinder. Table 7.3 provides quantitative characteristics of the investigated regimes.

For aspect ratios $8.5 \leq \chi \leq 10$ the threshold of the primary instability in the wake of freely moving cylinders (cyan line in Figures 7.10 and 7.11) lies above the secondary bifurcation

χ	G_{crit}	Re_{crit}	Re_{cf1}	Re_{cf2}	St	St_{fixed}
2	106.51	167.32	185.37	216.6	0.092	0.105
4	86.92	128.09	148.49	166.0	0.111	0.111
6	86.49	127.04	137.86	150.0	0.119	0.114
8	95.18	142.39	132.54	143.1	0.131	–

Table 7.2: Thresholds of the onset of the periodic flutter expressed in terms of the Galileo and terminal Reynolds number and the corresponding Strouhal numbers for aspect ratios $\chi \leq 8$. For comparison the thresholds Re_{cf1} and Re_{cf2} of the first two bifurcations and Strouhal numbers St_{fixed} found in the wake of fixed cylinders at the onset of oscillations are provided. For smaller aspect ratios, the free body degrees of freedom have clearly a destabilizing effect.

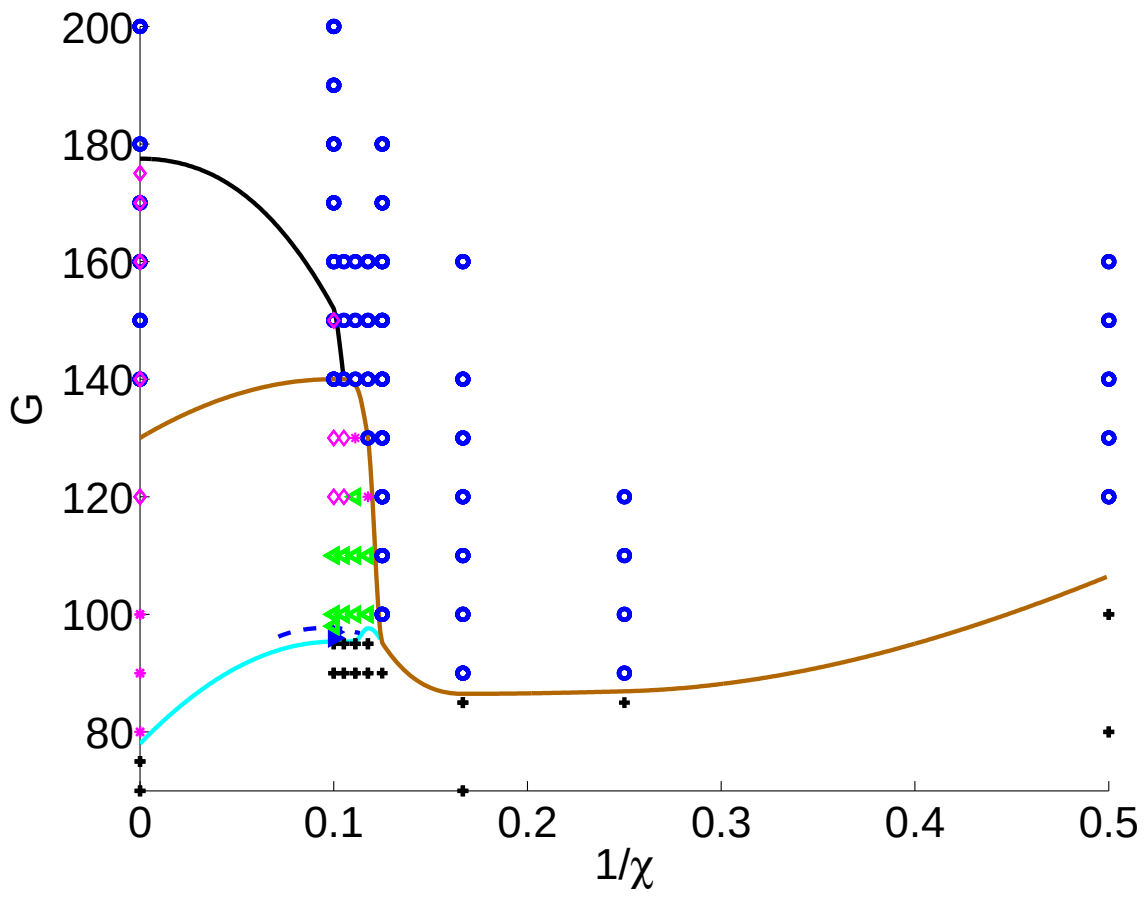

Figure 7.10: State diagram in the $1/\chi - G$ plane. The symbols denote regimes investigated by simulations. The full lines delimit the stability domains. Brown color: lower limit of stability of the fluttering state. Cyan line: threshold of the onset of quasi-vertical states. Black line: upper limit of stability of quasi-vertical chaotic states. Blue dashed line: limit of stability of steady oblique (SO) states. Black crosses: vertical state. Blue circles: periodic flutter state. Blue filled triangles: steady oblique state (SO). Green triangles: oblique states (OO). Magenta symbols - weakly oscillating periodic vertical states: asterisks, diamonds - quasi-vertical chaotic states.

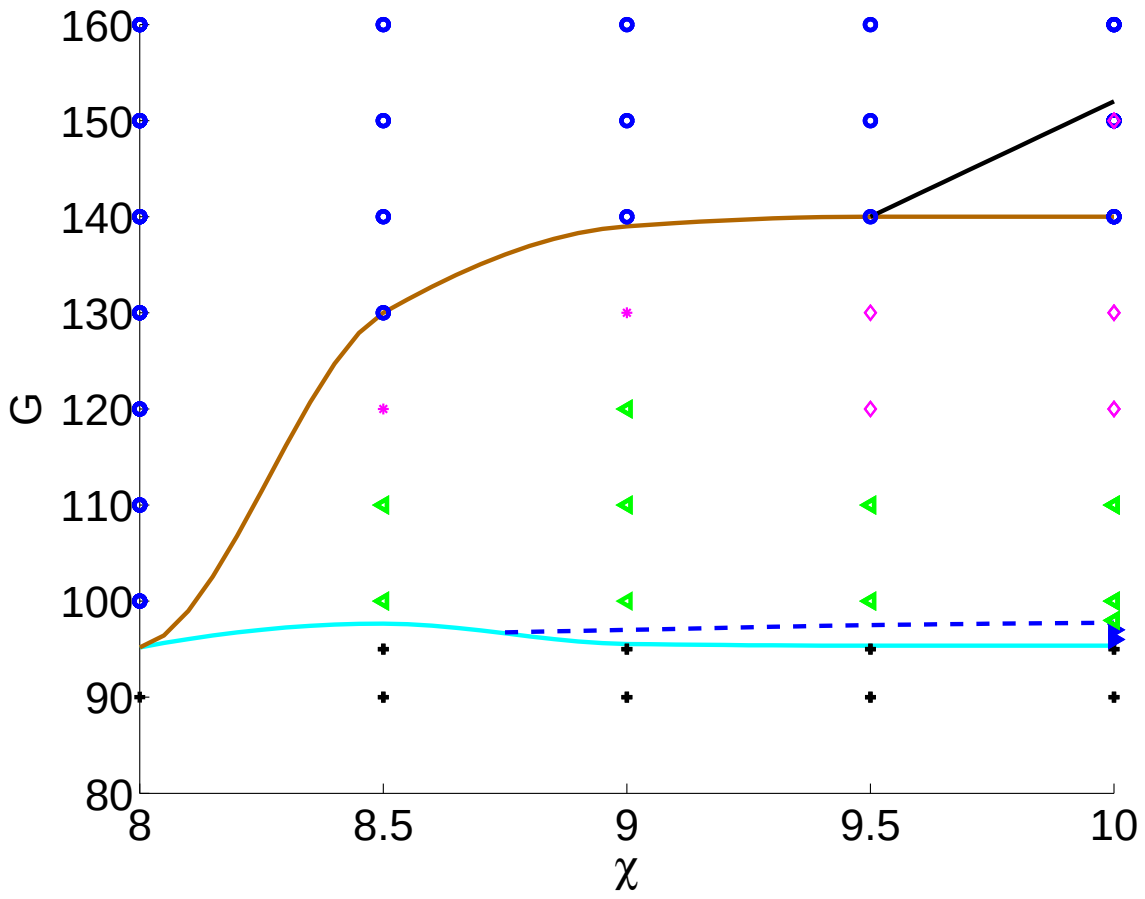

Figure 7.11: Detail of the state diagram in the $\chi - G$ plane. See caption of Figure 6.20 for the meaning of lines and symbols.

χ	G	Re	A_{u_h}/d	$\phi_{max}[rad]$	St
2	120	194.59	0.124	0.130	0.093
2	140	214.49	0.198	0.241	0.103
2	160	241.73	0.237	0.323	0.107
4	100	144.04	0.091	0.137	0.125
4	120	171.38	0.126	0.217	0.138
6	100	142.96	0.057	0.127	0.144
6	120	168.99	0.108	0.230	0.169
6	140	194.96	0.156	0.307	0.180
6	160	221.00	0.224	0.385	0.190
8	100	150.48	0.022	0.060	0.131
8	120	175.06	0.080	0.132	0.167
8	140	197.01	0.210	0.285	0.202
8	160	221.42	0.333	0.405	0.218
8	180	246.53	0.450	0.492	0.229

Table 7.3: Quantitative data for periodic fluttering state of thick cylinders $\chi \leq 8$. Meaning of symbols: A_{u_h} - amplitude of the horizontal component of the velocity, ϕ_{max} - maximal inclination angle, defined as the angle between the axis of the cylinder and the vertical direction, St - Strouhal number.

threshold in the wake of fixed bodies (see Tables 7.4 and 7.5 and Figure 7.12). For the freely moving cylinder of aspect ratio $\chi = 8.5$ the primary bifurcation is still a super-critical Hopf bifurcation setting in at $G = 97.66$ ($Re = 147.91$) but it leads to a different state (see Figure 7.4). It is a weakly oblique (slightly drifting) periodic state oscillating with a small amplitude and a frequency roughly half that of the periodic flutter setting in at higher Galileo number. At Galileo numbers smaller than 130, the amplitude of the horizontal component of the velocity and the maximum inclination of the cylinder remain small ($A_{u_h} < 0.045$ and $\phi_{max} < 6^o$). The Strouhal number is equal to $St \approx 0.13$. Further increase of the Galileo number leads, eventually, to the appearance of large amplitude oscillations corresponding to the periodic flutter. The critical Galileo number is $G_{crit} \approx 130$ ($Re = 187$) . The Strouhal number at the onset is $St \approx 0.19$. The bifurcation yielding the flutter at this aspect ratio is supercritical.

For cylinders of aspect ratio $\chi = 9$, 9.5 and 10, the primary bifurcation was found to be regular. It leads to a steady oblique (SO) state. At $\chi = 9$ it was identified using only the transients developing from a vertical regime. Converged steady oblique state was obtained at $\chi = 9.5$ and 10 (see Table 7.5). For the aspect ratio $\chi = 10$, Fabre *et al.* (2012) predict a threshold $Re_{FTM} = 143.94$. We find $G_{crit} = 95.37$, which corresponds, with account of the vertical velocity at the threshold ($u_z = 1.50$) to $Re = 143.3$. As can be seen from Table 7.5, the domain of stability of the steady oblique state is very narrow. As a consequence of a Hopf bifurcation, it is replaced by an oblique oscillating state similarly as for a free sphere. Subsequently this state becomes oblique quasi-periodic, intermittent (vertical in the

χ	G	Re	A_{u_h}/d	$\phi_{max}[rad]$	St
8.5	100	152.00	0.013	0.040	0.133
8.5	110	168.40	0.035	0.073	0.130
8.5	120	185.48	0.042	0.100	0.129
8.5	130	186.95	0.146	0.200	0.191
8.5	140	197.53	0.226	0.283	0.207
8.5	160	221.57	0.365	0.408	0.225

Table 7.4: Quantitative data for a cylinder of aspect ratio $\chi = 8.5$. At $G = 130$ a significant increase of the amplitude of the horizontal velocity A_{u_h}/d, maximum inclination angle ϕ_{max} and of the Strouhal number is observed. The threshold of the secondary bifurcation in the wake of a fixed cylinder of the same aspect ratio is $Re_{cf2} = 141.86$.

average) and, finally, chaotic. The maximum inclination ϕ_{max} and amplitude of horizontal displacements remaining small, all these regimes can be qualified as quasi vertical, similarly as the QVP and QVC regimes evidenced for a thin disc for $m^* < 0.05$. The bifurcation giving rise to the large amplitude periodic fluttering state becomes sub-critical between aspect ratios 9.5 and 10. The bi-stability region of quasi-vertical states and of the flutter widens rapidly towards large aspect ratios. At $\chi = 10$ its width represents already 10 units of Galileo number and, as seen in chapter 6, for a thin disc, it extends from $G = 130$ to almost $G = 180$. The upper limit of the bistability is represented by the black line in Figures 7.10 and 7.11.

The scenario found at $\chi = 10$ is already quite close to that of an infinitely thin disc. For $\chi \to \infty$, the represented regimes are taken from the state diagram 6.20 of chapter 6. It is therefore logical to represent the state diagram 7.10 in terms of $1/\chi$ rather than χ. In the interval $8 \leq \chi \leq 10$ there are important changes of the scenario within a small variation of the aspect ratio. The zoom of this subdomain of the parameter space is provided in terms of χ (see Figure 7.11).

7.3.3 Comparison with experimental results

Using the computed asymptotic mean vertical velocities, we can establish a correspondence between the Galileo numbers of Figure 7.10 and the Reynolds numbers determined in experiments. In Figure 7.12 we report the limits of stability of individual regimes described in section 7.3.1 in the $\chi - Re$ parameter plane. In the same way as in Figure 13 of Fernandes *et al.* (2007), these limits are to be compared with the thresholds of the primary and secondary bifurcations in the wake of fixed cylinders. Although there is little difference between our results of chapter 4 and those represented in Fernandes *et al.* (2007) we use our results published in the paper Chrust *et al.* (2010). The red and blue solid lines marking the threshold of the primary and secondary bifurcations in the wake of fixed cylinders are represented by red and blue solid lines, respectively. The primary bifurcation is regular and leads to a steady asymmetric state (see chapter 1.6) characterized by a planar symmetric wake and a non-zero lift. The secondary one is a Hopf bifurcation. For cylinders of aspect

χ	state	G	Re	A_{u_h}/d (u_h^*)	$\phi^*_{max}[rad]$	St
9	OO	100	150.64	0.005	0.057	0.121
9	OO	110	169.39	0.027	0.088	0.125
9	QVC	120	187.42	0.041	0.09	–
9	PF	130	188.44	0.143	0.175	0.193
9	PF	140	197.88	0.243	0.285	0.213
9	PF	150	209.52	0.322	0.357	0.223
9	PF	160	221.68	0.396	0.417	0.231
9.5	SO	100	150.51	0.008	0.057	–
9.5	QVC	110	166.10	0.022	0.080	–
9.5	QVC	120	181.29	0.041	0.095	–
9.5	QVC	130	197.60	0.060	0.105	–
9.5	PF	140	198.24	0.260	0.290	0.218
9.5	PF	150	209.58	0.348	0.364	0.229
9.5	PF	160	221.66	0.426	0.425	0.238
10	SO	97	145.79	0.008	0.047	–
10	OO	100	150.50	0.016	0.065	0.120
10	OO	110	166.10	0.035	0.090	0.131
10	QVC	120	182.52	0.040	0.095	–
10	QVC	130	199.55	0.070	0.110	–
10	QVC	150	232.50	0.084	0.115	–
10	PF	140	198.80	0.245	0.282	0.222
10	PF	150	210.75	0.336	0.366	0.234
10	PF	160	221.52	0.412	0.427	0.244
10	PF	180	246.42	0.592	0.520	0.255
10	PF	200	270.32	0.701	0.572	0.270

Table 7.5: Quantitative data for cylinders of aspect ratio $\chi = 9$, 9.5 and 10. Meaning of symbols: SO - steady oblique state, OO - oblique oscillating state, QVC - quasi-vertical chaotic state and PF - large amplitude periodic flutter state. *: For SO state the value in the column $A_{u_h}, (u_h)$ denotes the asymptotic value of the horizontal velocity component and ϕ_{max} is the constant asymptotic inclination, for OO and QVC the corresponding values denote the maximum of the horizontal velocity component and maximal inclination, respectively. For PF state A_{u_h} denotes the amplitude of oscillations and ϕ_{max} the maximal inclination of a cylinder. (Thresholds of the secondary bifurcation in the wake of fixed cylinders of aspect ratios 9, 9.5 and 10: $Re_{cf2}^{\chi=9} = 140.81$, $Re_{cf2}^{\chi=9.5} = 139.88$ and $Re_{cf2}^{\chi=10} = 139.05$). Primary bifurcation thresholds of free cylinders: $G_{crit}^{\chi=9} = 95.54$ ($Re_{crit}^{\chi=9} = 144.08$), $G_{crit}^{\chi=9.5} = 95.36$ ($Re_{crit}^{\chi=9.5} = 143.78$), $G_{crit}^{\chi=10} = 95.37$ ($Re_{crit}^{\chi=10} = 143.27$).

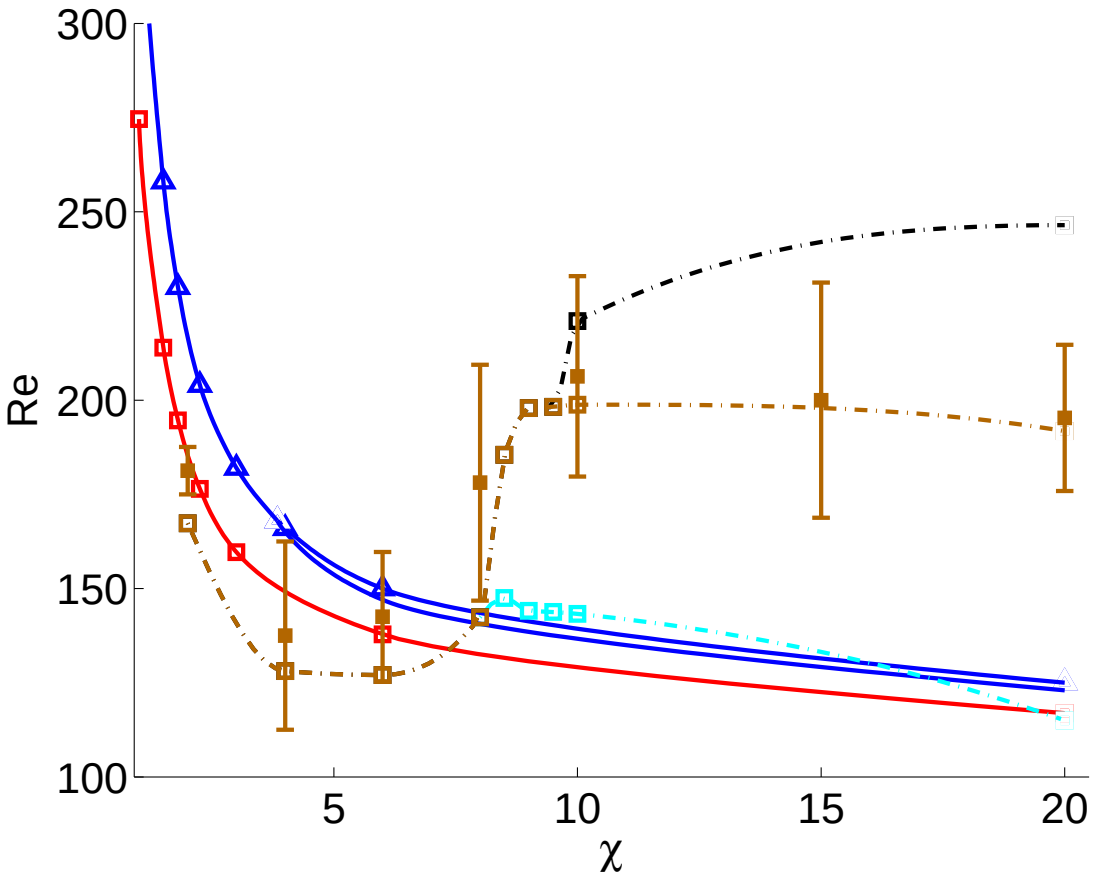

Figure 7.12: Critical Reynolds numbers characterizing onsets of instabilities for flat cylinders of aspect ratio χ. Red and blue lines mark the regular and secondary bifurcations in the flow past fixed bodies (Chrust *et al.*, 2010). For $\chi \geq 4$ the bifurcation is subcritical and the upper and lower bistability limits are represented. Freely moving cylinders: the dotted brown line represents the onset of periodic flutter (PF) state. Filled brown squares along with error bars represent onset of PF of Fernandes *et al.* (2007). Dotted cyan line marks the onset of small amplitude states. For $\chi \geq 10$ the periodic flutter and quasi vertical states coexist in the region delimited by brown and black dotted lines.

ratio $\chi < 4$ it leads to a periodic state with a planar symmetry and is supercritical. At large aspect ratios $\chi \geq 4$ a periodic state without planar symmetry appears through a subcritical bifurcation. The blue line splits to represent the lower and upper limit of the bistability region (see Chrust *et al.*, 2010). The full black squares with intervals of experimental error bars denote the onset of path instabilities reported in Fernandes *et al.* (2007).

Figure 7.12 clearly shows that the experimentally observed onset of path instability corresponds to the primary bifurcation only for aspect ratios smaller than 8. The sudden rise of threshold observed between $\chi = 6$ and 10 is due, in the interval $6 \leq \chi \leq 8$, to the stabilizing effect of the free body degrees of freedom, shifting the primary stability threshold above the onset of the first two bifurcations in the wake of a fixed body and, in the interval $8 \leq \chi \leq 10$ to the onset of weakly oblique states difficult to discern from the vertical one. For aspect ratios $\chi \geq 10$ there exists a wide bi-stability domain of quasi-vertical and oscillating states. The experimental noise seems to have been strong enough to excite the oscillation as soon as the Reynolds number reached the lower limit of the bi-stability.

7.4 Conclusions

We have carried out Direct Numerical Simulations for flat cylinders, of aspect ratio χ ranging from 2 to ∞, immersed in a fluid of a density close to that of the solid phase $\rho_s/\rho = 0.99$ reproducing the experiments of Fernandes *et al.* (2007), which had been conducted for a similar configuration. In experiments only the onset of the large amplitude periodic fluttering state was determined. For $\chi \geq 6$ a significant upward shift of the threshold, far above the thresholds of the first bifurcations in the wake of fixed cylinders, was reported. The results of our simulations confirm the theoretical prediction of situations where the primary instability threshold is shifted upward due to a stabilizing effect of the additional degrees of freedom of a free body. However, this effect only partly explains the experimentally observed upward shift of the flutter. The main effect, observed at large aspect ratios, is due to several quasi-vertical regimes (steady oblique, oblique oscillating, quasi-vertical periodic (zig-zagging) and quasi-vertical chaotic) either unobservable or discarded in experiments as inessential side-effects.

Chapter 8

Oblate spheroids freely falling or rising in a Newtonian fluid

8.1 Introduction

The aim of this chapter is to study the influence of the aspect ratio on the transition scenario of oblate spheroids. The problem depends on three independent parameters: the aspect ratio χ, the solid/fluid density ratio ρ_s/ρ and the Galileo number. In order to keep a continuous transition to infinitely thin spheroids we replace the solid/fluid density ratio ρ_s/ρ by the non-dimensionalized mass m^*. The extreme case of infinitely thin spheroids is very close to the thin disc investigated in detail in chapter 6. The only difference is that in the limit $\chi \to \infty$ the mass is not distributed in a homogeneous manner which yields a different m^*/I^* ratio (20 instead of 16, see Eqs. (2.37) and (2.40)). A sphere of aspect ratio $\chi = 1$ can be considered as the other extreme case. It is, however, to be expected that the limit of $\chi \to 1$ will be non-trivial. If we assume that vertical paths of spheroids of aspect ratio close to one become unstable due to a regular bifurcation, a perfectly spherical body can easily rotate (and the regular bifurcation is, indeed, accompanied by a rotation, while even a small asphericity can be expected to prevent the rotation yielding an oblique state similar to that evidenced for a cylinder of aspect ration 10 in chapter 7).

Since for spheroids no data are available concerning the transition scenario we covered the three-dimensional box $G < 200$, $0 \leq m^* \leq 1$, $0 \leq 1/\chi < 1$ by a practically homogeneous mesh of regimes defined by values: $m^* = O, 0.1, 0.25, 0.5, 0.75, 1$, $\chi = \infty, 6, 3, 2, 1.5$ and $30 < G < 200$, incremented by 10 or 25 (with some refinement close to the primary bifurcation threshold in some cases starting from higher Galileo numbers for small aspect ratios). 344 simulations are available so far. They provide a coarse view on the transition scenario.

8.2 Numerical implementation

The numerical implementation required a specific mesh for each aspect ratio. In the same way as for cylinders, the meshes tested and used for fixed spheroids (see chapter 4) were adapted for the implementation of the spherical interface. The radius of the interface was

close to $1d$ for all simulations. All simulations were run with the azimuthal Fourier and the spherical function expansion truncated at $m = 15$ and $\ell_{max} = 15$, respectively.

8.3 Preliminary discussion of raw results

The presentation of the results is organized by planes of constant aspect ratio.

8.3.1 $\chi = \infty$

As expected, the differences between the scenario for homogeneous thin discs and for infinitely flat spheroids are marginal. The so far obtained coarse results covering the $m^* - G$ parameter plane did not allow for the fine investigation of bi-stability domains expected to lie along the line of the primary bifurcation for $m^* > 0.1$. The line $m^* = 0$ is copied from the state diagram 6.20. As compared to Figure 6.20, the thresholds (represented by solid lines) in Figure 8.1 are only slightly shifted upward (towards higher Galileo numbers). The scenario is dominated by the periodic flutter (blue circles) and by the tumbling regime (red triangles) separated by intermediate regimes at which the body switches intermittently or periodically between the flutter and the tumbling.

8.3.2 $\chi = 6$

At $\chi = 6$ we found a considerable extension of the domain of quasi-vertical states (delimited by the magenta dash-dotted line in Figure 8.2. The finite thickness of the body enables steady oblique and steady oscillating states similarly as for the flat cylinder investigated in chapter 7. Figure 8.3 shows the development of a steady oblique state close to threshold (at $G = 92$) of the primary bifurcation for $m^* = 0.1$ ($\rho_s/\rho = 1.15$). Only at a slightly higher Galileo number ($G = 94$) we evidenced an oblique oscillating regime. Again, two units of the Galileo number higher, the mean value of the horizontal velocity (and of the angle of inclination of the spheroid) vanishes and a vertical oscillating (zig-zagging) state sets in. The amplitude of oscillations remains, however, small (0.05 radian for the inclination angle) which distinguishes this and other similar states classified as quasi-vertical periodic form the periodic flutter. In Figures 8.6 and 8.7 a typical periodic flutter is represented in terms of the velocity components and of the inclination angle and as a visualization of the positions of the spheroid along the trajectory over about a period. Unlike in a quasi-vertical state, the amplitude of the inclination is very significant. The state approaches actually a tumbling with an amplitude close to $\pi/2$. Unlike for thin discs (and spheroids) we did not find a significant difference between the frequencies of the periodic quasi-vertical and periodic fluttering states. The transition between them still necessitates a finer investigation.

The domain of intermittent or periodical switching between tumbling and flutter, resulting in changes of the drift direction is narrower than for thin spheroids of infinite aspect ratios. A typical intermittent state is represented in Figures 8.8 and 8.9.

A periodic tumbling state is represented in Figures 8.10 and 8.11. Unlike for a thin disc, we no longer find stages of an almost horizontal flight at this aspect ratio.

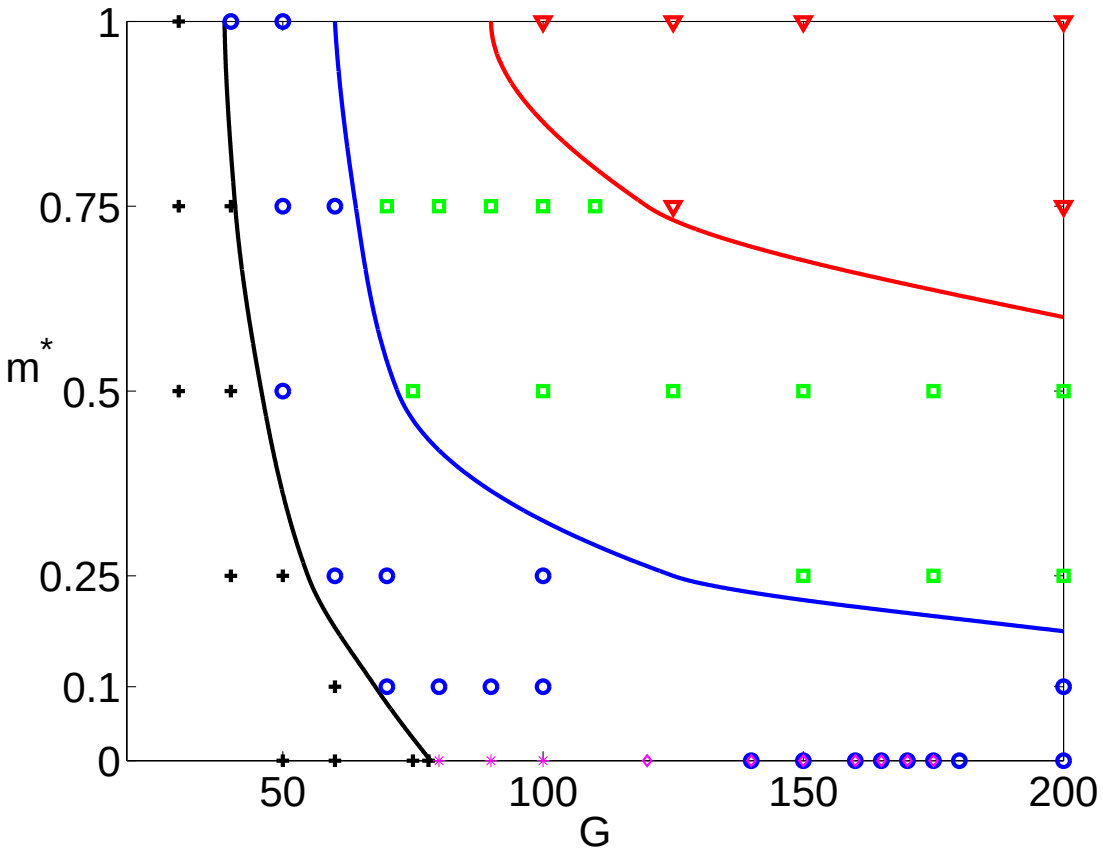

Figure 8.1: State diagram for the infinitely thin spheroid $\chi = \infty$ in the $G - m^*(\rho_s/\rho)$ plane. The symbols denote regimes investigated by simulations. The full lines delimit the stability domains. Black line: limit of stability of the steady vertical state. Blue line: limit of stability of periodic fluttering states. Red line: lower limit of stability of tumbling states. Black crosses: vertical state. Blue circles: periodic flutter state. Green squares - intermittent regimes. Red triangles - tumbling regimes. Magenta symbols - weakly oscillating periodic vertical states: asterisks, diamonds - quasi-vertical chaotic states.

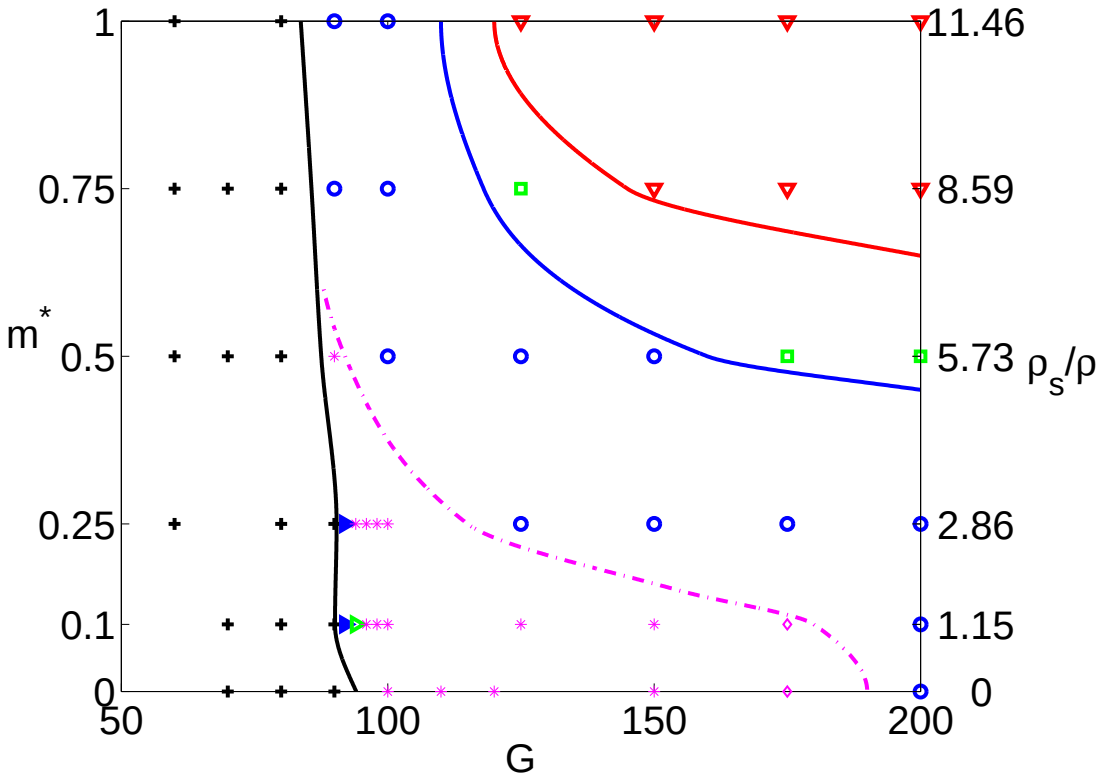

Figure 8.2: State diagram for a spheroid $\chi = 6$ in the $G - m^*(\rho_s/\rho)$ plane. The symbols denote regimes investigated by simulations. The full lines delimit the stability domains. Black line: limit of stability of the steady vertical state. Magenta dashed-dotted line: limit of stability of quasi-vertical states (QVP,QVC). Blue line: limit of stability of periodic fluttering states. Red line: lower limit of stability of tumbling states. Black crosses: vertical state. Blue circles: periodic flutter state. Green squares - intermittent regimes. Red triangles - tumbling regimes. Magenta symbols - weakly oscillating periodic vertical states: asterisks, diamonds - quasi-vertical chaotic states. Blue triangles: steady oblique state (SO). Green triangles: oblique oscillating states (OO). Magenta symbols - weakly oscillating periodic vertical states: asterisks, diamonds - quasi-vertical chaotic states.

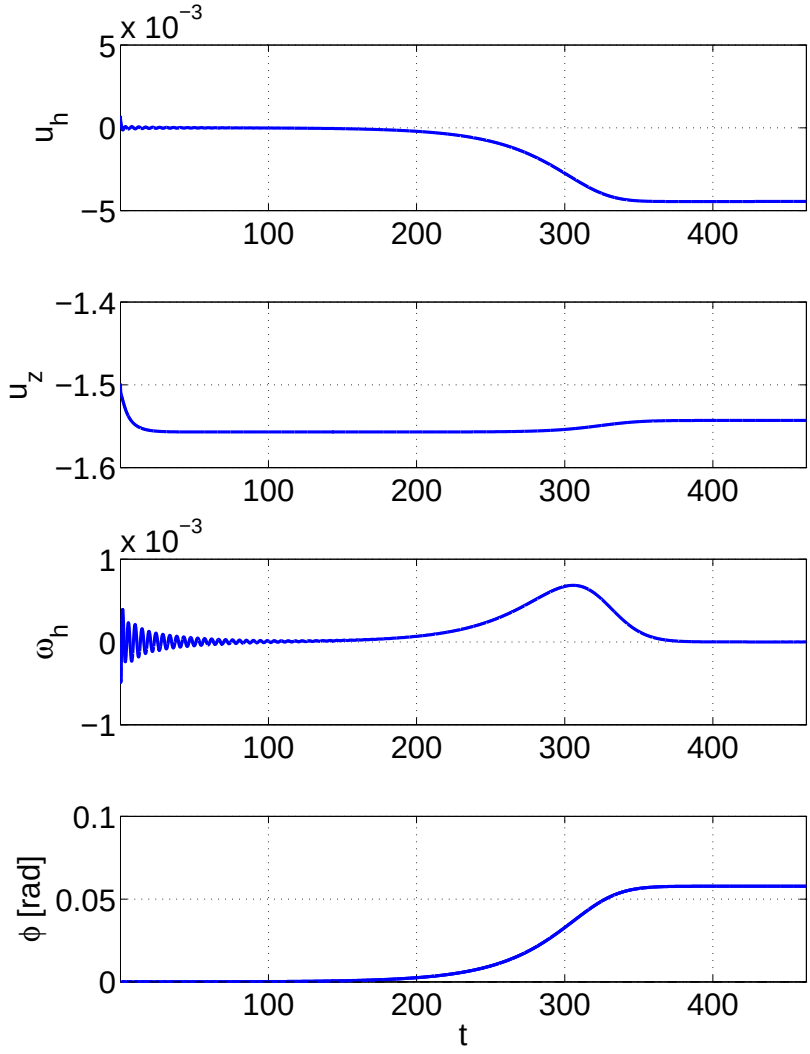

Figure 8.3: $\chi = 6$, $m^* = 0.1$ ($\rho_s/\rho = 1.146$), $G = 92$. Steady oblique state (SO). Meaning of symbols: u_h and u_z - horizontal and vertical component of the velocity, respectively, w_h - angular velocity, ϕ - inclination of the spheroid, defined as the angle between its axis and the vertical direction.

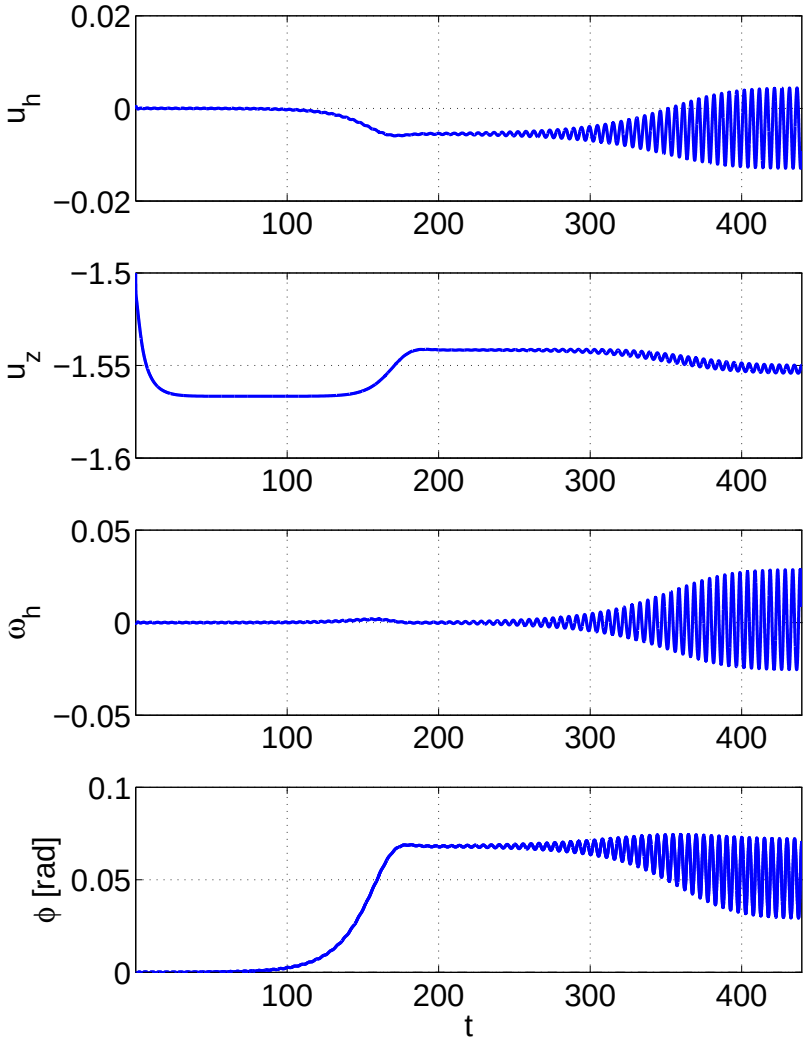

Figure 8.4: $\chi = 6$, $m^* = 0.1$ ($\rho_s/\rho = 1.146$), $G = 94$. Oblique oscillating state (OO). See caption of Figure 8.3 for the meaning of lines and symbols.

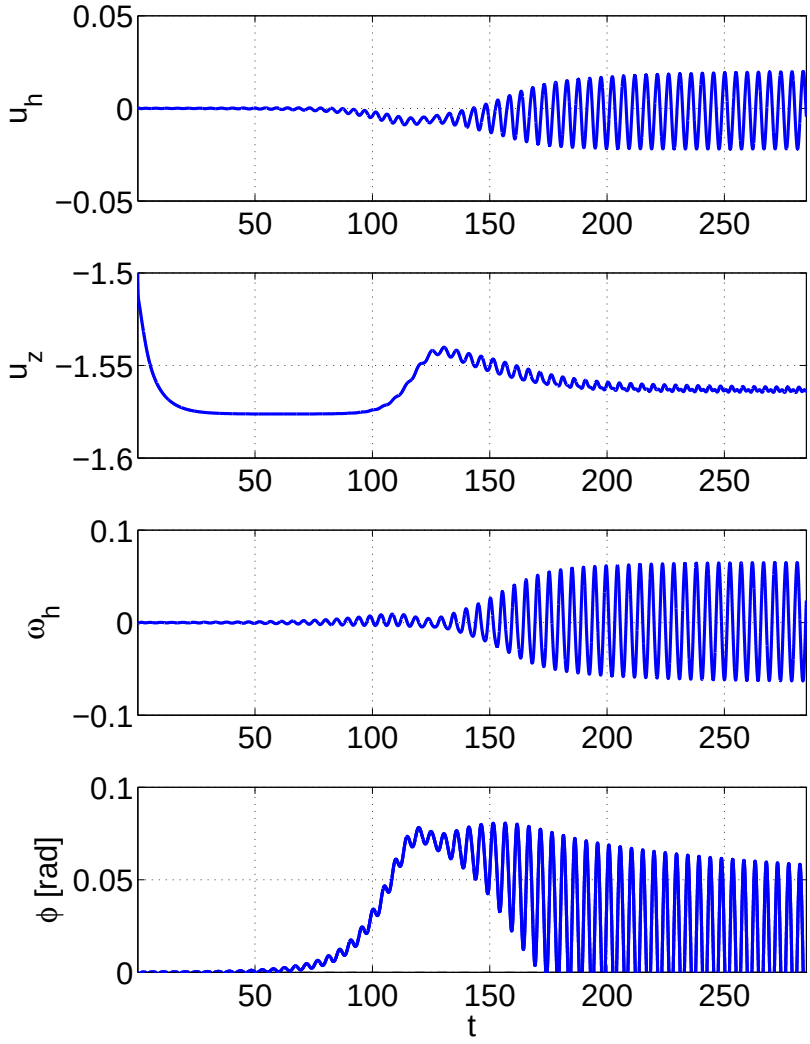

Figure 8.5: $\chi = 6$, $m^* = 0.1$ ($\rho_s/\rho = 1.146$), $G = 96$. Quasi-vertical periodic state. See caption of Figure 8.3 for the meaning of lines and symbols.

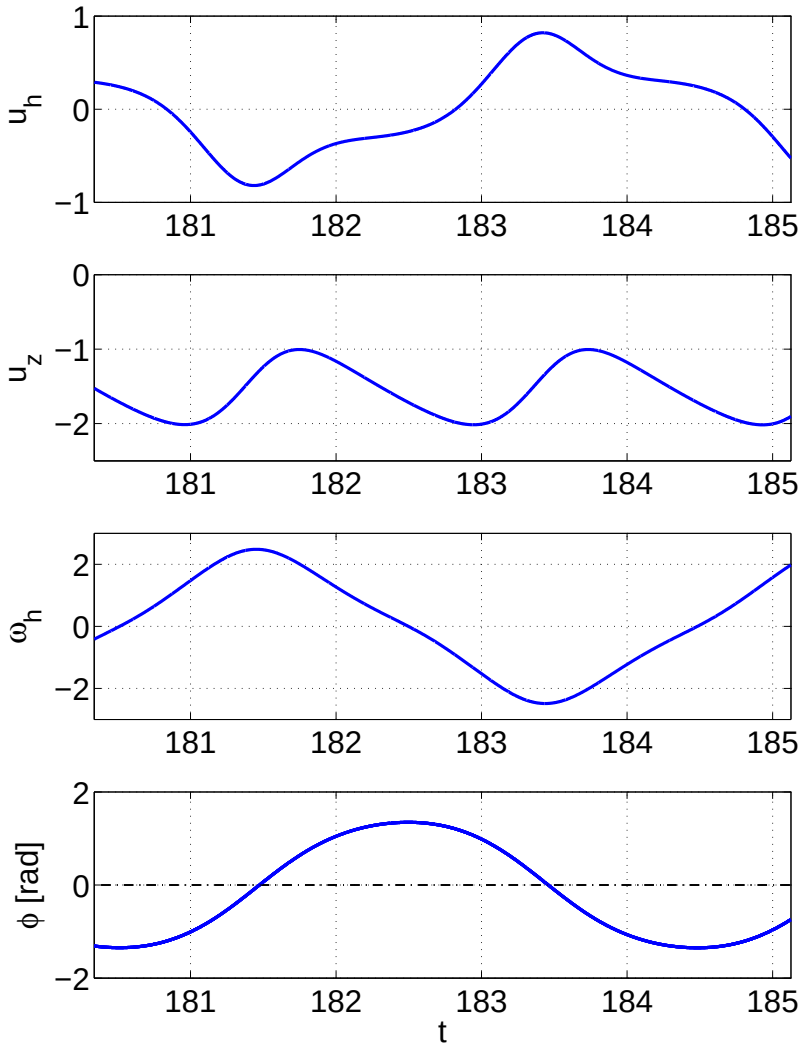

Figure 8.6: $\chi = 6$, $m^* = 0.5$ ($\rho_s/\rho = 5.730$), $G = 150$. Periodic flutter. See caption of Figure 8.3 for the meaning of lines and symbols.

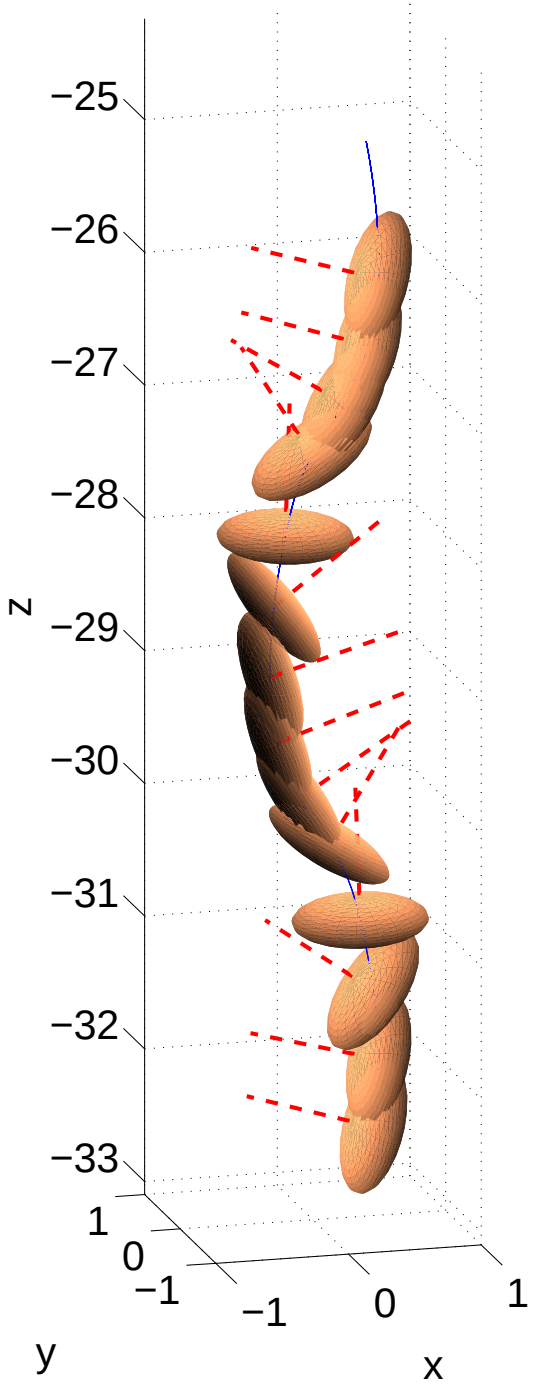

Figure 8.7: $\chi = 6$, $m^* = 0.5$ ($\rho_s/\rho = 5.730$), $G = 150$. Periodic flutter. Trajectory corresponding to the time interval represented in Figure 8.6.

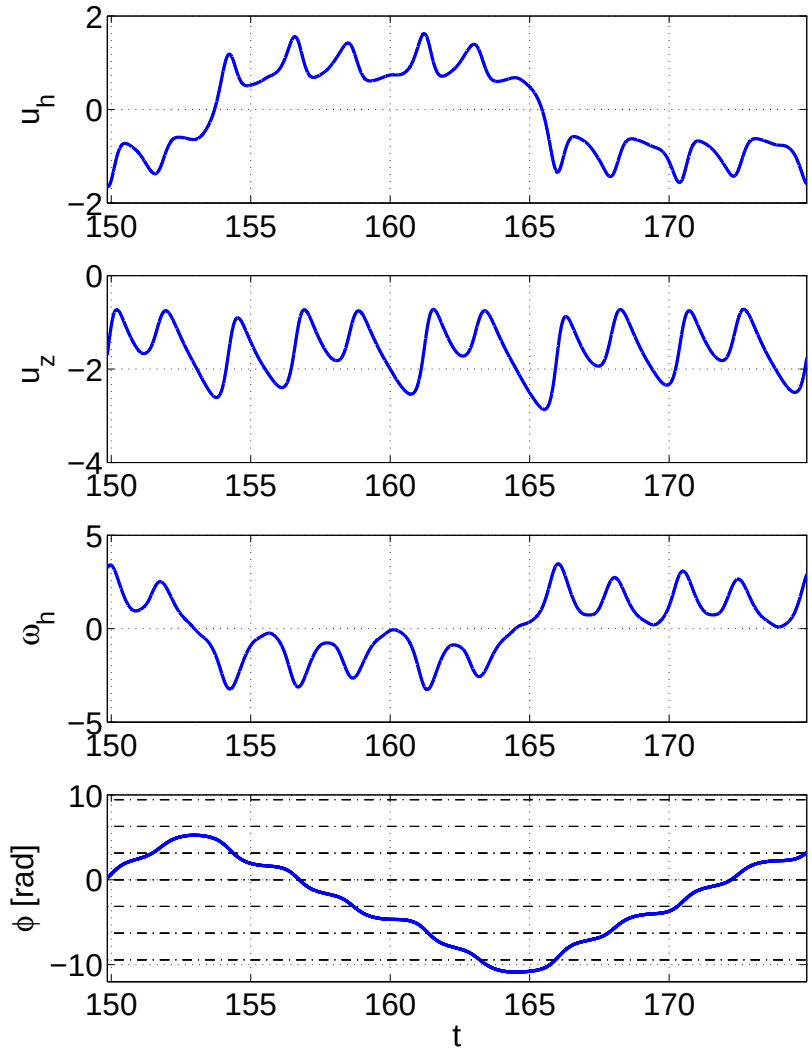

Figure 8.8: $\chi = 6$, $m^* = 0.5$ ($\rho_s/\rho = 5.730$), $G = 200$. Intermittent state. See caption of Figure 8.3 for the meaning of lines and symbols.

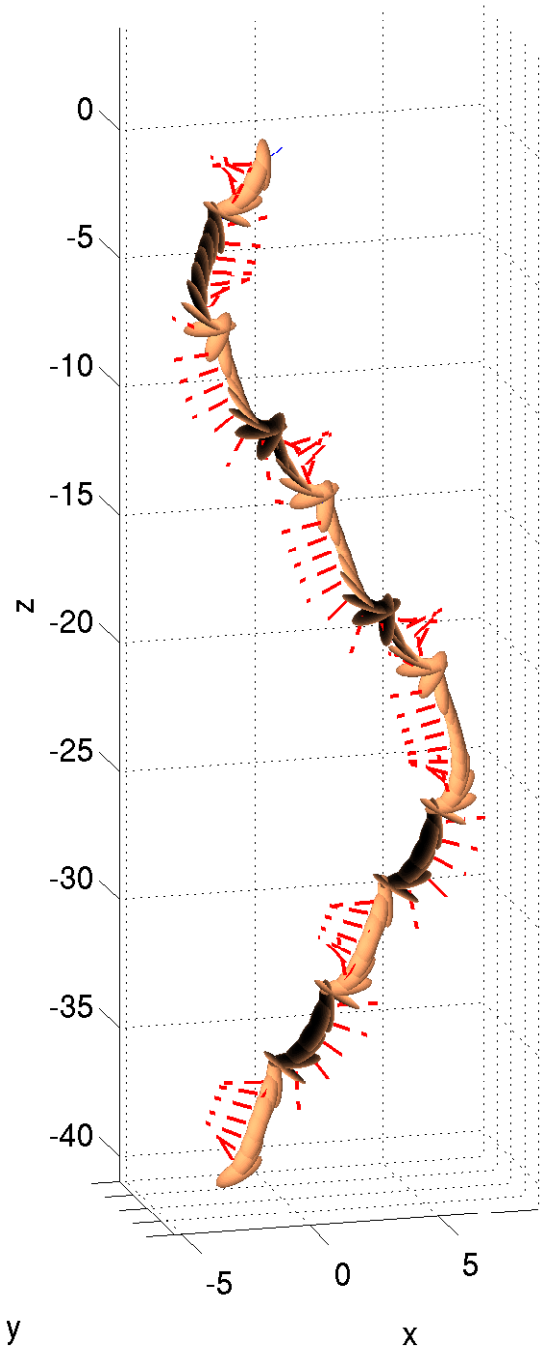

Figure 8.9: $\chi = 6$, $m^* = 0.5$ ($\rho_s/\rho = 5.730$), $G = 200$. Intermittent state. Trajectory corresponding to the time interval represented in Figure 8.8.

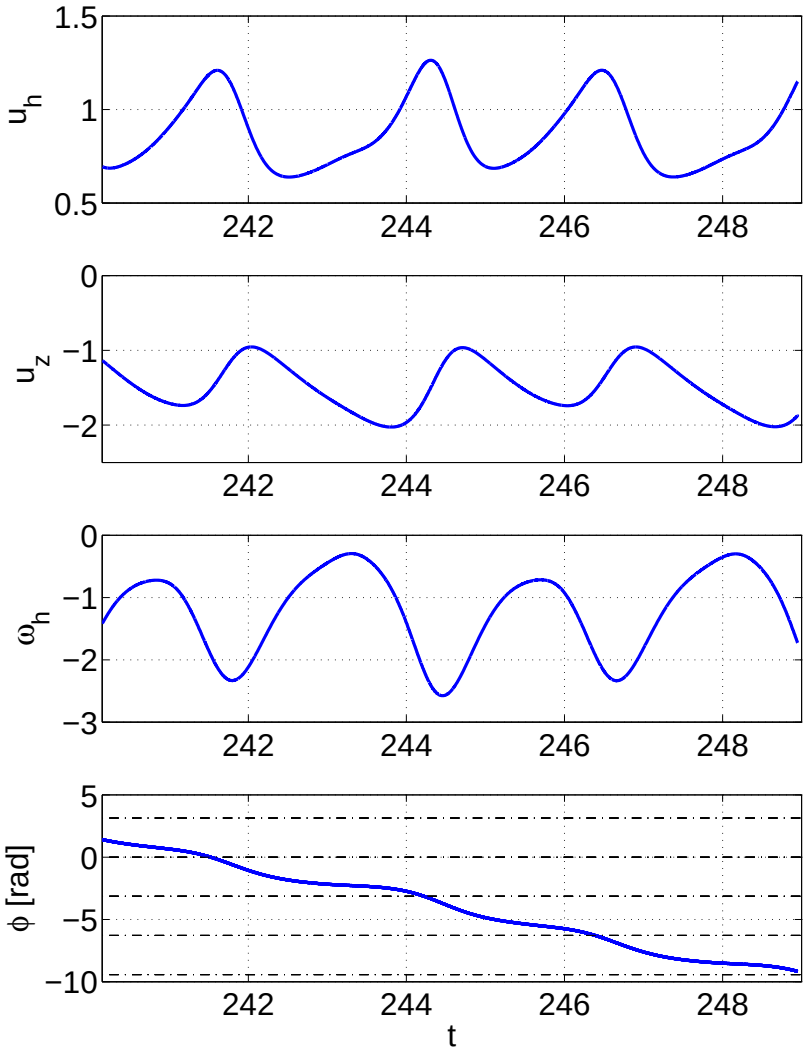

Figure 8.10: $\chi = 6$, $m^* = 0.75$ ($\rho_s/\rho = 8.594$), $G = 150$. Periodic tumbling state. See caption of Figure 8.3 for the meaning of lines and symbols.

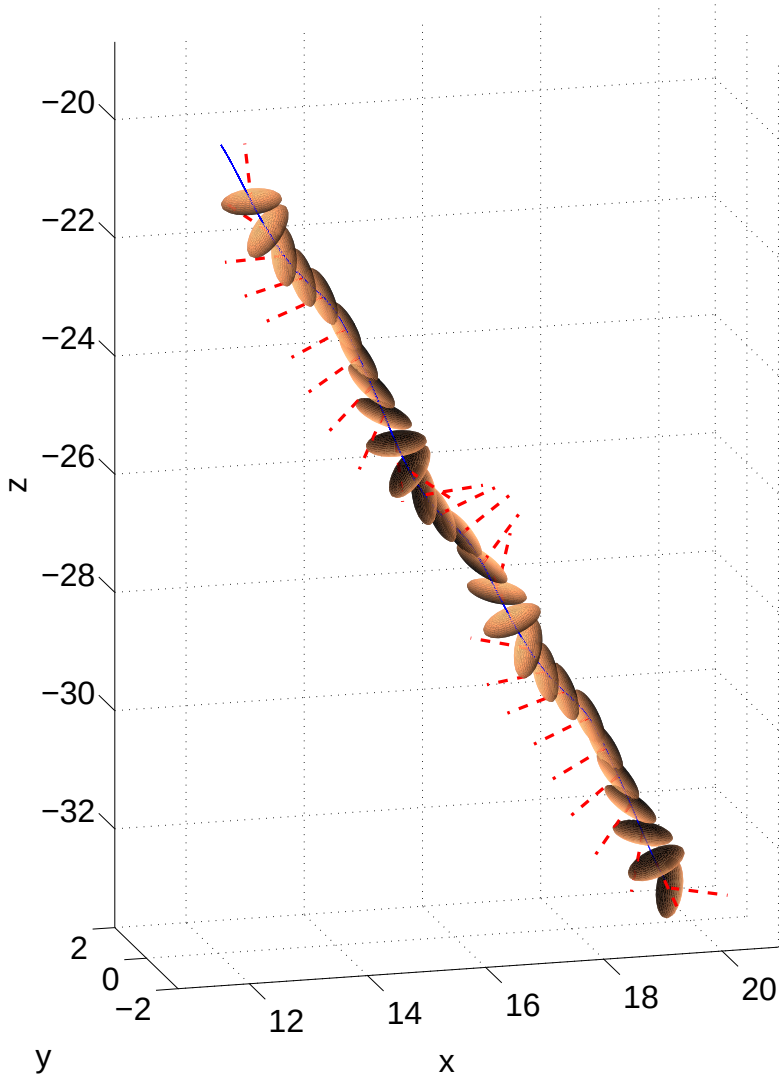

Figure 8.11: $\chi = 6$, $m^* = 0.75$ ($\rho_s/\rho = 8.594$), $G = 150$. Periodic tumbling state. Trajectory corresponding to the time interval represented in Figure 8.10.

8.3.3 $\chi = 3$

Next we considered the aspect ratio $\chi = 3$. The $G - m^*$ parameter plane is represented in Figure 8.12. The scenario is significantly different as compared to $\chi = 6$. We found no intermittent states and only one tumbling state was evidenced in the investigated domain. The difference between 'quasi-vertical' and 'fluttering' states is no longer obvious. In Figure 8.13 we represent an example of a periodic regime of a spheroid ascending along a wavy, in the average vertical, trajectory. The term of flutter no longer applies. Firstly, the round shape hardly evokes a fluttering object, secondly the amplitude of oscillations of the inclination angle remain small. We did not evidence oblique states at the primary bifurcation threshold. The primary bifurcation is a Hopf one for all investigated values of m^* and the transients of the regimes close to the primary bifurcation threshold do not carry, neither, any trace of a close to unstable real eigenvalue. In contrast to the case of $\chi = 6$, the oblique states set in at rather higher Galileo numbers (see Figures 8.14 and 8.15). At still higher Galileo number a complicated quasi-periodicity (with a still plane trajectory) lets expect a close transition to chaos (Figures 8.16 and 8.17). It is to be noted that the inclination angle of the spheroid remains very small (about 0.1 - 0.2 radian). It remains to clarify how the tumbling state develops (see Figure 8.18, note the positive sign of the angular velocity indicating the tumbling rotation and the rotation of the axis of the spheroid visible in Figure 8.19).

8.3.4 $\chi = 2$

For the aspect ratio $\chi = 2$ we evidenced again a competition between a regular and a Hopf bifurcation (see Figure 8.20). Unlike for $\chi = 6$ the primary bifurcation is regular for higher m^* (density ratios) and of the Hopf type for smaller m^* (density ratio). The threshold of the regular bifurcation is (in agreement with the theory) independent of the inertia of the body. The corresponding critical Reynolds number was found to be 153.5, i.e. slightly higher than the critical Reynolds of the regular bifurcation in the wake of a fixed spheroid of the same shape (151.5). No tumbling state was evidenced for this aspect ratio. An example of settling to a steady oblique regime with a constant inclination (of about 0.09 radian) is given in Figure 8.21. At higher Galileo numbers the mean value of early oblique regimes decays to yield zig-zagging states (vertical in the mean - Figure 8.22). For $m^* < 0.75$ they set in at the primary Hopf bifurcation. The periodic zig-zagging state becomes oblique and quasi-periodic at higher G and m^* (see Figures 8.23 and 8.24). The investigation should, very likely, be enlarged in this direction to evidence an onset of chaos and of fully three-dimensional paths.

8.3.5 $\chi = 1.5$

The smallest investigated aspect ratio was $\chi = 1.5$. In this case the primary bifurcation is regular virtually for all non-dimensionalized masses (except 0). The inertia independent threshold lies at $Re = 170$, still a little higher than the threshold of the primary bifurcation of a fixed spheroid (169). The sphere-like scenario fills a larger domain of the parameter plane. An example of settling to a steady oblique state is represented in Figure 8.26. The vertically zig-zagging state has the same frequency as the oblique oscillating state. It has thus nothing in common with the slow zig-zagging state of a perfect sphere. (An example

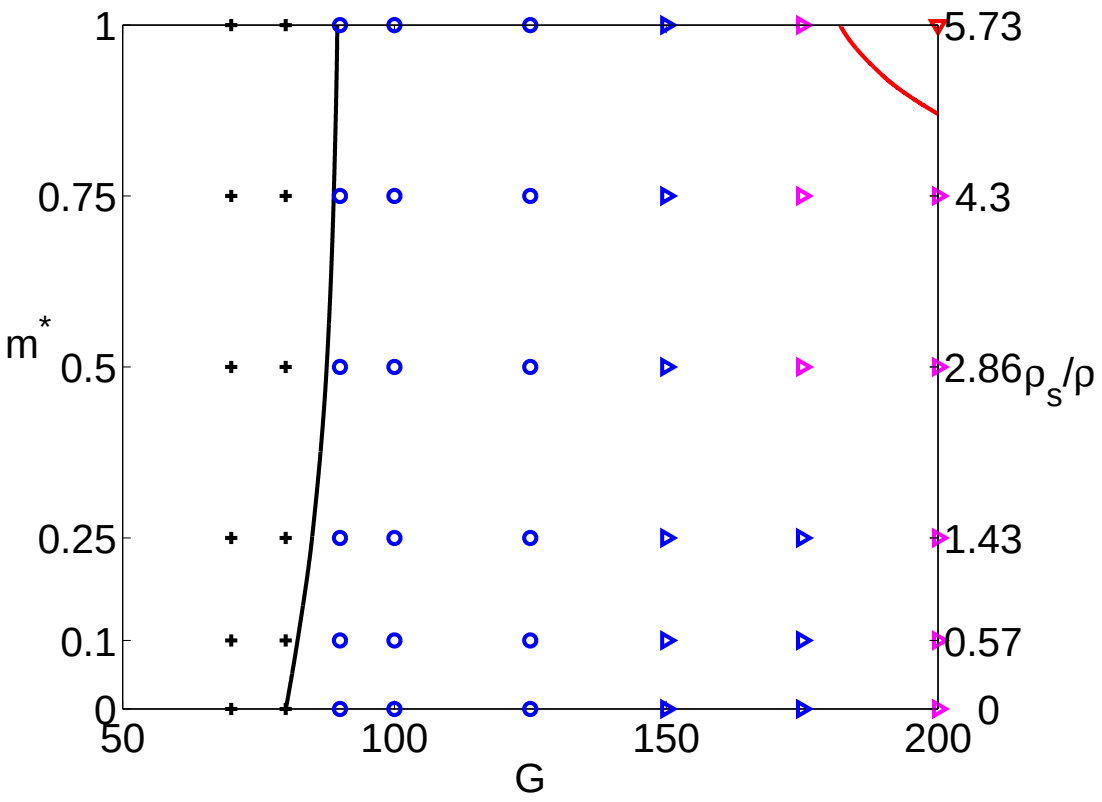

Figure 8.12: State diagram for a spheroid $\chi = 3$ in the $G - m^*(\rho_s/\rho)$ plane. The symbols denote regimes investigated by simulations. The full lines delimit the stability domains. Black line: limit of stability of vertical state. Red line: lower limit of stability of tumbling states. Black crosses: vertical state. Blue circles: periodically oscillating state, vertical in the average. Blue triangles: weakly oblique periodic fluttering state. Magenta triangles: quasi-periodic states. Red downward pointing triangle: tumbling regime.

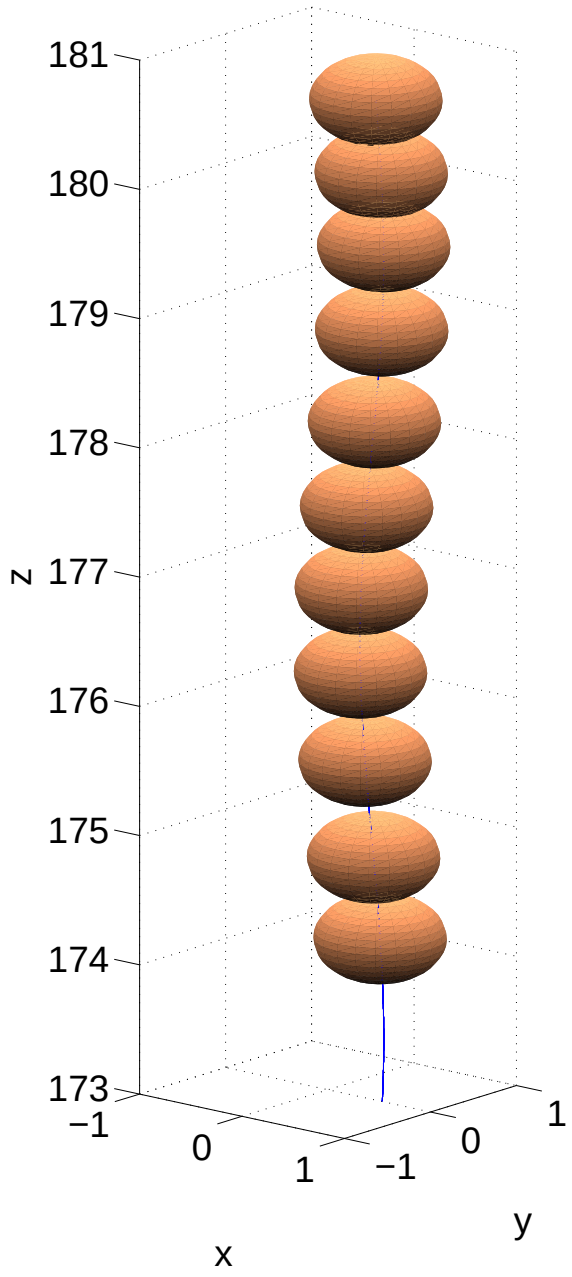

Figure 8.13: $\chi = 3$, $m^* = 0$ ($\rho_s/\rho = 0$), $G = 125$. Periodic oscillating state. Trajectory.

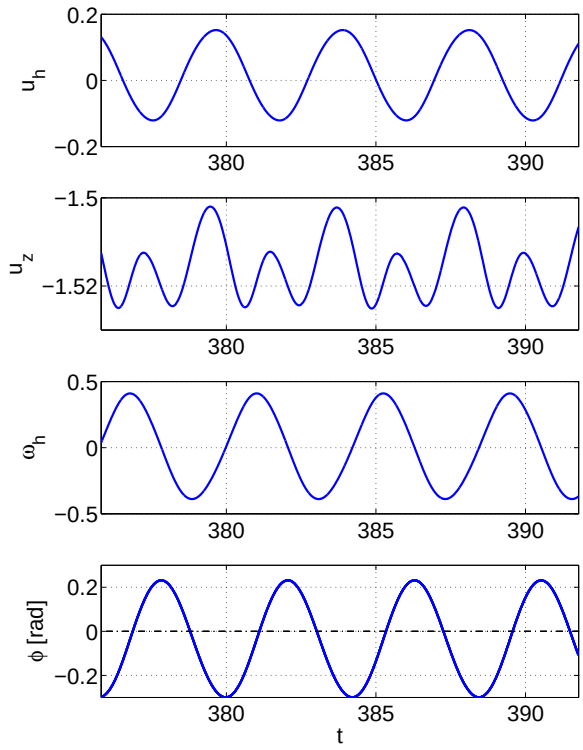

Figure 8.14: $\chi = 3$, $m^* = 0.25$ ($\rho_s/\rho = 1.432$), $G = 150$. Oblique periodic oscillating state. See caption of Figure 8.3 for the meaning of lines and symbols.

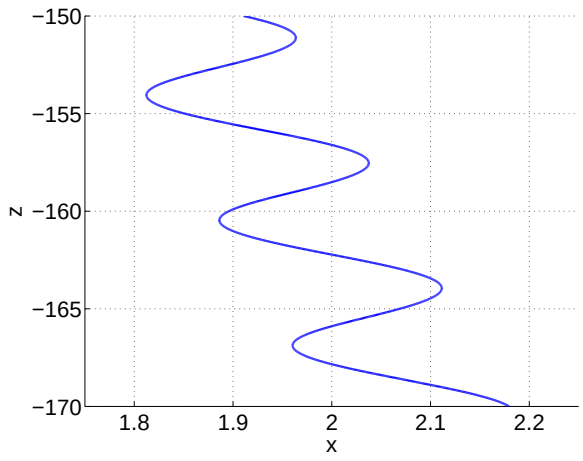

Figure 8.15: $\chi = 3$, $m^* = 0.25$ ($\rho_s/\rho = 1.432$), $G = 150$. Oblique periodic oscillating state. Trajectory corresponding to the time interval represented in Figure 8.14.

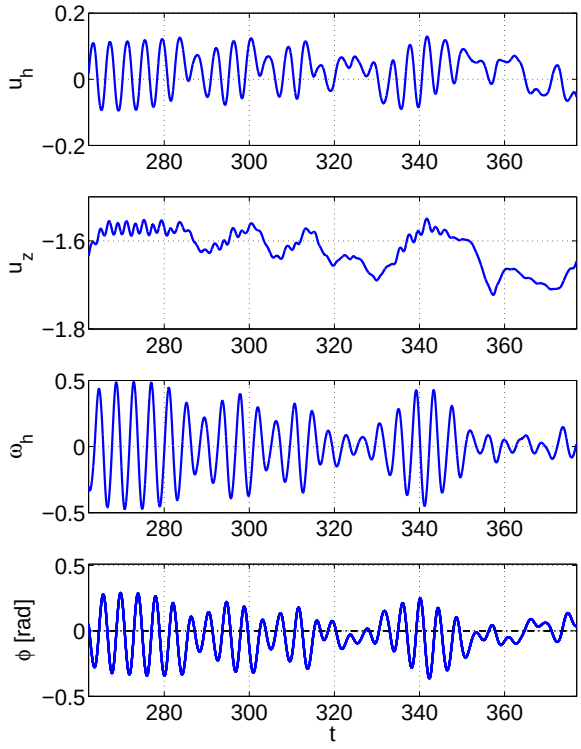

Figure 8.16: $\chi = 3$, $m^* = 0.75$ ($\rho_s/\rho = 4.297$), $G = 200$. Quasi periodic state. See caption of Figure 8.3 for the meaning of lines and symbols.

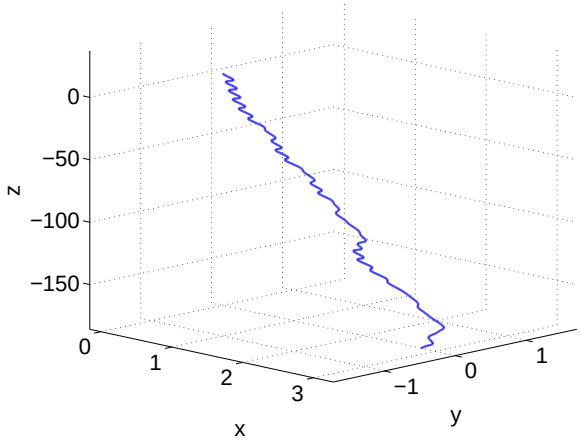

Figure 8.17: $\chi = 3$, $m^* = 0.75$ ($\rho_s/\rho = 4.297$), $G = 200$. Quasi periodic state. Trajectory corresponding to the time interval represented in Figure 8.16.

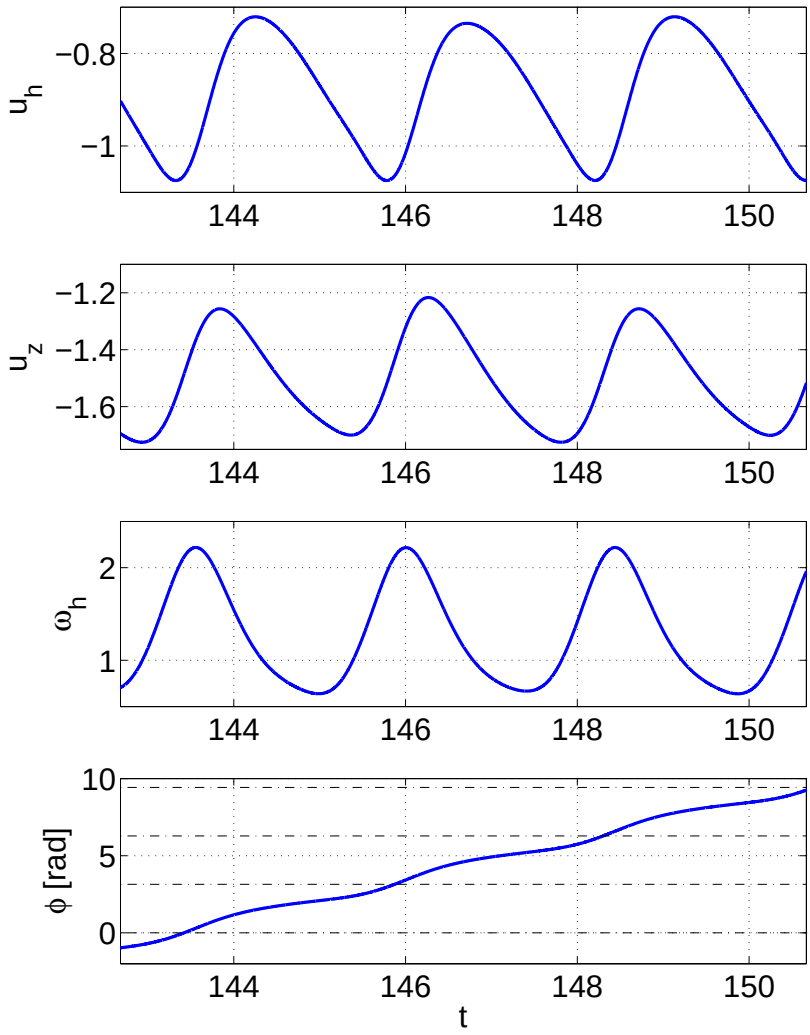

Figure 8.18: $\chi = 3$, $m^* = 1$ ($\rho_s/\rho = 5.730$), $G = 200$. Periodic tumbling state. See caption of Figure 8.3 for the meaning of lines and symbols.

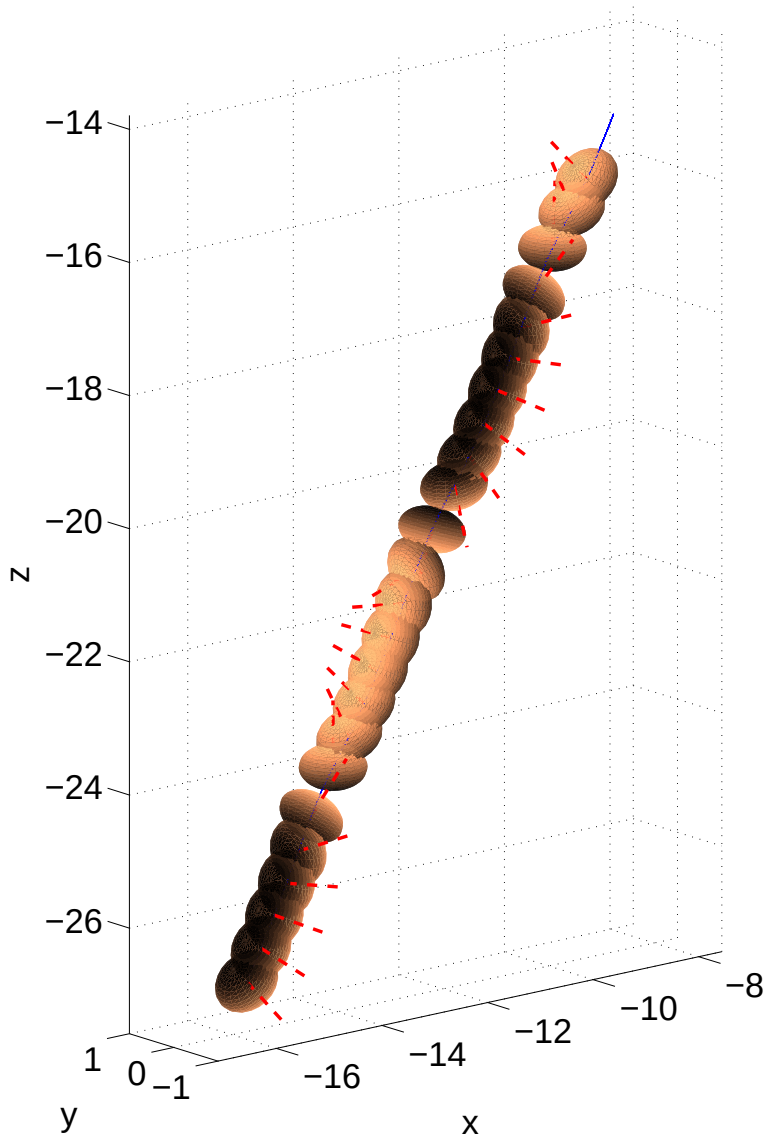

Figure 8.19: $\chi = 3$, $m^* = 1$ ($\rho_s/\rho = 5.730$), $G = 200$. Periodic tumbling state. Trajectory corresponding to the time interval represented in Figure 8.18.

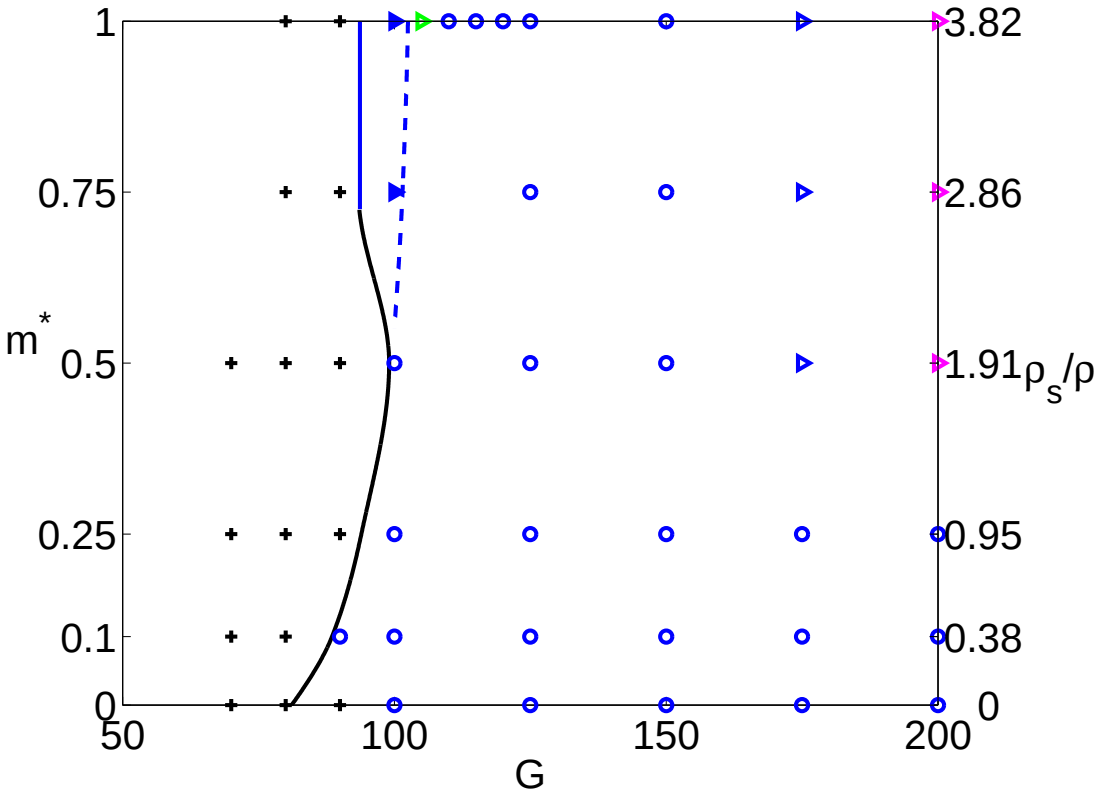

Figure 8.20: State diagram for a spheroid $\chi = 2$ in the $G - m^*(\rho_s/\rho)$ plane. The symbols denote regimes investigated by simulations. The full lines delimit the stability domains. Black line: lower limit of stability of periodic state. Blue line: lower limit of stability of steady oblique states (SO). Blue dashed line: limit of stability of steady oblique states (SO). Black crosses: vertical state. Blue circles: periodic zig-zagging states. Blue triangles: weakly oblique zig-zagging states. Blue filled triangles: steady oblique states (SO). Green triangles: oblique oscillating states (OO). Magenta triangles: quasi-periodic states. Threshold of the steady oblique state: $G_{crit}^{\chi=2} = 93.39$ ($Re_{crit}^{\chi=2} = 153.47$). Threshold of the primary bifurcation of a fixed spheroid: $Re_{cf1}^{\chi=2} = 151.45$.

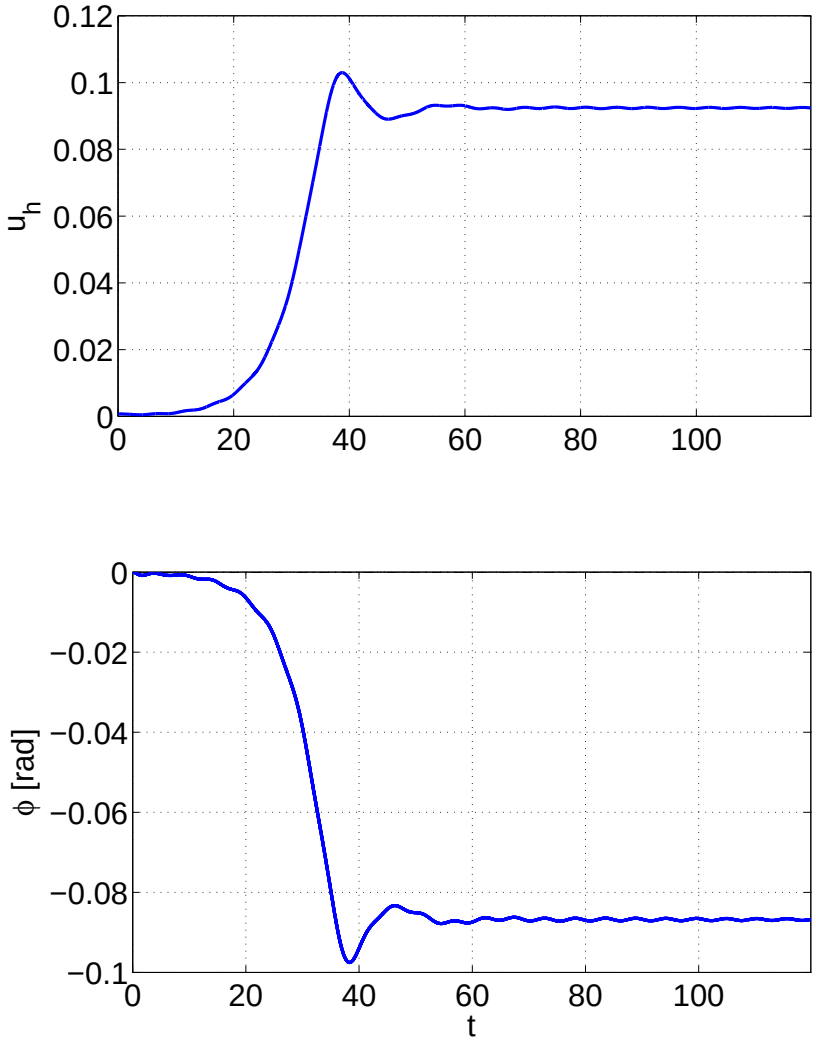

Figure 8.21: $\chi = 2$, $m^* = 0.75$ ($\rho_s/\rho = 2.865$), $G = 100$. Steady oblique state (SO). Meaning of symbols: u_h - horizontal component of the velocity, ϕ - inclination of the spheroid, defined as the angle between its axis and the vertical direction.

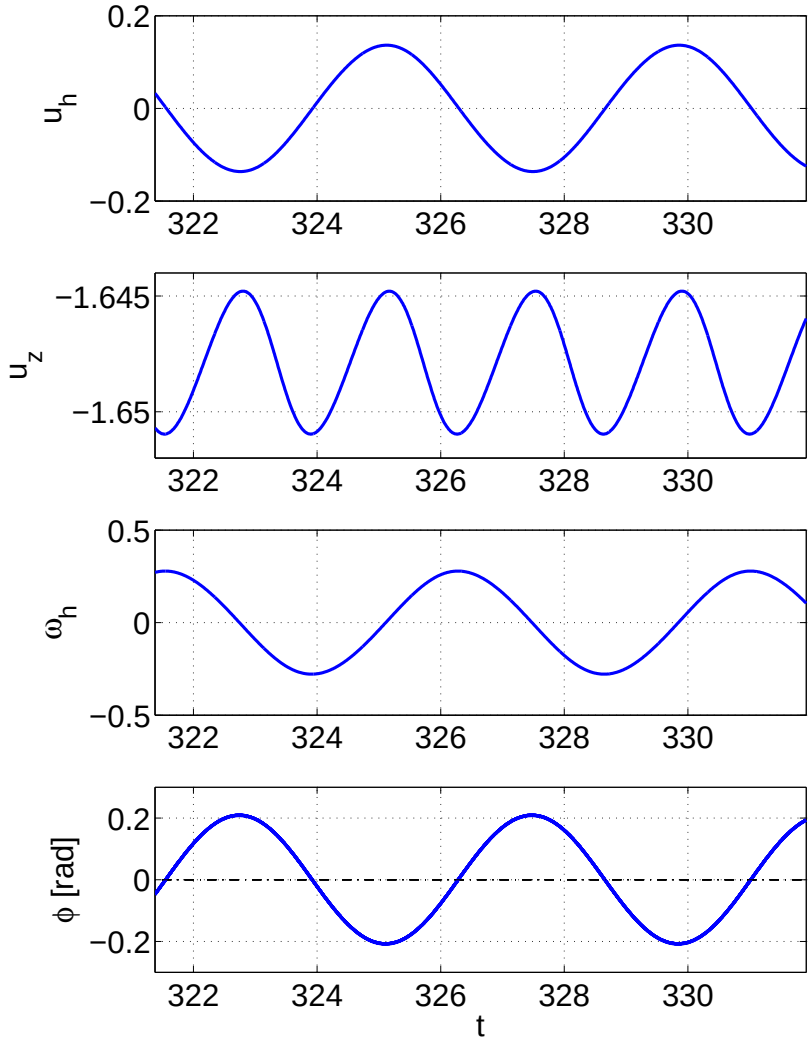

Figure 8.22: $\chi = 2$, $m^* = 0.5$ ($\rho_s/\rho = 1.910$), $G = 150$. Periodic oscillating state. See caption of Figure 8.3 for the meaning of lines and symbols.

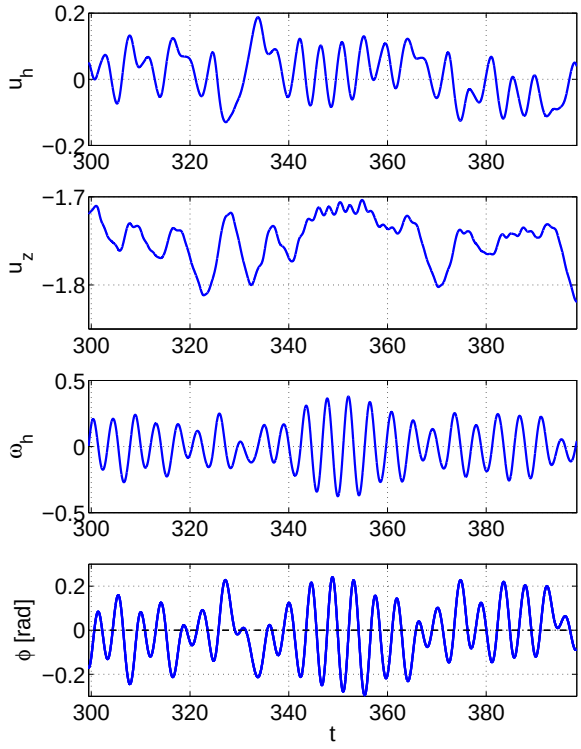

Figure 8.23: $\chi = 2$, $m^* = 1$ ($\rho_s/\rho = 3.820$), $G = 200$. Quasi periodic state. See caption of Figure 8.3 for the meaning of lines and symbols.

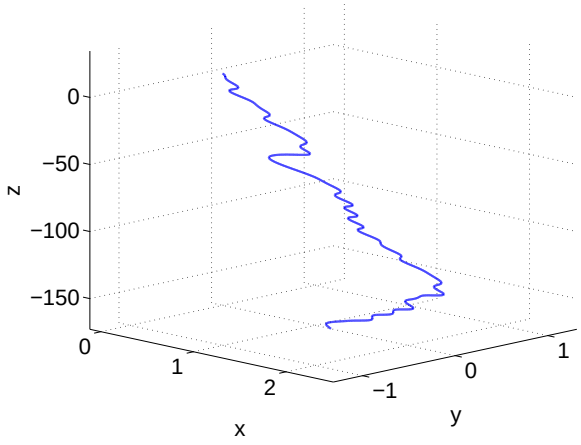

Figure 8.24: $\chi = 2$, $m^* = 1$ ($\rho_s/\rho = 3.820$), $G = 200$. Quasi periodic state. Trajectory corresponding to the time interval represented in Figure 8.23.

of a zig-zagging state for this aspect ratio is in Figure 8.27. Again a likely beginning of a transition to chaos is captured in the upper left corner of the investigated region of the parameter plane (Figures 8.28 and 8.29).

8.4 Conclusion

In spite of several open questions that require a finer and more complete investigation of the parameter space, the results presented above convey an idea about the evolution of the transition scenario from thin discs to almost spherical bodies. The flat body scenario can be considered as limited by the aspect ratio of 3. Beyond this aspect ratio, the earliest stages of transition are close to that observed for a perfect sphere except for the lack of rotation in oblique states. The absence of rotation may be a significant feature distinguishing imperfect spheres (spheroids of aspect ratio of almost one) from perfect ones. A fine investigation of the regular bifurcation for a progressively varying aspect ratio tending to one will be carried out. (An arbitrary selected single value of m^* should be sufficient for this purpose.)

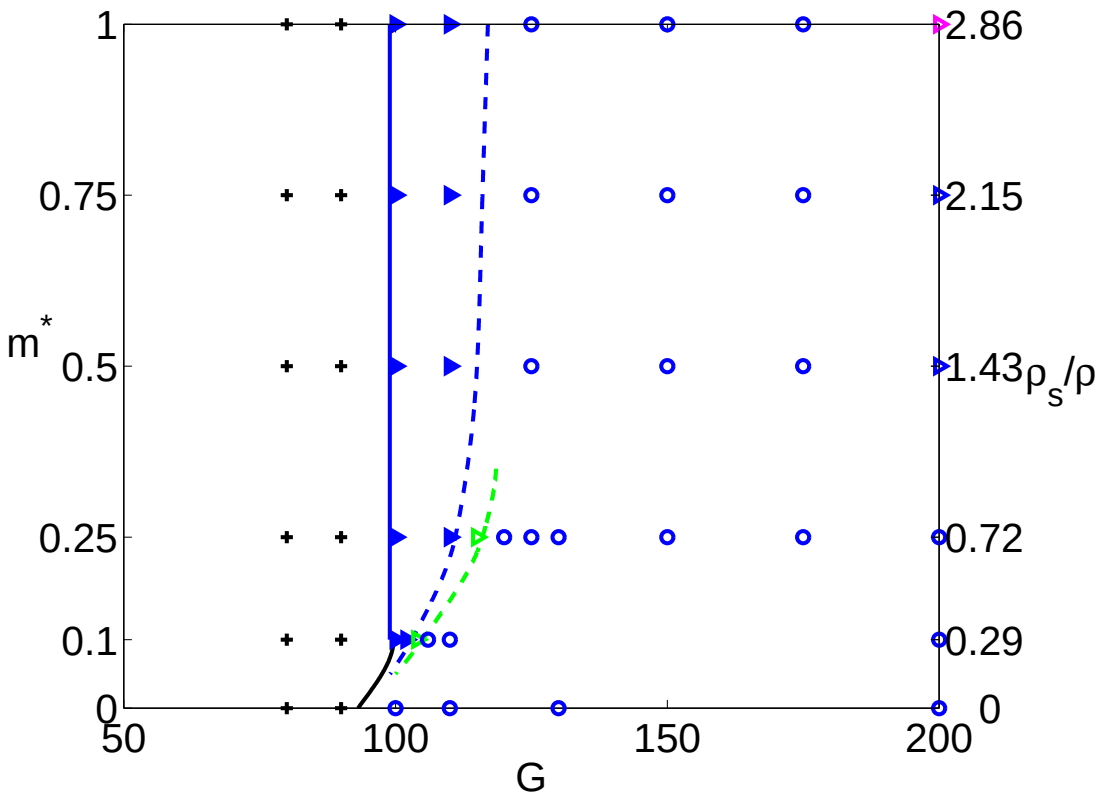

Figure 8.25: State diagram for a spheroid $\chi = 1.5$ in the $G - m^*(\rho_s/\rho)$ plane. The symbols denote regimes investigated by simulations. The full lines delimit the stability domains. Black line: lower limit of stability of periodic state. Blue line: lower limit of stability of steady oblique states (SO). Blue dashed line: limit of stability of steady oblique states (SO). Green dashed line: limit of stability of oblique oscillating states (OO). Black crosses: vertical state. Blue circles: periodic flutter state. Blue triangles: weakly oblique periodic fluttering state. Blue filled triangles: steady oblique states (SO). Green triangles: oblique oscillating states (OO). Magenta triangles: chaotic states. Threshold of the steady oblique state: $G_{crit}^{\chi=2} = 99.31$ ($Re_{crit}^{\chi=2} = 170.14$). Threshold of the primary bifurcation of a fixed spheroid: $Re_{cf1}^{\chi=2} = 168.89$.

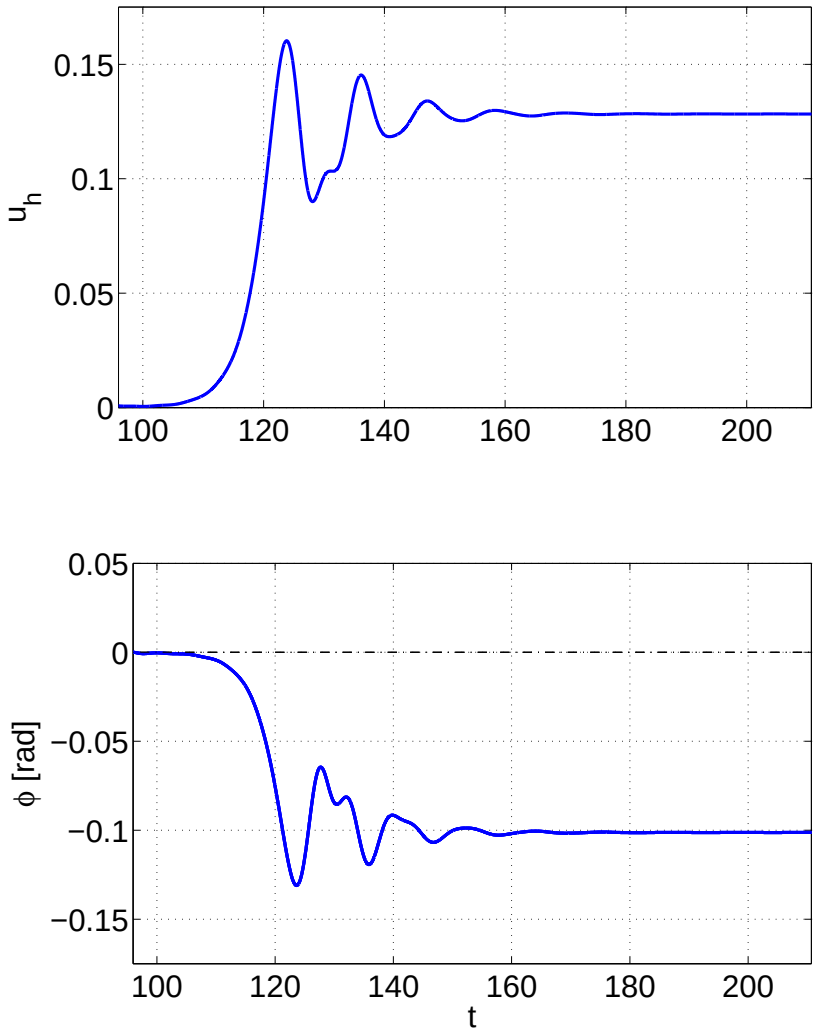

Figure 8.26: $\chi = 1.5$, $m^* = 0.75$ ($\rho_s/\rho = 2.149$), $G = 110$. Steady oblique state (SO). See caption of Figure 8.21 for the meaning of lines and symbols.

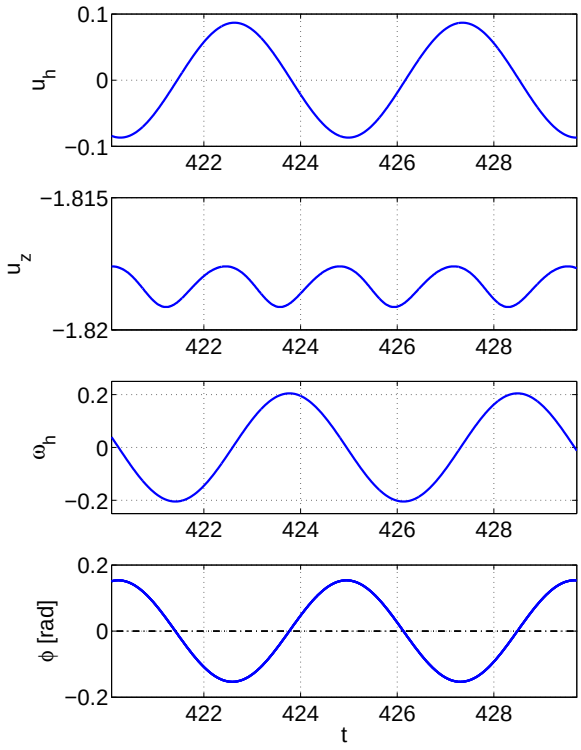

Figure 8.27: $\chi = 1.5$, $m^* = 1$ ($\rho_s/\rho = 2.865$), $G = 175$. Periodic oscillating state. See caption of Figure 8.3 for the meaning of lines and symbols.

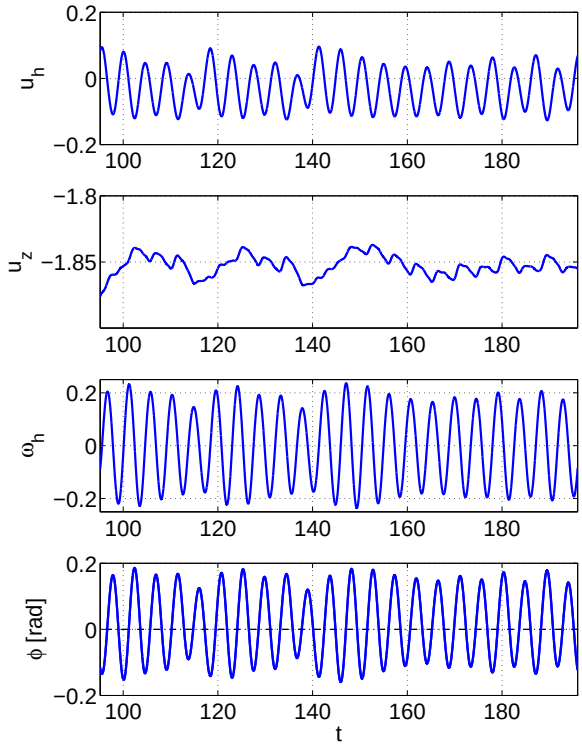

Figure 8.28: $\chi = 1.5$, $m^* = 1$ ($\rho_s/\rho = 2.865$), $G = 200$. Quasi periodic state. See caption of Figure 8.3 for the meaning of lines and symbols.

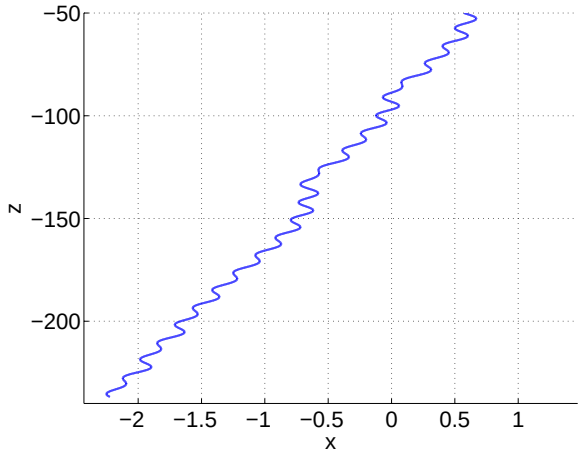

Figure 8.29: $\chi = 1.5$, $m^* = 1$ ($\rho_s/\rho = 2.865$), $G = 200$. Quasi periodic state. Trajectory corresponding to the time interval represented in Figure 8.23.

Chapter 9

Conclusions and perspectives

The present thesis was devoted to the study of transitional regimes in the wakes of axisymmetric bodies, fixed with their axis both parallel and inclined to the free stream direction and to path instabilities of bodies freely moving under the action of buoyancy, gravity and hydrodynamic forces.

The crucial starting point of this thesis was the adaptation of the efficient and accurate spectral-spectral element code used previously for the study of spherical particles to the study non-spherical bodies. Indeed, as shown in the bibliographic review, the absence of available sufficiently efficient and accurate numerical method was the decisive obstacle explaining the absence of numerical results on this topic. The goal was achieved by decomposing the cylindrical computational domain into a spherical subdomain rotating with the object and the remaining cylindrical part. The interface between the two subdomains was discretized by expansion in spherical functions. The optimality of the representation of the rotation group in the basis of spherical functions minimized the computational cost necessary to dynamically reconnect the two subdomain within an implicit algorithm assuring both a sufficient stability and very high accuracy. Within both subdomains, the spectral azimuthal expansion, used for many years with success by the research team, was applied. The code was validated by reproducing the scenarios of fixed cylinders and of a freely moving sphere obtained with the previous version of the code.

The study of fixed bodies, although important in its own right, helped to a large extent to shed light on the origins of complex trajectories found later on for freely moving counterparts. At the beginning of the present study, only the transition scenarios of extreme cases of a fixed sphere and of a fixed infinitely thin disc were well explored. Interestingly, they were found to differ significantly. There were also few results published on the transition of flat cylinders of intermediate aspect ratios of $\chi = 10$ and 3. However, the link between the scenario of a disc and a sphere was missing. We established the connection between the two bodies by studying the transition in the wake of oblate spheroids of intermediate aspect ratios $1 \leq \chi \geq \infty$. This choice of body shape was not only original (to our knowledge we were the first to study these geometries) but it sheds more light on the effect of aspect ratio than the study of flat cylinders. Nevertheless, we have also considerably completed the knowledge on the wake of flat cylinders for the same range of aspect ratios. We found a

significant qualitative similarity between both configurations. At large aspect ratios ($\chi > 2.3$ for spheroids and $\chi \geq 4$ for cylinders), the secondary bifurcation giving rise to a periodic state without planar symmetry is subcritical with a small, but clearly identified hysteresis interval of about two Reynolds number units. For small aspect ratios ($\chi \geq 1$ are considered), the sphere-like scenario is recovered only at aspect ratios very close to one for spheroids. For cylindrical bodies the same scenario holds for $\chi \leq 1.7$. For intermediate aspect ratios, a domain of states with non zero net helicity separates states typical for the sphere wake from those of an infinitely flat disc.

Although reproduced by several independent numerical studies, the transition scenario predicted numerically for the wake of a disc placed perpendicularly to the flow direction has never been confirmed experimentally. We decided to address this question by joint experimental and numerical investigation. (The experimental part of the work was done at the PPMH laboratory of ESPCI in Paris.) We demonstrated that the scenario predicting the appearance of the periodic state without planar symmetry at the secondary Hopf bifurcation in the wake of an infinitely thin disc is purely theoretical. Experiments show that the observed scenario is qualitatively similar to that of a sphere. We linked this result to the impossibility of realization of a perfect axisymmetric configuration due to holding constraints. Therefore, using the possibility of simulating axisymmetric bodies inclined arbitrarily with respect to the flow direction, we considered discs (and cylinders of aspect ratio $\chi = 6$) with their symmetry axis weakly inclined to the free stream direction. We evidenced that the theoretical scenario can be found only for very small inclination angles $\phi < 4^o$ (still the influence of the holding in experimental set-up might lower this threshold), otherwise the periodic state without planar symmetry is suppressed. At angles larger or equal than 4^o the experimentally evidenced sphere-like scenario was numerically confirmed. Moreover, the investigation was completed by a study of the effect of larger inclination angles (up to 50^o) on the onset of unsteadiness and on the Strouhal number of arising oscillations. Old experimental results of Calvert (1967) were very faithfully reproduced, confirming the weak dependence of the Strouhal number on the Reynolds number.

Our work was originally mainly motivated by the intriguing behavior of thin bodies (falling discs, cards, leafs) that had been recurrently the topic of a large number investigations ranging from simple observations to highly theoretical papers. The paper by Field *et al.* (1997) was even published in Nature. The efficiency of the developed code has allowed us to run many hundreds of simulations yielding an extensive parametric study of the transition scenario of freely falling infinitely thin discs. We explored the parameter space spanned by dimensionless masses $0 < m^* < 10$ and Galileo numbers $30 < G < 500$. We confirmed the existence of four well-known states reported in experiments of Field *et al.* (1997). Their stability domains were found to be in a relatively good agreement with those reported therein but could be determined with a much better accuracy. For $m* < 0.1$ we found a domain of co-existence of quasi-periodic and fluttering states important for the explanation of other experimental data discussed in the framework of our study of flat cylinders. For the discs, it allowed us to explain the intriguing upward shift of the onset of path oscillations observed for discs of weak inertia by Willmarth *et al.* (1964) for discs and recently by Fernandes *et al.* (2007) for flat cylinders of the aspect ratio $\chi \geq 10$. For discs characterized by more significant inertia (higher values of non-dimensionalized mass m^*) we evidenced the tumbling

states. We could dissipate all doubts (see Field *et al.* (1997)) concerning their periodicity. For intermediate values of m^* we found the transition to periodic fluttering and to the intermittent state at lower Galileo (Reynolds) numbers than in experiments. This disagreement is to be elucidated by further carrying out analyzing experimental studies, similarly as we have done for inclined fixed cylinders. Perhaps the most intriguing feature of the evidenced scenario is the role of sub-critical bifurcations leading to several sub-domains of co-existence of regimes, be it the already mentioned quasi-vertical and fluttering ones or the vertical and periodic fluttering states for $0.1 < m^* < 1$ and the tumbling and fluttering states for discs with high inertia. We witnessed also the existence of three dimensional, spiral states reported by Zhong *et al.* (2011). We demonstrate that for all considered m^* for high Galileo numbers all trajectories lose their initial planarity. We discovered a new spiral tumbling state characterized by a regular helical trajectory of a very large diameter accompanied by the tumbling disc. The obtained results can be expected to have a similar impact as those published in the research team several years ago on the scenario of freely falling or ascending spheres Jenny *et al.* (2004).

As another application we addressed the open question raised by the experiments of Fernandes *et al.* (2007) devoted to the study of the transition of freely rising (ρ_s/ρ=0.99) flat cylinders of aspect ratios $2 \leq \chi \leq \infty$. Fernandes *et al.* (2007) evidenced an intriguing upward shift (towards higher Reynolds numbers) of the onset of observed path instabilities for flat cylinders of aspect ratio larger than 6. By our numerical parametric study we demonstrated that the observed shift of the onset of periodic fluttering states for thin cylinders $\chi > 6$ is related in part (for aspect ratios up to 10) to the stabilizing effects of the additional degrees of freedom of the free body (confirming recent theoretical predictions of Fabre *et al.* (2012)) and (for aspect ratios larger or equal to 10) to the bi-stability domain of small amplitude states: steady oblique, oblique oscillating, quasi vertical periodic and chaotic, discarded as experimental noise with the fluttering regime. We showed that the lower limit of the bi-stability domain agrees exceptionally well with the experimental results.

Eventually, we have carried out an extensive parametric study of the transition scenario of freely moving oblate spheroids of aspect ratios $\chi = \infty, 6, 3, 2$ and 1.5, the purpose of which is to establish the link between the transition scenario of an infinitely thin disc, studied in the framework chapter 6 of the present thesis, and the scenario of a spherical particle. For each aspect ratio we explored the parameter space spanned by the dimensionless mass m^* and the Galileo number G in the range $0 \leq \chi \leq 1$ and $50 \leq G \leq 200 >$, respectively. In spite of the fact that the results need to be refined and more accurately interpreted before publication, it can be said that $\chi \leq 3$ the found scenario can be considered as a thin-disc like, while that observed for $\chi \geq 2$ resembles that of free spheres.

The present thesis provides a very complete picture of the transition scenarios of fixed and freely moving spheroids and of flat cylinders of aspect ratios ranging from 1 to ∞ demonstrating the abundance of transitional states preceeding chaos. Our direct numerical simulations yield not only the global picture of transition scenarios, but also provide extensive information on the transitional regimes themselves by listing important characteristics and giving details of the wake structures. Therefore this thesis might serve as a reference both for the study of complex multi-particle flows and for benchmarking of multi-purpose multi-particle codes. Last but not least, the large quantity of data demonstrate the efficiency of

the developed numerical tool.

Nevertheless, a few points still require clarification and further studies. As already mentioned, the reported early onset of periodic flutter compared to the experimental data should be elucidated, possibly by carrying our a joint experimental-numerical study. We shall also continue the study of freely moving oblate spheroids for aspect ratios in the range $1 < \chi < 1.5$. Finally we considered freely moving flat cylinders for only one density ratio leaving scenarios pertaining to other ratios uncovered.

Bibliography

Augspurger, C. K. 1996 Morphology and dispersal potential of wind-dispersed diaspores of neotropical trees. *American Journal of Botany* **73**, 353–363.

Auguste, F. 2010 Instabilités de sillage générées derrière un corps solide cylindrique, fixe ou mobile dans un fluide visqueux. PhD thesis, Université Paul Sabatier, Toulouse.

Auguste, F., Fabre, D. & Magnaudet, J. 2010 Bifurcations in the wake of thick circular disk. *Theor. Comput. Fluid Dyn.* **24**, 305–313.

Auton, T. 1983 The dynamics of bubbles, drops and particles in motion in liquids. PhD thesis, Cambridge University.

Baker, A.J. 1983 *Finite Element Computational Fluid Mechanics*. Hemisphere, New York, Washington, Philadelpia, London.

Basset, A.B. 1888 *A Treatise on Hydrodynamics*. Cambridge University Press.

Bönisch, S. & Heuveline, V. 2007 On the numerical simulation of the unsteady free fall of a solid in a fluid: I. the newtonian case. *Comput. Fluids* **36**, 1434–1445.

Bönisch, S., Heuveline, V. & Wittwer, P. 2005 Adaptive boundary conditions for exterior flow problems. *J. math. fluid. mech.* **7**, 85–107.

Bönisch, S., Heuveline, V. & Wittwer, P. 2008 Second order adaptive boundary conditions for exterior flow problems: Non-symmetric stationary flows in two dimensions. *J. math. fluid. mech.* **10**, 45–70.

Bouchet, G., Mebarek, M. & Dušek, J. 2006 Hydrodynamic forces acting on a rigid fixed sphere in early transitional regimes. *European Journal of Mechanics, B/Fluids* **25**, 321–336.

Boussinesq, J. 1985 Sur la résistance qu'oppose ... soient négligeables. *C. R. Acad. Sci. Paris, volume = 100, pages = 935-937* .

Brown, Phillip P. & Lawler, Desmond F. 2003 Sphere drag and settling velocity revisited. *Journal of Environmental Engineering* **129** (3), 222–231.

Caballina, O. 2002 Etude de l'instabilité d'un panache a bulles et comparaison avec les structures organiseees d'un panache a masse volumique variable. PhD thesis, Université Louis Pasteur, Strasbourg.

Calvert, J. R. 1967 Experiments on the flow past an inclined disk. *Journal of Fluid Mechanics* **29** (04), 691–703.

Cassadevall, T.J. 1992 Volcanic hazards and aviation safety: Lessons of the past decade. *FAA Aviation Safety Journal, volume = 2, number = 3, pages = 1-11,* .

Chrust, M., Bouchet, G. & Dušek, J. 2010 Parametric study of the transition in the wake of oblate spheroids and flat cylinders. *J. Fluid Mech.* **665**, 199–208.

Danaila, I., Dušek, J. & Anselmet, F. 1998 Nonlinear dynamics at a hopf bifurcation with axisymmetry breaking in a jet. *Physical Review E* **57**, 3695–3698.

Deloze, T., Hoarau, Y. & Dušek, J. 2010 Chimera method applied to the simulation of a freely falling cylinder in a channel. *European Journal of Computational Mechanics* **19**, 575–590.

Dušek, J., Gal, P. Le & Fraunié, P. 1994 A numerical and theoretical study of the first Hopf bifurcation in a cylinder wake. *J. Fluid Mech.* **264**, 59–80.

Einstein, A. & Fürth, R. 1956 *Investigations on the Theory of the Brownian Movement*. Dover Publications.

Ellingsen, K. & Risso, F. 2001 On the rise of an ellipsoidal bubble in water: oscillatory paths and liquid-induced velocity. *J. Fluid Mech.* **440**, 235–268.

Ern, P., Risso, F., Fabre, D. & Magnaudet, J. 2012 Wake-indused oscillatory paths of bodies freely rising of falling in fluids. *Ann. Rev. of Fluid Mech.* **44**, 97–121.

Fabre, D., Auguste, F. & Magnaudet, J. 2008 Bifurcations and symmetry breaking in the wake of axisymmetric bodies. *Physics of Fluids* **20**, 051702.

Fabre, D., Tchoufag, J. & Magnaudet, J. 2012 The steady oblique path of buoyancy-driven disks and spheres. *Journal of Fluid Mechanics* **707**, 24–36.

Fernandes, P. C., Risso, F., Ern, P. & Magnaudet, J. 2007 Oscillatory motion and wake instability of freely rising axisymmetric bodies. *J. Fluid Mech.* **573**, 479–502.

Field, S.B., Klaus, M. & Moore, M.G. 1997 Chaotic dynamics of falling disks. *Nature* **388**, 252–254.

Fonseca, F. & Herrmann, H.J. 2005 Simulation of the sedimentation of a falling oblate ellipsoid. *Physica A* **345**, 341–355.

García-Villalba, Manuel, Kidanemariam, Aman G. & Uhlmann, Markus 2012 Dns of vertical plane channel flow with finite-size particles: Voronoi analysis, acceleration statistics and particle-conditioned averaging. *International Journal of Multiphase Flow* **46** (0), 54 – 74.

Ghidersa, B. & Dušek, J. 2000 Breaking of axisymetry and onset of unsteadiness in the wake of a sphere. *J. Fluid Mech.* **423**, 33–69.

Glowinski, R., Pan, T.W., Hesla, T.I., Joseph, D.D. & Périaux, J. 2001 A fictitious domain approach to the direct numerical simulation of incompressible viscous flow past moving rigid bodies: Application to particulate flow. *Journal of Computational Physics* **169**, 363–426.

Goldburg, A. & Florsheim, B. H. 1966 Transition and strouhal number for the incompressible wake of various bodies. *Physics of Fluids* **9**, 45–50.

Gumowski, K., Miedzik, J., Goujon-Durand, S., Jenffer, P. & Wesfreid, J. E. 2008 Transition to a time-dependent state of fluid flow in the wake of a sphere. *Physical Review E* **77**.

Hecht, K.T. 2000 *Quantum Mechanics*. Springer.

Horowitz, M. & Williamson, C. H. K. 2010*a* The effect of reynolds number on the dynamics and wakes of freely rising and falling spheres. *Journal of Fluid Mechanics* **651**, 251–294.

Horowitz, M. & Williamson, C. H. K. 2010*b* The effect of reynolds number on the dynamics and wakes of freely rising and falling spheres. *Journal of Fluid Mechanics* **651**, 251–294.

Hu, H.H. 1996 Direct simulation of flows of solid–liquid mixtures. *Int. J. Multiphase Flow* **22**, 335–352.

Hu, H.H., Patankar, N.A. & Zhu, M.Y. 2001 Direct numerical simulations of fluid–solid systems using the arbitrary lagrangian–eulerian technique. *Journal of Computational Physics* **169**, 427–462.

Höfler, Kai, Müller, Matthias, Schwarzer, Stefan & Wachmann, Bernd 1998 Interacting particle-liquid systems. *High Perf. Comput. in Sc. and Eng.* pp. 54–64.

Jenny, M. 2003 Etude de la transition au chaos d'une sphère en ascension ou en chute libre dans un fluide newtonien. PhD thesis, Université Louis Pasteur.

Jenny, M., Bouchet, G. & Dušek, J. 2003 Nonvertical ascension or fall of a free sphere in a Newtonian fluid. *Physics of Fluids* **15**, L9–L12.

Jenny, M. & Dušek, J. 2004 Efficient numerical method for the direct numerical simulation of the flow past a single light moving spherical body in transitional regimes. *Journal of Computational Physics* **194**, 215–232.

Jenny, M., Dušek, J. & Bouchet, G. 2004 Instabilities and transition of a sphere falling or ascending freely in a Newtonian fluid. *J. Fluid Mech.* **508**, 201–239.

Johnson, T.A. & Patel, V.C. 1999 Flow past a sphere up to a Reynolds number of 300. *J. Fluid Mech.* **378**, 19–70.

Karamanev, Dimitar G. & Nikolov, Ludmil N. 1992 Free rising spheres do not obey newton's law for free settling. *AIChE Journal* **38** (11), 1843–1846.

Karniadakis, G.E., Israeli, M. & Orszag, S.A. 1991 High-order splitting methods for the incompressible navier-stokes equations. *Journal of Computational Physics* **97** (2), 414–443.

Kim, J., Kim, D. & Choi, H. 2001 An immersed-boundary finite-volume method for simulations of flow in complex geometries. *Journal of Computational Physics* **171**, 132–150.

Komori, S. & Kurose, R. 1996 The effect of shear and spin on particle lift and drag in shear flow at high reynolds numbers. *Kluwer Academic Publishers, Advances in Turbulence* **VI**, 551–554.

Kotouč, M. 2008 Transition à la turbulence du sillage d'une sphère fiwe ou libre en convection mixte. PhD thesis, Université Louis Pasteur, Strasbourg I.

Kotouč, M., Bouchet, G. & Dušek, J. 2008 Loss of axisymmetry in flow past a heated sphere - assisting flow. *Int. J. Heat Mass Transfer* **51**, 2686–2700.

Kotouč, M., Bouchet, G. & Dušek, J. 2009*a* Drag and flow reversal in mixed convection past a heated sphere. *Physics of Fluids* **21**, 054104.

Kotouč, M., Bouchet, G. & Dušek, J. 2009*b* Transition to turbulence in the wake of a fixed sphere in mixed convection. *J. Fluid Mech.* **625**, 205–248.

Kry, P. R. & List, Roland 1974 Angular motions of freely falling spheroidal hailstone models. *Physics of Fluids* **17** (6), 1093–1102.

Levi, E. 1980 Three-dimensional wakes - origin and evolution. *Journal of the American Society of Civil Engineers* **106**, 659–676.

Liu, D., Keaveny, E.E., Maxey, M.R. & Karniadakis, G.E. 2009 Force coupling method for flows with ellipsoidal particles. *Journal of Computational Physics* **228**, 3559–3581.

Lunde, K & Perkins, RJ 1998 Shape oscillations of rising bubbles. *Applied Scientific Research* **58** (1-4), 387–408.

Magarvey, R. H. & Bishop, Roy L. 1961*a* Transition ranges for three-dimensional wakes. *Can. J. Phys.* **39**, 1418.

Magarvey, R. H. & Bishop, Roy L. 1961*b* Wakes in liquid-liquid systems. *Physics of Fluids* **4** (7), 800–805.

Magarvey, R. H. & MacLatchy, C. S. 1965 Vortices in sphere wakes. *Canadian Journal of Physics* **43** (9), 1649–1656.

Magnaudet, J. 1997 The forces acting on bubbles and rigid particles. *ASME Fluids Engineering Division Summer meeting* pp. 1–9.

Magnaudet, J. & Eames, I. 2000 The motion of high-reynolds-number bubbles in inhomogeneous flows. *Ann. Rev. of Fluid Mech.* **32**, 659–708.

Magnaudet, Jacques, Rivero, Mayela & Fabre, Jean 1995 Accelerated flows past a rigid sphere or a spherical bubble. part 1. steady straining flow. *Journal of Fluid Mechanics* **284**, 97–135.

Mahadevan, L., Ryu, William S. & Samuel, Aravinthan D. T. 1999 Tumbling cards. *Physics of Fluids* **11** (1), 1–3.

Maxey, M.R. & Patel, B.K. 2001 Localized force representation for particles sedimenting in stokes flow. *Int. J. Multiphase Flow* **27**, 1603–1626.

Maxey, Martin R. & Riley, James J. 1983 Equation of motion for a small rigid sphere in a nonuniform flow. *Physics of Fluids* **26** (4), 883–889.

Meliga, P., Chomaz, J.M. & Sipp, D. 2009 Global mode interaction and pattern selection in the wake of a disk: a weakly nonlinear expansion. *J. Fluid Mech.* **633**, 159–189.

Mittal, R. 1999 A Fourier-Chebyshev spectral collocation method for simulating flow past spheres and spheroids. *Int. J. Numer. Meth. Fluids* **30**, 921–937.

Monkewitz, Peter A. 1988 A note on vortex shedding from axisymmetric bluff bodies. *Journal of Fluid Mechanics* **192**, 561–575.

Mougin, G. & Magnaudet, J. 2002 Path instability of a rising bubble. *Phys. Rev. Lett.* **88**, 014502.

Nakamura, Isao 1976 Steady wake behind a sphere. *Physics of Fluids* **19** (1), 5–8.

Natarajan, R. & Acrivos, A. 1993 The instability of the steady flow past spheres and disks. *J. Fluid Mech.* **254**, 323–344.

Newton, Isaac 1726 *The Principia: Mathematical Principles of Natural Philosophy*.

Ormières, Delphine & Provansal, Michel 1999 Transition to turbulence in the wake of a sphere. *Phys. Rev. Lett.* **83**, 80–83.

Pan, T-W, Glowinski, R. & Galdi, G.P. 2002 Direct simulation of the motion of a settling ellipsoid in newtonian fluid. *J. Comput. Applied Math.* **149**, 71–82.

Pan, T-W, Joseph, D.D. & Glowinski, R. 2005 Simulating the dynamics of fluid–ellipsoid interactions. *Comput. Struct.* **83**, 463–478.

Patera, A. 1984 A spectral element method for fluid dynamics: laminar flow in a channel expansion. *Journal of Computational Physics* **54** (3), 468–488.

Peskin, C.S. 2002 The immersed boundary method. *Acta Numerica* **11**, 479–517.

Przadka, A., Miedzik, J., Gumowski, K., Goujon-Durand, S. & Wesfreid, J. E. 2008 The wake behind the sphere; analysis of vortices during transition from steadiness to unsteadiness. *Arch. of Mech.* **60** (6), 467–474.

Rimon, Y. & Cheng, S. I. 1969 Numerical solution of a uniform flow over a sphere at intermediate reynolds numbers. *Physics of Fluids* **12**, 949–959.

Rivero, M, Magnaudet, J. & Fabre, J. 1991 Quelques résultats nouveaux concernant les forces exercées sur une inclusion sphérique par un écoulement accéléré = new results on the forces exerted on a spherical body by an accelerated flow. *Acad. Sci. Paris Serie II* **284** (312), 1499–1501.

Russel, W.B., Saville, D.A. & Schowalter, W.R. 1992 *Colloidal Dispersions*. Cambridge University Press.

Sakamoto, H. & Haniu, H. 1995 The formation mechanism and shedding frequency of vortices from a sphere in uniform shear flow. *J. Fluid Mech.* **287**, 151–171.

Schiller, L. & Neumann, A. 1933 Self-sustained oscillations in the wake of a sphere. *Zeit. Ver. Deut. Ing.* **77**, 318–320.

Shenoy, A.R. & Kleinstreuer, C. 2010 Influence of aspect ratio on the dynamics of a freely moving circular disk. *J. Fluid Mech.* **653**, 463–487.

Shenoy, A. R. & Kleinstreuer, C. 2008 Flow over a thin circular disk at low to moderate Reynolds number. *J. Fluid Mech.* **605**, 253–262.

Sherwood, J.D. & Stone, H.A. 1997 Added mass of a disc accelerating within a pipe. *pof* **9**, 3141–3148.

Stringham, G.E., Simons, D.B. & Guy, H.P. 1969 *The Behavior of Large Particles Falling in Quiescent Liquids*. U.S. Government Printing Office.

Strogatz, S.H. 1994 *Nonlinear Dynamics and Chaos*. Addison-Wesley.

Szaltys, P., Chrust, M., Przadka, A., Goujon-Durand, S., Tuckerman, L.S. & Wesfreid, J.E. 2011 Nonlinear evolution of instabilities behind spheres and disks. *Journal of Fluids and Structures* **27** (5–6), 743 – 747.

Tanabe, Yoshihiro & Kaneko, Kunihiko 1994 Behavior of a falling paper. *Phys. Rev. Lett.* **73**, 1372–1375.

Taneda, Sadatoshi 1956 Experimental investigation of the wake behind a sphere at low reynolds numbers. *Journal of the Physical Society of Japan* **11**, 1104.

Tomboulides, Ananias G. & Orszag, Steven A. 2000 Numerical investigation of transitional and weak turbulent flow past a sphere. *J. Fluid Mech.* **416**, 45–73.

Tomboulides, A. G., Orszag, S. A. & Karniadakis, G. E. 1993 Direct and large-eddy simulation of axisymmetric wakes. In *31st Aerospace Sciences Meeting & Exhibit*.

Udaykumar, H.S., Mittal, R., Rampunggoon, P. & Khanna, A. 2001 A sharp interface cartesian grid method for simulating flows with complex moving boundaries. *Journal of Computational Physics* **174**, 345–380.

Uhlmann, M. 2005 An immersed boundary method with direct forcing for the simulation of particulate flows. *Journal of Computational Physics* **209**, 448–476.

Uhlmann, M. 2008 Interface-resolved direct numerical simulation of vertical particulate channel flow in the turbulent regime. *Physics of Fluids* **20**, 053305.

Veldhuis, C.H.J. & Biesheuvel, A. 2007 An experimental study of the regimes of motion of spheres falling or ascending freely in a newtonian fluid. *International Journal of Multiphase Flow* **33** (10), 1074 – 1087.

Walker, G. 1981 Generation and dispersal of fine ash and dust by volcanic eruptions. *Journal of Volcanology and Geothermal Research* **11**, 81 – 92.

Willmarth, W.W., Hawk, N.E. & Harvey, R.L. 1964 Steady and unsteady motions and wakes of freely falling disks. *Physics of Fluids* **7**, 197–208.

Wu, Mingming & Gharib, Morteza 2002 Experimental studies on the shape and path of small air bubbles rising in clean water. *Physics of Fluids* **14** (7), L49–L52.

Zastawny, Marian, Mallouppas, George, Zhao, Fan & van Wachem, Berend 2012 Derivation of drag and lift force and torque coefficients for non-spherical particles in flows. *International Journal of Multiphase Flow* **39** (0), 227 – 239.

Zhong, Hongjie, Chen, Shiyi & Lee, Cunbiao 2011 Experimental study of freely falling thin disks: Transition from planar zigzag to spiral. *Physics of Fluids* **23** (1), 011702.